FINAL REPORT

UPDATE OF THE PROBABILISTIC SEISMIC HAZARD ANALYSIS AND DEVELOPMENT OF SEISMIC DESIGN GROUND MOTIONS AT THE LOS ALAMOS NATIONAL LABORATORY

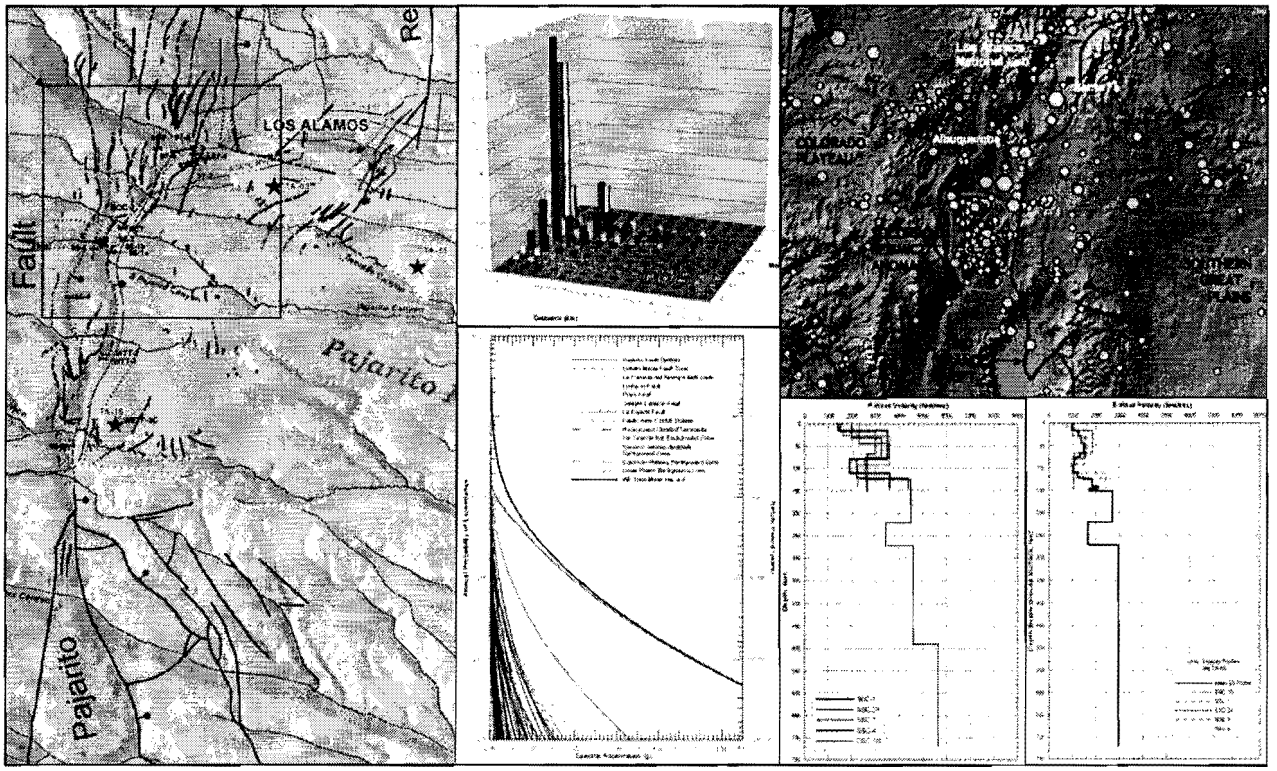

Prepared for
Los Alamos National Laboratory

25 May 2007

Prepared by
Ivan Wong, Walter Silva, Susan Olig, Mark Dober, Nick Gregor, Jamie Gardner, Claudia Lewis, Fabia Terra, Judith Zachariasen, Kenneth Stokoe, Patricia Thomas, and Shobhna Upadhyaya

As a subcontractor to Burns and Roe Enterprises, Inc.

URS

URS Corporation
Seismic Hazards Group
1333 Broadway, Suite 800
Oakland, California 94612

Job No. 24342433

TABLE OF CONTENTS

TABLE OF CONTENTS

TABLE OF CONTENTS

Appendices

Tables

Figures

Plates

APE	annual probabilities of exceedance
CDF	cumulative distribution function
CEUS	central and eastern U.S.
CMRR	Chemistry and Metallurgical Research Replacement
D	material damping ratio
DBE	Design/Evaluation Basis Earthquake
DMIN	distance to the closest seismographic station
D^{mode}	modal distance
DOE	U.S. Department of Energy
DRS	Design Response Spectrum
EPRI	Electric Power Research Institute
ERZ	standard error in focal depth
g	gravitational acceleration (980 cm/sec^2)
G	shear modulus
GM	Guaje Mountain
ka	thousand years
ky	thousand years ago
LANL	Los Alamos National Laboratory
M	moment magnitude
M	unspecified magnitude scale
M_D	duration magnitude
M_{max}	maximum magnitude
M^{mode}	modal magnitude
NGA	Next Generation of Attenuation
NMBGMR	New Mexico Bureau of Geology and Mineral Resources
NMIMT	New Mexico Institute of Mining and Technology
P(a)	probability of activity
PAF	Pajarito fault
PDEs	Preliminary Determination of Epicenters (USGS)
PE&A	Pacific Engineering & Analysis
PEER	Pacific Earthquake Engineering Research
PFS	Pajarito fault system
PGA	peak horizontal ground acceleration
PSHA	probabilistic seismic hazard analysis
Q(f)	frequency-dependent crustal attenuation parameter
Qbo	Otowi member of the Bandelier Tuff
Qbog	Guaje Pumice Bed
Qbt1	Tshirege member of the Bandelier Tuff
	Subunits
	Qbt1g
	Qbt1v
	Qbt2
	Qbt3L
	Qbt3U
	Qbt4
Qbtt	Tsankawi Pumice Bed

Qct	Cerro Toledo Rhyolite epiclastic deposits
RC	Rendija Canyon
RCTS	resonant column and torsional shear
RGR	Rio Grande rift
RVT	random vibration theory
SA	spectral acceleration
SC	Sawyer Canyon
SCC	Santa Clara Canyon fault
SDC	Seismic Design Category
SRSS	square root of the sum of the squares
SSA	Socorro Seismic Anomaly
SSCs	structures, systems, and components
SSHAC	Senior Seismic Hazard Analysis Committee
SSI	soil-structure interaction
TFI	Technical Facilitator Integrator
TI	Technical Integrator
UHRS	Uniform Hazard Response Spectrum
URS	URS Corporation
UTA	University of Texas at Austin
V_P	compressional-wave velocity
V_S	shear-wave velocity
VSP	vertical seismic profiling
WCFS	Woodward-Clyde Federal Services
WGCEP	Working Group for California Earthquake Probabilities
WUS	western U.S.

At the request of the Los Alamos National Laboratory (LANL), URS Corporation and Pacific Engineering & Analysis (PE&A), with support from the Earth and Environmental Sciences Division at LANL, have updated the 1995 probabilistic seismic hazard analysis (PSHA) of LANL (Wong *et al.*, 1995), and developed Design/Evaluation Basis Earthquake (DBE) ground motion parameters. Both Uniform Hazard Response Spectra (UHRS) and Design Response Spectra (DRS) have been calculated per ASCE/SEI 43-05 for the site of the Chemistry and Metallurgical Research Replacement (CMRR) building and for Technical Areas TA-3, TA-16, and TA-55. Site-wide and reference rock-outcrop (dacite) ground motions have also been developed and are recommended for use in the design of facilities in other Technical Areas. DRS were computed for Seismic Design Categories (SDC)-3 (2,500-year return period), -4 (2,500 years), and -5 (10,000 years).

The PSHA was conducted following the guidelines of the Senior Seismic Hazard Analysis Committee for a Level 2 PSHA. Principal inputs required for the development of the DBE ground motions include a seismic source model, ground motion attenuation relationships, and velocity and nonlinear dynamic properties of the lower Quaternary (1.2 to 1.6 Ma) Bandelier Tuff beneath each site.

Since 1995, the only new geotechnical, geologic, and geophysical data available to characterize the dynamic properties of the subsurface geology beneath LANL, particularly the Bandelier Tuff, are the results of investigations performed at the CMRR site. Downhole-velocity, OYO-suspension velocity, and seismic crosshole surveys were performed in boreholes drilled in 2005 at that site. The boreholes include four shallow holes at the corners of the proposed CMRR building footprint (SSC-1 to SSC-4), one deep hole in the center of the footprint (DSC-1B), and a deep hole outside and to the east of the footprint (DSC-2A). Dynamic laboratory testing was also performed by the University of Texas at Austin (UTA) on 22 samples collected in the CMRR boreholes. The dynamic properties that were evaluated are the strain-dependent shear modulus (G) and material damping ratio (D) of the samples. Based principally on the new CMRR data and data collected in 1995, base-case profiles of low-strain shear-wave velocity (V_S) and compressional-wave velocity (V_P) were developed for the CMRR, TA-3, TA-16, and TA-55 sites. Of particular significance to the site response analysis was the existence of the geologic unit Qbt3L, a low-velocity zone within the Bandelier Tuff. Unit-specific shear-modulus reduction and damping curves were developed on the basis of the dynamic laboratory testing results, including the 1995 testing. One set of curves for each unit was corrected for sample disturbance by adjusting reference strains by the ratio of laboratory-to-field V_S measurements.

The 50-km-long Pajarito fault system (PFS) extends along the western margin of LANL and is the dominant contributor to the seismic hazard at the laboratory because of its close proximity and rate of activity. The current (or new) characterization of the PFS is significantly revised from the 1995 study in order to incorporate a considerable amount of new mapping, displacement measurements, and paleoseismic data for the PFS. The PFS is a broad zone of faults that form an articulated monoclinal flexure, which consists of several distinct fault segments that have linked together. The PFS exhibits complex rupture patterns and shows evidence for at least two, probably three surface-faulting earthquakes since 11 ka. This recent temporal clustering of events is in contrast to evidence for the occurrence of only six to nine events since 110 ka although this longer record is likely incomplete. For the new analysis, both segmented and unsegmented rupture models were considered for the PFS, favoring the latter

which is characterized by a 36-km-long, floating earthquake rupture source. Two types of multisegment ruptures for the PFS were also considered: simultaneous (a single large earthquake) and synchronous (two subevents). The preferred range of maximum earthquakes is from moment magnitude (**M**) 6.5 to 7.3. Recurrence rates are dependent on rupture model and both long-term slip rate and late Quaternary recurrence interval data were considered. For the preferred unsegmented rupture model, the weighted-mean slip rate was 0.21 mm/yr, and weighted mean recurrence intervals were 4,400 years (for the logic tree branch assuming temporal clustering) and 17,600 years (for the not-in-a-cluster branch). For the segmented rupture model, a moment-balancing approach was used similar to that used by the Working Group on California Earthquake Probabilities (2003) to partition the slip rate of a segment into earthquakes representing various rupture scenarios and to keep the fault in moment equilibrium. Thus, rates vary for each rupture scenario but overall were consistent with the long-term slip rates of the segmented rupture model.

In addition to the dominant PFS, 55 additional fault sources were included in the PSHA. Parameters that were characterized for each fault include: (1) rupture model including independent versus dependent, single plane versus zone, segmented versus unsegmented, and linked configurations; (2) probability of activity; (3) fault geometry including rupture length, rupture width, fault orientation, and sense of slip; (4) maximum magnitude (**M**); and (5) earthquake recurrence, including both recurrence models and rates (using recurrence intervals and/or fault slip rates). There are sparse data on rates of activity for many faults so the approach developed by McCalpin (1995) was applied to characterize fault slip rate distributions. McCalpin's analysis was updated, adding 15 slip rate observations from six additional faults.

In addition to active faults, three areal earthquake source zones were defined based on seismotectonic provinces in the LANL region: the Rio Grande rift, Southern Great Plains, and Colorado Plateau. Due to its high level of seismicity, the Socorro Seismic Anomaly was also modeled as an areal source zone and differentiated from the Rio Grande rift. Earthquake recurrence rates computed for each areal source zone are based on an updated (through 2005) historical seismicity catalog. In addition to the traditional approach of using areal source zones, Gaussian smoothing with a spatial window of 15 km was used to address the hazard from background seismicity and to incorporate a degree of stationarity. The two approaches, areal sources and Gaussian smoothing were weighted equally to compute the hazard from background seismicity in the PSHA.

A combination of both empirical and site-specific attenuation relationships were used in the PSHA. The empirical models were weighted as follows: Abrahamson and Silva (1997), modified for normal faulting, 0.45; Spudich *et al.* (1999), 0.35; Campbell and Bozorgnia (2003), 0.10; Sadigh *et al.* (1997), 0.05; and Boore *et al.* (1997), 0.05. The relationships were weighted based on their appropriateness for the extensional Rio Grande rift. Because the epistemic variability was deemed insufficient as provided by the five attenuation relationships, they were all scaled to obtain a total sigma (ln) of 0.4.

To compensate for the lack of region-specific attenuation relationships, the stochastic ground motion modeling approach was used, as it was in 1995, to develop site-specific relationships for LANL. The point-source version of the stochastic methodology was used to model earthquakes from **M** 4.5 to 8.5 in the distance range of 1 to 400 km. To accommodate finite-source effects at large magnitudes (**M** > 6.5), model simulations included an empirical magnitude-dependent

short-period saturation as well as a magnitude-dependent far-field fall off. Relationships were developed for the CMRR, TA-3, TA-16, and TA-55 sites. A relationship for dacite was also developed. Aleatory variabilities in stress drop, magnitude-dependent point-source depths, the crustal attenuation parameters Q_o and η, and kappa were included in the computations of the attenuation relationships through parametric variations. Site-specific profiles (low-strain V_S, and V_P down to dacite) as well as modulus-reduction and hysteretic-damping curves were also randomly varied.

Variability (aleatory) in the regression of the simulated data is added to the modeling variability to produce 16th, 50th (median), and 84th percentile attenuation relationships. Thirty simulations were made for each magnitude and distance, and the results fitted with a functional form that accommodates magnitude-dependent saturation as well as far-field fall-off. Twelve attenuation relationships developed for the CMRR site were derived from three stress drops, two velocity models, and two sets of dynamic material properties. For the TA-3, TA-16, and TA-55 sites there were nine attenuation relationships derived from three stress drops, one velocity profile, and three sets of dynamic curves. There were six attenuation relationships for dacite derived from one profile, two sets of dynamic curves, and three stress drops.

In the 1995 study, attention was focused on potential topographic effects on ground motions due to the location of LANL facilities on mesas. In this study, a suite of topographic amplification factors was developed for LANL on the basis of (1) recent LANL modeling results, (2) other modeling results and observations in the literature, and (3) recommendations of Eurocode 8. The amplification factors are based on slope angles following Eurocode 8 as well as the French Seismic Code. To accommodate a fully probabilistic hazard analysis, both median estimates and standard deviations were developed, based on ranges of factors in modeling results and observations.

Probabilistic seismic hazard was calculated for the ground surface at CMRR, TA-3, TA-16, TA-55 and the top of dacite at TA-55. The hazard from the site-specific stochastic and empirical western U.S. soil attenuation relationships was calculated separately for each type of relationship. The modeling shows that the probabilistic hazard for peak horizontal ground acceleration (PGA) at all the above sites is controlled primarily by the PFS at all return periods. The PFS similarly controls the hazard at LANL for longer-period ground motions, such as 1.0 sec spectral acceleration (SA). Background seismicity in the Rio Grande rift, which contributed to the hazard at LANL in the 1995 study, is not a significant contributor in this new analysis, probably due to the increased activity rate of the PFS in the Holocene (clustering).

In calculating the probabilistic ground motions at LANL, the surface motions must be hazard consistent; that is, the annual exceedance probability of the soil UHRS should be the same as the rock UHRS. In NUREG/CR-6728, several site response approaches are recommended for use to produce soil motions consistent with the rock outcrop hazard. These approaches also incorporate site-specific aleatory variabilities of soil properties into the soil motions. To compute the site-specific ground-shaking hazard at LANL, we used two different approaches: (1) empirical attenuation relationships for the western U.S. (WUS) generic deep firm soil and (2) site-specific attenuation relationships. In the case of the latter, the site response is contained in the stochastic attenuation relationships (Approach 4). For the empirical attenuation relationships, the

computed generic soil hazard curves from the PSHA were adjusted for the site-specific site conditions at each of the LANL sites using computed amplification factors (Approach 3).

The point-source version of the stochastic ground motion model was used to generate the amplification factors (the ratios of the response spectra at the top of the site profiles to the WUS soil). They are a function of the reference (WUS deep firm soil) peak acceleration, spectral frequency, and nonlinear soil response. Amplification factors were computed for CMRR (4 sets), TA-3 (3 sets), TA-16 (3 sets), and TA-55 (3 sets), based on the velocity profiles and properties, but only one set was computed for the top of dacite. The point-source stochastic model was also used to compute site-specific vertical-to-horizontal (V/H) ratios. To accommodate model epistemic variability following the approach used for the horizontal hazard analyses, empirical deep firm soil V/H ratios were also used with equal weights between the stochastic and empirical models.

The hazard curves derived from the empirical attenuation relationships and the amplification factors were used to calculate site-specific hazard curves using Approach 3. These hazard curves and the hazard curves based on site-specific stochastic attenuation relationships (Approach 4) were then weighted equally and the topographic amplification factors and V/H ratios were applied. In seismic hazard analyses, epistemic uncertainty (due to lack of knowledge) of parameters and models is typically represented by a set of weighted hazard curves. Using these sets of curves as discrete probability distributions, they can be sorted by the frequency of exceedance at each ground-motion level and summed into a cumulative probability mass function. The weighted-mean hazard curve is the weighted average of the exceedance frequency values.

Based on the final site-specific hazard curves, mean horizontal UHRS were computed for CMRR, TA-3, TA-16, and TA-55. The TA-55 UHRS is based on an envelope of the hazard curves of CMRR and the hazard curve developed on basis of the 1995 borehole velocity profiles (SHB-1). Dacite and site-wide mean horizontal UHRS were also computed. The site-wide UHRS is derived from an envelope of the hazard curves of CMRR, TA-3, TA-16, and TA-55. Table ES-1 lists the horizontal and vertical PGA values for the UHRS.

The new PSHA shows that the horizontal surface PGA values are about 0.5 g at a return period of 2,500 years. The vertical PGA values at the same return period are about 0.3 g. The 1995 horizontal PGA values for a return period of 2,500 years are about 0.33 g. The estimated hazard has increased significantly (including other spectral values) from the 1995 study due to the increased ground motions from the site-specific stochastic attenuation relationships and increase in the activity rate of the PFS. The site response effects as modeled in this study with the newer site geotechnical data appears to amplify ground motions more than in the 1995 analysis. Other factors could be the increased epistemic uncertainty incorporated into the empirical attenuation relationships and in the characterization of the PFS.

Horizontal and vertical DRS for CMRR, TA-3, TA-16, TA-55, dacite, and site-wide were calculated for SDC-3, -4, and -5. Table ES-2 lists the horizontal and vertical PGA values for the DRS. DRS at other dampings levels of 0.5%, 1%, 2%, 3%, 7%, and 10% were computed from the 5%-damped DRS using empirical damping ratios.

Strain-compatible properties including V_S, V_S sigma, S-wave damping, S-wave damping sigma, V_P, V_P sigma, P-wave damping, and strains as a function of depth were calculated for return periods of 2,500 and 10,000 years. The strain-compatible properties are consistent with the mean hazard.

Time histories were developed through spectral matching following the recommended guidelines contained in NUREG/CR-6728. The phase spectra were taken from accelerograms of the 23 November 1980 (1934 GMT) **M** 6.9 Irpinia, Italy, earthquake recorded at the Sturno strong motion site.

Table ES-1
LANL Mean PGA Values (g) From the UHRS

Return Period (years)	CMRR		TA-3		TA-16		TA-55		Site-Wide		Dacite	
	Horiz.	Vert.	Horiz.	Vert.	Horiz.	Vert.	Horiz.	Vert.	Horiz.	Vert.	Horiz.	Vert.
1,000	0.27	0.32	0.27	0.32	0.25	0.31	0.27	0.32	0.27	0.32	0.13	0.12
2,500	0.52	0.60	0.52	0.59	0.47	0.57	0.52	0.60	0.52	0.60	0.27	0.27
10,000	1.03	1.21	1.03	1.10	0.93	1.05	1.03	1.21	1.03	1.21	0.65	0.65
25,000	1.47	1.79	1.45	1.57	1.33	1.50	1.47	1.79	1.47	1.79	1.01	0.97
100,000	2.30	3.01	2.29	2.79	2.11	2.57	2.30	3.01	2.30	3.01	1.69	1.65

Table ES-2
LANL PGA Values (g) From the DRS

SDC	CMRR		TA-3		TA-16		TA-55		Site-Wide		Dacite	
	Horiz.	Vert.	Horiz.	Vert.	Horiz.	Vert.	Horiz.	Vert.	Horiz.	Vert.	Horiz.	Vert.
3	0.47	0.56	0.47	0.53	0.43	0.50	0.47	0.60	0.47	0.56	0.28	0.27
4	0.72	0.87	0.71	0.78	0.65	0.74	0.72	0.86	0.72	0.86	0.47	0.45
5	1.17	1.50	1.17	1.39	1.07	1.29	1.17	1.50	1.17	1.50	0.84	0.82

SDC = Seismic Design Category

At the request of the Los Alamos National Laboratory (LANL), the following report describes and summarizes an update of the probabilistic seismic hazard analysis (PSHA) of LANL and development of Design/Evaluation Basis Earthquake (DBE) ground motions for the Chemistry and Metallurgical Research Replacement (CMRR) site and Technical Areas TA-3, TA-16, and TA-55. Site-wide and a reference rock outcrop (dacite) ground motions have also been developed and are recommended for use in the design of facilities in other Technical Areas. Both Uniform Hazard Response Spectra (UHRS) and Design Response Spectra (DRS) have been calculated per ASCE/SEI 43-05. DRS were computed for Seismic Design Categories (SDC)-3 (2,500-year return period), -4 (2,500 years), and -5 (10,000 years). This study was performed by URS Corporation and Pacific Engineering & Analysis (PE&A) with support from the Earth and Environmental Sciences Division at LANL. The project was initiated in September 2004.

LANL is managed and operated by the Los Alamos National Security LLC for the U.S. Department of Energy (DOE). As part of DOE Order 420.1 (2002), LANL is required to:

1. *Review and update the natural phenomena hazards assessments, as necessary, if there are significant changes in natural phenomena hazards assessment methodology or site-specific information, and*

2. *Conduct a review of the natural phenomena hazards assessment at least every 10 years. The review shall include recommendations to DOE on the need for updating the existing natural phenomena hazard assessments based on identification of any significant changes in methods or data.*

The purpose of this project is to update the LANL PSHA performed by Woodward-Clyde Federal Services (WCFS) in 1995 and to revise the DBE ground motions prescribed in the LANL Engineering Standards Manual, Chapter 5, Structural. The 1995 WCFS study was the most comprehensive seismic hazard evaluation ever performed for LANL. The study had as its basis several years of studies previously performed by LANL staff (Gardner and House, 1987). The results of the WCFS study, published in an internal report titled "Seismic Hazards Evaluation of the Los Alamos National Laboratory" and dated 24 February 1995, provided DBE ground motions that were subsequently incorporated into the LANL Engineering Standards Manual as the basis for the design of new or updated facilities. A supplementary report to this report that contains final vertical DRS for LANL has also been prepared and submitted to LANL for incorporation into the Engineering Standards Manual.

Since the 1995 study was completed, new guidelines, data and information have emerged. Pertinent to any new PSHA for LANL are the following:

1) DOE has changed the definitions of ground motions to be used for their facilities *(Natural Phenomena Hazards Design and Evaluation Criteria for U.S. Department of Energy Facilities*, DOE-STD-1020-2002, January 2002);

2) New guidelines for conducting a PSHA have been developed (SSHAC, 1997);

3) Ground motion-attenuation models for extensional tectonic regimes such as the Basin and Range Province, have been developed;

4) Geotechnical data on the subsurface geology of the CMRR have been collected;

5) LANL geologists have performed a number of additional geologic investigations, including new mapping of the Pajarito fault system (PFS);

6) Additional information on the paleoseismic chronology of events from new trenches along the PFS and other faults in the region has become available; and

7) Issues relevant to site response and topographic effects have become the focus of the recent geotechnical siting of the CMRR.

1.1 SCOPE OF WORK

To address and incorporate the above changes in an update of the LANL PSHA, the following scope of work was performed (Figure 1-1). Task descriptions are provided to give an overview of the work that was performed. Details can be found in the relevant sections of the report. The study was performed as a SSHAC (1997) Level 2 analysis (Section 2.4).

1.1.1 Task Description

Task 1 Updating and Revision of Seismic Source Model

This task consisted of three primary subtasks: (1) updating the seismic source characterization of the PFS; (2) reviewing and revising the McCalpin slip rate frequency distribution first developed for the 1995 study; and (3) revising the characterization of regional faults. In subtask 1, the initial PFS model is the model developed in the probabilistic fault displacement hazard analysis for TA-16 (Olig *et al.*, 2001). This model was revised based on recent LANL mapping and paleoseismic investigations. A key issue is whether the PFS exhibits temporal clustering and if so, is the fault still in a cluster. For subtask 2, new paleoseismic data on Rio Grande rift (RGR) faults were compiled and reviewed and the slip rate frequency distribution was revised. For subtask 3, our RGR fault model (Wong *et al.*, 2004) was revised by including (a) new data for faults within 50 km of LANL that contribute more than 5% to the hazard at LANL, (b) slip rates with the new RGR frequency slip-rate distribution, and (c) reassessed maximum magnitude for each fault. The characterization of longer more active faults that contribute more than 5% of the hazard at the site within 100 km was also revised. The recurrence models (e.g., characteristic, maximum magnitude, or truncated exponential) were re-evaluated.

Task 2 Updating Catalog and Evaluation of Historical Seismicity

This task consisted of updating the WCFS (1995) historical seismicity catalog, which includes both pre-instrumental and instrumental seismicity, and evaluating the earthquake record in the LANL region. The objectives of this task were to (1) characterize seismogenic sources in the LANL region in terms of their geometry and earthquake-generating parameters; (2) evaluate the possible association of seismicity with specific faults or other geological structures; and (3) characterize the regional tectonic stresses. The network-determined earthquake locations were reviewed for their accuracy. Earthquake recurrence rates for the regional source zones (i.e., areal zones of background seismicity) were estimated using the updated catalog, which was corrected for completeness and had dependent events removed. The resulting homogeneous

catalog of independent events was also used for the alternative approach of Gaussian smoothing of the regional seismicity in the PSHA.

Task 3 Compilation, Review, and Analyses of Site Geotechnical Data

The objective of this task was to update the characterization of the subsurface geology for CMRR and the three technical areas to depths beneath the Bandelier tuff, which is extensive beneath the entire LANL and is primarily responsible for the site response effects on ground motions. All geotechnical and site geologic data collected since 1995 were compiled, reviewed, and analyzed. Of particular interest were the new shear-wave velocity data and dynamic laboratory testing results from the site investigations conducted for the CMRR. Site-specific shear-wave and compressional velocity profiles were developed for CMRR based on these new data. Site-specific profiles for each of the three technical areas were revised based on the new data. Shear-modulus reduction and damping curves were reassessed for their appropriateness. Because the seismic hazard was calculated for annual probabilities of exceedance (APE) as low as 10^{-6}, the probabilistic hazard calculations used a three-sigma truncation on the aleatory uncertainty of the ground motion attenuation relationships.

Task 4 Evaluation of Kappa

Kappa (κ), the parameter that characterizes the near-surface attenuation beneath a site was evaluated. Values of κ were previously derived in 1995 from an analysis of earthquakes recorded at several stations of the LANL seismographic network whose subsurface geology was similar to that of the technical areas of interest. Waveforms from selected local and regional events recorded since 1995 were analyzed to evaluate the validity of the kappa value of 0.035 sec that was used in 1995, along with an estimate of its uncertainty.

Task 5 Review and Selection of Empirical Attenuation Relationships and Development of Site-Specific Relationships

It was expected that new empirical attenuation relationships for normal faulting developed by the Pacific Earthquake Engineering Research (PEER) Center-sponsored NGA (Next Generation of Attenuation) Project would be available by mid-March 2005. However, no attenuation relationship became available in time to be used for this study. Thus existing ground motion prediction relationships for soil were evaluated for their appropriateness and used in our study.

Site-specific attenuation relationships for CMRR and TA-3, TA-16, and TA-55 were derived from numerical modeling based on the stochastic point-source ground motion model as was done in 1995. The attenuation relationships were developed for the ground surface. Relationships for a site-wide reference rock datum, the top of dacite, were also developed. Input parameters included magnitude-dependent stress drops and focal depths, the crustal attenuation parameters Q and η, and kappa (κ). Epistemic and aleatory uncertainties were partitioned in the attenuation relationships. An RVT-equivalent-linear approach was used to incorporate nonlinear site response in the attenuation relationships.

Task 6 Evaluation of Topographic Effects for Design

The effects of mesa and canyon topography at LANL on ground motions were re-evaluated. In addition, a review of earthquake recordings made since 1995 at the LANL by the local seismograph network was performed to assess topographic effects. Adjustments to design spectra were based on the results of this task as well as other available information relating to topographic effects.

Task 7 PSHA Calculations

The objective of this task was to perform a state-of-the-art PSHA that incorporates the most up-to-date information on seismic sources, ground motion attenuation, and site effects. Epistemic uncertainty was addressed through the use of logic trees. Coseismic rupture of multiple faults was modeled. Site-specific hazard curves were calculated for CMRR, TA-3, TA-16, TA-55, and top of dacite. The probabilistic hazard was calculated using site-specific stochastic attenuation relationships and empirical relationships for deep firm soil. Deaggregation of the hazard was performed to define the modal M (magnitude) and D (distance). As part of sensitivity analyses, key parameters for the PFS, e.g., recurrence intervals/slip rates and rupture scenarios, were varied to evaluate their impact on the hazard at the LANL.

Task 8 Development of Site-Specific V/H Ratios

Site-specific V/H ratios for ground motion were computed in a fashion similar to what was done in 1995. The stochastic point-source model and empirically-based V/H ratios were used to develop V/H ratios for each site and the top of dacite.

Task 9 Development of DBE Ground Motions

Approach 3 (NUREG-6728; McGuire *et al.*, 2002) was used to determine the site-specific hazard at each site by modifying the hazard calculated using the empirical attenuation relationships and amplification factors. The amplification factors were calculated using an RVT-based equivalent-linear site response approach and the site data from Task 3. This hazard was then combined with the hazard calculated from the stochastic attenuation relationships to arrive at the final hazard. Topographic effects and V/H were also incorporated probabilistically into the final hazard. Hazard-consistent hazard curves, UHRS, and DRS were calculated for CMRR and the three technical areas. Site-wide UHRS/DRS were also calculated by enveloping the site-specific hazard curves. Top of dacite UHRS/DRS were also calculated. UHRS/DRS were defined at APEs of 10^{-3}, $4x10^{-4}$, 10^{-4}, $4x10^{-5}$, and 10^{-5} (return periods of 2500, 10,000, 25,000, and 100,000 years, respectively). DRS were also calculated at dampings of 0.5%, 1%, 2%, 3%, 4%, 7%, and 10% using empirical damping ratios.

Task 10 Development of Risk-Consistent Spectra

UHRS down to an APE of 10^{-5} were calculated so that risk-consistent 5%-damped DRS could be developed for each of the four sites, site-wide, and the top of dacite consistent with ASCE-43. Risk-consistent spectra are derived by adjusting the UHRS by factors related to the appropriate

slopes of the hazard curves. Horizontal and vertical time histories were calculated based on the DRS for return periods of 2500 and 10,000 years.

Task 11 Meetings and Final Report

A series of workshop meetings was held at LANL with the Steering Committee and LANL staff to ensure a comprehensive participatory review of the PSHA process and the development of DBE parameters throughout the project; the project participants were also engaged in biweekly conference calls. This final report, which describes and summarizes the project, reflects iterative refinements resulting from those meetings and biweekly conference calls. A draft version of the report was reviewed by the Steering Committee and LANL, prior to the final (stakeholders) meeting and all comments were addressed and documented.

Task 12 Quality Assurance

URS worked under the URS' DOE Western Branch Quality Assurance Program, which meets NQA-1 standards. QA documentation has focused on reviews made by the Steering Committee during the process of the project and the final report. Responses to review comments were documented. Computer programs for the PSHA and site response analyses were validated and verified by URS. The QA Program manual was submitted to LANL for their review. The final report was reviewed by our contractor Burns & Roe to ensure that it conformed to the QA Program requirements.

1.1.2 Amended Scope

It should be noted that a significant change in our scope of work occurred about one year into the study when URS/PE&A proposed to LANL and the Steering Committee to use several new approaches in hazard analysis including the incorporation of site response and topographic effects fully probabilistically into the LANL hazard based on the guidance provided in NUREG/CR-6728 (McGuire *et al.*, 2001) (Section 8). Both LANL and the Steering Committee concurred with this recommendation. To our knowledge, this is the first time that these new approaches have been applied to a DOE facility. Because of the innovative nature of these approaches, a significant amount of additional effort was required including the development of new computational procedures and software. URS/PE&A strongly believe the final design ground motions described in this report represent a more accurate representation of the hazard at LANL and we believe this project significantly advanced the state-of-the-practice in several respects. These new approaches included:

(1) Moment balancing of the fault rupture model of the Pajarito fault system to properly partition the slip rates of the segments into events, which expressed the various rupture scenarios keeping the fault in moment equilibrium. This approach was first used by the Working Group on California Earthquake Probabilities (2003) and is the first application outside of California (Section 5.1.1).

(2) Implementation of a site-response analysis approach described in NUREG/CR-6728 (McGuire *et al.*, 2001), which results in hazard-consistent surface motions (Section 8.1).

(3) Accommodation of increased epistemic variability in attenuation relations requiring development and implementation of a procedure to do so (Section 6.1).

(4) Incorporation of topographic effects in a fully probabilistic manner. This required several new developments: a) computation of separate horizontal and vertical factors, mean estimates, median estimates, and associated standard deviations (different for horizontal and vertical components), and b) determination of a defensible means of modifying hazard curves with the topographic factors that preserves probability(hazard consistent) (Section 6.4).

(5) Development of site-specific vertical motions which have the same probability as the horizontal components. Typically either a generic or site-specific V/H ratio is developed and applied to the horizontal design motions, which does not preserve the desired probability. To achieve hazard consistency for the vertical and have them be site-specific necessitated developing an extended suite of vertical motions by running an inclined P-SV model with properties for each site.

1.2 DOE SEISMIC DESIGN CRITERIA

DOE Order 420.1 and associated NPH Guide, DOE G-420.1-2 requires that structures, systems, and components (SSCs) at DOE facilities be designed and constructed to withstand the effects of natural phenomena hazards using a graded approach. The graded approach is implemented by the five Performance Categories established for SSCs based on criteria provided by DOE-STD-1021-93. The following DOE documents include criteria for which this study was designed and under which it was performed:

- DOE Standard 1020-2002 Natural Phenomena Hazards Design and Evaluation Criteria for DOE Facilities
- DOE Standard 1022-94 Natural Phenomena Hazards Site Characterization Criteria
- DOE Standard 1023-95 Natural Phenomena Hazard Assessment Criteria

1.3 PROJECT ORGANIZATION

DOE Standard 1023-95 recommends that the input into a PSHA be derived through either (1) the elicitation of multiple experts, or (2) peer review. The objective of both processes is to ensure that the diversity (or uncertainty) of opinion on how to model both earthquake occurrence and the seismic wave propagation is properly incorporated into the hazard analysis (SSHAC, 1997). In this study, the latter approach was taken as appropriate for a SSHAC Level 2 analysis. Guidance and review were provided by a Steering Committee selected by LANL.

This study was performed by URS and PE&A under subcontract to Burns and Roe Enterprises, Inc. (BREI). The Project Team consisted of the following members: Ivan Wong (Project Manager), Susan Olig, Mark Dober, Fabia Terra, Judith Zachariasen, Patricia Thomas, Shobhna Upadhyaya, and Mark Hemphill-Haley of URS; Walter Silva and Nick Gregor of PE&A; Jamie Gardner and Claudia Lewis of LANL; Norm Abrahamson, Consultant; and Kenneth Stokoe of the University of Texas. LANL support was provided by Michael Salmon (Project Manager),

Tom Houston, Richard Lee, Stephanie Luscher; Doug Volkman, Dennis Basile, and Tom Whitacre (DOE). Zia Zafir of Kleinfelder, Inc., also provided assistance. Members of the Steering Committee included Walter Arabasz, University of Utah; Carl Costantino, Consultant; and Michael Machette, USGS. Jeff Kimball contributed to the Steering Committee's deliberations during much of the project while a member of the staff of DOE. Toby Walters (URS) and Peter Lujan (BREI) provided project management support. We acknowledge and thank the LANL and DOE staff and the Steering Committee for their contributions to this study.

This section provides a general description of the PSHA methodology used to calculate ground motions at LANL. Input parameters used in the LANL PSHA are described in subsequent sections.

The PSHA methodology used in this study allows for the explicit inclusion of a range of possible interpretations for different components of the PSHA model, including seismic source characterization and ground motion estimation. In this study, extensive efforts were made to assemble and use up-to-date geologic and seismologic data to evaluate and characterize potential seismic sources, the likelihood of earthquakes of various magnitudes occurring on those sources, and the likelihood of earthquakes producing ground motions greater than specified levels. Uncertainties due to incomplete knowledge about parameters and models are incorporated into the hazard analyses through the use of logic trees in which variously weighted alternatives reflect an informed evaluation of the current state of knowledge, refined by peer review.

2.1 METHODOLOGY

The seismic hazard approach used in this study follows a methodology developed principally by Cornell (1968). The production of earthquakes by an identified fault or other seismic source zone is assumed to be a Poisson process. The Poisson assumption is widely used and is reasonable in regions where data are sparse and only provide an estimate of average recurrence rate (Cornell, 1968). The occurrence of ground motions at a site in excess of a specified level also is a Poisson process if (1) the occurrence of earthquakes is a Poisson process and (2) the probability that any one event will result in ground motions at the site in excess of a specified level is independent of the occurrence of other events.

The probability that a ground motion parameter "Z" exceeds a specified value "z" in a time period "t" is given by:

$$p(Z > z) = 1\text{-}e^{-\nu(z)\cdot t} \qquad (2\text{-}1)$$

where $\nu(z)$ is the annual mean number (or rate) of events in which Z exceeds z. It should be noted that the assumption of a Poisson process for the number of events is not critical. This is because the mean number of events in time t, $\nu(z)\cdot t$, can be shown to be a close upper bound on the probability $p(Z > z)$ for small probabilities (less than 0.10) that generally are of interest for engineering applications. The annual mean number of events is obtained by summing the contributions from all earthquake sources, that is:

$$\nu(z) = \sum_{n} \nu_n(z) \qquad (2\text{-}2)$$

where $\nu_n(z)$ is the annual mean number (or rate) of events on source n for which Z exceeds z at the site. The parameter $\nu_n(z)$ is given by the expression:

$$\nu_n(z) = \sum_{i}\sum_{j} ß_n(m_i)\cdot p(R=r_j|m_i)\cdot p(Z>z|m_i,r_j) \qquad (2\text{-}3)$$

where:

$ß_n(m_i)$ = annual mean rate of recurrence of earthquakes of magnitude increment m_i on source n;

$p(R=r_j|m_i)$ = probability that given the occurrence of an earthquake of magnitude m_i on source n, r_j is the closest distance increment from the rupture surface to the site;

$p(Z > z|m_i,r_j)$ = probability that given an earthquake of magnitude m_i at a distance of r_j, the ground motion exceeds the specified level *z*.

The hazard calculations for vibratory ground motion were made using the computer program HAZ38 developed by Norm Abrahamson (consultant, unpublished, 2006). The computer program has undergone verification testing under the LANL project-specific procedure PSNQAP-3.3.1, which is contained in the URS DOE West Nuclear Quality Assurance Manual.

2.2 SEISMIC SOURCE CHARACTERIZATION

Two types of earthquake sources are characterized in this seismic-hazard analysis: (1) fault sources and (2) areal source zones (Section 5). *Fault sources* are identified faults or zones of faults, represented as three-dimensional surfaces that define the locations of future earthquakes. *Areal source zones* are regions (more correctly, volumes) in which future earthquakes are assumed to occur randomly in space and time, independent of mapped faults. As part of the seismic source characterization, seismic sources are modeled in terms of their probability of activity, source geometry, and earthquake recurrence.

The geometric source parameters for faults include location, segmentation model, dip, and thickness of the seismogenic zone. The recurrence parameters include recurrence model, recurrence rate (slip rate or average recurrence interval for the maximum event), slope of the recurrence curve (*b*-value), and maximum earthquake magnitude. The parameters for geometry and recurrence are not totally independent. For example, if a fault is modeled with several small segments instead of large segments, the maximum magnitude is lower and a given slip rate requires many more small earthquakes to accommodate a cumulative seismic moment. For areal source zones, we need only to define the geometric bounds, maximum depth, maximum magnitude, and recurrence parameters based on the historical earthquake record.

Uncertainties in the source parameters are included in the hazard model using logic trees (Section 5). In the logic tree approach (Kulkarni *et al.*, 1979), we include discrete values of the source input parameters along with our estimate of the likelihood that the discrete values represent the actual values. Generally, in the LANL PSHA most input parameters are represented by three to five values: a best estimate or 50th percentile together with lower and upper values that are part of a distribution about the best estimate (Section 5).

2.2.1 Probability of Activity

Probability of activity [P(a)] expresses the likelihood that a fault is active, ranging from 1.0 (definitely active and therefore seismogenic) to 0.0 (completely inactive). Faults with definitive evidence for repeated Quaternary movement were generally assigned probabilities of being active and seismogenic of 1.0 unless other evidence suggests they may not be seismogenic

structures (Section 5.1). A probability of activity of less than 1.0 was assigned to faults that do not show definitive evidence for repeated Quaternary movement. Each fault was judged individually, based on available data and the above criteria (Section 5).

2.2.2 Source Geometry

The geometry of seismic sources needs to be defined in the PSHA. Because fault geometries are not well constrained in some cases, variable configurations are considered for each fault (typically three fault dips and three depths for the seismogenic crust, giving rise to nine possible combinations). Generic constraints on fault dip applicable to the majority of faults in the region come from seismic-reflection data, earthquake hypocenters, and the focal mechanisms of instrumentally recorded earthquakes.

For fault sources in this PSHA, it is assumed that earthquakes of a certain magnitude may occur randomly along the length of a given fault or fault segment. The distance from an earthquake source to the site depends on the fault geometry, the size and shape of the rupture on the fault plane, and the likelihood of the earthquake occurring at different points along the fault length. The distance to the fault is defined to be consistent with the specific attenuation relationship used to calculate the ground motions. The distance, therefore, is dependent on both the dip and depth of the fault plane; a separate distance function is calculated for each geometry and each attenuation relationship. The size and shape of the rupture on the fault plane depend on the magnitude of the earthquake, with larger events rupturing longer and wider (downdip) portions of the fault plane.

2.2.3 Style of Faulting

For each fault, the style of faulting was specified as normal, strike-slip, or oblique-normal. This parameter was required by each of the attenuation relationships (Section 6.1). No reverse faults, which are sparse in the RGR, are deemed significant seismic sources for the LANL region.

2.2.4 Types of Multisegment Ruptures

Large earthquakes on faults having multiple segments can rupture as multiple subevents (synchronous rupture) rather than just a single large event (simultaneous rupture), as is typically assumed and modeled in standard PSHAs. The type of multisegment rupture (synchronous versus simultaneous) can significantly impact ground motion estimates, depending on the location of the site relative to the segments (e.g., CRWMS M&O, 1998). Several LANL facilities are located between different segments of the PFS, and so we explicitly considered both simultaneous and synchronous types of multisegment ruptures for the PFS (Section 5.1.2.3).

PSHA calculations typically consider each fault to be a single rupture plane and for each fault to rupture independently including any segments. However, modeling synchronous ruptures in PSHAs is somewhat new and more complex, therefore, we discuss our approach further here. Synchronous model parameters and their weights are discussed in Section 5.1.1.

In the case of the synchronous rupture one fault is considered to be the location of the main event or first subevent, and the other fault is considered to be the location of the second subevent. In

the hazard calculations, the first subevent's rupture plane is defined in detail (that is its curvilinear surface, dip, and downdip extent), but the second subevent is only defined by magnitude and distance to the site. The second subevent is allowed to rupture only when a defined minimum magnitude of the first subevent is achieved and when the rupture distance between the two subevents is within a defined range (Table 2-1). The final ground motion value of the two ruptures is calculated by taking the square root of the sum of the squares (SRSS) of the two subevent ground motions values. This approach is similar to what was done in the Yucca Mountain PSHA (CRWMS M&O, 1998). The principal issue with this approach is whether the ground motions from multiple ruptures are correlated or independent. In the Yucca Mountain PSHA, the ground motion experts generally considered the ground motions to be independent (CRWMS M&O, 1998).

The total sigma for the synchronous rupture is calculated using the following equation:

$$\sigma = \sqrt{\frac{\sigma_1^2 \cdot (\exp(\ln Y_1))^4 + \sigma_2^2 \cdot (\exp(\ln Y_2))^4}{(\exp(\ln Y_1))^2 + (\exp(\ln Y_2))^2}} \qquad (2\text{-}4)$$

where $\ln Y_1$ = the log ground motion value of the first subevent, $\ln Y_2$ = the log ground motion value of the second subevent, σ_1 = the sigma of the first subevent and σ_2 = the sigma of the second subevent.

2.2.5 Maximum Magnitudes

Consistent with current state-of-the-practice, we estimate the maximum magnitude for each fault source based on empirical relations between expected slip and/or rupture dimensions (i.e., displacement per event and/or fault rupture length and width, and the resultant area) and magnitude. Estimates of maximum earthquakes from empirical data such as rupture length and displacement are limited by uncertainties in the empirical data, the range of observed rupture parameters underlying the empirical relations, and uncertainties in the assessment of rupture parameters for the fault under investigation. Therefore, the final assessment of maximum magnitude is a judgment that incorporates an understanding of specific fault characteristics, the regional tectonic environment, similarity to other faults in the region, and seismicity data.

The most common approach to estimating maximum magnitude is to use an empirical relation based on worldwide fault rupture lengths and earthquake magnitudes. There have been no historical earthquake surface ruptures in New Mexico. However, considerable uncertainty often exists in the selection of the appropriate rupture length to be used in the analysis (Schwartz *et al.*, 1984). Rupture lengths of historical surface-rupture events on a specific fault may provide direct evidence.

The empirical relationships for surface rupture length and fault displacement used in the maximum magnitude assessments are those developed by Wells and Coppersmith (1994). Specific relations are given in Section 5. The regressions on which these particular relationships are based have high correlation coefficients and the standard deviations range from 0.28 to 0.40 magnitude unit (Wells and Coppersmith, 1994). Maximum magnitudes for the areal sources are based on arguments of the minimum threshold for surface faulting (Section 3.2.4).

2.2.6 Fault Recurrence Models

Earthquake recurrence for the fault sources is modeled using three alternative recurrence models: A) the characteristic earthquake model, B) the maximum magnitude model, and C) the truncated exponential model. These models are individually weighted to represent our judgment on their applicability to the sources. Only the truncated exponential recurrence relationship is assumed appropriate for the areal source zones.

We have used the form of the truncated exponential model of Youngs and Coppersmith (1985), which was first proposed by Cornell and Van Marke (1969). The number of events exceeding a given magnitude, $N(m)$, for the truncated exponential relationship is

$$N(m) = \alpha(m^o)\frac{10^{-b(m-m^o)} - 10^{-b(m^u-m^o)}}{1-10^{-b(m^u-m^o)}} \qquad (2\text{-}5)$$

where $\alpha(m^o)$ is the annual frequency of earthquakes greater than the minimum magnitude (m^o); b is the Gutenberg-Richter parameter defining the slope of the recurrence curve; and m^u is the upper-bound magnitude event that can occur on the source. A value of m^o equal to moment magnitude (**M**) 5.0 was used for the hazard calculations because smaller events are not considered likely to produce ground motions with sufficient energy to damage well-designed structures.

We have included a model that allows faults to rupture with a specific "characteristic" magnitude on individual segments. This model is described by Aki (1983) and Schwartz and Coppersmith (1984) and numerically modeled by Youngs and Coppersmith (1985) (Figure 2-1). For the characteristic model, the number of events exceeding a given magnitude is the sum of the characteristic events and the non-characteristic events. The characteristic events are typically distributed uniformly over ± 0.25 magnitude unit (ΔM_{char}) around the characteristic magnitude (M_{char}) and the remainder of the moment is distributed exponentially using the above equation with a maximum magnitude one unit lower ($\Delta M2$) than the characteristic magnitude (Figure 2-1; Youngs and Coppersmith, 1985). We used this model for segmented faults. For unsegmented faults, we used a slightly wider distribution with $\Delta M_{char} = 0.3$ to reflect our belief that faults in the RGR show a broader distribution in size of the characteristic magnitude than typical range-bounding faults elsewhere in the Basin and Range Province (Section 5.1.1.4).

We adopted the maximum-magnitude model proposed by Wesnousky (1986), which can be regarded as an extreme version of the characteristic model. In the maximum magnitude model, there is no exponential portion of the recurrence curve, i.e., no events occur between the minimum magnitude of **M** 5.0 and the distribution about the maximum magnitude.

2.2.7 Fault Recurrence Rates

The recurrence rates for the fault sources are defined by either the slip rate or the average recurrence interval for the maximum or characteristic event and the recurrence b-value. The slip rate is used to calculate the moment rate on the fault arising from the following equation for defining the seismic moment of a single earthquake:

$$M_o = \mu A D \quad (2\text{-}6)$$

where M_o is the seismic moment, μ is the shear modulus, A is the area of the rupture plane, and D is the average slip (or displacement) on the fault plane. Dividing both sides of the equation by time results in the moment rate as a function of slip rate:

$$\dot{M}_o = \mu A S \quad (2\text{-}7)$$

where $\dot{M}_o$ is the moment rate and S is the slip rate. Hanks and Kanamori (1979) derived the following relation between M_o and **M**:

$$\mathbf{M} = 2/3 \log M_o - 10.7 \quad (2\text{-}8)$$

Using this relationship and the relative frequency of different magnitude events from the recurrence model, the slip rate can be used to estimate the absolute frequency of different magnitude events. The average recurrence interval for the characteristic or maximum magnitude event controls the high magnitude (low-likelihood) end of the recurrence curve (Figure 2-1; Youngs and Coppersmith, 1985).

2.3 GROUND MOTION ATTENUATION

To characterize the ground motions at a specified site resulting from earthquakes considered in the PSHA, we used both empirical and site-specific stochastic attenuation relationships for spectral accelerations (Section 6). The empirical relationships used in this study were selected on the basis of the appropriateness of the site conditions and tectonic environment for which they were developed.

The uncertainty in ground-motion attenuation was included in the probabilistic analysis by using the log-normal distribution about the median values as defined by the standard deviations (epsilons) associated with each attenuation relationship. Three standard deviations about the median value were included in the analysis. This is standard practice but has recently been challenged by Abrahamson and Bommer (2006). Their study concluded that there is no technical basis for truncating the ground motion distribution at an epsilon value of less than 3. The authors recommend that "an untruncated lognormal ground motion distribution in PSHA is appropriate for ground motions that are below the physical limits of the underlying rock or soils." This issue is discussed in Section 8.4.

2.4 ADHERENCE TO THE SSHAC PROCESS

Methodological guidance on how to perform a PSHA has been developed as part of a major project sponsored by the U.S. Nuclear Regulatory Commission, DOE, and the Electric Power Research Institute. Referred to as the SSHAC (Senior Seismic Hazard Analysis Committee) guidelines, they have become the standard by which PSHAs for critical and important facilities are now judged. These guidelines are applicable to all levels of analyses.

In view of epistemic uncertainties, the objective of a PSHA is to estimate the composite probability distribution of the inputs to the analysis based on an evaluation and integration of the

informed technical community's state-of-knowledge of seismogenic processes and ground motions (SSHAC, 1997). To satisfy this objective, the analyst conducts an evaluation process that systematically identifies and evaluates the sources and quantifies the epistemic uncertainty in the PSHA.

Two basic principles underlie the SSHAC (1997) approach to PSHAs: (1) the inputs should represent the composite distribution of the informed technical community and (2) the analyst must establish ownership of these inputs. SSHAC (1997) recommends two different approaches to performing PSHAs based on the makeup of the analyst or what is called the "integrator." These two approaches are called the Technical Integrator (TI) and Technical Facilitator Integrator (TFI) approaches. The TI and TFI are defined in the following (SSHAC, 1997):

> *TI: a single entity (individual, team, company, etc.) who is responsible for ultimately developing the composite representation of the informed technical community (herein called the community distribution) for the issues using the TI approach. This could involve deriving information relevant to an issue from the open literature or through discussions with experts.*
>
> *TFI: a single entity (individual, team, company, etc.) who is responsible for aggregating the judgments and community distributions of a panel of experts to develop the composite distribution of the informed technical community for the issues using the TFI approach.*

The major differences between the TI and TFI approaches are the TFI is responsible for facilitating the discussions and interactions between experts versus the TI who are the "evaluator" experts, who act as individual integrators, in the development of the community distribution (SSHAC, 1997).

The PSHA process should be developed in a manner consistent with the study level. The process can range from a modest to complex. In the parlance of SSHAC (1997) these would be Level 1 to 4 evaluations. Most PSHAs (Levels 1 to 3) are performed using the TI approach. SSHAC (1997) recommends the following 5-step process:

Step 1. Identify and select peer reviewers;

Step 2. Identify available information and design analyses and information retrieval methods;

Step 3. Perform analyses, accumulate information relevant to issue and develop representation of community distribution;

Step 4. Perform data diagnostics and respond to peer reviews; and

Step 5. Document process and results.

For the LANL PSHA, the TI consisted of Susan Olig, Jamie Gardner, Claudia Lewis, and Ivan Wong for seismic source characterization. For ground motion characterization, the TIs were Walt Silva, Ivan Wong, and Norm Abrahamson. External expert input was provided by Richard Lee, Kenneth Stokoe, Mark Hemphill-Haley, Alexis Lavine, Tom Houston, Steve Reneau, Michael Machette, Keith Kelson, James McCalpin, David Love, Scott Minor, Bob Kirkham,

Tony Crone, Larry Anderson, Mike Timmons, Ram Kulkarni, and Daniel Koning. Peer review was provided by the members of the Steering Committee.

Table 2-1
Threshold Magnitudes and Distances for Synchronous Rupture of the PFS

Rupture Scenario*	Minimum Magnitude of First Subevent to Trigger Second Subevent (M)	Maximum Rupture Distance to First Subevent (km)
RS-e	6.46	10
RS-f	6.45	10
RS-g	6.44	10
RS-h	6.29	10

* See Section 5.1.1 for explanation of rupture scenarios and calculation of maximum magnitudes for the PFS.

LANL is located within the RGR, an intracontinental Neogene structural feature that dominates the seismotectonic setting of the LANL region. The rift is a physiographic and structural depression bordered by the southern Rocky Mountains Province to the north, the Colorado Plateau Province to the west, and the Great Plains Province to the east (Figure 3-1). It is a continental rift system characterized by basin subsidence, Quaternary extensional faulting, Quaternary volcanism, high heat flow, and moderate seismicity. These elements are reflected in the local and regional geology around LANL, which is situated on the Pajarito Plateau, a fault-bounded plateau underlain by the early Quaternary Bandelier Tuff and traversed by several late Quaternary normal faults. LANL is also located at the western edge of the Española Basin, one of several fault-bounded basins in the RGR (Figure 3-2). The following section summarizes the seismotectonic setting of LANL and the historical and contemporary seismicity of northern New Mexico. A more detailed description can be found in the 1995 LANL study (Wong *et al.*, 1995).

3.1 SEISMOTECTONIC SETTING

The seismotectonic provinces within the LANL region and the basins of the northern and central RGR are described below (Figures 3-1 and 3-2).

3.1.1 Seismotectonic Provinces

LANL's location on the Parajito Plateau places it at the transition between the tectonically active RGR and flanking regions of tectonic stability. LANL is at the western margin of the RGR, where it abuts the Valles Volcanic Field to the west (Figure 3-2). The rift and volcanic field are bordered on the west by the Colorado Plateau. To the north and east of LANL, two prongs of the Southern Rocky Mountains Province extend southward into the region from Colorado and bound both sides of the RGR. Lastly, to the east of LANL is the Great Plains Province (Figures 3-1 and 3-2). We have divided the region into seismotectonic provinces for the purposes of delineating background seismicity based on similar seismotectonic characteristics (Section 5.2; Figure 3-1).

Rio Grande Rift

The RGR, extending from central Colorado to Texas and northern Mexico (Figure 3-1), is a continental rift that is a part of the greater Basin and Range Province, which accommodates extension across a broad swath of the western United States (Chapin, 1971; Hawley, 1986). The rift is a relatively narrow feature compared to most of the Basin and Range (Figure 3-1) and has geologic and geophysical characteristics similar to continental rifts elsewhere in the world, such as the Kenya rift of the East African rift system and the Baikal rift of the Mongolian Plateau (Keller *et al.*, 1991). The rift occupies a region of elevated topography, with rift flanks as high as 4,000 m that is in some measure a remnant of broad uplift during the Laramide orogeny (Chapin and Cather, 1994). However, the high elevations are also due to more recent isostatic uplift in response to unloading from lithospheric thinning during extension and thermally driven uplift caused by asthenospheric upwelling (Davis, 1991; Keller *et al.*, 1991). Gravity, seismic-refraction, and other geophysical studies show that the lithospheric mantle is anomalously thin or absent beneath the axis of the RGR, as it is in the Kenyan rift (Russell and Snelson, 1994). Mantle lithosphere is replaced beneath the rifts with warm, buoyant asthenospheric mantle,

which probably accounts for the regional elevated topography, high heat flow, low gravity, and late Cenozoic magmatism (Keller *et al.,* 1991).

The RGR widens southward, from narrow graben-like basins in Colorado to wide, multi-basin horst and grabens in southern New Mexico. Structurally, the rift consists of a suite of north-trending, right-stepping *en echelon* basins that began forming in the late Oligocene in response to generally east-west directed extension. Previously during Laramide time, this region had undergone compression and crustal thickening that drove regional uplift; collapse of this uplift in the late Oligocene led to the formation of structural basins along the rift (Chapin and Cather, 1994; Figure 3-2). In general, these basins are broad asymmetric half-grabens as much as 65 km wide and 240 km long. The grabens are tilted either to the east or west and typically have deep, narrow inner grabens, half-grabens, and horsts. The inner half-grabens contain as much as 10 km of late Cenozoic volcanic deposits and rift-fill sediments derived from the flanks of basin-border uplifts. The top of Precambrian basement is substantially deeper in the rift than in the adjacent parts of the Colorado Plateau transition zone and Great Plains Provinces (Baltz, 1978), indicating net structural lowering of the intrarift. The half-grabens are typically bordered on one side by down-to-the-east or down-to-the-west faults, such as the Pajarito and Sangre de Cristo faults, both of which exhibit evidence of late Pleistocene to Holocene displacement (Figure 3-2).

Clastic deposits (alluvial, colluvial, eolian, lacustrine and volcaniclastic sediments) of the Santa Fe Group and associated volcanic rocks make up the Plio-Pleistocene syn-rift sedimentary fill of RGR basins (e.g., Hawley *et al.*, 1969). These basin-fill deposits are as thick as 4,570 m in the Albuquerque Basin (Hawley *et al.*, 1995). Although extension in the region started between 27 to 32 Ma, rift basins were not integrated by the through-going ancestral drainage of the Rio Grande until much later in the Pliocene.

The Jemez lineament, a 50 to 80 km-wide northeast-trending alignment of hundreds of Miocene to Quaternary volcanic centers between southeastern Colorado and central Arizona, traverses the RGR (Aldrich, 1986; Goff *et al.*, 1989). It includes the Jemez volcanic complex (Sanford *et al.*, 1991; Figure 3-2), which is of particular importance to LANL. Jemez volcanism culminated in the formation of Valles Caldera, a multi-phase, intercontinental resurgent caldera nested within the Jemez Mountains, at the transition between the RGR and the stable Colorado Plateau, about 20 km west of LANL (Smith and Bailey, 1968; Self *et al.*, 1988; Figure 3-2).

Colorado Plateau Province

The Colorado Plateau Province is a broad zone of relative tectonic stability between the extensional RGR and Basin and Range Province to the west (Figure 3-1). The Colorado Plateau is also topographically elevated as a consequence of Laramide uplift. However, the uplift of the Plateau occurred over a broad region that rose as a block; Mesozoic and younger rocks within the interior of the Plateau region remain relatively undeformed. Heat flow in the region is low (< 80 mW/m^2) relative to the RGR (> 90 mW/m^2), and there is low to moderate seismicity (Reiter *et al.*, 1979; Figure 3-1 and Plate 1). Seismicity is somewhat elevated at the transition between the RGR and the Colorado Plateau compared to that in the interior of the province. The seismicity rate for the Colorado Plateau is similar to that in the rift and focal mechanisms of earthquakes indicate northeast-southwest directed extension with both normal and strike-slip faulting (Wong and Humphrey, 1989).

Southern Great Plains Province

The Southern Great Plains Province defines the western edge of the stable cratonic interior of the United States. It borders the eastern edge of the RGR (Figure 3-1). The province has similar characteristics to the Colorado Plateau in that it has low heat flow, low seismicity (Figure 3-1), and is composed of uplifted Precambrian basement overlain by relatively undeformed Mesozoic and younger rocks (Baltz, 1978). The Southern Great Plains is a region of thickened crust (40 to 50 km thick), very low rates of crustal deformation, and northeast to southwest-directed extension as shown by focal mechanisms and borehole breakouts (Zoback and Zoback, 1991).

Southern Rocky Mountains Province

The Southern Rocky Mountains are located in southern Colorado and northernmost New Mexico. They include (1) the Brazos uplift that extends southward from Colorado between the RGR and the Colorado Plateau as well as (2) the northern Sangre de Cristo Mountains, which extends into northern New Mexico on the eastern edge of the RGR, between it and the Great Plains Province to the east. There are few Quaternary faults and there is sparse dispersed seismicity within the Southern Rocky Mountains Province, although there is significant late Quaternary faulting at the western edge of the Sangre de Cristo Mountains, which bound the RGR on the east. The Southern Rocky Mountains are physiographically distinct from the other provinces in the region. However, in terms of recent seismicity and Quaternary faulting they are similar to the relatively stable Colorado Plateau and Great Plains Provinces. Consequently, we include the portions of the Southern Rocky Mountains near LANL in the Colorado Plateau and Great Basin Provinces for the purposes of characterizing background seismicity.

Valles Volcanic Field

The Valles Volcanic Field (an informal province, herein) is bordered by the RGR on the east and by the Colorado Plateau transition zone on the west (Figure 3-2). The province is a late Cenozoic volcanic edifice that coincides with the intersection of the RGR and the Jemez lineament (Aldrich, 1986; Goff *et al.*, 1989). The volcanic edifice is a cumulative product of more than 13 Ma of eruptive activity (Gardner *et al.*, 1986) that culminated in the formation of the Valles caldera, which is a classic example of an intercontinental resurgent caldera (Smith and Bailey, 1968; Self *et al.*, 1988). The volcanism is spatially related to tectonic activity associated with the rift and the Jemez lineament (Goff *et al.*, 1989). The province is characterized by high heat flow, with values of generally more than 180 mW/m^2 (Reiter *et al.*, 1979), and a low Bouguer gravity anomaly (Keller *et al.*, 1984). The Valles Volcanic Field lacks significant microearthquake activity (Plate 1), a marked contrast to strong activity observed in other parts of the rift such as Socorro, where a mid-crustal magma body is thought to exist (Sanford *et al.*, 1979). The lack of seismicity in the volcanic field is probably related to the elevated temperatures and high heat flow at shallow crustal depths (Sanford *et al.*, 1979).

3.1.2 Rio Grande Rift Basins

The RGR in north-central New Mexico consists of several north-trending asymmetric structural basins. The LANL region includes four structural basins that constitute the northern and central

RGR: from north to south they are the San Luis, Española, Santo Domingo and Albuquerque basins (Figure 3-2). These rift basins are generally half grabens that are tectonically inverted Laramide upthrust blocks (Keller and Cather, 1994). The regional stratigraphic dip changes between these major basins, with differential movement taken up by southwest-northeast-trending accommodation zones that traverse the rift at high angles. In northern New Mexico, the most easily recognized accommodation zone is marked by the Jemez lineament and Embudo fault zone. Extension within each major basin increases southward, with about 8 to 12% extension in the San Luis Basin, at least 17% in the northern Albuquerque Basin, and a minimum of 28% in the southern Albuquerque Basin (Keller and Cather, 1994; Kluth and Schaftenaar, 1994; Russell and Snelson, 1994). This north-south increase in extension can be explained by 1 to 1.5 degrees of counter-clockwise (westward) rotation of the Colorado Plateau about an Euler pole in northeastern Utah (Chapin and Cather, 1994), which produces more extension at greater distances from the pole of rotation. Below, we describe the basins of the RGR near Los Alamos.

San Luis Basin

The San Luis Basin is a 240-km-long, elongate structural basin that extends from Poncha Pass in south-central Colorado to near the town of Taos in north-central New Mexico (Keller *et al.*, 1984; Figure 3-2). The San Luis Basin is flanked by the San Juan and Tusas Mountains on the west and by the Sangre de Cristo Mountains on the east, whereas the Española Basin borders it to the south. Precambrian basement rocks beneath the basin are overlain by pre-rift Oligocene volcanic rocks (Steven, 1975) and Miocene to Quaternary rift-fill sedimentary and volcanic deposits. Seismic reflection and gravity data show that the depth to the base of the rift-fill sediments is greatest (about 6 km) in the Baca sub-basin, along the eastern margin of the basin northeast of Alamosa, Colorado (Kluth and Schaftenaer, 1994; Brister and Gries, 1994). The Sangre de Cristo fault exhibits prominent geologic and geomorphic evidence of late Pleistocene and, locally, Holocene displacement (Machette and Personius, 1984; Menges, 1988, 1990a, 1990b; Crone and Machette, 2005). The San Luis Basin is an internally complicated, east-tilted, asymmetric half-graben, with several kilometers of down-to-the-west displacement on the Sangre de Cristo fault along its eastern margin and a gentle homocline along its western margin (Chapin and Cather, 1994).

Compared with other major half grabens in the RGR, the San Luis Basin appears to contain few or no major mapped faults (Chapin and Cather, 1994; Kluth and Schaftenaer, 1994). However, south of Alamosa Oligocene volcanic rocks are elevated in a structural horst that effectively subdivided the San Luis Basin into northern and southern sub-basins. New mapping and aeromagnetic data in the basin indicate abundant intrabasin faulting beneath the Quaternary sedimentary cover. Syn-rift sediments within the basin dip eastward as much as 12°. Kluth and Schaftenaar (1994) estimate that there has been about 8 to 12% extension across the basin, based on seismic-reflection data. The southern margin of the Taos Plateau and San Luis Basin coincides with the southwest-northeast-trending Embudo fault (Figure 3-2), which is an accommodation zone that transfers strain between the east-tilted San Luis Basin on the north and the west-tilted Española Basin on the south. The Embudo fault shows evidence of late Pleistocene displacement near its intersection with the Sangre de Cristo fault (Muehlberger, 1979; Machette and Personius, 1984; Kelson *et al.*, 1997), but has poor geomorphic expression and lateral continuity to the southwest where it traverses the rift and separates the southernmost San Luis Basin and the northernmost Española Basin. The Taos Plateau occupies the southern

part of the San Luis Basin, and is physiographically distinct from the rest of the basin. It comprises primarily locally-derived, gently east-dipping, Pliocene basaltic rocks interlayered with alluvial fan deposits of the Chamita Formation (Bauer *et al.*, 1999). The Plateau is in general only slightly dissected, although the Rio Grande and its tributaries are deeply incised into it.

Española Basin

The Española Basin is a 90-km-long, approximately 40-km-wide structural basin that extends from the Taos Plateau of the southern San Luis Basin on the north to the northern Albuquerque and Santo Domingo Basins on the south (Figure 3-2). The nearly 4000-m-high Sangre de Cristo Mountains border the eastern side of the basin, and the 3400-m-high Jemez Volcanic Field borders the western side of the basin. The Española Basin is an asymmetric structural depression that contains a deep, narrow graben along one margin, similar to the adjacent San Luis and Albuquerque Basins. In contrast, however, the Española Basin is tilted to the west with the greatest amount of late Cenozoic fault displacement and thickest section of rift-fill sediment (about 3 km) along its western margin near Española and Los Alamos (Manley, 1979a; Cather, 1992). The Española Basin is structurally and topographically higher on its hinged side, rather than on the side associated with the master basin-controlling fault. This likely is related to structural and topographic relief inherited from Laramide uplift (Chapin and Cather, 1994). The down-to-the-east Pajarito fault system forms the western margin of the basin, along which 1.5 km or more of late Cenozoic displacement has occurred (Gardner and Goff, 1984). As noted by several previous workers and documented during this investigation, faults within the PFS display geologic and geomorphic evidence of late Pleistocene and, in some cases, Holocene displacement (Section 4), similar to the Sangre de Cristo fault to the north.

The eastern margin of the Española Basin is poorly defined, but similar to the western margin of the San Luis Basin is not likely bounded by a well defined, Quaternary continuous fault (Baltz, 1978). Manley (1979a) observed that the eastern margin of the Española Basin appears to lack a throughgoing border fault, and Baltz (1976) notes that there is little or no evidence of significant down-to-the-west fault displacement; Kelley (1995), however, suggested 400 m of late Cenozoic, down-to-the-west separation occurred on the Picuris-Pecos fault in the Sangre de Cristo Mountains. Syn-rift sediments in the eastern part of the basin dip about 6° to 8° westward, and thicken to the west from an eroded homoclinal edge of the basin (Chapin and Cather, 1994). Discontinuous faults in the central and eastern parts of the basin exhibit down-to-the-east displacement and are probably related to structural adjustments related to middle or late Pliocene basin tilting to the west (Baltz, 1976). Thus most likely there is no discrete eastern structural boundary of the Española Basin, and relatively minor structures such as the Nambe and Pojoaque faults (Vernon and Riecker, 1989) accommodate minor distributed strain related to westward tilting of the basin.

Santo Domingo Basin

The 50-km-long and 40- to 60-km-wide Santo Domingo Basin is located between the southwestern part of the Española Basin and the northeastern part of the Albuquerque Basin (Figure 3-2). The basin may be a northeastern sub-basin of the Albuquerque Basin, because it

also is an east-tilted half-graben bordered on the east by a relatively large-displacement fault and on the west by a distributed zone of faults and flexures. The down-to-the-west La Bajada fault borders the eastern margin of the basin (Stearns, 1953; Kelley, 1978) (Figure 3-2). The San Felipe fault zone, which is as much as 8-km-wide and consists of several down-to-the-east and down-to-the-west faults (Smith *et al.*, 1970), may be associated with a broad, anticlinal bend or hinge along the western margin of the basin (Baltz, 1978). This pattern is similar to the eastern part of the Española Basin and to the western parts of the Albuquerque Basin, which have evidence of distributed strain. Intersections between the La Bajada and Pajarito faults at the northern end of the basin and between the San Felipe and Sandia fault zones at the southern end of the basin suggest that the Santo Domingo Basin itself may be an accommodation zone (block) between the Española Basin and the northern Albuquerque Basin (Figure 3-2).

The Santo Domingo Basin contains several features that are characteristic of accommodation zones, such as interfingering fault traces having opposing senses of displacement, the presence of a major through-going fluvial system in the central part of the basin, and its location between two structural basins with opposite senses of tilt (Morley *et al.*, 1990; Bosworth, 1985; Rosendahl, 1987). No late Pleistocene or Holocene displacement has been documented along the La Bajada or San Francisco faults, although aerial reconnaissance and analysis of aerial photography suggests that there are several potentially fault-related features, including west- or southwest-facing topographic scarps, along both of these faults (Wong *et al.*, 1995). In addition, the intersections of these faults with the PFS and the Rio Grande-Sandia fault provide supporting evidence that these faults may have had late Quaternary displacement.

Albuquerque Basin

The Albuquerque Basin is nearly 120-km-long, 40- to 60-km-wide, and is the largest and deepest rift basin in New Mexico (Hawley *et al.*, 1995; Figure 3-2). Clastic and volcanic basin-fill deposits of the Miocene-Pleistocene Santa Fe Group are as thick as 4,570 m in the Albuquerque Basin (Hawley *et al.*, 1995). The axial fluvial and tributary deposits of the ancestral Rio Grande in the Albuquerque Basin are part of the Sierra Ladrones Formation of Machette (1978), and were deposited from 7 Ma to sometime after 1.2 Ma (Connell *et al.*, 2001). Post-depositional incision by the Rio Grande led to abandonment of the alluvial surface developed on these deposits, which is currently 100 to 200 m above the present river level (Machette and McGimsey, 1983; Machette, 1985). Based on recent mapping and stratigraphic studies, Connell *et al.* (2001) estimate that the Rio Grande started to incise the Albuquerque Basin sometime between 0.7 and 1.2 Ma.

The Albuquerque Basin is flanked on the east by the east-tilted, fault-block uplift of the Sandia, Manzanita, Manzano, and Los Pinos mountains (Kelley, 1977). These ranges expose Precambrian plutonic and metamorphic rocks that are unconformably overlain by Paleozoic limestones, sandstones and shales. The resulting structural relief along the eastern rift margin is as much as 8,500 m (Woodward, 1977). The basin is flanked to the west by the lower-relief uplifts of the Colorado Plateau, which abuts the rift zone across a faulted monocline (Russell and Snelson, 1994).

Based on seismic lines, drill holes and gravity data, Lozinsky (1994) and Russell and Snelson (1994) subdivided the Albuquerque Basin into: (1) a sub-basin north of Tijeras Canyon with at

least 17% extension and basin-fill sediment tilted to the east, and (2) a sub-basin to the south of Los Lunas that has 30% extension and basin-fill sediment tilted dominantly to the west. The northern sub-basin lies closest to the LANL region. It is flanked on the east by the Sandia and Rincon faults and on the west by the Sand Hill and other of east-dipping normal faults (Machette *et al.*, 1998). The southern sub-basin is a west-tilted half graben that is controlled along its western margin by a system of east-dipping normal faults and on the east by the Manzano, Los Pinos, and Hubbell Springs faults (Russell and Snelson, 1994; Machette *et al.*, 1998). Lozinsky (1994) and Russell and Snelson (1994) proposed that the Tijeras accommodation zone, a buried west-southwest extension of the Tijeras fault in the Sandia Mountains, separates these subbasins. However, more recent studies have suggested a buried northwest-trending structure, the Mountain View fault zone, separates the sub-basins (Maldonado *et al.*, 1999, Hawley *et al.*, 1995).

3.2 HISTORICAL AND CONTEMPORARY SEISMICITY

Earthquake activity in New Mexico since 1869 has been relatively sparse, of small to moderate size ($\mathbf{M} < 6$), and broadly dispersed through all seismotectonic and physiographic provinces (Figure 3-1; Plate 1). The observed seismicity is largely unrelated to any mapped Quaternary faults and areas of concentrated seismicity appear to be related more to volcanism than tectonic faulting(Sanford *et al.*, 2002). Regional and local-scale seismicity do not delineate the RGR or any faults within it, although New Mexico's largest earthquakes (Richter local magnitude [M_L] > 4.5) since 1869 have occurred predominantly in the rift (Sanford *et al.*, 2002). There is a persistent clustering of seismicity near Socorro, referred to as the Socorro Seismic Anomaly (SSA), which accounts for almost 25% of the recorded seismicity between 1962 and 1998 (Sanford *et al.*, 2002; Figure 3-1) and some of the larger historic (felt) earthquakes in the rift. This seismicity is caused by extension related to inflation of a broad, thin mid-crustal magma body. Magma injection is the probable cause for recorded uplift at rates of as much as 1.8 mm/yr (Sanford *et al.*, 2002; Larsen *et al.*, 1986), which are geologically unsustainable and unrecorded in the Quaternary geology. Apart from the SSA, there are few significant alignments or clusters of seismicity evident in Figure 2-1. Relevant to LANL, there is a weak alignment of seismicity along the Jemez lineament. The Jemez Volcanic Field, including Valles Caldera west of Los Alamos is largely aseismic (Plate 1).

Detailed studies of the Albuquerque and Socorro areas, within the RGR, show that seismicity is limited to the upper 12 to 13 km of the crust (Sanford *et al.*, 1991), which is consistent with other rift systems that show seismicity to be concentrated in the upper crust (Doser and Yarwood, 1991). Earthquake focal mechanisms from the Albuquerque and Socorro areas indicate both strike-slip and normal faulting (Sanford *et al.*, 1991). These data also suggest that the direction of extensional tectonic stress (minimum principal stress) may vary locally within the rift, but its general orientation is interpreted to be approximately east-west (Sanford *et al.*, 1991). This observation is consistent with the pattern of Quaternary normal faults in the rift (Machette, 1998).

The largest historical earthquake within the RGR of New Mexico was probably an earthquake on 15 November 1906, part of a swarm of earthquakes around Socorro in 1906 to 1907 (Sanford *et al.*, 1991; 2002). Earthquakes were felt almost daily from 2 July 1906 to 21 July 1907 with the three strongest shocks occurring on 12 July, 16 July, and 15 November 1906. The 12 July

earthquake lasted 15 to 20 sec, causing adobe walls to crack, some chimneys to fall, and a rockslide, which damaged a nearby railroad (Modified Mercalli [MM] VII-VIII). Many aftershocks followed, including the 16 July earthquake, which damaged additional chimneys and houses, caused a brick gable to partially fall down, and triggered the failure of the southeast corner of a brick post office (Reid, 1911). The 15 November event was felt throughout an area of approximately 250,000 km^2 in central New Mexico (Reid, 1911; Sanford *et al.*, 1991). Its maximum intensity was estimated at MM VIII and it caused additional damage to structures already weakened in previous events on 12 and 16 July. The largest historical earthquake in the northern portion of the RGR occurred in 1918 near the town of Cerrillos. Olsen (1979) assigned a maximum intensity of MM VII and a magnitude of M_L 5¼ to this earthquake.

The great Sonoran earthquake of 1887 (**M** 7.4) was the largest earthquake within the entire RGR. It was associated with 101 km of surface rupture on the Pitaycachi fault and two other (lesser) faults in Sonora, Mexico, just south of the southwestern corner of New Mexico (outside of Figure 3-1) (Machette, 1998; Suter and Contreras, 2002). This earthquake was felt over an area of 1.5 to 2.0 million km^2 and caused numerous landslides and ground cracking (DuBois *et al.*. 1982). The earthquake caused 51 deaths, primarily due to the collapse of unreinforced adobe structures.

Sanford *et al.* (2002) have determined rates of earthquake activity for New Mexico based on the seismicity from 1962 to 1998. The activity rate in the SSA is relatively high, whereas rates elsewhere in New Mexico are quite low. Ground shaking hazard based on rates of seismicity alone appears to be low, but the presence of numerous Quaternary faults suggests recent seismicity alone may underestimate the long-term hazard (Machette, 1998; Sanford *et al.*, 2002). The following discusses the historical seismicity catalog used in this study and some analyses of the data.

3.2.1 Update of the Historical Catalog

Earthquake recurrence estimates are required for characterizing seismic hazard within the individual seismotectonic provinces. The estimates were produced from a catalog of historical earthquakes in New Mexico (1849 to 2005) compiled for this project (Task 2; Section 1.1) from hereon called the "LANL catalog." Our catalog was composed primarily of data from the revised New Mexico catalog compiled by New Mexico Tech (NMIMT) (Sanford *et al.*, 2002) supplemented by Stover, Reager, and Algermissen's U.S. Historical Earthquake Catalog, the USGS Preliminary Determination of Epicenters (PDEs), and the catalog from the LANL seismographic network (1998 to 2005) (P. Robert, LANL, written communication). In the NMIMT catalog, epicentral locations and magnitudes for felt earthquakes (1849 to 1961) and for instrumentally recorded earthquakes (1862 to 1998) were reevaluated and, in a majority of cases, revised (Sanford *et al.*, 2002). A major effort was made by Sanford *et al.* (2002) to have all NMIMT magnitudes in their catalog based on duration magnitudes (M_D) empirically calibrated to M_L. The completeness of the LANL catalog is discussed in Section 2.2.4.

For most of the events in the LANL catalog, the magnitudes are the NMIMT M_D values with some M_L, and m_b values. The m_b values were assumed to be equivalent to M_L for this region. All M_L values are assumed to be equivalent to **M** in subsequent calculations.

3.2.2 Spatial Distribution and Geologic Association

The map of relocated earthquakes ($M_L \leq 2.9$) used in the 1995 LANL study (Wong *et al*, 1995) showed that earthquakes were generally diffusely distributed throughout northern New Mexico with a few concentrations of events (Plate 1). After adding data up through 2005, the spatial pattern has generally remained the same (Plate 1). With few exceptions, the spatial distribution of events is similar to what is commonly observed throughout the Basin and Range Province, that is, seismicity occurring with no apparent spatial correlation with mapped faults or structures. This "background" seismicity probably represents low-level strain release on low-slip rate faults or short faults for which repeated movement is too small to manifest themselves at the earth's surface.

Seismicity is low around LANL with only a few historical earthquakes located in the vicinity of the PFS (Plate 1). A few clusters of epicenters along the Puye and La Bajada faults suggest that these two structures may be seismically active. There is a dense cluster of epicenters adjacent to the Jemez Sierrita fault, possibly indicating seismic slip on this fault or on a north-trending structure which has been mapped directly to the south (Plate 1). A north-trending, somewhat-linear zone of epicenters lies north of the Embudo fault along the La Canada del Amagre-Clara Peak fault zone (Plate 1).

As observed in previous studies (e.g., Sanford *et al*, 1991), Plate 1 shows aligned clusters of epicenters just to the east of the Nacimiento and Gallina faults (Plate 1). Historically, seismicity appears to be concentrated on a northward, but somewhat diffuse, extension of the Gallina fault. No other mapped faults appear to exhibit any significant recorded seismicity to date.

Although not evident in the distribution of well-located earthquakes (Plate 1), Sanford *et al.* (1979, 1981, 1991) noted that portions of the Jemez lineament, particularly in the Taylor volcanic field, appear to be seismically active. However, one particular area that seems to be characterized by seismic quiescence, both in historical and contemporary times, is the Valles Caldera (Plate 1). Elevated crustal temperatures due to high heat flow or stress release on surrounding fault zones may explain this quiescence (Sanford *et al.*, 1991).

Well-determined focal mechanisms for the LANL region calculated by Leigh House (Wong *et al*, 1995) exhibit both normal and strike-slip faulting similar to what is often observed throughout the Basin and Range Province. At least one, sometimes both nodal planes of the focal mechanisms trend in a northerly direction (ranging from northwest to northeast) parallel to the structures of the RGR (Wong *et al.*, 1995).

3.2.3 Focal Depth Distribution

As discussed in the 1995 study, earthquakes in the LANL region as typical of the majority of western U.S. seismicity appear to be confined to the brittle upper crust (Wong and Chapman, 1990). Cross sections based on the updated LANL historical catalog suggest that most events occur at focal depths less than about 15 km (Figures 3-3 and 3-4). In Figure 3-5 all events in the catalog with the distance to the closest seismographic station (DMIN) $\leq$ 20 km and rms errors less than 0.5 sec are shown as a function of focal depth. Figure 3-6 shows the best-located events in terms of focal depth, with DMIN $\leq$ focal depth. The events were not sorted by the standard error in focal depth (ERZ) because there would have been too few events to analyze for

a reasonable ERZ such as ≤ 5 km. Thus we recognize that the focal depths of the selected events may still be highly uncertain. Based on these histograms, few recorded earthquakes have focal depths ≥ 20 km. Although deep earthquakes (20 to ≥ 40 km) have been observed within the Colorado Plateau where crustal temperatures conducive to brittle failure (less than 350° ± 100°C.) extend to depths of 20 to 30 km (Wong and Humphrey, 1989; Wong *et al.*, 1984), we believe it is highly unlikely that significant seismicity will occur beneath a depth of 18 km within the RGR (Figures 3-5 and 3-6). Events within the entire 100-km-radius region surrounding LANL, which includes the rift, the adjacent Colorado Plateau and the Southern Great Plains, appear to be generally confined to focal depths of less than 20 km (Wong *et al.*, 1995).

3.2.4 Earthquake Recurrence

Earthquake recurrence relationships were estimated using the maximum likelihood procedure developed by Weichert (1980) and estimated completeness intervals for the region. Time intervals for which the earthquake catalog is complete above specified magnitude thresholds were estimated for the LANL catalog based on the history of western settlement and seismographic installation and operation in the region (Wong *et al.*, 1995; 2004). These intervals were used in the earthquake recurrence computations. In computing recurrence for background seismicity, all fault-associated events should be removed from the earthquake catalog. In this case, there was no clear association of events with mapped faults, so no earthquakes were deleted.

Dependent events, such as aftershocks, foreshocks, and smaller events within an earthquake swarm, were identified and removed from the catalog using the technique developed by Youngs *et al.* (2000). Three sets of empirical criteria for foreshock and aftershock sequence size were used: Gardner and Knopoff (1974) for southern California; Uhrhammer (1986) for California; and Arabasz and Robinson (1976) for California and New Zealand. Time and distance windows as a function of magnitude are specified in Youngs *et al.* (2000). After adjusting the earthquake catalog for dependent events and completeness, 320 events remained in the range of **M** 3.0 to 6.0 from which to estimate the recurrence for the seismotectonic provinces (Figure 3-7).

The resulting mean recurrence relationships for the SSA, Colorado Plateau, and Southern Great Plains (assuming the truncated exponential form of the Gutenberg-Richter relationship: $\log N = a - bM$) are shown in Figures 3-8 to 3-10. Also shown are the completeness intervals, the number of events, and curves for mean and mean ± one-standard-deviation confidence interval. All the curves are well determined due to relatively robust datasets. The calculated return periods are listed in Table 3-1.

Characterizing earthquake recurrence within the RGR, particularly in the vicinity of LANL, was more difficult because of the small number of independent events. The steps taken are illustrated in Figure 3-11. Six sets of calculations were performed for two regions (Figure 3-7): (1) the RGR within New Mexico as defined by Machette (1998), and (2) the northern RGR within New Mexico north of the SSA for minimum magnitudes of **M** 2.5, 3.0, and 3.5 (Table 3-2; Figures 3-12 to 3-17). The resulting recurrence intervals of **M** ≥ 3.0, 5.0, and 6.0 are also shown in Table 3-2.

To quantify the uncertainty in the *b*-values from the six sets of recurrence estimates for the RGR, we assumed that *b*-values follow a Student t-distribution defined by the mean and variance of "*b*" estimated from the Weichert (1980) method. Because a sample estimate of the true variance is used, the assumption of a Student t-distribution is appropriate. The t-distribution is similar to the normal distribution but has a lower height and wider spread. As the sample size increases, the t-distribution approaches the standard normal distribution. The main variable in the t-distribution is the number of degrees of freedom, which is the number of observations that can be chosen freely. For each of the six recurrence calculations, we created a cumulative distribution function (CDF) from the t-distribution (Figure 3-18).

Recurrence rates for the northern RGR where the LANL is located may be considered more appropriate for use in the LANL hazard assessment than the whole rift in New Mexico because there are significant tectonic differences between the northern and southern RGR in New Mexico (Machette, 1998). For example, south of Socorro, New Mexico, the rift expands into multiple horst and grabens, extension is spread over a wider region, and fault-bounded ranges become prominent. However, the recurrence rates are better constrained for the whole RGR due to the larger number of events used in the calculations (Figures 3-12 to 3-17). Thus we have assigned a total weight of 0.6 to the three CDFs for the northern RGR and 0.4 weight to the three CDFs for the whole RGR. Each CDF within the two groups was equally weighted. The median, 16th and 84th percentile values were determined from the average CDF (Figure 3-18). A median *b*-value of 0.58 and 16th and 84th percentile values of 0.43 and 0.73, respectively, were calculated from the six cases relating to the RGR.

A similar process was followed for the *a*-value. We used the normal distribution to determine a CDF for each model, which were then averaged (Figure 3-19). The normal distribution for "*a*" is well-determined given the large number of events used to estimate its value. From the average CDF (Figure 3-19), the median, 16th and 84th percentile values are -3.29, -3.48, and -2.95, respectively, normalized for area.

Given the three *a*- and *b*-values from these distributions, there are nine possible pairs to calculate recurrence intervals for the RGR. The combinations are shown on Table 3-3 together with the calculated return periods for earthquakes of **M** 3.0, 5.0, or 6.0 and greater for areas of 10,000 km^2, and about 100,600 km^2 (area of the RGR), respectively. Based primarily on the implied return periods of the larger, more potentially damaging **M** 5.0 and **M** 6.0 events, compared to the historical earthquake record, we selected four pairs of *a*- and *b*-values to indicate the epistemic uncertainty in a logic tree. Our reasoning for the selection was as follows.

The 137-year historical record contains only two independent earthquakes of $\mathbf{M} \geq 5.0$ located in the RGR outside the SSA: (1) 1893 north of Socorro and (2) 1918 near Cerrillos, both within the northern rift. Given the observation of two events in 137 years, and assuming a Poisson process, the maximum-likelihood estimate of the underlying recurrence interval is 69 years with 5th and 95th percentile confidence limits of 22 and 168 years, respectively (Walter Arabasz, University of Utah, written communication, 2006). Although the median *a*- and *b*-value pair of 0.58 and -3.29 would normally be the preferred combination, its predicted recurrence interval for $\mathbf{M} \geq 5.0$ earthquakes is only 15 years (Table 3-3), which is clearly not consistent with the historical record for the RGR. Guided by the maximum-likelihood distribution of recurrence intervals for $\mathbf{M} \geq 5.0$, a four-point distribution of weights (0.2, 0.3, 0.3, and 0.2) was assigned to four *a*- and *b*-

value pairs as shown in Table 3-3. The corresponding recurrence intervals for **M** ≥ 5. are 24, 40, 86, and 133 years, respectively, for the whole RGR (Table 3-3). For comparison, the recurrence interval for **M** ≥ 5.0 earthquakes in the northern RGR from the original recurrence modeling calculations (Table 3-2) ranges from 29 to 33 years. Figure 3-20 shows the four recurrence curves and the seismicity data. For the magnitudes of most relevance (**M** ≥ 5.0), the data lie at the center of all four recurrence curves.

In the 1995 analysis, the recurrence interval of **M** ≥ 6.0 earthquakes in the RGR in northern New Mexico was about 800 years (Wong *et al.*, 1995). When normalized to an area of 10,000 km^2, the recurrence interval is about 900 years. This value is at the low end of the range of 900 to 7,200 years resulting from the *b*- and *a*-values that were assigned weights in this study (Table 3-3). The longer recurrence intervals used in this study may be due to a number of factors including the use of an updated catalog by Sanford *et al.* (2002) and a more statistically robust approach to calculate the recurrence from the sparse historical catalog for the RGR. As will be discussed in Section 7.1.1, the RGR background seismicity is not a major contributor to the hazard at LANL.

Elsewhere in the hazard calculations, we have used a *b*-value of 0.73 rather than the median value of 0.58 (a) in the Gaussian smoothing of background seismicity (Section 5.2) and (b) in recurrence models for fault sources, both in applying the exponential recurrence model and the exponential portion of the characteristic model (Section 5). We made this choice because a *b*-value of 0.73 appears in three of the four weighted pairs of *a*- and *b*-values described earlier (Table 3-3). Sensitivity analyses show that the probabilistic hazard is not very sensitive to the choice of *b*-value between 0.58 and 0.73.

Table 3-1
Calculated Seismotectonic Province Recurrence Parameters

Province	*a*-value (per km^2)	*a*-value (whole area)	*b*-value	Magnitude (M)	N (for whole area)	RI (yrs)
Socorro Seismic Anomaly	-1.91	1.80	0.68	6	0.0054	185.2
	-1.91	1.80	0.68	5	0.0259	38.6
	-1.91	1.80	0.68	3	0.5886	1.699
Colorado Plateau	-3.44	1.67	0.63	6	0.0073	137.0
	-3.44	1.67	0.63	5	0.0313	31.9
	-3.44	1.67	0.63	3	0.5811	1.721
Southern Great Plains East of Rift	-2.58	2.95	0.89	6	0.0042	238.1
	-2.58	2.95	0.89	5	0.0324	30.9
	-2.58	2.95	0.89	3	1.9353	0.5167

RI = Recurrence Interval

N = Number of events/area

Note: Above *b*- and *a*-values have been rounded so exact recurrence values may not be reproducible from the significant figures reported in the table.

Table 3-2
Calculated Recurrence Intervals

	Area[1] (km^2)	*a*-value (per km^2)	*a*-value (whole area)	*a*-value (per 10,000 km^2)	*b*-value	M	N (for whole area)	RI (for whole area)	N (per 10,000 $km)^2$	RI (for 10,000 $km)^2$
RGR	100,649	-3.28	1.72	0.72	0.64	6	0.0072	138.89	0.0007	1428.57
Mmin=2.5	100,649	-3.28	1.72	0.72	0.64	5	0.0318	31.45	0.0032	312.50
	100,649	-3.28	1.72	0.72	0.64	3	0.6250	1.60	0.0612	16.34
RGR	100,649	-3.25	1.75	0.75	0.65	6	0.0069	144.93	0.0007	1428.57
Mmin=3.0	100,649	-3.25	1.75	0.75	0.65	5	0.0310	32.26	0.0031	322.58
	100,649	-3.25	1.75	0.75	0.65	3	0.6235	1.60	0.0619	16.16
RGR	100,649	-2.72	2.28	1.28	0.78	6	0.0039	256.41	0.0004	2500.00
Mmin=3.5	100,649	-2.72	2.28	1.28	0.78	5	0.0235	42.55	0.0023	434.78
	100,649	-2.72	2.28	1.28	0.78	3	0.8616	1.16	0.0856	11.68
Northern RGR	24,427	-3.36	1.02	0.64	0.50	6	0.0110	90.91	0.0045	222.22
Mmin=2.5	24,427	-3.36	1.02	0.64	0.50	5	0.0347	28.82	0.0142	70.42
	24,427	-3.36	1.02	0.64	0.50	3	0.3419	2.93	0.1400	7.14
Northern RGR	24,427	-3.45	0.94	0.56	0.48	6	0.0121	82.64	0.0049	204.08
Mmin=3.0	24,427	-3.45	0.94	0.56	0.48	5	0.0362	27.62	0.0148	67.57
	24,427	-3.45	0.94	0.56	0.48	3	0.3254	3.07	0.1332	7.51
Northern RGR	24,427	-3.11	1.28	0.89	0.56	6	0.0084	119.05	0.0035	285.71
Mmin=3.5	24,427	-3.11	1.28	0.89	0.56	5	0.0305	32.79	0.0125	80.00
	24,427	-3.11	1.28	0.89	0.56	3	0.3990	2.51	0.1633	6.12

[1] Areas probably have an uncertainty of ± 5%

RI = Recurrence Interval

N = Number of events/area

Note: Above *b*- and *a*-values have been rounded so exact recurrence values may not be reproducible from the significant figures reported in the table.

Table 3-3
Calculated Recurrence Intervals for Rio Grande Rift Using t-Analysis

2006 Analysis Weighted	Area	*a*-value (per km^2)	*a*-value (per 10,000 km^2)	*a*-value (per RGR)	*b*-value	M	N (per 10,000 km^2)	RI (per 10,000 km^2)	RI (RGR)	Adopted Weights
RGR	100,649	-3.29	0.71	1.71	0.43	6	0.0135	74.07	7.34	
		-3.29	0.71	1.71	0.43	5	0.0364	27.47	2.73	
		-3.29	0.71	1.71	0.43	3	0.2639	3.79	0.38	
RGR		-3.48	0.52	1.53	0.43	6	0.0088	113.64	11.33	
		-3.48	0.52	1.53	0.43	5	0.0236	42.37	4.21	
		-3.48	0.52	1.53	0.43	3	0.1710	5.85	0.58	
RGR		-2.95	1.05	2.05	0.43	6	0.0294	34.01	3.38	
		-2.95	1.05	2.05	0.43	5	0.0790	12.66	1.26	
		-2.95	1.05	2.05	0.43	3	0.5724	1.75	0.17	
RGR		-3.29	0.71	1.71	0.58	6	0.0017	588.24	58.31	
(preferred)		-3.29	0.71	1.71	0.58	5	0.0065	153.85	15.34	
		-3.29	0.71	1.71	0.58	3	0.0936	10.68	1.06	
RGR		-3.48	0.52	1.53	0.58	6	0.0011	909.09	90.02	0.20
		-3.48	0.52	1.53	0.58	5	0.0042	238.10	23.68	
		-3.48	0.52	1.53	0.58	3	0.0607	16.47	1.64	
RGR		-2.95	1.05	2.05	0.58	6	0.0037	270.27	26.89	
		-2.95	1.05	2.05	0.58	5	0.0140	71.43	7.07	
		-2.95	1.05	2.05	0.58	3	0.2031	4.92	0.49	
RGR		-3.29	0.71	1.71	0.73	6	0.0002	5000.00	463.19	0.30
		-3.29	0.71	1.71	0.73	5	0.0012	833.33	86.25	
		-3.29	0.71	1.71	0.73	3	0.0332	30.12	2.99	
RGR		-3.48	0.52	1.53	0.73	6	0.0001	10000.00	715.02	0.20
		-3.48	0.52	1.53	0.73	5	0.0007	1428.57	133.14	
		-3.48	0.52	1.53	0.73	3	0.0215	46.51	4.62	
RGR		-2.95	1.05	2.05	0.73	6	0.0005	2000.00	213.56	0.30
		-2.95	1.05	2.05	0.73	5	0.0025	400.00	39.77	
		-2.95	1.05	2.05	0.73	3	0.0721	13.87	1.38	

RI = Recurrence Interval

N = Number of events/area

In the 1995 study, there were limited geotechnical and geophysical data available to develop shear-wave velocity (V_S) and compressional-wave velocity (V_P) profiles and to develop or select nonlinear dynamic material properties (shear modulus reduction and damping curves). The velocity profiles and dynamic material curves are the input into the site response analyses, which incorporate the site-specific effects of the unique LANL geology on ground shaking. Due to the sparcity of data, a geotechnical/geophysical program was carried out as part of the 1995 study (Wong *et al.*, 1995). In that study, it became evident that the Bandelier Tuff exerted the greatest influence on the ground motions at LANL (Wong *et al.*, 1995).

Since 1995, the only new data that have become available on the Bandelier Tuff are primarily the result of investigations conducted at CMRR, which are described below. We begin with a general overview of the site geology to provide a context for the geotechnical investigations and then describe the efforts of Task 3 (Section 1.1), and the data used in the site response analyses. We refer the reader to the 1995 study for more detailed descriptions of the LANL geology and the 1995 geotechnical program (Wong *et al.*, 1995).

In this report, we are using the engineering definition of "soil." That is soil consists of unconsolidated or poorly consolidated deposits whose shear wave velocity (V_S) is less than about 2500 ft/sec or 760 m/sec, e.g., Bandelier Tuff.

4.1 OVERVIEW OF SITE GEOLOGY

The Pajarito Plateau is located at the base of the Jemez Mountains. It has a gently sloping surface that extends from the base of the Pajarito fault, eastward to the Rio Grande. The plateau is underlain by Bandelier Tuff (Figure 4-1) that has been deeply incised by many east-trending tributaries of the Rio Grande, leaving finger-like mesas radiating out from the base of the Jemez Mountains. Most of the LANL technical areas are located on these mesas. Figure 4-1 shows the generalized stratigraphy of the Bandelier Tuff.

In general, the basement rocks beneath the Pajarito Plateau consist of igneous and metamorphic rocks typical of the Sangre de Cristo Mountains to the east, and pre-rift Paleozoic-Mesozoic rocks typical of the Colorado Plateau to the west (e.g., Stearns, 1953; Griggs, 1964). These rocks are overlain by rift-fill sediments that are, in part, concomitant with volcanism associated within the Jemez volcanic field (e.g., Galusha and Blick, 1971; Gardner, 1985). The following describes the stratigraphic units from generally shallowest to deepest beneath the Pajarito Plateau that are most significant to the ground shaking hazard at LANL.

4.1.1 Bandelier Tuff

The following is a generalized description of the lower Quaternary (1.2 to 1.6 Ma) Bandelier Tuff (Figure 4-1), which is the most significant geologic unit with respect to ground motions at LANL. The Bandelier Tuff airfall units were erupted from the Jemez Caldera, which is centered about 20 km west of LANL. Owing to its close proximity, the airfall units show markedly different properties as one moves radially away from the caldera. Although the lithology of these beds remains relatively constant, there are significant variations in degree of welding (owing to emplacement temperature), porosity, grain size, and thickness, especially for the older

units that filled preexisting topography. There are two principal members of the Bandelier Tuff: the Otowi and Tshirege members.

4.1.1.1 Otowi Member

The 1.61 Ma Otowi Member of the Bandelier Tuff (Griggs, 1964) consists of a basal air-fall pumice bed, the Guaje Pumice Bed (Qbog), which is overlain by a sequence of pyroclastic flows (Figure 4-1). The Guaje Pumice Bed consists of unconsolidated air-fall pumice that is massive to poorly bedded and lithic poor. Clasts range in size from silt to 5 cm in diameter. The overlying pyroclastic-flow deposit consists of two sequences of a nonwelded, highly pumiceous, comparatively lithic-rich, poorly sorted tuff to lapilli tuff. Locally, vapor phase alteration has caused induration of the tuff.

4.1.1.2 Tshirege Member

The 1.2 Ma Tshirege Member of the Bandelier Tuff (Griggs, 1964) forms the surface of the Pajarito Plateau and rests unconformably on the Otowi Member (Figure 4-1). It also rests both unconformably and conformably on Cerro Toledo Rhyolite epiclastic deposits (Qct). The Tshirege Member forms the major part of the canyon cliffs of the plateau. It consists of a basal air-fall pumice, the Tsankawi Pumice Bed (Qbtt), which is overlain by ash-flow deposits (Figure 4-1). The Tsankawi Pumice consists of loose, tuff to lapilli tuff, air-fall deposits similar to the Guaje Pumice, but contains larger pumice clasts. Ash-flow deposits typically become moderate to densely welded westward towards the Jemez Mountains.

The following is a description of the subunits of the Tshirege member, from bottom to top, summarized from Broxton and Vaniman (2005):

Qbt1 overlies the basal Tsankawi Pumice Bed and consists of two parts, the lower Qbt1g and the upper Qbt1v, which are distinguished from one another on the basis of crystallization of glass. Qbt1g, which consists of poorly-sorted, non-welded, porous, and poorly-indurated ash flow tuffs, with occasional basal pyroclastic surge deposits, shows no crystallization from devitrification or vapor-phase alteration. Qbt1v, by contrast, consists of both cliff- and slope-forming porous, non-welded tuffs that are characterized by vapor-phase crystallization and devitrification of glass. The lower part, Qbt1vc, which is in sharp contact with Qbt1g, is an orange-brown, resistant, colonnade tuff, whereas the upper part, Qbt1vu, consists of white, alternating cliff- and slope-forming tuffs.

Qbt2 is a brown, cliff-forming, strongly-welded tuff with basal surge deposits in the eastern part; in the west, it is gradational with Qbt1v. Vapor-phase alteration of glass is extensive. Qbt2 is distinguished from the other subunits by its greater density, jointing, and welding, which also increases upsection.

Qbt3 is a variably welded, vapor-phase altered tuff that is the Caprock in the center of the Pajarito Plateau. The lower part is a purple-grey weathering to white, slope-forming, porous, unconsolidated, crystal-rich, non-welded tuff. The upper part is a cliff-forming, partly-welded tuff, with welding increasing to the west. In the far western part, Qbt3t, moderately to densely welded ash-flow tuff, occurs as the uppermost portion of Qbt3 and is transitional with Qbt4.

Qbt3 has been subdivided into a moderately hard and welded Qbt3U and the soft, poorly welded to nonwelded Qbt3L (Kleinfelder, 2006). The latter was a major factor in the site response at LANL (Sections 4.3 and 8.5).

Qbt4 is present only in the western part of the Pajarito Plateau. It comprises a suite of highly variable, non-welded to densely welded, largely vapor-phase altered and devitrified but locally vitric, ash-flow tuffs. The lower part includes non-welded to partly welded ash-flow tuffs with intercalated surge deposits. The upper portion consists of densely welded, cliff-forming ash flow tuffs that form the mesa Caprock.

4.1.2 Cerro Toleda Rhyolite/Epiclastic Reworked Pyroclastics

As referred to in this study and discussed by Gardner *et al.* (1994) and Heiken *et al.* (1986), the Cerro Toledo Rhyolite is a sequence of epiclastic deposits between the Otowi and Tshirege Members of the Bandelier Tuff that best correlates with the Cerro Toledo Rhyolite inside the Toledo Caldera. The deposits consist of unconsolidated sand and gravel with interbeds of Cerro Toledo Rhyolite pyroclastic deposits.

4.1.3 Tschicoma Formation

The Tschicoma Formation is composed of dacite with some pyroxene andesite flows (Griggs, 1964) that unconformably overlie Abiquiu Tuff and the Santa Fe Group in the northern Jemez Mountains (Gardner *et al.*, 1986). It is exposed at the surface in the upper parts of the canyons that drain the eastern Jemez Mountains. Flows of the Tschicoma Formation underlie the Bandelier Tuff on the western side of the plateau and interfinger with the Puye Formation.

4.1.4 Basalts

Olivine basalt flows erupted from centers southeast of the Pajarito Plateau and flowed northwestward into the LANL area, where they interfinger with the Puye Formation. Five separate flows were identified by Griggs (1964) with most described as thinning to the north. Basalt is exposed near the town of White Rock at the surface and within Los Alamos Canyon, where a 37-m-thick flow is characterized as massive and commonly brecciated at its base and edges.

4.2 GEOTECHNICAL INVESTIGATIONS

The following summarizes the studies performed at LANL that provided the basic data to develop velocity profiles and characterize the dynamic material properties used in the site response analyses (Section 8).

4.2.1 1992 Geotechnical Investigations

In 1992, the subsurface geology of the LANL was evaluated by compiling and evaluating all available data and information including geophysical and borehole data and by drilling four continuously-cored boreholes to depths of up to 846 ft. This was the first comprehensive effort

to characterize the site for assessing seismic hazards. Figure 4-2 shows the approximate locations of water supply and test wells, test holes, core holes, which existed in 1994 and which exceeded a depth of 200 ft (Wong *et al.*, 1995).

Core holes for seismic hazards evaluations were drilled at TA-55 (SHB-1), TA-3 (SHB-2), TA-16 (SHB-3), and TA-18 (SHB-4) (Figure 4-2). After coring, each hole was reamed to a diameter of 6 inches and PVC casing was lowered and set with cement slurry. The PVC casing (approximately 2.8 inches inside diameter) provided a conduit for lowering instruments to measure downhole velocities.

Downhole velocity surveys were carried out by Redpath Geophysics, from 25 through 30 May 1992, in the four boreholes to measure V_S and V_P as a function of depth. The resulting velocity profiles are shown on Figures 4-3 to 4-6. Measured V_S and V_P values are tabulated in Figures 4-7 to 4-9 for SHB-1 to SHB-3 in addition to lithologic units. A detailed discussion of the 1992 borehole program is contained in Wong *et al.* (1995).

4.2.2 CMRR Investigations

As part of a new geotechnical program to characterize the subsurface velocity structure, downhole-velocity, OYO-suspension-velocity, and seismic-crosshole surveys were performed in boreholes drilled in 2005 at the CMRR site in TA-55 (Figure 4-2) under the management of Kleinfelder, Inc. (2006). The boreholes include four shallow holes in the corners of the proposed CMRR footprint (SSC-1 to SSC-4), one deep hole in the center of the footprint (DSC-1B), and a deep hole outside and to the east of the footprint (DSC-2A). The CMRR borehole locations are shown on Figure 4-10. The depths of the boreholes are shown below:

Borehole	Depth (ft)
SSC-1	150
SSC-2A	150
SSC-3	150
SSC-4	150
DSC-1B	741
DSC-2A	550

Downhole Velocity Data

Both V_S and V_P downhole velocity measurements were made by Redpath Geophysics in the six CMRR boreholes in a manner very similar to the surveys performed in 1992 (Wong *et al.*, 1995). A detailed description of the surveys and results is contained in Redpath Geophysics (2005). The surveys were performed from 14 to 18 April 2005. Measurements were made at 3-ft intervals above depths of 96 ft, at 5-ft intervals between 100 and 300 ft, and at 10-ft intervals below 300 ft. The velocity profiles are shown on Figure 4-11 to 4-16 along with the lithologic units as interpreted by Alexis Lavine (LANL, written communication, 2005). As in the 1992 surveys, the velocity layers generally correlate well with specific units with the Bandelier Tuff, given that Redpath interpreted the travel time curves without prior knowledge of the borehole

lithology. This interpretative approach is preferred as it maintains changes in velocity that are consistent with the velocity surveys, reflecting best estimate *in-situ* velocities as well as depths where velocities change, which is not always coincident with inferred changes in lithology.

Examination of both V_P and V_S profiles (e.g., Figure 4-16) indicates Poisson's ratios based on V_P/V_S ratios generally are in the range of 0.15 to 0.4 typical of geologic materials. In a couple of instances, Poisson's ratio may be as low as 0.1 as indicated by the V_P/V_S ratio in Qbt2 in borehole SSC-1 (Figure 4-11). This type of variability has been observed in downhole velocity data at many sites including Yucca Mountain (Bruce Redpath, Redpath Geophysics, personal communication, 2006). Because the base case profiles are generally derived from the mean of several velocity profiles, unusually low or high V_P/V_S ratios are not an issue.

A review of the downhole velocity data by Richard Lee (2005) concluded that the "interpretations of P- and S-wave velocity are judged appropriate for site response purposes. Additional reinterpretation of the data is judged unnecessary." Based on our own evaluation of the data and results and the conclusions of Lee (2005), the CMRR downhole velocity data formed the basis for the base case velocity profiles used in this study.

OYO Suspension Data

OYO suspension measurements were made at 1.6 and 3.3 ft (0.5 and 1.0 m) intervals from top to bottom in the six CMRR boreholes by Geovision Geophysical Services from 18 to 20 April 2005 (Geovision, 2005; Kleinfelder, 2006). Both V_S and V_P measurements were made. Because of the less than ideal borehole conditions in which the OYO suspension surveys were conducted, i.e., the boreholes were cased, the quality of the data "ranged from fair to unusable" (Geovision, 2005). The results from SSC-1 to SSC-4 were either "unreliable" or "marginal." Data below a depth of 120 ft were considered fair in DSC-1B (Figure 4-17). In DSC-2A, data below 120 ft depth were fair except from 250 to 316 ft where it is unusable (Geovision, 2005) (Figure 4-18). Our review of the suspension data and a review by Lee (2005) were consistent with the description of the quality of the data as given by Geovision (2005). Because of the generally poor nature of the suspension data, it was not used in the development of the base case velocity profiles used in this study. Intervals where the data were deemed "fair" by Geovision were compared to the downhole data and they compared reasonably well.

Seismic Crosshole Testing

P- and S-wave seismic crosshole testing was also performed in boreholes SSC-1, SSC-2A, DSC-1A, and DSC-1B as the receiver holes by the University of Texas at Austin (2006a) during the week of 9 January 2006. The source was placed in three newly drilled holes. Measurements were generally taken at depths of 10, 20, 30, 40, 50, and 60 ft and then at 5-ft intervals down to 150-ft depth. The purpose of the crosshole testing was to evaluate the V_S of units Qbt3 and Qbt4 as measured by the downhole and suspension surveys. In particular, because of the effect of the lower velocity Qbt3 unit in the Bandelier Tuff on ground motions, an effort was made to better define possible transition zones in velocity between Qbt3 and the overlying and underlying units.

Crosshole test results were reviewed by Richard Lee (2006a). He concluded that the V_P data should not be used for the site response analysis. Comparison of the downhole and crosshole V_S

in Qbt3L indicated "excellent agreement," somewhat faster V_S with the crosshole in Qbt3u (2,000 ft/sec versus 1,600 ft/sec) but the "crosshole signals are more emergent" and some mismatch in Qbt2. Lee (2006a) also commented on the attempt to characterize the boundaries between the tuff units, i.e., whether they were sharp or transitional. He recognized, along with the authors of this study, that the use of crosshole tests to image a low-velocity zone will likely result in a degree of ambiguity as the source or receiver approaches the boundaries. For vertically-polarized SV-waves, there are three critical angles expected at CMRR based on downhole V_S and V_P velocities. Corresponding to each critical angle there are potential early (head wave) arrivals prior to the direct wave, resulting in an ambiguity in interpretation. This ambiguity, even with very closely spaced holes, could lead to the interpretation of gradual transition velocity zones between the tuff units. Based on the crosshole results, Kleinfelder (2006) reinterpreted the downhole velocity data to introduce the transitional layers "Qbt3-t and Qbt2-t" above and below Qbt3L, respectively. The crosshole results were not used directly by URS/PE&A in the development of the base case V_S models but were considered as confirmatory data except at the boundaries of the tuff units. The results of the sensitivity studies indicate that the influence of the transitional zones on site response is negligible (Section 4.3).

4.2.3 Mortandad Canyon Pilot Studies

In May and June 2002, Geophex, Ltd. performed two pilot geophysical studies in Mortandad Canyon (Figure 4-2). Vertical seismic profiling (VSP) was performed in two holes R-13 and R-15 to a depth of 1,000 ft. Preliminary interpretations of the data were performed by Lee (2006b) to assess V_P for the Puye Formation and Cerros del Rio basalt. (The Puye Formation is a fanglomerate that immediately underlies the dacite or the Guaje pumice [Wong *et al.*, 1995].) There are no measured V_S for these lithologic units and so the V_P results from Geophex VSP provided the only information available. Lee (2006b) interprets two layers for the basalt with the shallow layer having a V_P of 4,000 to 6,000 ft/sec and the lower layer 9,000 to 10,000 ft/sec. The V_P for the lower Puye Formation was about 7,000 to 8,000 ft/sec.

For this study, we are most interested in obtaining a reasonably reliable estimate of V_S for dacite, which underlies much of LANL because it represents the reference rock datum (Section 4.3). Only one estimate of dacite V_S was obtained in the CMRR boreholes (DSC-1B) and no velocity measurements are available from any other hole at LANL. The DSC-1B value of 2950 ft/sec is not regarded as reliable because the dacite was only penetrated to a depth of 25 ft at the bottom of the borehole (Bruce Redpath, Redpath Geophysics, personal communication, 2006). The most similar geologic material that has any V_S or V_P measurements is the Cerros del Rio basalt. Based on gross similarities in physical properties, we believe that V_S values corresponding to the higher V_P values for the Cerros del Rio basalt (i.e., 9,000 to 10,000 ft/sec) would be representative of the V_S for the dacite (J. Gardner, LANL, personal communication, 2006). Assuming Poisson's ratios of 0.25 to 0.30 typical of rock would indicate corresponding V_S values for the fastest basalt ranging from 4,800 to 5,800 ft/sec. Thus we adopted a lognormal average of about 5,300 ft/sec for the dacite.

4.3 SITE-SPECIFIC VELOCITY PROFILES

In this section, we describe the base case V_S and V_P profiles used in this study based on the downhole data. The V_S profiles were used in the site response analysis (Section 8.2.2). The V_P profiles were used to compute V/H ratios (Section 8.3). As previously stated, the suspension and crosshole velocity data were only used in a confirmatory sense. Because of the limited amount of velocity data for LANL outside of CMRR, we assumed that velocities and lithologic units were correlated across LANL and so in Tables 4-1 and 4-2, we computed average depth-dependent velocities for each lithologic unit for which there were downhole data. The approximate depth range and log-normal average velocities are shown on Tables 4-1 and 4-2 based on the CMRR boreholes and the boreholes SHB-1 to SHB-4.

After careful review of the suspension log and downhole reports for CMRR, Richard Lee's review of the data, and extensive discussions with Bruce Redpath, we believe the downhole velocities are correctly interpreted and reliable. Whereas there is more uncertainty in the downhole results for the shallow velocity zone (Qbt3L) than is usually encountered, additional measurements are not likely to provide greater resolution. We believe this is especially true for the crosshole techniques applied to the CMRR facility as the uncertainty in this survey is largest for the exact boundaries (location) of the low-velocity zone. The actual velocity within Qbt3L from the crosshole and downhole surveys are very consistent across the CMRR site and at borehole SHB-1, far outside the building footprint. Thus based on the results of the downhole surveys within the CMRR footprint (excluding DSC-2A), we have adopted the log-normal mean V_S and V_P profiles (Figures 4-19 and 4-20) as the bases for the base case profiles for CMRR. Note that only borehole DSC-1B extends below a depth of 150 ft.

By smoothing the mean V_S profile (Figure 4-19), two base case profiles have been developed. These smoothed V_S base cases A and B in Figure 4-21 are intended to capture the range in shallow mean V_S profiles across CMRR, principally the range in mean thicknesses of the shallow low velocity layer (Qbt3L) and the range in velocity of the high velocity caps above Qbt3L. Thus the thickness of Qbt3L was set at two thicknesses: 50 ft and 75 ft. The Qbt4/Qbt3 thicknesses were defined at 50 ft and 60 ft. The V_S of Qbt4/Qbt3 were set at 1500 ft/sec and 1800 ft/sec (Figure 4-21). These variations were based on the variability observed in the CMRR boreholes (Figures 4-11 to 4-16 and 4-19b) with some consideration to additional variability that may not be observed in the limited number of boreholes. Two corresponding A and B V_P base cases for CMRR were developed by using the site-specific Poisson's ratio (Figure 4-21).

To evaluate the sensitivity of the Qbt3L properties in the velocity profiles, the stochastic point-source ground motion model (Section 6.3) was used. A point-source model assuming a **M** 6.5 event at a distance of 1 km (depth 8 km) was modeled, based on the M and D deaggregation in 1995 (Wong *et al.*, 1995). This is used only to provide reasonably appropriate control motions for about 2,500-year return period hazard. A second event was also simulated where the source depth was reduced to 3 km to confirm that base case profile B dominates at high loading levels. Figure 4-22 shows median spectra for base case profiles A and B. Figure 4-23 is a similar plot at much higher loading levels showing the same trend of base case B having amplitudes generally greater than or about equal to base case A. Figure 4-24 compares base case profiles A and B spectra with the measured profile DSC-1B (the only deep measured profile at CMRR, near the center). This comparison confirms the thickness of the high velocity unit above Qbt3L is not a significant player.

We also analyzed the issue of sharp versus transitional boundaries for QbtL. Figure 4-25 compares the spectra for base case profile B using a correlation model that smoothes boundaries (puts in steps) and one that preserves discontinuities (rough). Figures 4-26 and 4-27 show the corresponding median and ± 1σ profiles. From Figure 4-25, smoothing of discontinuities has little impact on motions, as expected based on wavelength considerations. Figure 4-28 compares median point-source spectra for base cases A and B using rough profiles (compare to Figure 4-24 using smooth profiles).

The base case velocity models for TA-3 and TA-16 are shown in Figures 4-29 and 4-30, respectively. They reflect a combination of the measured velocities from SHB-2 and SHB-3, respectively, and average velocities (Tables 4-1 and 4-2) or inferred values (Figures 4-8 and 4-9). No other velocity data exist for these two technical areas. Figure 4-31 shows the TA-55 base cases developed primarily from SHB-1 (Figure 4-7). The V_S base case profile and the CMRR V_S base case profiles were used for calculating the hazard at TA-55.

A product of this study was ground motions at a selected "reference rock datum" to allow future site-specific site response analyses. The top of dacite (outcrop), which underlies most but not all LANL, was selected and agreed upon by Walt Silva, Ivan Wong, Carl Costantino, and Tom Houston. This unit was chosen because it was the shallowest unit with a consistent "rock-like" velocity (about 5300 ft/sec) and it was deep enough for purposes of soil-structure interaction (SSI) analyses.

4.4 DYNAMIC LABORATORY TESTING

Similar to what was done in the 1995 study, dynamic laboratory testing was performed by the University of Texas at Austin (UTA) on 22 samples collected in the CMRR boreholes (UTA, 2006b). The dynamic properties that were evaluated are the shear modulus (G) and material damping ratio (D) of the samples. Values of G and D were measured in the linear strain range where they are independent of strain amplitude and in the nonlinear strain range where they vary with strain amplitude. All measurements were performed in the Soil and Rock Dynamics Laboratory at UTA. Combined resonant column and torsional shear (RCTS) equipment was used to perform the measurements (UTA, 2006b). All laboratory work was conducted under NQA-1 Standards with the equipment within the calibration period.

Table 4-3 lists the 22 samples that were tested. The dacite, Qbt2 and Qbt3u samples and one Qbt1v sample were recovered as HQ (2.5-inch diameter) cores. The remaining samples (Qbt1v, Qbt1g, Qbo, Qct, and Qbt3L) were recovered with either 3-in. or 6-in.- (76 mm or 152 mm) diameter Pitcher samplers. The dacite and Qbt2 samples that were tested with the RCTS equipment were recorded from the field cores obtained during sampling. All other samples were trimmed by hand to the final dimensions. In some cases, only the ends were trimmed and in other cases, the sides and ends were trimmed.

The influence of the following variables on G and D were analyzed (UTA, 2006b): (1) magnitude of the isotropic state of stress, σ_o; (2) time of confinement at each σ_o; (3) shearing strain amplitude, γ; (4) number of cycles of loading, N; (5) excitation frequency, f; and (6) stress history. The most important variables affecting G and D of these materials were isotropic stress, σ_o, and shearing strain amplitude, γ (UTA, 2006b). The impact of σ_o in the linear strain range

(where the properties are independent of γ) on V_S, small-strain shear modulus, G_{max}, and small-strain material damping ratio, D_{min}, were evaluated. In general, the effect of σ_o on V_S, G_{max}, and D_{min} is (UTA, 2006b): (1) essentially none for the very hard dacite and the moderately to strongly welded tuff, Qbt2; (2) very little for the moderately welded tuff, Qbt3u; and (3) typical of lightly cemented to uncemented soils for the poorly welded tuffs (Qbt1v, Qbt1g, and Qbo), the silty sand (Qct) and the poorly welded tuff in the Qbt3L layer. In the nonlinear strain range, γ has an impact on G, G/G_{max} and D. The values of G and G/G_{max} decreased and D increases as γ increases. Overall, the effects of γ on G/G_{max} and D is rather small for the very hard dacite and the strongly welded to moderately welded tuff, Qbt2; and significant for the moderately welded tuff (Qbt3u) and the poorly welded tuffs and silty sand (Qbt1v, Qbt1g, Qbo, Qct, and Qbt3L). The relative effect is nearly the same on the Qbt3u and Qbt3L materials.

4.5 SELECTION OF DYNAMIC MATERIAL PROPERTIES

Table 4-4 indicates which shear modulus reduction and damping curves were used for various stratigraphic units in 1995 (Wong *et al.*, 1995). Two sets of modulus reduction curves were used: tuff and sand. Four sets of damping curves were used: shallow tuff, deep tuff, sand (rhyolite), and sand (pumice). Also shown are the number and type of samples tested in 1993 and 2006 by UTA (Stokoe *et al.*, 1993; UTA, 2006b).

To extrapolate the UTA (2006b) test results to higher strains, the EPRI (1993) G/Gmax and hysteretic damping curves were used. The EPRI curves were based on a simple hyperbolic soil model with depth dependencies (suite of curves) reflecting distinct reference strains (EPRI, 1993). The EPRI (1993) curves have been validated by modeling recorded motions at over 500 sites (19 earthquakes) to cyclic shear strains of about 1% (Silva *et al.*, 1996).

The extrapolation process involves adjusting the reference strains of the closest EPRI (1993) curves to provide a fit to the measured values and then using the resulting curve to model the strain dependencies of that lithologic unit. Separate fitting is done for the G/Gmax and hysteretic damping curves.

Sample disturbance corrections are also based on modeling recorded motions using the EPRI (1993) curves and involves adjusting reference strains by the ratio of laboratory-to-field downhole V_S measurements (Table 4-5). This approach was used in adjusting the G/Gmax curves used on the Yucca Mountain Project (Bechtel SAIC, 2004). For cases where there is more than about a 20% difference in V_S (Table 4-5), corrections are applied. Note, for the EPRI curves (Figure 4-32), a factor of two in depth corresponds to about a 50% change in reference strain, which may result in significantly different motions, depending on strains developed. We treat the adjustments, (correction for sample disturbance/biased sampling) as epistemic variability with equal weights between the data driven curves (case 1) and the adjusted curves (case 2). All curves are shown in Figures 4-33 to 4-46. The models, adjustments, and weights have been reviewed and accepted by Kenneth Stokoe as appropriately reflecting laboratory test results as well as extrapolations to larger strains. As will be shown in Section 8, the impact on hazard between using the adjusted or unadjusted curves is insignificant.

Figures 4-47 (base case profile A) and 4-48 (profile B) compare median spectra using the unadjusted curves and curves adjusted for *in-situ* large scale fracturing (V_S lab greater than V_S

field, resulting in more nonlinear adjusted curves) and sample disturbance (V_S lab less than V_S field resulting in more linear adjusted curves). The differences in the spectra are small indicating that the adjustment for field versus laboratory is not significant in terms of the ground motions.

As a comparison of the impact of the dynamic curves on ground motions, Figure 4-49 shows spectra using the 1993 versus 2006 curves for SHB-1 (TA-55). Clearly the 1993 curves result in lower short-period motions, to a significant degree (≥ 20% for peak acceleration). Kenneth Stokoe reviewed his 1993 test results, believes they are valid, and suggests the differences reflect within-unit changes in geology both within and between technical areas. It is recommended for the sites other than CMRR that both sets of curves be used with equal weighting. This would apply to both unadjusted and adjusted curves, for a total of four cases of epistemic variability, all equally weighted.

Table 4-1
Average Depth-Dependent Unit V_S

Unit	Borehole										Depth Range (ft)	Log-normal Average (ft/sec)
	DSC-1B (CMRR)	DSC-2A (TA-55)	SSC-1 (CMRR)	SSC-2A (CMRR)	SSC-3 (CMRR)	SSC-4 (CMRR)	SHB-1 (TA-55)	SHB-2 (TA-3)	SHB-3 (TA16)	SHB-4 (TA-18)		
Qbt4		**1000**	**750**	**1050**	**1000**	**1000**	**760**	**1160**			**0-30**	**949**
		(0-25)	(0-15)	(0-17)	(0-27)	(0-16)	(0-20)	(0-30)				
Qbt4									**1765**		**0-40**	**1765**
									(0-40)			
Qbt4									**1086**		**40-50**	**1086**
									(40-50)			
Qbt4								**1570**	**1695**		**30-75**	**1631**
								(30-75)	(50-64)			
Qbt3t									**3135**		**64-210**	**3135**
									(64-210)			
Qbt3U	**1000**										**0-45**	**1000**
	(0-45)											
Qbt3U		**1700**	**1600**	**1850**		**1550**	**1820**				**15-79**	**1700**
		(25-65)	(15-79)	(17-67)		(32-78)	(20-40)					
Qbt3U	**1550**				**1500**		**1345**				**27-92**	**1462**
	(47-75)				(27-92)		(40-92)					
Qbt3U								**1174**			**75-90**	**1174**
								(75-90)				
Qbt3U								**3027**			**90-144**	**3027**
								(90-144)				
Qbt3?									**2047**		**210-242**	**2047**
									(210-242)			
Qbt3L	**1000**	**1050**	**950**	**1050**	**1050**	**1000**	**995**				**65-128**	**1013**
	(75-125)	(65-125)	(79-111)	(67-128)	(92-125)	(78-122)	(92-120)					
Qbt3L								**1690**			**144-180**	**1690**
								(144-180)				
Qbt2	**2700**	**1900**	**2400**			**2800**	**2145**				**111-220**	**2365**
	(125-220)	(125-205)	(111-145)			(122-145)	(120-220)					
Qbt2									**3510**		**242-320**	**3510**
									(242-320)			

Table 4-1
Average Depth-Dependent Unit V_S

Unit	Borehole										Depth Range (ft)	Log-normal Average (ft/sec)
	DSC-1B (CMRR)	DSC-2A (TA-55)	SSC-1 (CMRR)	SSC-2A (CMRR)	SSC-3 (CMRR)	SSC-4 (CMRR)	SHB-1 (TA-55)	SHB-2 (TA-3)	SHB-3 (TA16)	SHB-4 (TA-18)		
Qbt1v										**990** (0-27)	**0-27**	**990**
Qbt1v	**1650** (220-272)	**1900** (205-252)					**1690** (220-254)				**205-272**	**1743**
Qbt1g										**1625** (27-80)	**27-80**	**1625**
Qbt1g										**2495** (80-140)	**80-140**	**2495**
Qbt1g		**1900** (252-285)									**252-285**	**1900**
Qbt1g	**2950** (272-330)	**2850** (285-310)					**2305** (254-300)				**254-330**	**2686**
Qct	**2950** (330-390)	**2850** (310-370)					**2825** (300-350)		**2715** (320-424)		**300-424**	**2834**
Qct							**3250** (350-450)				**350-450**	**3250**
Qbo										**2015** (140-180)	**140-180**	**2015**
Qbo	**2950** (390-665)	**2850** (370-500)							**2400** (424-570)		**370-665**	**2722**
Qbog	**2950** (665-695)										**665-680**	**2950**
Dacite	**2950** (695-720)										**695-720**	**2950**

Note: Values in bold are V_S in ft/sec. Values in parentheses are the depth interval for that V_S value.

Table 4-2
Average Depth-Dependent Unit V_P

Unit	Borehole											
	DSC-1B (CMRR)	**DSC-2A (TA-55)**	**SSC-1 (CMRR)**	**SSC-2A (CMRR)**	**SSC-3 (CMRR)**	**SSC-4 (CMRR)**	**SHB-1 (TA-55)**	**SHB-2 (TA-3)**	**SHB-3 (TA16)**	**SHB-4 (TA-18)**	**Depth Range (ft)**	**Log-normal Average (ft/sec)**
Qbt4		1850 (0-10)	1400 (0-15)	1500 (0-17)	1600 (0-27)	2000 (0-32)	1700 (0-20)	1800 (0-30)			0-32	1682
Qbt4								3100 (30-75)			30-75	3103
Qbt4									None			
Qbt4												
Qbt3t												
Qbt3t									None			
Qbt3U	2300 (0-45)	3200 (10-65)	3500 (15-79)	3000 (17-67)	3600 (27-92)	3250 (32-78)	3264 (20-39)	1800 (75-92)*			0-45	2300
Qbt3U	3600 (45-75)						2800 (39-92)				10-92	3338
Qbt3U											39-92	2800
Qbt3U								4400? (92-144)			75-92	1800
Qbt3U									None		92-144	4400?
Qbt3U												
Qbt3?												
Qbt3L	2550 (75-125)	2400 (65-125)	1900 (79-111)	2650 (67-125)	2250 (92-125)	2200 (78-122)	2325 (92-121)	3103 (144-197)			65-125	2355
Qbt3L									None		144-197	3103

Table 4-2
Average Depth-Dependent Unit V_P

Unit	Borehole											
	DSC-1B (CMRR)	**DSC-2A (TA-55)**	**SSC-1 (CMRR)**	**SSC-2A (CMRR)**	**SSC-3 (CMRR)**	**SSC-4 (CMRR)**	**SHB-1 (TA-55)**	**SHB-2 (TA-3)**	**SHB-3 (TA16)**	**SHB-4 (TA-18)**	**Depth Range (ft)**	**Log-normal Average (ft/sec)**
Qbt2 Qbt2	4500 (125-220)	4500 (125-210)	3600 (111-145)	2650? (125-150)	2250? (125-140)	4400 (122-145)	3897 (121-200)		None		111-200	4163
Qbt1v Qbt1v	3450 (220-272)	3250 (210-240)					2903 (220-256)				210-272	3349
Qbt1g Qbt1g Qbt1g Qbt1g	4600 (272-330)	3250 (240-285) 4850 (285-310)									240-285 272-330	3250 4723
Qct Qct	4600 (330-390)	4850 (310-370)									310-390	4723
Qbo Qbo	4600 (390-490) 5650 (490-665)	4850 (370-500)									370-500 490-665	4723 5650
Qbog	5650 (665-695)										665-695	5650
Dacite	5650 (695-720)										695-720	5650

Note: Values in bold are V_P in ft/sec. Values in parentheses are the depth interval for that V_P value.

Table 4-3
Samples Tested by the University of Texas in 2005

Sample Description	Unit	Number of Samples
Moderately welded tuff	Qbt3U	2
Poorly welded tuff	Qbt3L	8
Moderately to strongly welded tuff	Qbt2	2
Poorly welded tuff	Qbt1v	2
Poorly welded tuff	Qbt1g	2
Silty sand	Qct	2
Poorly welded tuff	Qbo	2
Hard to very hard	Dacite	2

Table 4-4
Dynamic Laboratory Testing and Shear Modulus Reduction and Damping Curves Used

Unit	Stokoe *et al.* (1993) Samples Tested	UTA (2006b) Samples Tested	1995 Modulus Reduction	1995 Damping
Qbt4			Shallow Tuff	Tuff
Qbt3t			Shallow Tuff	Tuff
Qbt3	1	Qbt3U tested	Shallow Tuff	Tuff
Qbt3L		8	Shallow Tuff	Tuff
Qbt2	1	2	Shallow Tuff	Tuff
Qbt1v		2	Shallow Tuff	Tuff
Qbt1g		2	Shallow Tuff	Tuff
Qct	2	2	Sand (Rhyolite)	Sand
Qbo		2	Deep Tuff	Tuff
Qbog			Sand (Pumice)	Sand

Table 4-5
Ratios of Laboratory and Field V_S Measurements

Unit	Lab/Field V_S Ratio**
Qbt3U	1.20*
Qbt3L	0.93*
Qbt2	1.68
Qbt1v	0.94*
Qbt1g	0.64
Qct	0.64
Qbo	0.72
Dacite	1.60

Source: Kenneth Stokoe, UTA, written communication, 2006

* No correction was applied for sample disturbance for differences in V_S less than 20%.

** Ratios are computed from UTA average laboratory measurements of V_S (UTA, 2006b) and downhole V_S from Redpath Geophysics (2005), except for the dacite. For the latter, the suspension velocity measurement of the dacite (Geovision, 2005) was used.

The first step in a probabilistic assessment of earthquake hazards is a characterization of the seismic sources that will produce ground motions of engineering significance at the site or area of interest. Two general types of seismic sources were considered in this probabilistic hazard analysis: (1) active or seismogenic faults and (2) areal source zones (generally coincident with the seismotectonic provinces described in Section 3.1.1). Areal source zones include all potential seismic sources that can generate earthquakes that may be too small or deep to rupture to the surface. For both faults and areal source zones, the seismic source characterization depends on three fundamental elements: (1) the identification, location, geometry, and rupture characteristics of significant sources of earthquakes; (2) the maximum or characteristic size of these earthquakes (M_{max}); and (3) the rate at which the earthquakes occur. Our overall approach to seismic source characterization and the seismic source parameters that are globally the same for both faults and areal source zones (e.g., maximum seismogenic depth) are discussed first in the introduction to this section. Parameters specific to faults are discussed next (Section 5.1), followed by parameters for background seismicity areal source zones (Section 5.2).

This analysis expands on our previous probabilistic hazard studies in the region (Wong *et al.*, 1995, 1996a; Olig *et al.*, 1998, 2005), but is based primarily on our most recent study (Wong *et al.*, 2004). The seismic source characterization of Wong *et al.* (2004) was updated and modified for this study as discussed below with particular attention given to characterization of the Pajarito fault system (PFS) because it dominates the hazard at LANL. Our characterization of the PFS in this study is significantly revised from Wong *et al.* (2004) in that it was very simplified for that regional study. Our new characterization of the PFS is also significantly revised from Wong *et al.* (1995, 1996) to incorporate a considerable amount of new fault data, which are discussed in detail below. However, we note that these data are all from previous studies and no new geologic or geophysical investigations were conducted as part of this study.

Specific earthquake parameters needed for the seismic source characterization are fault location, geometry, sense of slip, M_{max}, and earthquake recurrence rate. Uncertainties in these seismic source parameters are sometimes large and include (1) those arising from lack of knowledge (epistemic uncertainties) and (2) those due to inherent variability in the earthquake process (aleatory uncertainties). The second type of uncertainty was handled by integration in the hazard calculations (Section 2); the first, by use of a logic-tree approach. In the latter procedure, values of the source parameters are represented by the branches of logic trees with weights that define the distribution of values. An example logic tree is shown in Figure 5-1. In general, three to five values for each parameter were weighted and used in the analysis. In the current state of practice for PSHA, and as was done in this study, logic tree parameters are primarily assigned using expert judgment on the basis of applicable data, which are often sparse. To help guide our judgment in assigning values and weights, we used the following studies. Statistical analyses suggest that a three-point distribution of 5th, 50th, and 95th percentiles weighted 0.185, 0.63 and 0.185 (herein rounded to 0.2, 0.6, and 0.2 weights), respectively, is the best three-point approximation of a continuous, symmetric distribution (Keefer and Bodily, 1983). Alternatively, they found that the 10th, 50th, and 90th percentiles weighted 0.3, 0.4, and 0.3, respectively, can be used when limited data make it difficult to determine the extreme values (i.e., the 5th and 95th percentiles) of a distribution. For parameters that we judged to be symmetrically distributed, such as maximum magnitudes, we generally applied these guidelines in assigning values and weights unless data suggested it was somehow inappropriate or needed to be adjusted. For parameters that we believe to be asymmetrically distributed, such as for slip rates of many faults

in the RGR, we used a five-point approximation from Miller and Rice (1983), which is described as follows:

Percentile	Weight (rounded to nearest 100th)
3.5	0.10
21	0.24
50	0.32
79	0.24
96.5	0.10

This distribution was developed using a discrete approximation procedure based on Gaussian quadrature, which Miller and Rice (1983) found provided a better approximation of the variance, skew, and kurtosis of continuous distributions, particularly for asymmetric distributions. We note that we assigned weights to two decimal places for these distributions because we found that rounding can measurably shift the weighted mean for asymmetric distributions; not because we mean to imply that we know these distributions to a higher degree of precision.

All seismic sources (both faults and areal source zones), except for the PFS, were assigned a range of maximum seismogenic depths of 12, 15 and 18 km, weighted 0.2, 0.6 and 0.2, respectively, as was done by Wong *et al.* (2004). This results in a weighted-mean seismogenic depth of 15 km. This distribution of depths was primarily based on regional analyses of well-located earthquakes in the RGR and incorporates a measure of variability (3 km) often observed in the seismicity catalog (e.g., Sanford *et al.* 1991; Wong *et al.*, 1995). In addition, it has been observed that large earthquakes such as the 1983 **M** 6.8 Borah Peak earthquake can extend down into the brittle-plastic transition zone (Mendoza and Hartzell, 1988); hence the inclusion of the value of 18 km.

5.1 QUATERNARY FAULTS

Machette (1998) discusses the importance of integrating Quaternary fault data into seismic hazard assessments in the RGR despite the lack of historical surface-faulting earthquakes in the rift. In accordance with DOE Standard 1022-94, we considered all known and suspected Quaternary faults (<1.6 Ma) within the study region for inclusion in this update of the LANL PSHA. Appendix B includes a detailed discussion of our criteria for incorporating faults into this study. To update and augment the seismic source characterization of Wong *et al.* (2004) as set forth in Appendix B, we reviewed new data from a variety of sources including USGS, New Mexico Bureau of Geology and Mineral Resources (NMBGMR), and LANL geologic studies. We also contacted numerous geoscientists regarding previously unpublished and ongoing work in the region. These include: Daniel Koning, Scott Minor, Keith Kelson, James McCalpin, Tony Crone, Mike Machette, Bob Kirkham, David Love, Larry Anderson, and Mike Timmons. Specific citations are included below and in numerous tables and figures, and we gratefully acknowledge the contributions of these individuals.

A total of 56 fault sources were characterized in this analysis, including the PFS. Plate 1 shows the location of all the fault sources. Fault parameters required in the probabilistic hazard analysis include (1) rupture model (including independent vs. dependent, single plane vs. zone, segmented vs. unsegmented, and linked configurations); (2) probability of activity; (3) fault

geometry including rupture length, rupture width, fault orientation, and sense of slip; (4) M_{max} (or the characteristic magnitude); and (5) earthquake recurrence, including both recurrence model and rates. Except for the PFS, specific fault parameters and their weights are summarized in Table 5-1 and discussed in general below. For convenience, we refer to these other faults herein as regional faults. Due to its importance and complexity, our characterization of the PFS is discussed separately and in more detail in Section 5.1.1. Parameters in Table 5-1 are shown in this abbreviated tabulated form rather than the expanded graphical form of Figure 5-1 to save space, but the outline of the seismic source model as shown in Figure 5-1 is essentially similar for all regional faults. Except as noted, fault nomenclature and numeric identifiers generally follow those used by Machette *et al.* (1998) and the USGS Quaternary Fault and Fold Database (URL: http://earthquake.usgs.gov/regional/qfaults). Faults that have been added or whose geometry has been modified from the USGS database are designated with an "A" preceding the fault number (e.g., the Ojo Caliente fault, No. A2144; and Chili fault, No. A2145). Faults are listed in numerical order in Table 5-1 and those parameters that have been revised from Wong *et al.* (2004) are shown in bold type.

5.1.1 Regional Fault Parameters

5.1.1.1 Rupture Models and Geometries

Where the data permit, we have tried to accommodate structural variations that are potentially significant to the hazard analyses by including a variety of rupture behavior models and fault geometries in our source characterization (Table 5-1). All faults were modeled as a single plane or multiple planes. However, faults that are close to LANL (including the PFS, Sawyer Canyon fault, and the southwestern section of the Embudo fault system; Nos. A2008, 2028, and A2007b, respectively) were modeled using curvilinear planes to more accurately represent source-to-site distances. We digitized the primary, most active fault trace and projected these curves down-dip using a weighted-mean strike to model the curvilinear geometries of these faults. Thus, these simple curvilinear surfaces retain a constant dip and do not accommodate complexities like listric geometries (i.e., decreasing dip with depth).

We consider a variety of rupture models including single independent planes, segmented faults, linked faults, and zones of faults. Most faults were included as single independent (unsegmented) planar sources, unless the paleoseismic data suggest otherwise. The rupture behavior of most of the faults in the region is poorly understood and is likely more complex than our simplifying assumptions. Nevertheless, we have addressed uncertainties that are significant to the hazard given the published data. Alternatives to the single-plane, independent fault model are "potentially segmented faults" or "linked faults." Some faults show good evidence for being segmented (e.g., the Tijeras-Canoncito fault, No. 2033); that is, they have relatively persistent boundaries that have confined prehistoric surface ruptures to particular portions of the faults (segments). For other faults, the evidence is more ambiguous as to whether persistent rupture-segment boundaries exist (e.g., Jemez-San Ysidro fault, No. 2029). Potentially linked faults may experience spatially related coseismic rupture (either along or across strike), such as the Bernalillo, Sandia, Rincon and Placitas faults (respectively Nos. 2034, 2037, 2036 and 20430). Finally, earthquakes on fault zones are modeled as random ruptures on multiple subparallel planes within discrete boundaries, and we typically use this model when multiple fault traces are

short, and/or discontinuous, and distributed over a broad area (e.g., faults near Cochiti Pueblo, 2142).

Other important fault geometry parameters include length and dip, which can influence source to site distances and maximum magnitudes. Fault lengths were measured end to end in a straight line, consistent with convention when measured fault length is to be used as an empirical estimator of maximum earthquake magnitude. Fault dips are averaged over their full extent in the seismogenic crust. Most (but not all) faults show or are inferred as having dominantly normal slip. For most typical range-bounding normal faults, preferred dips are assumed to be 60 ± 15° unless noted otherwise (Table 5-1). Exceptions include zones of intrabasin faults and faults inferred to be dominantly strike-slip, which were assumed to be generally steeper (e.g., the Embudo fault system and the Tijeras-Canoncito fault zone).

5.1.1.2 Maximum Magnitudes

Our preferred values of maximum or characteristic magnitudes (M_{max}) were estimated using the empirical relationships developed by Wells and Coppersmith (1994) based on all types of faults, as noted in footnote 4 and others of Table 5-1. Depending on the data available for individual faults, we used relations based on displacement and surface-rupture length, although data for displacement are generally lacking for most RGR faults. For faults without displacement data, our preferred maximum magnitude is the best estimate from the empirical relation using surface rupture length as input. For faults with displacement data, we generally averaged best estimates from displacement-based relations and the length-based relation to determine our preferred values, which is consistent with the model used in the 2002 National Seismic Hazard Maps (Frankel *et al.*, 2002), and seems reasonable as preferred values are based on median estimates from the regression relations. The specific displacement values used, the data sources, and how these data were used to estimate a preferred maximum magnitude are included in fault-specific footnotes throughout Table 5-1. Maximum magnitudes were generally assumed to be symmetrically distributed about the preferred values. We weighted preferred values 0.6, whereas uncertainties of ± 0.3 magnitude units about preferred values were each weighted 0.2. Note that these alternative branches in the logic tree (± 0.3 magnitude units) account for epistemic uncertainties; additional aleatory uncertainties of ± 0.25 (segmented) to ± 0.3 (unsegmented) are also included within the hazard calculations to the characteristic magnitude (Section 2.2.6) so that the full range of uncertainty is as much as ±0.6 magnitude units. Following Wong *et al.* (2004), we did not use the area-based empirical relation of Wells and Coppersmith (1994) because it may systematically underestimate maximum magnitudes for RGR faults. Additionally, rupture areas are often difficult to determine given the complex, multiple-strand and overlapping geometries of many fault systems in the rift, such as the PFS (Plate 2).

5.1.1.3 Probabilities and Rates of Activity

In assigning probabilities of activity for each fault source, we considered both the likelihood that the fault is structurally capable of independently generating earthquakes and the likelihood that it is still active within the modern stress field. We addressed many factors in assessing these likelihoods, such as orientation in the modern stress field, fault geometry (length, continuity, and dip), relation to other faults, time of youngest movement, rate of activity, geomorphic

expression, amount of cumulative offset, and any evidence for a non-tectonic origin. Faults with definitive evidence for repeated Quaternary activity were generally considered to be active (seismogenic) and assigned probabilities of 1.0 (Table 5-1). Exceptions include faults that may be secondary and dependent on other faults, mapped faults or fault-like features that may have a non-seismogenic origin, and faults that may be too short (< ~10 km) to independently generate surface-rupturing earthquakes. The probability of activity for faults that do not show definitive evidence for repeated Quaternary activity was individually judged on the basis of the criteria explained above. Resulting values of probability of activity range from 0.3 to 1.0 (Table 5-1). Machette (1998) discusses the tendency to underestimate seismic hazards in areas of slow extension and low seismicity, such as the RGR, by not adequately including contributions from Quaternary faults. We believe that using the criteria of repeated Quaternary activity for judging probability of activity adequately addresses this issue, even for faults with recurrence intervals on the order of hundreds of thousands of years (e.g., Pitaycachi fault; Bull and Pearthree, 1988) or faults that show evidence of temporal clustering and extreme variations in rates of activity (e.g., Caballo and La Jencia faults, respectively Nos. 2088 and 2109; Machette, 1998).

We considered both recurrence intervals and slip rates, depending on the data available, to characterize rates of earthquake activity on faults. However, recurrence interval data are lacking for most faults in the RGR and so we necessarily used just fault slip rates for most faults. We considered both long- (≤ 1.6 Ma) and short-term (≤ 130 ka) data in developing slip rate or recurrence distributions, but we preferred short-term data whenever they were available. In addition to the time period, we also considered the type and quality of data in determining slip or recurrence rate distributions. Ideally, slip rates should be average net rates over the entire fault plane, so whenever possible we made the necessary adjustments to make values consistent with this. For example, we converted vertical slip rates to net slip rates for most faults by assuming 100% dip slip and a preferred fault dip. For faults showing a measurable component of strike-slip we calculated a net slip rate using an inferred rake and preferred fault dip (e.g., Embudo fault system; see footnotes 14 and 16 in Table 5-1). Variations of displacements along strike can significantly affect the calculation of slip rates (Wong and Olig, 1998), but very few faults have enough data to calculate average rates for the entire fault (e.g., PFS). More typically there are only a few data points from one or two sites along the fault (e.g., Hubbell Spring fault, No. 2120) or no fault-specific data at all (e.g., Gallina fault, No. 2001). In the latter case, we assumed slip rate distributions that are the same as or similar to nearby structures, taking into account such factors as style of deformation, geomorphic expression, and time of youngest movement.

Unfortunately, many of the Quaternary faults in the study area only have limited long-term slip rate data or no slip rate data at all (Machette *et al.*, 1998). These faults were respectively termed Class B and C faults by Wong *et al.* (1995). In his compilation of slip rate data for RGR faults, McCalpin (1995) found that short-term (≤ 130 ka) rates were often much higher than long-term rates (>130 ka), resulting in a very asymmetric overall distribution skewed toward higher slip rates for the upper percentiles. In some cases this may be due to temporal clustering of earthquakes, which has been observed on many faults in the rift (McCalpin, 1995; Machette, 1998). Alternatively it may be due to: (1) overall lower rates of extension in the rift prior to the late Quaternary; (2) overestimation of short-term rates on some faults due to inclusion of the open-ended time interval since the time of the most recent event; or (3) underestimation of long term rates due perhaps to unrecognized slip on buried faults, miscorrelation of markers due to

subsequent footwall erosion and hanging wall deposition, or inclusion of larger open-ended time periods in long-term rates (Wong and Olig, 1998).

To account for unknown uncertainties and possible variations in rates on poorly understood faults, we used an approach similar to that described by McCalpin (1995) to develop slip-rate distributions for faults where only limited or long-term data are available. We have used this approach in previous studies and additional discussion is provided in Wong *et al.* (1995, 1996a, 2004) and Wong and Olig (1998).

The method for assessing slip rate distributions is based on an ergodic substitution of space for time. This means that the slip rate dataset for better-studied faults in the rift is used to determine a slip rate distribution for a poorly understood fault. This substitution is accomplished by normalizing the slip rates for all the well-studied faults to a common rate factor relevant to the poorly understood fault, such as the long-term rate (N). A cumulative frequency plot of these normalized rates then has the 50th percentile "anchored" at this long-term rate. The plot of the distribution then shows the expected variation in rates assuming that the fault of interest behaves like other better-studied faults in the rift. An example for N = 0.1 mm/yr is shown in Table 5-2 and Figure 5-2. This normalized frequency plot can be used to determine a five-point slip-rate distribution (3.5, 21, 50, 79 and 96.5 percentiles) as previously described. For the example of N = 0.1 mm/yr, the resulting distribution is:

Percentile	Slip Rate	Weight
3.5	0.015	0.1
21	0.047	0.24
50	0.09	0.32
79	0.19	0.24
96.5	0.85	0.1

Note that all of our distributions were actually calculated in Microsoft Excel using the percentile function and not measured from plots.

Since the previous PSHA at LANL in 1995, numerous paleoseismic studies have been conducted on faults in the RGR and so we incorporated these new data and updated McCalpin's (1995) analysis. These new data are shown in **bold** in Table 5-2. It was our belief that some of the asymmetry to McCalpin's original distribution may have been artificial and due to the inclusion of data for open-ended intervals or incomplete seismic cycles, so in our new analysis we have only included new short-term data for complete seismic cycles; that is, where the slip per event and recurrence interval for the preceding seismic cycle were known. These criteria have resulted in the revision of data for one fault (the County Dump fault, No. 2038) and the addition of data from 8 more sites on 6 additional faults (Table 5-2). Thus, we have increased the number of slip-rate observations in the analysis from 34 to 49, and although the asymmetry is reduced, it still is significant as seen in Figure 5-3. Interestingly, the plot of slip-rate data that only includes complete seismic cycles (2005 subset on Figure 5-3) shows little asymmetry. The comparison in Table 5-3 shows that decreasing the asymmetry shifts the weighted mean slip rate closer to the 50th percentile or preferred value, which would effectively lower the hazard for any particular fault. However, the reduced asymmetry in the 2005 subset may partly be an artifact of the small

sample size (only 17 slip-rate observations), and so we used the entire 2005 dataset for this study. Although it was beyond the scope of this study, we believe that reviewing all the original data and redoing the entire analysis to only include data for complete seismic cycles could further reduce the asymmetry, and we strongly recommend doing this for any future seismic hazard analyses for LANL.

5.1.1.4 Recurrence Models

As previously discussed in Section 2, we considered three earthquake recurrence models: truncated exponential, maximum-magnitude, and characteristic. Our weights for each model in the logic trees depended on fault geometry and type of rupture model (Table 5-4). Observations of historical seismicity and paleoseismic investigations suggest that a characteristic-behavior model is more likely for individual faults, whereas seismicity in broader fault zones or regions is better fit by a truncated exponential model (Schwartz and Coppersmith, 1984; Youngs and Coppersmith, 1985). Therefore, we generally favored the characteristic model for all fault sources except zones of faults. For all unsegmented faults (including linked and independent rupture models) we assigned a slightly higher weight to the truncated exponential model and used a slightly wider range for the characteristic magnitude (Section 2.2.6) since RGR faults often show complex, overlapping and distributed rupture patterns with broader variations in displacements per event (and likely broader variations in earthquake magnitude) than might be expected for standard characteristic earthquake models (e.g., Hubbell Spring fault [Olig *et al.*, 2007], County Dump fault [McCalpin *et al.*, 2006], PFS [Gardner *et al.*, in review; this study]. Using these same lines of reasoning, we generally down-weighted the maximum-magnitude model (Wesnousky, 1986) because, except for aftershocks, it does not allow smaller events to occur on mapped fault sources, and we judge this to be less likely for the faults with broad, complex rupture patterns, which are common in the RGR.

For comparison, weightings on recurrence models used for faults included in the 2002 National Seismic Hazard Maps were also primarily dependent on rupture model (Frankel *et al.*, 2002), but the models and weights were different than our study. The 2002 National Seismic Hazard Maps only include two types of fault rupture models, segmented (Type A) and unsegmented (Type B) faults, with all faults in New Mexico classified as Type B faults, which are given equal weight (0.5/0.5) to characteristic and Gutenberg-Richter recurrence models. However, it is important to point out that although their Gutenberg-Richter model is similar to our truncated exponential model, the characteristic model used in the 2002 National Seismic Hazard Maps is not the same as the characteristic model defined by Youngs and Coppersmith (1995) that we used (Section 2.2.6).

5.1.2 Pajarito Fault System (PFS)

The north-striking, east-dipping PFS is about 50 km long, extending along the western margin of LANL (Figure 5-4). This major Quaternary normal fault forms the boundary between the Espanola Basin (on the east) and the Pajarito Plateau (on the west)—as such, it is the active western boundary of the RGR at the latitude of Los Alamos (Plates 1 and 2). The PFS is actually a broad (>10 km wide), complexly distributed zone of faults that includes numerous discontinuous features such as fault scarps, graben, fissures, monoclinal warps and folds, all of which accommodate an overall east-west extension and allow early Quaternary deposits to be

displaced nearly 200 m down to the east (Plate 2; McCalpin, 1997; Lewis *et al.*, 2005, in review). The PFS shows compelling evidence for repeated late Quaternary faulting, but individual rupture patterns are complex and the timing of some events remains ambiguous (e.g., Gardner *et al.*, in review; McCalpin, 2005).

Before we further discuss characteristics of the PFS and their implications to our seismic source model, we need to define some terms that have specific meanings as used here to describe our PFS model. The terminology we use generally, but not entirely, follows that of the Working Group on California Earthquake Probabilities (WGCEP 2003) and includes:

Fault segments – Like the WGCEP, we divide faults and fault systems (in this case the PFS and EFS) into segments (five for the PFS and two for the EFS, which are described further below). These segments are considered to be the basic building blocks for earthquake ruptures on each fault. Each fault segment has length, width (the down-dip dimension), and geologic slip rate. Unlike the faults in the WGCEP model, the PFS has overlapping segments, which makes the geometry of earthquake ruptures more complicated. Another difference for our model is that neither the PFS nor the EFS show any evidence for aseismic geologic slip, in contrast to faults in the WGCEP model which do, and therefore needed to have this parameter characterized. The segments of the PFS are shown in Figure 5-4 and are discussed in more detail below.

Rupture sources – Like the WGCEP, we allow for the simultaneous rupture of two or more adjacent fault segments of the PFS. Each possible combination of segments is a rupture source. For various structural and behavioral reasons, which are discussed further below, we did not include every possible combination of PFS fault segments in our model.

Floating earthquakes – In our model the PFS can host floating earthquakes – earthquakes of a specified magnitude, but without a fixed location. This is similar to the WGCEP model. The concept of floating earthquakes allows for the fact that some (and indeed for the PFS we believe most) earthquakes are not represented by the prescribed segmentation. Floating earthquakes are classified and treated as rupture sources.

Rupture scenarios – A rupture scenario is a combination of rupture sources that describes a possible mode of failure of the fault during one seismic cycle. This is similar to the definition used by the WGCEP, but we define a seismic cycle to be the time from when a surface-faulting earthquake occurs on the PFS to the time of the next surface-faulting earthquake, not necessarily failure of the entire fault system as defined by the WGCEP.

Fault rupture models – A rupture model is a weighted combination of the rupture scenarios for a fault, each combination representing one possibility for the long-term behavior of the fault system (e.g., the next 100 surface-faulting ruptures). Thus, the weights assigned to the various rupture scenarios within a rupture model reflect the number of times a particular scenario is expected to occur during the next 100 ruptures. Based on structural and paleoseismic data, we originally developed three rupture models for the PFS, but eliminated one on the basis of the moment balancing results (discussed further below and in Appendix C).

Moment balancing – This approach involves analysis of a fault rupture model to appropriately partition the slip rate of a segment into earthquakes representing the various rupture scenarios of

the fault rupture model to keep the fault in moment equilibrium. The moment is balanced when the long-term moment accumulation is equal to the long-term moment release:

$$S \times A \times \mu = M_o \times R \quad (5\text{-}1)$$

where S is the long-term slip rate, A is the fault plane area, μ is the shear modulus (3E+11 dyne/cm^2), M_o is the average moment per earthquake, and R is the rate of earthquakes. Our moment-balancing approach for the PFS is described in Appendix C and is theoretically similar to that used by the WGCEP, but is necessarily more complex due to overlapping fault segments with opposing dips.

As defined here, the PFS includes five fault segments: the main element is (1) the 36-km-long Pajarito fault (PAF), the main east-dipping segment to the south; secondary elements include (2) the 12-km-long Santa Clara Canyon fault (SCC), the main east-dipping segment to the north; (3) the Rendija Canyon (RC) and Guaje Mountain (GM) faults, two shorter west-dipping segments that extend between the PAF and SCC; and, (4) the Sawyer Canyon fault, a short west-dipping segment that is outboard and subparallel to the RC and GM (Figure 5-4). In this study we modeled the Sawyer Canyon fault as a separate rupture source for simplicity and because it is north of LANL and dips away from the lab (see Table 5-1 for parameters of the Sawyer Canyon fault, No. 2028), as was done previously in the characterization of Wong *et al.* (1995). We believe this simplifying assumption is slightly conservative, but is justified by the minor role of the Sawyer Canyon fault within the PFS and the need to simplify an already extremely complex model. In addition, this allows us to focus on the PFS fault segments that are much more significant to LANL because of their proximity and geometry.

There is a considerable amount of new data on the PFS as a result of detailed mapping (e.g., McCalpin, 1997; Gardner *et al.*, 2001; Lewis *et al.*, 2002; Lavine *et al.*, 2003a, 2003b), structural studies (e.g., Schultz *et al.*, 2003; Lewis *et al.*, 2005, in review) and paleoseismic investigations (e.g., McCalpin, 1998, 1999, 2005; Reneau *et al.*, 2002; Gardner *et al.*, 2003, in review) conducted since 1995. Plate 2 shows the results of the new detailed mapping, the location of paleoseismic study sites, and the location of the three sites where the ground motion hazard was calculated for this study. Figure 5-4 is a slightly simplified version of the PFS that shows locations of schematic cross-sections (Figure 5-5) and displacement profiles (Figure 5-6). Figure 5-7 schematically illustrates our structural model for the PFS. Table 5-5 summarizes the age data for deposits constraining the timing of surface-faulting events on the PFS based on all previous paleoseismic studies. Tables 5-6 and 5-7 illustrate two surface-faulting chronologies that we judge to be reasonable end-member scenarios based on our review and interpretations of all the PFS paleoseismic data.

We have significantly revised the seismic source model of Wong *et al.* (1995) for this study on the basis of these data and interpretations (which are discussed further below). Figure 5-8 shows the revised PFS logic tree and Table 5-8 shows the footnotes corresponding to the logic tree. Figures 5-9a through 5-9d show the revised rupture scenarios and corresponding rupture sources. These figures, along with numerous tables associated with the logic tree, summarize the parameters for the new PFS model. Some of the more notable changes in the revised PFS characterization include an overall simplification of rupture models, consideration of both simultaneous and synchronous types of multisegment ruptures, and explicit incorporation of Holocene temporal clustering of surface-faulting earthquakes on the PFS (Figure 5-8). Another

significant difference was the use of a moment-balancing approach to ensure that moment rate was appropriately proportioned in the segmented fault rupture models of the PFS. Given the complexity of the PFS and its proximity to LANL, we believe that the moment balancing was particularly useful because it provided insight on the internal consistency of our model and how it compares with the paleoseismic data.

The following subsections describe the details of the PFS seismic source model and the relevant data that our choices were based on. We start with our structural model, which forms the framework for our seismic source characterization. We then discuss the various specific features of the model, generally following the order shown on the logic tree, including rupture models and geometries, types of multisegment ruptures, maximum magnitudes, and rates of activity. This last section includes discussions of the recurrence intervals, slip rates and weights assigned, and moment balancing of rates. Note that recurrence models for the PFS were the same as for other regional faults in this analysis and the basis for these were discussed in previous sections.

5.1.2.1 Structural Model

Based on detailed mapping of the PAF, McCalpin (1997) concluded that the PFS is better characterized on the surface as a complex, articulated monoclinal flexure rather than a discrete range-bounding normal fault. Recent high-precision mapping of the PFS in selected areas where key LANL facilities are located (Gardner *et al.*, 1998, 1999, 2001, Lavine *et al.*, 2003a, 2003b; Lewis *et al.*, 2002) coupled with displacements measured on the top of the Tshirege member of the Bandelier Tuff (Olig *et al.*, 1996; Lewis *et al.*, 2005; in review) have provided some key insights into the complex deformation patterns of this distributed zone.

One key insight is that, although the PAF and SCC segments form the main western margin of the Espanola basin, there appears to be a large gap (about 5 km) between presently mapped traces of each segment (Figure 5-4). This gap is coincident with a major change in strike of the PFS from northerly to northeasterly. Additional high-precision mapping should be done at the southern end of the SCC to confirm this gap. Observations that support existence of the gap include the rapid decrease of displacement at the northern end of the PAF and the southern end of the SCC (Figure 5-6), as well as the broad fanning out of fault splays in a horsetail-like pattern at the northern end of the PAF (Figure 5-4).

Another related key insight is in our understanding of the secondary antithetic faults of the PFS. Although the RC and GM are smaller antithetic faults to the PAF and SCC, they are probably not just shallow space-accommodation features that do not release earthquake moment, as is typical for many antithetic faults. Instead they appear to be transfer or relay faults (Acocella *et al.*, 2005), which form linkages that transfer strain between the PAF and SCC (Lewis *et al.*, in review). This interpretation is supported by the map and displacement patterns, which show that the RC and GM (along with the Sawyer Canyon fault) partly fill the deformation gap between the PAF and SCC, and may eventually form a more complete half-ellipse displacement pattern for the entire PFS (Figures 5-4 and 5-6).

This deformation pattern is illustrated in more detail by comparing a series of cross-sections across the PFS (Figures 5-4 and 5-5) with displacement patterns (Figure 5-6) from south to north (cross-sections S1 through S7, respectively). Only the PAF exists at the southern end of the PFS

(S1 and S2 on Figure 5-5) and it accommodates all of the slip at these latitudes (Figure 5-6). As the southern end of the RC is encountered (S3 and S4), displacement on the PAF starts to decrease whereas displacement on the RC rapidly increases (Figure 5-6). As the southern end of the GM is encountered (S5 on Figure 5-5) and displacement on it rapidly increases, displacement on the RC starts to slowly decrease. Displacement on the PAF continues to decrease northward, dying out to zero just north of Rendija Canyon (Figure 5-4). Thus, at the latitude of S6 only the RC, GM, and Sawyer Canyon faults appear to accommodate any strain at the surface. Displacements on both the RC and GM continue to decrease northward, dying out as they each intersect the SCC. At the latitude of S7 (Figure 5-5), the SCC accommodates all of the slip on the PFS and displacement appears to rapidly increase (as part of the projected elliptical displacement envelope for the entire PFS, Figure 5-6) and then falls off toward the northern end. More displacement data and more detailed mapping are sorely needed to better define deformation patterns on the SCC, but landowner access restrictions have hampered study of the SCC to date.

Overall, the deformation patterns for the PFS suggest that it is composed of several distinct fault segments and associated fault splays that have recently grown together to become at least partially structurally linked, but are not yet completely integrated (Lewis *et al.*, in review). Evidence for this includes faults that branch and splay in a horsetail pattern (Figure 5-4) at the northern and southern ends of the PAF as displacement dies out to zero (Figure 5-6). This horsetail pattern is typical at the tips or rupture terminations of normal faults (Kneupfer, 1989). The southern end of the west-dipping RC also shows a similar horsetail pattern as it curves toward the northern end of the PAF, strongly suggesting interaction and initial linkage developing between the RC and PAF. A developing linkage of the PAF with the RC, and indeed the GM and SCC as well, is also supported by displacement patterns which are individually elliptical, but asymmetric toward fault tips (Figure 5-6). Indeed this pattern is seen on many individual fault splays or fault sections of the system, although the cumulative displacement pattern for the entire system forms a symmetric ellipse, except at major fault intersections where some large displacement deficits exist (Lewis *et al.*, in review). Structural linkage of faults of the PFS is also supported by the geometry and close spatial association of faults, which suggests that the faults intersect and merge at depth (Figure 5-5).

Additional supporting evidence that the PFS is composed of discrete faults that have grown together can be seen in map and displacement patterns for the entire PFS. Individual fault traces show multiple sharp bends, changing strike from north to northeast. These bends are present at many scales on the PFS and are evident on faults throughout the RGR (Plate 1). The three largest and most prominent bends on the PFS are in the Cochiti Canyon area, near St. Peter's Dome, and at the intersection of the RC, GM and Sawyer Canyon faults with the SCC (Figure 5-4). These bends are characterized by fault intersections with dramatic displacement deficits, suggesting they may have formed by linkage of originally distinct north- and northeast-striking faults that have subsequently grown together (Lewis *et al.*, in review; Figure 5-6).

Very few kinematic data regarding fault-slip direction are available for the PFS. Slip directions measured on the RC and GM indicate dominantly normal slip with rakes that are typically between 80° and 90°, but occasionally range as low as 70° (Karen Carter, personal communication 1994, cited in Wong *et al.*, 1995, Table 7-1, footnote 9). Unfortunately, slip-direction data are lacking on the PAF, but with its similar northerly strike one would expect slip

directions similar to the RC and GM. In contrast, the SCC strikes northeast and could have a larger component of oblique slip, although data are lacking to check this hypothesis.

Figure 5-7 shows views of our 3-D structural model for the PFS. These views were extracted from an interactive 3-D representation created by Claudia Lewis in Arcsine using digital elevation data to model the ground surface, digital fault traces to accurately represent complex geometries, and assumed fault dips (which are within the ranges used in our seismic source characterization for the PFS, Figure 5-8). It is noteworthy that the fault dips are the most poorly constrained part of the model due to the lack of subsurface structural data.

Although the PAF and SCC form the western margin of the Espanola basin, there is a gap of ~ 3½ km between the fault planes at the surface, which can extend to considerable depths in the model depending on the assumed dips. For the dips shown in Figure 5-7, the gap extends to 12 km, but the PAF and SCC intersect at shallower depths for shallower dips. However, regardless of the fault dips that are used, there is always a gap that extends to at least a depth of 4 to 5 km. Another key aspect to the model is that although the RC and GM are smaller antithetic structures to the PAF and SCC, we believe that they still play an important role in rupture behavior of the system by filling the gap between the PAF and SCC, transferring or relaying slip between the north-striking PAF and northeast-striking SCC, and providing linkage of the entire system. The presence of much smaller Quaternary displacements of the RC and GM than the PAF suggests that this linkage may be a relatively recent development in the evolution of the fault system. However, the paleoseismic record (discussed in the next section, Table 5-5) also strongly supports coseismic rupture of the PAF and RC and the PAF and GM during the Holocene, which indicates to us that this linkage, however new, will likely continue in future earthquake ruptures.

5.1.2.2 Rupture Models and Geometries

5.1.2.2.1 Paleoseismic Data

In addition to the structure of a fault system, the paleoseismic record is critical to understanding its rupture behavior. Since this and other faults in the area lack historical surface-faulting earthquakes, the prehistoric record of surface-ruptures provides valuable data for modeling future large earthquakes. Table 5-5 summarizes the timing of surface-faulting events identified at numerous sites on various segments of the PFS based on all the available data. Since a comprehensive compilation of the PFS did not previously exist, we have tried to thoroughly reference original sources, provide information about the types of data through color coding, and provide comments and qualifiers as needed through the use of footnotes in Table 5-5. Table 5-5 shows our preferred correlation of events (P1 being the youngest surface-faulting paleoearthquake and P14 the oldest), but some time ranges are broad enough to allow for other potential correlations and we have tried to indicate this by using dashed lines between likely alternatives. For many events, particularly older ones, the timing of individual events is not known and so groups of events are shown as open blocks. Note that interpretations at some of the sites differ among various investigators, and we have tried to represent this uncertainty by using multiple columns for these sites (e.g., trench sites 97-3 and 97-7). Also note that Table 5-5 does not include displacement per event data. Although displacement data for individual faults are available for many sites along the PAF (see Table 3-1 in Olig *et al.*, 2001 for a compilation), net displacements per event on the PAF are lacking due to the very wide, complex nature of

faulting. Displacements per event on the RC and GM are unexpectedly large (> 1 m) for these short faults (< 10 km), and the details of the data from previous studies are discussed in Footnotes 8 and 9 of Table 5-10.

Despite the complexity in the PFS paleoseismic data, four observations are readily apparent from the compilation: (1) data are lacking on the SCC; (2) overall rupture patterns are complex, but the PAF appears persistently to be a primary fault, if not the primary fault during rupture events; (3) the record is most complete for the past 40,000 years and is too incomplete to use before 110 ka; and, (4) the time between events (recurrence interval) has not been uniform since 110 ka. Indeed, a cluster (two or three) of surface-faulting events during the Holocene results in much higher rates of activity during this period than during the late Quaternary on average (Gardner *et al.*, in review). McCalpin (2005) did not reach this conclusion in his recent summary paper on the PFS, partly because (1) he did not include results from recent studies at the WETF site (Gardner *et al.*, in review), at the EOC site (Reneau *et al.*, 2002), and on the GM fault at Chupaderos Canyon (Gardner *et al.*, 2003), and (2) he interpreted the timing of the youngest event at Trench 97-4 differently than Gardner *et al.* (in review, Table 5-5).

The variability of PFS recurrence intervals throughout the late Quaternary (≤ 130 ka) as deciphered from the paleoseismic record is very significant to the seismic hazard at LANL, so some additional discussion is warranted especially given differing interpretations and uncertainties. Unfortunately, the paleoseismic record is fraught with uncertainties due to 1) missing sections of the latest Pleistocene and Holocene stratigraphy; 2) discrepancies between dating methods; 3) difficulties in identifying faulting-event horizons (the ground surface at the time of faulting); and interpreting timing relations (particularly for fissures) along an articulated monocline (versus a typical range-bounding normal fault with more "well-behaved" colluvial wedges); and, 4) the complex and often wide distributed zone of deformation for the PFS. We have considered these uncertainties in developing rupture models and characterizing recurrence interval distributions for the entire PFS, and in many cases have gone back to review original reports, trench logs and the age data. Mark Hemphill-Haley assisted us with our review of the paleoseismic data and James McCalpin generously provided preprints of his 2007 summary papery and answered many questions. We have attempted to compare and accurately represent different interpretations and their uncertainties in Table 5-5, while still keeping it comprehensible and useable. The following paragraphs provide a brief synopsis of the post-1995 studies cited in Table 5-5.

During 1997, McCalpin (1998) excavated seven trenches along an E-W transect near Los Alamos Canyon; he found evidence for at least six surface-faulting events that occurred since about 110 ka, with the youngest event having occurred between about 1.5 and 2.5 ka (1260 and 2290 cal yr B.P.). Based on this record, McCalpin (1998) calculated an average recurrence of 21.7 kyr, but stressed this may be a maximum because the record may not be complete, especially for the entire PAF. In addition, soil development indices suggest that individual recurrence intervals have varied from less than 10 kyr to just over 60 kyr (McCalpin, 1998).

In a subsequent study, McCalpin (1999) excavated seven additional trenches located between Highway 4 and Pajarito Canyon; three of these (Trenches 98-4, 98-5 and 98-6), each exposed evidence for at least two events, but the timing of events was only broadly constrained. Based on preliminary ages, McCalpin (1999) suggested that the youngest event in each trench occurred

between 2 and 20 ka, and the timing of the penultimate events ranged from 8.7 to 18.9 ka for Trench 98-4, to 41 to 58 ka for Trench 98-6. He concluded that the youngest event in the 1998 trenches may correlate to the youngest event in four of the 1997 trenches, but the age constraints from the 1998 trenches were "insufficiently precise" to make a definitive correlation. Given the even larger uncertainties for the timing of older events, McCalpin (1999) did not attempt correlating older events, but instead estimated the following trench–specific recurrence intervals: (1) 5 to 11.6 kyr (trench 98-4); (2) 11.3 to 21.6 kyr (trench 98-5); and (3) 28.6 to 48.9 kyr (trench 98-6). However, he also noted that the deformation in Trench 98-4 included folding and thrust faulting that was likely related to landsliding, and so could have been entirely nontectonic (although the landsliding could have been triggered by earthquakes).

Subsequently, McCalpin (2000) re-evaluated the timing for faulting events identified in his 1998 and 1999 reports. In this analysis he suggested that all previous soil-based age estimates (except modern soils) are actually minimums due to erosion. He speculated that discrepancies between his previous soil-based age estimates and true ages generally increased with depth to as much as 50%. The resulting increase in age estimates, effectively doubles his previous estimates for long-term recurrence intervals (i.e., from 21.7 kyr to about 43.0 kyr for the past six events identified in Trench 97-3, and from 34.0 kyr to 68.0 kyr for the past three events identified in Trench 97-7). McCalpin (2000) also revised time estimates for the youngest event identified in the 1997 trenches and suggested that it may be a separate event from the youngest event identified in the 1998 trenches because of a possible segment boundary between trenches.

Although there are some merits to McCalpin's (2000) revised analysis, it contains many serious inconsistencies (e.g., S.L. Reneau, LANL, written communication, 1-3-01), and many questions remain about the timing of surface-faulting events and the overall paleoseismic record for the PAF. Additionally, many of the revised reinterpretations presented in McCalpin (2000) are not presented in his most recent manuscript on the PAF, McCalpin (2005). Therefore, to compile his interpretations in Table 5-5, we have relied heavily on the data and interpretations presented in the original reports (McCalpin, 1998, 1999) and McCalpin (2005), supplemented by discussions with him to resolve apparent discrepancies.

Due to the problems and inconsistencies of the interpretations presented in McCalpin (2000), and more importantly to incorporate new data from recent studies (e.g., Reneau *et al.*, 2002; Gardner *et al.*, 2001; 2003), Gardner *et al.* (in review) re-evaluated the paleoseismic data and chronology of the PFS, focusing on the most recent events, and in particular, evidence for possibly three Holocene events. The summary of their interpretations as presented in Table 5-5 have benefited from considerable input from all the coauthors, and it reflects their most current depiction of the paleoseismic record for the PFS.

To summarize the paleoseismic data in Table 5-5, we believe that at least two and probably three surface-faulting events occurred on the PFS since 11 ka (events P3, P2, and P1 occurred between 10.9 ka and 1.3 ka; see also footnote 16 in Table 5-8 for details). This relatively rapid sequence of events is in contrast to available evidence for the apparently slower rate of surface-faulting earthquakes during the late Quaternary—with at least 5, probably 6 or more, and possibly 9 surface-faulting events occurring on the PFS since 110 ka (P1 through P9). However, the late Quaternary record is likely incomplete, timing ranges are generally larger for older events, and possible alternative correlations are more complex than for the Holocene record. To represent these uncertainties, Tables 5-6 and 5-7 show our end-member scenarios of six to nine events

having occurred since 110 ka. If the late Quaternary record is indeed incomplete, as we believe, then future paleoseismic investigations will, if anything, increase the number of surface-faulting events identified on the PFS. We have tried to consider the potentially incomplete record in developing and weighting rupture models and recurrence interval distributions for the PFS.

The paleoseismic data also indicate complex rupture behavior for the PFS. The most recent event on the PAF (Event P1) did not rupture the antithetic RC or GM faults (Table 5-5). In contrast, Event P2 on the PAF likely ruptured coseismically with the GM but not the RC, and Event P3 on the PAF likely ruptured coseismically with the RC but not the GM (Table 5-5). However, we cannot preclude independent rupture of the PAF and GM during P2 or of the PAF and RC during P3 since these events could be closely spaced in time due to triggering, and thus indistinguishable in the paleoseismic record. Still, the large displacements per event observed on both the RC and GM support coseismic rupture with the PAF as well as the evidence for structural linkages of faults discussed previously. For Event P4, the paleoseismic data permit all three faults (PAF, RC and GM) to rupture coseismically since times are poorly constrained, except on the GM fault at the Chupaderos Canyon site (Table 5-5). Before Event P4, uncertainties are too large and the record too incomplete to distinguish specific rupture patterns. Overall, the data indicate a variety of different types of rupture patterns for the PFS, with the PAF persistently rupturing, perhaps as the "driver" of the system, although we know little of the rupture behavior of the SCC and its role within the system.

5.1.2.2.2 Rupture Models and Scenarios

Based on the structural relations between faults and fault segments of the PFS and the paleoseismic data and displacement patterns previously discussed, we originally developed three rupture models for the PFS: two segmented models (Models A and B), and an unsegmented, floating-earthquake model (Model C). These models included seven different rupture scenarios (RS-a through RS-h, with rupture sources as shown on Figures 5-9a through 5-9d), which were designed to represent possible complex rupture patterns of the different fault segments of the PFS. On the basis of the structural and paleoseismic data, all of the rupture scenarios assumed that the PAF is the primary fault segment and always ruptures in larger surface-faulting events. In addition, we also assumed that if the PAF ruptures with the SCC, then either the RC, or GM, or both, must also rupture to transfer the strain between the PAF and SCC. As a result of these assumptions, our scenarios all have only one rupture source that always includes the PAF.

Furthermore, in both segmented models, we considered a small chance that large events on the PFS might extend past the SCC and onto the southwestern section of the Embudo fault system (EFS/SW; RS-e on Figure 5-9c). This possibility was primarily based on the fact that the EFS/SW is kinematically compatible with the PFS and lies directly along strike of the northern tip of the SCC, whose geometry is apparently distinctly simple (i.e., one main strand), in direct contrast to the complex multiple splays that form a horsetail pattern at the southern end of the PAF (Figure 5-4). Finally, because of a lack of data on the SCC and EFS/SW fault segments, we cannot preclude occasional coseismic rupture on them. However, recent studies do indicate that Quaternary activity on the EFS/SW appears to be less—and the most recent faulting to be older—than on the PFS overall. Koning (2005) estimated 10 to 13 m of vertical displacement across the EFS/SW on terraces estimated to be about 620 ka, however, latest Quaternary (< 30 ka) terraces did not appear to be offset. This suggests that although the SW-EFS may

occasionally rupture with the PFS, it has apparently not done so in the past four events involving the PAF, and that the EFS/SW must have a much lower rate of Quaternary activity than the PAF.

We originally defined the two segmented rupture models, A and B, to reflect uncertainties in the rupture behavior of the SCC. In Rupture Model A, the SCC only ruptured in larger events when the entire system ruptured (i.e., RS-d and RS-e, Figures 5-9b and 5-9c, respectively). In contrast, Rupture Model B assumed that the SCC always ruptured when either the RC or GM ruptured (i.e., RS-f and RS-g on Figures 5-9c and 5-9d, respectively). An additional difference between the two segmented rupture models was that weights on rupture scenarios for Model A were based on the proportion of latest Quaternary events consistent with the rupture scenario. In contrast, weights on ruptures scenarios for Model B were originally based on proportions of Quaternary displacement on the system (initial weights shown in Table 5-9). However, during the process of moment balancing (discussed further below) we found that Rupture Model A required unreasonably large displacements per event on the SCC, resulting in offsets larger than 4 m and 50% larger than those on the PAF for the same scenario. Given the much shorter length of the SCC and the smaller total Quaternary displacement on the SCC than the PAF, we found this to be unreasonable and thus eliminated Rupture Model A (and rupture scenarios RS-b, RS-c and RS-d) from our seismic source characterization of the PFS (Figure 5-8). At this point in the process, we were left with four rupture scenarios under Rupture Model B and one rupture scenario for the unsegmented Rupture Model C.

We strongly favored (weighted 0.85) the unsegmented model (Rupture Model C on Figure 5-8), which allows a 36-km long partial rupture to "float" (occur randomly) along the PAF, RC, GM and SCC segments (RS-h). We believe that this model best fits the partial-linkage aspect of our structural model and the complex rupture patterns indicated by all the paleoseismic data, which really do not support the existence of persistent segment boundaries for this apparently immature fault system. However, given all of the uncertainties and the lack of data on the SCC (as well as on the EFS/SW), we cannot preclude Rupture Model B and retain it with a weight of 0.15 to address the uncertainties.

5.1.2.2.3 Fault Geometry

As previously discussed, we used curvilinear surfaces to better represent the geometries for all PFS faults and segments. The highlighted (red and bold) lines shown in Figures 5-9a through 5-9d show the fault traces used to represent the various rupture sources in the model for hazard calculations. We selected our best estimate of the primary, active trace for each segment, but given the width and complexity of some deformation zones, selecting a single trace is somewhat subjective, so when there was doubt we went with the trace that is closer to LANL. Fault dips and depths are as shown on Figure 5-8, and details are provided in Footnotes 4, 5, and 6 of Table 5-8. Note that for RS-e, the dip of the EFS/SW is restricted by the hazard code to be the same as that for the SCC (and PAF; cf., No. A2007b in Table 5-1 and Figure 5-8). Also note that RS-e only includes the portions of the EFS/SW mapped by Koning *et al.* (2004a) that show definite surface expression; his inferred or concealed traces were not included in RS-e (cf., Plate 1 and Figure 5-9c).

5.1.2.3 Types of Multisegment Ruptures

Large earthquakes involving multiple fault segments can rupture in multiple subevents (synchronous rupture) rather than in just a single large event (simultaneous rupture) as is typically assumed and modeled in standard PSHAs. The type of multisegment rupture (synchronous versus simultaneous) can significantly impact ground-motion estimates, depending on the location of the site relative to the slipping fault segments (e.g., CRWMS M&O, 1998). Several critical LANL facilities are located between segments of the PFS, and so we explicitly considered both simultaneous and synchronous types of multisegment ruptures for both rupture models of the PFS (Figure 5-8).

Characterizing synchronous ruptures and earthquake subevents is somewhat new in PSHA, so we reviewed some of the larger historical ruptures in the Basin and Range province for insight. From a geological basis, we probably cannot discriminate between prehistoric triggered or synchronous faulting events that are less than 100 years apart. We found it surprising that the 16 December 1954 Dixie-Valley Fairview Peak rupture was not a synchronous rupture because the two events (M_S 7.2 and M_S 6.8) were too far apart in time (four minutes) for strong ground motions to constructively interfere at local sites. So this sequence would be considered to have involved a triggered, but separate, second event. In contrast, initial studies identified two subevents for the **M** 7.2 1992 Landers rupture (Kanamori *et al.*, 1992; Hauksson *et al.* 1993), and it clearly involved multiple segments (five distinct but overlapping fault segments, Sieh *et al.*, 1993). However, based on more extensive modeling and analysis of seismological, geodetic and geologic data, Wald and Heaton (1994) concluded that it was actually one continuous mainshock (i.e., a good example of a multisegment simultaneous rupture). So what are some good examples of multisegment synchronous ruptures in the Basin and Range province? Doser and Smith (1989) identified many large earthquakes in the western U.S. that were actually composed of subevents. Indeed, they found that all $\mathbf{M} \geq 7.0$ earthquakes were composed of subevents, but not all include multisegment fault ruptures or are clear examples of distinct subevents on different fault segments (i.e., most are not actually synchronous ruptures). The M_S 7.2 1932 Cedar Mountain earthquake included a **M** 6.8 subevent followed by a **M** 6.6 subevent, and it was likely a synchronous rupture. Another example of a synchronous rupture that is a possible analog for the PFS is the **M** 7.3 1959 Hebgen Lake earthquake, which involved multiple discrete faults and two subevents: a m_b 6.3 event followed 5 seconds later by a m_b 7.0 event (Doser, 1985). This is a good possible analog for the PFS because 1) it occurred in a region adjacent to a Quaternary caldera, as does the PFS; 2) it clearly involved multiple overlapping but distinct faults (rupture segments) with complex geometries, including opposing dips like the PFS; 3) it was dominantly extensional; and, 4) it had large displacements, as is suggested for the PFS. It should be noted however, that larger subevents do not always occur first and the subevents can be similar in size. Admittedly, our review here is not comprehensive. Nevertheless, the Hebgen Lake analog provides useful guidance in defining subevents for synchronous ruptures on the PFS.

In our model of a simultaneous type of multisegment rupture for the PFS, ground motions are calculated the same as for a single segment source, with the closest distance to the source being a key factor. In this approach, the distribution of events is uniform on all segments involved in a particular scenario (i.e., events are partitioned the same way, randomly and uniformly, on all segments involved in a particular scenario). In contrast, for synchronous ruptures, ground motions are summed at the site for each subevent location using a sum of the squares formulation

(Section 2.2.4). In this approach, we assumed two subevents and that the PAF was the "driver" for multisegment ruptures such that only characteristic events would also rupture the other additional segments. Thus, in our model the PAF forms the 1st subevent, with the remaining segments in the scenario hosting the second subevent. These subevents and their corresponding maximum magnitudes are discussed in the next section. Note that for RS-a in Rupture Model B, the PAF ruptures alone (Figure 5-9a), and therefore this is not a multisegment rupture, so it was not modeled as a synchronous rupture.

We slightly favored the simultaneous type rupture (weighted 0.6) over the synchronous type of rupture (Figure 5-8), since we believe that the large displacements on the RC and GM are more consistent with a single large simultaneous rupture rather than separate smaller subevents for these fault segments.

5.1.2.4 Maximum Magnitudes

Maximum magnitudes for the rupture sources of the five rupture scenarios of the final PFS rupture models were estimated using an approach similar to that previously described for regional faults, except we calculated preferred magnitudes for both simultaneous and synchronous ruptures. We weighted preferred values 0.6, whereas uncertainties of ± 0.3 magnitude units about preferred values were each weighted 0.2. We considered using both displacement- and length-based empirical relations for estimating preferred magnitudes and favored the latter (Figure 5-8) as displacement data are limited. Displacements, lengths, and the resulting maximum magnitudes for conventional simultaneous multisegment ruptures are shown in Table 5-10. Weighted mean-maximum magnitudes (used as the preferred value for each rupture scenario and weighted 0.6) range from **M** 6.94 (for RS-a) to **M** 7.27 (for RS-g) for simultaneous ruptures. We estimated maximum magnitudes for both subevents of the synchronous ruptures using the same approach and these are consistently slightly smaller than for the simultaneous ruptures (Table 5-11), but the sum of the moment for the two subevents is within 10% of the moment for the simultaneous rupture of the same rupture scenario.

5.1.2.5 Rates of Activity

The rate of activity on the PFS is one of the most important parameters to the seismic hazard at LANL. Our approach to characterizing rates was dependent on rupture models.

Rates for Rupture Model C (favored model). For the unsegmented, Rupture Model C, the hazard code balances the moment with respect to long-term slip rate as it randomly partitions earthquakes along the PFS segments. For this simple case, our characterization of rates can be shown completely on the logic tree (Figure 5-8). We used both slip rates and recurrence intervals (Figure 5-8), favoring the latter (weighted 0.7) for multiple reasons (see footnote 13 of Table 5-8 for further discussion), but primarily because recurrence interval data reflect more recent fault behavior (≤ 110 ka) than slip rate data (≤ 1.2 Ma). However, we still include the slip rate data because as previously discussed, the paleoseismic record that recurrence intervals are based on is likely incomplete, and the PFS slip rate data are exceptional in quantity and quality, even if they are long term.

For the recurrence-interval approach, we considered both random (not-clustered) and clustered behavior (Figure 5-8), strongly favoring the latter based on the evidence for Holocene clustering of events and the suggestive evidence for another older cluster of events that occurred around 80 to 110 ka (Table 5-5). Specific details of both clustered and not-clustered recurrence interval distributions are given in Footnotes 16 and 17 of Table 5-8 and are based on the previously discussed paleoseismic data. The resulting weighted-mean recurrence interval for the clustered branch is 4,400 years compared to a weighted mean of 17,600 years for the not-clustered branch (Figure 5-8).

Rates for Rupture Model B (secondary model). For the segmented rupture models of the PFS, we employed moment balancing to determine final rates of activity on individual fault segments and to constrain weights for the rupture scenarios. This approach was too complex to explicitly show all the details in the logic tree, but the overall process can be outlined as follows:

Paleoseismic Data (Table 5-5)	⇨	Poisson Maximum Likelihood Recurrence Estimates (Table 5-12)	⇨	Target Recurrence Intervals (Table 5-13)	⇨	Moment Balanced Segment Rates and Revised Rupture Scenario Weights (Table 5-14 and Table 5-9)

Upon recommendations from the Steering Committee, a normalized maximum-likelihood approach to estimating rates was used to systematically represent recurrence distributions. Various cases were selected to represent the behavior for each rupture scenario, with the number of events ("n" in Table 5-12) during a certain time period ("t" in Table 5-12) being based on the paleoseismic data in Table 5-5. Given an observation of n events in t years, and assuming a Poisson process, calculations of the 5th, 50th, and 95th percentiles for the normalized maximum-likelihood function of the "true" rate were done by Walter Arabasz (University of Utah, written communication, 2005) using a MathCAD program; (reciprocals of the calculated rates are shown as recurrence intervals in Table 5-12). These were then used to develop the various target recurrence interval distributions shown in Table 5-13 for each rupture scenario of Rupture Model B. The details of the basis for each distribution are described in the footnotes of Table 5-13 and are cross-referenced to the various cases in Table 5-12. The resulting weighted mean of the target recurrence intervals range from 24,000 to 133,000 years and are generally much longer than the weighted-mean rates for both the clustered branch of Rupture Model C (4,400 years) and the not-clustered branch (17,600 years) (cf., Table 5-13 and Figure 5-8).

To balance the moment for the four rupture scenarios of Rupture Model B, we used the FORTRAN program, Balance, written by Norm Abrahamson and described in Appendix C. The reason for using the moment balancing was to ensure that total earthquake moment was appropriately proportioned on the various fault segments of the PFS given the complexity of our model, and to provide insight on the internal consistency of the model and how it compares with the paleoseismic data.

Table 5-14 shows the PFS fault segment parameters used in moment balancing. The process was iterative using input on segment geometries and slip rates, rupture scenario weights, and maximum magnitudes to calculate the implied recurrence intervals for the rupture scenarios and

the displacements per event. To get the moment to balance and yield our target recurrence intervals we adjusted both segment slip rates and rupture scenario weights. We started with the long-term segment rates as shown in Table 5-14 and scaled these up or down as needed to achieve the target recurrence interval for RS-a (Table 5-13), and then adjusted rupture scenario weights to achieve the target recurrence intervals for the other scenarios. We kept adjusting weights and rates until the implied recurrence intervals were within 2% of target values. Although tedious, this was a relatively straightforward process for Rupture Model B as the displacements per event were reasonable and we did not need to adjust maximum magnitudes. Additionally, because we always kept the segment rates proportioned the same as their long-term rates, the weights on rupture scenarios did not need much adjusting (see revised weights in Table 5-9).

However, the iterative process for Rupture Model A was not so simple. Regardless of the weights and magnitudes used, this model yielded displacements for the SCC that exceeded 4 m and were 50% larger than those on the PAF in the same rupture scenario. This outcome was particularly unreasonable given that the PAF is about 3 times longer than the SCC. The only way to get the displacements on the SCC below those of the PAF was to proportionally lower the segment slip rate for the SCC. This also did not seem reasonable given that the long-term slip rate is clearly higher on the SCC than on the GM or RC (Figure 5-6). In Rupture Model A, the SCC segment only ruptures in RS-e and RS-d, which occur infrequently and yet somehow one needs to distribute more moment on the SCC than on the GM or RC. The only way to do that is to have excessively large displacements per event on the SCC. In short, what the moment balancing of Rupture Model A tells us is that this model is inconsistent with the available geologic data (cumulative slip and the paleoseismic data). Based on this observation, we eliminated Rupture Model A and associated rupture scenarios RS-b, RS-c and RS-d (Figures 5-9a, 5-9b, and 5-9c).

Interestingly, the scaling factor needed to adjust segment slip rates in order to achieve preferred target recurrence intervals is 2.11 (see footnote 6 of Table 5-14), which is essentially the same factor between the long term slip rate (0.1 mm/yr) and the weighted mean for the slip rate distribution derived from the RGR analysis (cf., slip rate branch for Rupture Model C on Figure 5-8). Thus, the moment balancing approach is implying that the late Quaternary rates are about twice as fast as the long-term Quaternary rates (and the Holocene rates are about 8 to 10 times faster than the Quaternary rates). We already knew this from the paleoseismic data, but it is reassuring to see that our moment-balanced rates for Rupture Model B are consistent with our slip rates assigned to Rupture Model C.

Figure 5-10 shows a cumulative recurrence curve for the entire PFS, including both Rupture Models B and C. The average recurrence interval of **M** 6½ and greater earthquakes is about once every 3,000 years and 12,500 years for **M** 7 and greater.

5.2 BACKGROUND SEISMICITY

The hazard from background (floating or random) earthquakes that are below the magnitude threshold of surface rupture and not associated with known or mapped faults needs to be incorporated into the hazard analysis. Earthquake-recurrence estimates in the study region and maximum magnitude estimates are required to assess the hazard from background earthquakes.

In most of the western U.S., particularly the Basin and Range Province, the maximum magnitude of earthquakes not associated with known faults usually ranges from **M** 6 to 6½. Repeated events larger than these magnitudes probably produce recognizable fault- or fold-related features at the earth's surface (e.g., Doser, 1985; dePolo, 1994; Youngs *et al.*, 2003).

Three seismotectonic provinces in the LANL region were used to define areal source zones (Section 3.2.4): the RGR, Southern Great Plains, and Colorado Plateau (Figure 3-1). The SSA was also modeled as an areal source zone and differentiated from the RGR due to its higher level of seismicity, probably associated with mid-crustal magmatism (Sanford *et al.*, 1991). Earthquake recurrence rates computed for each areal source zone are described in Section 3.2.4. For the Colorado Plateau, Southern Great Plains, and SSA areal source zones, we used three *b*-values in each case: the best estimate (Table 3-1) and ± 0.1 values. The best estimate was weighted 0.6; the upper and lower bounds, 0.2 each. Corresponding *a*-values were held fixed because the regressed recurrence curves are well anchored by small magnitude earthquakes. For the RGR areal source zone, we used four weighted pairs of *a*- and *b*-values (listed in Table 3-3) for reasons discussed in Section 3.2.4.

For the three seismotectonic provinces and the SSA, we adopted maximum magnitudes and seismogenic crustal thicknesses as listed in Table 5-15. The same values were used in Wong *et al.* (2004). The maximum magnitudes are generally higher than those used in the 1995 study (Wong *et al.*, 1995), but by only 0.2 to 0.3 magnitude unit. The values used in 1995 were judged to be slightly low considering the adopted seismogenic crustal thicknesses of 15 ± 3 km.

In addition to the traditional approach of using areal source zones with uniformly distributed seismicity, Gaussian smoothing (Frankel, 1995) with a spatial window of 15 km (Wong *et al.*, 2004) was used to address the hazard from background seismicity and incorporate a degree of stationarity. A computer program to perform this smoothing was provided to us by Art Frankel (USGS, written communication, 1998). The 15-km smoothing was selected based on sensitivity analyses performed as part of developing the hazard maps for the northern RGR in New Mexico (Wong *et al.*, 2004). The *b*-value used was 0.73, the value for the RGR (Section 3.2.4) since we were most interested in the hazard from the gridded seismicity within the rift. The cell size used to calculate the hazard was 0.2 degrees. Minimum magnitude was **M** 3.0. We weighted the two approaches, areal sources and Gaussian smoothing, equally at 0.50 to compute the hazard from background seismicity in the PSHA.

TABLE 5-1. SEISMIC SOURCE PARAMETERS FOR REGIONAL FAULTS INCLUDED IN THE LANL ANALYSIS[1]

Fault No.	Fault Name	Rupture Model[2]	Maximum Rupture Length[3] (km)	Maximum Magnitude[4] (M_w)	Dip[5] (degrees)	Approximate Age of Youngest Activity[6]	Probability of Activity[7]	Rate of Activity[8] (mm/yr)
2001	Gallina fault	Independent (1.0)	39	6.7 (0.2) 7.0 (0.6) 7.3 (0.2)	45 E (0.2) 60 E (0.6) 75 E (0.2)	Quaternary?	0.5	**0.004 (0.1)** **0.01 (0.24)** **0.02 (0.32)** **0.04 (0.24)** **0.20 (0.1)** **[WM = 0.04]** **[N = 0.02]**
2002	Nacimiento fault	Segmented (0.8)	N. Section (2002a) – 36	N. Section: 6.6 (0.2) 6.9 (0.6) 7.2 (0.2)	45 E (0.2) 60 E (0.6) 75 E (0.2)	N. Section – Quaternary	N. Section – 0.7	**0.004 (0.1)** **0.01 (0.24)** **0.02 (0.32)** **0.04 (0.24)**
			S. Section (2002b) – 45	S. Section: 6.7 (0.2) 7.0 (0.6) 7.3 (0.2)		S. Section – mid to late Pleistocene (possibly even Holocene)	S. Section – 1.0	**0.20 (0.1)** **[WM = 0.04]** **[N = 0.02]**
		Unsegmented (0.2)	Both – 82	Both: 7.0 (0.2) 7.3 (0.6) 7.6 (0.2)			Both – 1.0	(Same for all sections)
2003	**Cañones fault**	Independent (1.0)	29	6.5 (0.2) 6.8 (0.6) 7.1 (0.2)	45 SE (0.2) 60 SE (0.6) 75 SE (0.2)	Pliocene?	0.5	**0.004 (0.1)** **0.01 (0.24)** **0.02 (0.32)** **0.04 (0.24)** **0.20 (0.1)** **[WM = 0.04]** **[N = 0.02][9]**
2004	**Lobato Mesa fault zone**	Independent (1.0)	22	6.4 (0.2) 6.7 (0.6) 7.0 (0.2)	45 W (0.2) 60 W (0.6) 75 W (0.2)	Quaternary	1.0	**0.002 (0.1)** **0.005 (0.24)** **0.01 (0.32)** **0.02 (0.24)** **0.10 (0.1)** **[WM = 0.02]** **[N = 0.01][10]**
2005	**La Cañada del Amagre fault zone**	Independent (1.0)	**17**[11]	**6.2** (0.2) **6.5** (0.6) **6.8** (0.2)	60 E (0.3) 70 E (0.4) 80 E (0.3)	Pilo-Pleistocene	0.5	**0.02 (0.1)** **0.05 (0.24)** **0.10 (0.32)** **0.20 (0.24** **0.90 (0.1)** **[WM = 0.18]** **[N = 0.1]**
2006	Black Mesa fault zone	Independent (1.0)	19	6.2 (0.2) 6.5 (0.6) 6.8 (0.2)	70 NW (0.3) 90 (0.4) 70 SE (0.3)	Quaternary?	0.5	**0.003 (0.1)** **0.009 (0.24)** **0.02 (0.32)** **0.04 (0.24)** **0.17 (0.1)** **[WM = 0.03]** **[N = 0.02]**

TABLE 5-1. SEISMIC SOURCE PARAMETERS FOR REGIONAL FAULTS INCLUDED IN THE LANL ANALYSIS[1]

Fault No.	Fault Name	Rupture Model[2]	Maximum Rupture Length[3] (km)	Maximum Magnitude[4] (M_w)	Dip[5] (degrees)	Approximate Age of Youngest Activity[6]	Probability of Activity[7]	Rate of Activity[8] (mm/yr)
2007	***Embudo fault system***[12]	Segmented (0.8)	**Northeastern (2007a and A2007a) Section – 48**	**6.7 (0.2)** **7.0 (0.6)** **7.3 (0.2)**	**90 (0.4)** **80 NW (0.3)** **70 NW (0.3)**	latest Pleistocene[13]	**1.0**	**0.02 (0.1)** **0.05 (0.24)** **0.09 (0.32** **0.19 (0.24)** **0.85 (0.1)** **[WM = 0.17]** **[N = 0.1]**[14]
			Southwestern (A2007b) Section – 21	**6.3 (0.2)** **6.6 (0.6)** **6.9 (0.2)**	**90 (0.4)** **80 SE (0.3)** **70 SE (0.3)**	Quaternary	**0.99**[15]	**0.006 (0.1)** **0.02 (0.24)** **0.04 (0.32)** **0.08 (0.24** **0.34 (0.1)** **[WM = 0.07]** **[N = 0.04]**[16]
		Unsegmented (0.2)	*Both - 65*	6.9 (0.2) 7.2 (0.6) 7.5 (0.2)	**70 SE (0.3)** **90 (0.4)** **70 NW (0.3)**		**1.0**	**0.02 (0.1)** **0.05 (0.24)** **0.09 (0.32** **0.19 (0.24)** **0.85 (0.1)** **[WM = 0.17]** **[N = 0.1]**[14]
2009	**Puye fault**[17]	Independent (1.0)	**16**	**6.2 (0.2)** **6.5 (0.6)** **6.8 (0.2)**	65 E (0.2) 75 E (0.5) 90 (0.3)	Mid to late Quaternary	1.0	**0.005 (0.1)** **0.01 (0.24)** **0.03 (0.32)** **0.06 (0.24)** **0.26 (0.1)** **[WM = 0.05]** **[N = 0.03]**
2010	**Pojoaque fault**	Independent (1.0)	**47**[11]	**6.7** (0.2) **7.0** (0.6) **7.3** (0.2)	45 W (0.2) 60 W (0.6) 75 W (0.2)	Quaternary?	0.5	**0.004 (0.1)** **0.01 (0.24)** **0.02 (0.32)** **0.04 (0.24)** **0.20 (0.1)** **[WM = 0.04]** **[N = 0.02]**
2017	**Southern Sangre de Cristo fault**	Segmented (0.8)	Cañon & Hondo Sections (2017e & d) – 33	6.5 (0.2) 6.8 (0.6) 7.1 (0.2)	45 W (0.2) 60 W (0.6) 75 W (0.2)	Latest Pleistocene to Holocene Except San Pedro Mesa is late Quaternary	1.0	**Slip Rate (0.6):**[18] 0.06 (0.2) 0.12 (0.35) 0.17 (0.25) 0.29 (0.2) **[WM = 0.15]** **Recurrence Interval (0.4):**[18] **10,000 yrs (0.33)** **30,000 yrs (0.34)** **50,000 yrs (0.33)** **[WM = 30,000 yrs]** (Same for all sections)
			Questa & Urraca Sections (2017c & b) – 38	6.6 (0.2) 6.9 (0.6) 7.2 (0.2)				
			San Pedro Mesa Section (2017a) – **24**[11]	6.4 (0.2) 6.7 (0.6) 7.0 (0.2)				
		Unsegmented (0.2)	Unsegmented – **96**[11]	7.1 (0.2) 7.4 (0.6) 7.7 (0.2)				

TABLE 5-1. SEISMIC SOURCE PARAMETERS FOR REGIONAL FAULTS INCLUDED IN THE LANL ANALYSIS[1]

Fault No.	Fault Name	Rupture Model[2]	Maximum Rupture Length[3] (km)	Maximum Magnitude[4] (M_w)	Dip[5] (degrees)	Approximate Age of Youngest Activity[6]	Probability of Activity[7]	Rate of Activity[8] (mm/yr)
2020	Las Tablas fault	Independent (1.0)	15	6.1 (0.2) 6.4 (0.6) 6.7 (0.2)	45 W (0.2) 60 W (0.6) 75 W (0.2)	Early Pleistocene?	0.5	0.002 (0.2) 0.03 (0.6)[19] 0.2 (0.2) **[WM = 0.06]**
2021	Stong fault	Independent (1.0)	8	5.8 (0.2) 6.1 (0.6) 6.4 (0.2)	45 E (0.2) 60 E (0.6) 75 E (0.2)	Early Pleistocene?	0.5	0.001 (0.2) 0.01 (0.6)[20] 0.03 (0.2) **[WM = 0.01]**
2022	Los Cordovas faults	Independent (1.0)	12	6.0 (0.2) 6.3 (0.6) 6.6 (0.2)	45 W (0.2) 60 W (0.6) 75 W (0.2)	Early Pleistocene	1.0	0.01 (0.2) 0.02 (0.6)[21] 0.03 (0.2) **[WM = 0.02]**
2023	Picuris – Pecos fault	Independent (1.0)	98	7.1 (0.2) 7.4 (0.6) 7.7 (0.2)	70 W (0.1) 80 W (0.4) 90 (0.5)	Quaternary?	0.5	**0.007 (0.1)** **0.02 (0.24)** **0.05 (0.32)** **0.09 (0.24)** **0.42 (0.1)** **[WM = 0.09]** **[N = 0.05]**
2024	Nambe fault	Independent (1.0)	48	6.7 (0.2) 7.0 (0.6) 7.3 (0.2)	60 W (0.4) 90 (0.3) 60 E (0.3)	Quaternary?	0.1	**0.004 (0.1)** **0.01 (0.24)** **0.02 (0.32)** **0.04 (0.24)** **0.20 (0.1)** **[WM = 0.04]** **[N = 0.02]**
2028	***Sawyer Canyon fault***[22]	Independent (1.0)	9	**5.9 (0.2)** **6.2 (0.6)** **6.5 (0.2)**	65 E (0.2) 75 E (0.5) 90 (0.3)	Late Quaternary	1.0	**0.005 (0.1)** **0.01 (0.24)** **0.03 (0.32)** **0.06 (0.24)** **0.26 (0.1)** **[WM = 0.05]** **[N = 0.03]**
2029	Jemez-San Ysidro fault	Segmented (0.6)	Jemez (2029a)– 24	6.4 (0.2) 6.7 (0.6) 7.0 (0.2)	80 E (0.3) 90 (0.4) 80 W (0.3)	Quaternary	1.0	**0.008 (0.1)** **0.02 (0.24)** **0.05 (0.32)** **0.09 (0.24)**
			San Ysidro (2029b)– 34	6.6 (0.2) 6.9 (0.6) 7.1 (0.2)	45 E (0.2) 60 E (0.6) 75 E (0.2)	Mid to late Quaternary		**0.42 (0.1)** **[WM = 0.09]** **[N = 0.05]**
		Unsegmented (0.4)	48	6.7 (0.2) 7.0 (0.6) 7.3 (0.2)	60 E (0.5) 90 (0.5)			(Same for all sections)

TABLE 5-1. SEISMIC SOURCE PARAMETERS FOR REGIONAL FAULTS INCLUDED IN THE LANL ANALYSIS[1]

Fault No.	Fault Name	Rupture Model[2]	Maximum Rupture Length[3] (km)	Maximum Magnitude[4] (M_w)	Dip[5] (degrees)	Approximate Age of Youngest Activity[6]	Probability of Activity[7]	Rate of Activity[8] (mm/yr)
2030	**San Felipe fault zone**	Segmented (0.7)	**Santa Ana (2030a)– 44[11]**	6.7 (0.2) 7.0 (0.6) 7.3 (0.2)	50 E (0.3) 70 E (0.4) 90 (0.3)	Early Pleistocene	1.0	**0.008 (0.1)** **0.03 (0.24)** **0.05 (0.32)** **0.10 (0.24)** **0.45 (0.1)** **[WM = 0.09]** **[N = 0.05]**
			Algodones (2030b) – 16[11]	**6.3** (0.2) **6.5** (0.6) **6.8** (0.2)	50 W (0.3) 70 W (0.4) 90 (0.3)			
		Unsegmented (0.3) (Zone)	**44[11]**	6.7 (0.2) 7.0 (0.6) 7.3 (0.2)	60 E (0.3) 90 (0.4) 60 W (0.3)			(Same for all sections)
2031	**San Francisco fault**	Independent (1.0)	**26[11]**	**6.4** (0.2) **6.7** (0.6) **7.0** (0.2)	45 W (0.2) 60 W (0.6) 75 W (0.2)	**Pleistocene[21]**	1.0	**0.03 (0.1)** **0.08 (0.24)** **0.16 (0.32)** **0.33 (0.24)** **1.5 (0.1)** **[WM = 0.30]** **[N = 0.15][23]**
2032	**La Bajada fault**	Independent (1.0)	40	6.6 (0.2) 6.9 (0.6) 7.2 (0.2)	45 W (0.2) 60 W (0.6) 75 W (0.2)	**Late Pleistocene(?)[24]**	1.0	**0.04 (0.1)** **0.11 (0.24)** **0.21 (0.32)** **0.44 (0.24)** **1.9 (0.1)** **[WM = 0.40]** **[N = 0.2][25]**
2033	Tijeras-Canoncito fault	Segmented (0.9)	Galisteo Section (2033a) – 37	6.6 (0.2) 6.9 (0.6) 7.2 (0.2)	80 E (0.3) 90 (0.4) 80 W (0.3)	Quaternary?	0.5	**0.01 (0.1)** **0.04 (0.24)** **0.08 (0.32)** **0.17 (0.24)**
			Canyon Section (2033b) - 42	6.7 (0.2) 7.0 (0.6) 7.3 (0.2)		Late Quaternary	1.0	**0.76 (0.1)** **[WM = 0.15]** **[N = 0.09]**
		Unsegmented (0.1)	79	7.0 (0.2) 7.3 (0.6) 7.6 (0.2)			1.0	(Same for all sections)
2034, 2036, 2037, 2043	Bernalillo fault (#2034) **Sandia fault (#2037)** Rincon fault (#2036) Faults north of Placitas (#2043)	Linked (0.4)	41	6.7 (0.2) 7.0 (0.6) 7.3 (0.2)	45 W (0.2) 60 W (0.6) 75 W (0.2)	Mid to late Quaternary	1.0	**0.02 (0.1)** **0.05 (0.24)** **0.10 (0.32)** **0.22 (0.24)** **0.98 (0.1)** **[WM = 0.20]** **[N = 0.1]**
		Independent (0.6)	Sandia – **28[11]**	**6.5** (0.2) **6.8** (0.6) **7.1** (0.2)		Late Quaternary		**0.009 (0.1)** **0.03 (0.24)** **0.05 (0.32** **0.11 (0.24)** **0.49 (0.1)** **[WM = 0.10]** **[N = 0.05]**

TABLE 5-1. SEISMIC SOURCE PARAMETERS FOR REGIONAL FAULTS INCLUDED IN THE LANL ANALYSIS[1]

Fault No.	Fault Name	Rupture Model[2]	Maximum Rupture Length[3] (km)	Maximum Magnitude[4] (M_w)	Dip[5] (degrees)	Approximate Age of Youngest Activity[6]	Probability of Activity[7]	Rate of Activity[8] (mm/yr)
			Rincon – 13	6.4 (0.2) 6.7 (0.6) 7.0 (0.2)		Latest Pleistocene		**0.02 (0.1)** **0.05 (0.24)** **0.10 (0.32)** **0.22 (0.24)** **0.98 (0.1)** **[WM = 0.20]** **[N = 0.1]**
			Placitas – 10	5.9 (0.2) 6.2 (0.6) 6.5 (0.2)		Mid to late Quaternary		**0.007 (0.1)** **0.02 (0.24)** **0.04 (0.32)** **0.09 (0.24)** **0.39 (0.1)** **[WM = 0.08]** **[N = 0.04]**
			Bernalillo - 10	5.9 (0.2) 6.2 (0.6) 6.5 (0.2)		Mid to late Quaternary		**0.004 (0.1)** **0.01 (0.24)** **0.02 (0.32)** **0.04 (0.24)** **0.20 (0.1)** **[WM = 0.04]** **[N = 0.02]**
2035	**Calabacillas fault**	Independent (1.0)	40	6.6 (0.2) 6.9 (0.6) 7.2 (0.2)	45 E (0.2) 60 E (0.6) 75 E (0.2)	**Latest Pleistocene[26]**	1.0	**18,000 yrs (0.3)** **45,000 yrs (0.4)[27]** **75,000 yrs (0.3)** **[WM = 46,000 yrs]**
2038	**County Dump fault**	Independent (1.0)	35	6.6 (0.2) 6.9 (0.6) 7.2 (0.2)	45 E (0.2) 60 E (0.6) 75 E (0.2)	Late Quaternary	1.0	**Recurrence (0.6):** **5,000 yrs (0.1)** **10,000 yrs (0.4)** **35,000 yrs (0.4)[28]** **90,000 yrs (0.1)** **[WM = 27,500 yrs]** **Slip Rate (0.4):** **0.004 (0.1)** **0.01 (0.24)** **0.02 (0.32)** **0.04 (0.24)** **0.20 (0.1)** **[WM = 0.04]** **[N = 0.02][29]**
2039	Sand Hill fault	Independent (1.0)	36	6.3 (0.2) 6.6 (0.6) 6.9 (0.2)	45 E (0.2) 60 E (0.6) 75 E (0.2)	Early Pleistocene?	0.8	**0.004 (0.1)** **0.01 (0.24)** **0.02 (0.32)** **0.04 (0.24)** **0.20 (0.1)** **[WM = 0.04]** **[N = 0.02]**
2040	**East Paradise fault**	Independent (1.0)	**13[11]**	**6.4** (0.2) **6.7** (0.6)[30] **7.0** (0.2)	45 W (0.2) 60 W (0.6) 75 W (0.2)	Late Quaternary	1.0	**0.004 (0.2)[30]** **0.01 (0.5)** **0.02 (0.3)** **[WM = 0.01]**

TABLE 5-1. SEISMIC SOURCE PARAMETERS FOR REGIONAL FAULTS INCLUDED IN THE LANL ANALYSIS[1]

Fault No.	Fault Name	Rupture Model[2]	Maximum Rupture Length[3] (km)	Maximum Magnitude[4] (M_w)	Dip[5] (degrees)	Approximate Age of Youngest Activity[6]	Probability of Activity[7]	Rate of Activity[8] (mm/yr)
2041, 2045, 2047	Zone of older intrabasin faults near northern margin of Albuquerque-Belen basin (includes: Picuda Peak faults [2041] Loma Barbon faults [2045] Loma Colorado de Abajo faults [2047]	Zone (1.0)	19	6.3 (0.2) 6.6 (0.6) 6.9 (0.2)	60 E (0.2) 90 (0.5) 60 W (0.3)	Early Pleistocene	1.0	**0.006 (0.1)** **0.02 (0.24)** **0.04 (0.32)** **0.08 (0.24)** **0.34 (0.1)** **[WM = 0.07]** **[N = 0.04]**
2042, 2048, 2049	Zone of younger intrabasin faults in central Albuquerque-Belen basin (includes: West Paradise fault [2042] Star Heights faults [2048] Albuquerque Volcanoes faults [2049]	Zone (1.0)	26	6.4 (0.2) 6.7 (0.6) 7.0 (0.2)	70 E (0.3) 90 (0.4) 70 W (0.3	Mid to late Quaternary	1.0	**0.006 (0.1)** **0.02 (0.24)** **0.04 (0.32)** **0.08 (0.24)** **0.34 (0.1)** **[WM = 0.07]** **[N = 0.04]**
2046	**Zia fault**	Independent (1.0)	32	**6.6** (0.2) **6.9** (0.6)[31] **7.2** (0.2)	45 E (0.2) 60 E (0.6) 75 E (0.2)	Mid to late Quaternary	1.0	**0.04 (0.3)**[32] **0.09 (0.4)** **0.15 (0.3)** **[WM = 0.09]**
2050	El Oro fault	Independent (1.0)	27	6.4 (0.2) 6.7 (0.6) 7.0 (0.2)	45 W (0.2) 60 W (0.6) 75 W (0.2)	Mid to late Quaternary	1.0	**0.009 (0.1)** **0.03 (0.24)** **0.05 (0.32)** **0.11 (0.24)** **0.49 (0.1)** **[WM = 0.10]** **[N = 0.05]**
2059	Unnamed fault northeast of Longhorn Ranch	Independent (1.0)	10	5.9 (0.2) 6.2 (0.6) 6.5 (0.2)	60 W (0.5) 90 (0.5)	Quaternary ?	0.3	**0.003 (0.1)** **0.009 (0.24)** **0.02 (0.32)** **0.04 (0.24)** **0.17 (0.1)** **[WM = 0.03]** **[N = 0.02]**
2072	Quebraditas fault zone	Independent (1.0)	15	6.1 (0.2) 6.4 (0.6) 6.7 (0.2)	45 W (0.2) 60 W (0.6) 75 W (0.2)	Mid to late Quaternary	1.0	**0.009 (0.1)** **0.03 (0.24)** **0.05 (0.32)** **0.11 (0.24)** **0.49 (0.1)** **[WM = 0.10]** **[N = 0.05]**
2108	**Socorro Canyon fault zone**	Independent (1.0)[33]	49	6.7 (0.2) 7.0 (0.6) 7.3 (0.2)	60 W (0.2) 90 (0.5) 80 W (0.3)	**Holocene**	1.0	**0.005 (0.1)** **0.02 (0.3)** **0.04 (0.3)**[34] **0.08 (0.2)** **0.34 (0.1)** **[WM = 0.07]**
2109	La Jencia fault	Independent (1.0)[33]	34	6.6 (0.2) 6.9 (0.6) 7.2 (0.2)	45 E (0.2) 60 E (0.6) 75 E (0.2)	Late Quaternary for northern portion and latest Pleistocene to Holocene for southern portion	1.0	**0.005 (0.1)** **0.02 (0.24)** **0.03 (0.32)** **0.07 (0.24)** **0.29 (0.1)** **[WM = 0.06]** **[N = 0.03]**

TABLE 5-1. SEISMIC SOURCE PARAMETERS FOR REGIONAL FAULTS INCLUDED IN THE LANL ANALYSIS[1]

Fault No.	Fault Name	Rupture Model[2]	Maximum Rupture Length[3] (km)	Maximum Magnitude[4] (M_w)	Dip[5] (degrees)	Approximate Age of Youngest Activity[6]	Probability of Activity[7]	Rate of Activity[8] (mm/yr)
2110	West Joyita fault	Independent (1.0)	48	6.7 (0.2) 7.0 (0.6) 7.3 (0.2)	45 W (0.2) 60 W (0.6) 75 W (0.2)	Early Pleistocene	1.0	**0.002 (0.1)** **0.005 (0.24)** **0.01 (0.32)** **0.02 (0.24)** **0.10 (0.1)** **[WM = 0.02]** **[N = 0.01]**
2111	Cliff fault	Independent (1.0)	19	6.3 (0.2) 6.6 (0.6) 6.9 (0.2)	45 W (0.2) 60 W (0.6) 75 W (0.2)	Late Quaternary	1.0	**0.009 (0.1)** **0.03 (0.24)** **0.05 (0.32)** **0.11 (0.24)** **0.49 (0.1)** **[WM = 0.10]** **[N = 0.05]**
2112	Loma Blanca fault	Independent (1.0)	23	6.3 (0.2) 6.6 (0.6) 6.9 (0.2)	45 E (0.2) 60 E (0.6) 75 E (0.2)	Late Quaternary	1.0	**0.01 (0.1)** **0.03 (0.24)** **0.06 (0.32)** **0.13 (0.24)** **0.59 (0.1)** **[WM = 0.12]** **[N = 0.06]**
2113	Loma Pelada fault	Independent (1.0)	24	6.4 (0.2) 6.7 (0.6) 7.0 (0.2)	45 E (0.2) 60 E (0.6) 75 E (0.2)	Late Quaternary	1.0	**0.02 (0.1)** **0.05 (0.24)** **0.10 (0.32)** **0.22 (0.24** **0.98 (0.1)** **[WM = 0.20]** **[N = 0.1]**
2114	Coyote Springs fault	Independent (1.0)	17	6.2 (0.2) 6.5 (0.6) 6.8 (0.2)	45 E (0.2) 60 E (0.6) 75 E (0.2)	Latest Pleistocene to Holocene	1.0	**0.007 (0.1)** **0.02 (0.24)** **0.04 (0.32)** **0.09 (0.24)** **0.39 (0.1)** **[WM = 0.08]** **[N = 0.04]**
2115	Zone of intrabasin faults west of Rio Puerco	Zone (1.0)	22	6.3 (0.2) 6.6 (0.6) 6.9 (0.2)	60 W (0.3) 90 (0.4) 60 E (0.3)	Mid to late Quaternary	1.0	**0.006 (0.1)** **0.02 (0.24)** **0.04 (0.32)** **0.08 (0.24)** **0.34 (0.1)** **[WM = 0.07]** **[N = 0.04]**
2116 & 2121 (southern group)	Southern zone of intrabasin faults on the Llano de Albuquerque (includes the Sabinal faults 2116)	Zone (1.0)	40	6.6 (0.2) 6.9 (0.6) 7.2 (0.2)	70 E (0.3) 90 (0.4) 70 W (0.3)	Mid to late Quaternary	1.0	**0.006 (0.1)** **0.02 (0.24)** **0.04 (0.32)** **0.08 (0.24)** **0.34 (0.1)** **[WM = 0.07]** **[N = 0.04]**

TABLE 5-1. SEISMIC SOURCE PARAMETERS FOR REGIONAL FAULTS INCLUDED IN THE LANL ANALYSIS[1]

Fault No.	Fault Name	Rupture Model[2]	Maximum Rupture Length[3] (km)	Maximum Magnitude[4] (M_w)	Dip[5] (degrees)	Approximate Age of Youngest Activity[6]	Probability of Activity[7]	Rate of Activity[8] (mm/yr)
2117 (northern group)	Zone of intrabasin faults on the Llano de Manzano	Zone (1.0)	17	6.2 (0.2) 6.5 (0.6) 6.8 (0.2)	60 W (0.3) 75 W (0.4) 90 (0.3)	Mid to late Quaternary	1.0	**0.003 (0.1)** **0.01 (0.24)** **0.02 (0.32)** **0.04 (0.24)** **0.18 (0.1)** **[WM = 0.04]** **[N = 0.02]**
2117 (southern group)	Rift margin fault on the Llano de Manzano	Independent (1.0)	33	6.5 (0.2) 6.8 (0.6) 7.1 (0.2)	45 W (0.2) 60 W (0.6) 75 W (0.2)	Mid to late Quaternary	1.0	**0.004 (0.1)** **0.01 (0.24)** **0.02 (0.32)** **0.04 (0.24)** **0.20 (0.1)** **[WM = 0.04]** **[N = 0.02]**
2118	Los Piños fault	Independent (1.0)	18	6.2 (0.2) 6.5 (0.6) 6.8 (0.2)	45 W (0.2) 60 W (0.6) 75 W (0.2)	Quaternary?	0.5	**0.002 (0.1)** **0.005 (0.24)** **0.01 (0.32)** **0.02 (0.24)** **0.10 (0.1)** **[WM = 0.02]** **[N = 0.01]**
2119	Manzano fault	Independent (1.0)	54	6.8 (0.2) 7.1 (0.6) 7.4 (0.2)	45 W (0.2) 60 W (0.6) 75 W (0.2)	Mid to late Quaternary	1.0	**0.004 (0.1)** **0.01 (0.24)** **0.02 (0.32)** **0.04 (0.24)** **0.20 (0.1)** **[WM = 0.04]** **[N = 0.02]**
2120	**Hubbell Spring fault zone[35]**	**Independent (1.0)**	**43**	**6.7 (0.2)** **7.2 (0.6)[36]** **7.5 (0.2)**	**45 W (0.2)** **60 W (0.6)** **75 W (0.2)**	**Latest Pleistocene**	**1.0**	**Slip Rate (0.3):[37]** **0.04 (0.25)** **0.2 (0.6)** **0.5 (0.15)** **[WM: 0.21]** **Recurrence Interval (0.7):[38]** **10,000 yrs (0.3)** **20,000 (0.4)** **30,000 (0.3)** **[WM: 20,000 yrs]**
2121 (northern group)	Northern zone of intrabasin faults on the Llano de Albuquerque	Zone (1.0)	35	6.6 (0.2) 6.9 (0.6) 7.2 (0.2)	70 E (0.3) 90 (0.4) 70 W (0.3)	Mid to late Quaternary	1.0	**0.002 (0.1)** **0.005 (0.24)** **0.009 (0.32)** **0.02 (0.24)** **0.08 (0.1)** **[WM = 0.02]** **[N = 0.01]**
2122	Cat Mesa fault	Independent (1.0)	20	6.3 (0.2) 6.6 (0.6) 6.9 (0.2)	50 E (0.2) 75 E (0.6) 90 (0.2)	Middle Quaternary?	1.0	**0.002 (0.1)** **0.005 (0.24)** **0.009 (0.32)** **0.02 (0.24)** **0.09 (0.1)** **[WM = 0.02]** **[N = 0.01]**

TABLE 5-1. SEISMIC SOURCE PARAMETERS FOR REGIONAL FAULTS INCLUDED IN THE LANL ANALYSIS[1]

Fault No.	Fault Name	Rupture Model[2]	Maximum Rupture Length[3] (km)	Maximum Magnitude[4] (M_W)	Dip[5] (degrees)	Approximate Age of Youngest Activity[6]	Probability of Activity[7]	Rate of Activity[8] (mm/yr)
2123	Santa Fe fault	Independent (1.0)	30	6.5 (0.2) 6.8 (0.6) 7.1 (0.2)	45 E (0.2) 60 E (0.6) 75 E (0.2)	Quaternary?	0.7	**0.002 (0.1)** **0.005 (0.24)** **0.01 (0.32)** **0.02 (0.24)** **0.10 (0.1)** **[WM = 0.02]** **[N = 0.01]**
2124	Faults west of Mountainair	Independent (1.0)	14	6.1 (0.2) 6.4 (0.6) 6.7 (0.2)	45 W (0.2) 60 W (0.6) 75 W (0.2)	Mid to late Quaternary	1.0	0.01 (0.2) 0.03 (0.6)[39] 0.35 (0.2) [WM = 0.09]
2128	Coyote	Independent (1.0)	11	6.0 (0.2) 6.3 (0.6) 6.6 (0.2)	45 W (0.2) 60 W (0.6) 75 W (0.2)	Mid to late Quaternary	1.0	0.01 (0.2) 0.04 (0.6)[40] 0.3 (0.2)
2135	McCormick Ranch faults	Zone (1.0)	14	6.1 (0.2) 6.4 (0.6) 6.7 (0.2)	60 E (0.2) 90 (0.6) 60 W (0.2)	Mid to late Quaternary	1.0	**0.003 (0.1)** **0.009 (0.24)** **0.02 (0.32)** **0.04 (0.24)** **0.17 (0.1)** **[WM = 0.03]** **[N = 0.02]**
2142	Faults near Cochiti Pueblo	Zone (1.0)	32	6.5 (0.2) 6.8 (0.6) 7.1 (0.2)	50 E (0.4) 90 (0.3) 50 W (0.3)	Pleistocene	1.0	**0.01 (0.1)** **0.04 (0.24)** **0.07 (0.32)** **0.15 (0.24)** **0.66 (0.1)** **[WM = 0.13]** **[N = 0.06]**
A2144, A2145[41]	**Ojo Caliente (A2144) and Chili (A2145) faults**	**Linked (1.0)**	**16**	**6.2 (0.2)** **6.5 (0.6)** **6.8 (0.2)**	**45 W (0.2)** **60 W (0.6)** **75 W (0.2)**	**late Quaternary**	**1.0**	**0.009 (0.1)** **0.03 (0.24)** **0.05 (0.32)** **0.11 (0.24)** **0.49 (0.1)** **[WM = 0.10]** **[N = 0.05][42]**
A2146[43]	**Palace-Pipeline**	Independent(1.0)	**48[43]**	**6.7** (0.2) **7.0** (0.6) **7.3** (0.2)	55 W (0.2) 70 W (0.6) 85 W (0.2)	Pleistocene	1.0	**0.003 (0.1)** **0.01 (0.24)** **0.02 (0.32)** **0.04 (0.24)** **0.18 (0.1)** **[WM = 0.04]** **[N = 0.02]**

1. For all faults except the Pajarito fault system. See Plate 1 for location and trace geometry of all faults. See logic tree, shown on Figure 5-8, for parameters of the Pajarito fault system. Fault number and nomenclature after Machette *et al.* (1998) unless noted otherwise. Fault parameters are generally from Wong *et al.* (2004) with revised parameters shown in **bold**. Faults shown in *italics* were modeled with curvilinear geometries, all other were modeled as rectangular planes.

2. Possible rupture models include: zones, independent single faults, segmented and unsegmented faults, and linked faults. Zones are modeled as multiple subparallel planes within the zone boundary. Segmented and unsegmented faults allow for independent rupture for sections (or segments) of the fault. A linked model allows for coseismic rupture of faults, either along or across strike.

3. Measured straight-line, end to end on Plate 1.

4. Preferred values estimated using the empirical relation of Wells and Coppersmith (1994) for all fault types. Estimates are based on displacement per event and/or maximum surface rupture length, depending on available data. Relations are as follows:

   $M_W = 5.08 + 1.16 \log (SRL)$, $\sigma = 0.28$;

   $M_W = 6.93 + 0.82 \log (AD)$, $\sigma = 0.39$; and

   $M_W = 6.69 + 0.74 \log (MD)$, $\sigma = 0.40$

   Where M_W is moment magnitude, SRL is surface rupture length in km, AD is average displacement in meters, and MD is maximum displacement in meters

TABLE 5-1. SEISMIC SOURCE PARAMETERS FOR REGIONAL FAULTS INCLUDED IN THE LANL ANALYSIS[1]

[5] Dips are averages for the seismogenic crust.

[6] Based on data in Machette *et al.* (1998) unless noted otherwise. Categories are: Pliocene (1.6 to 5.3 Ma); Quaternary (<1.6 Ma); Pleistocene (10 ka to 1.6 Ma); early Pleistocene (750 ka to 1.6 Ma); late and middle Quaternary (<750 ka); late Quaternary (<130 ka); latest Pleistocene (10 to 15 ka); and Holocene (<10 ka).

[7] Probability of activity, p(a), considers the likelihood that a fault is an independent seismogenic structure and is still active within the modern stress field unless noted otherwise.

[8] Rates of fault activity are average net slip rates. For most faults, we assumed pure normal slip (100% dip slip). Slip rate distributions were developed with the same approach as in Wong *et al.* (1995), which was also used in Wong *et al.* (2004), except: a 5-point instead of 3-point distribution was used here, and the McCalpin (1995) analysis of slip rates for Rio Grande rift faults was updated for this study to incorporate new paleoseismic data (Table 5-8). The slip rate analysis is discussed further in the text. The 5-point distribution used here is after Miller and Rice (1983) and is as follows:

Percentile	Weight
3.5	0.1
21	0.24
50	0.32
79	0.24
96.5	0.1

The preferred rate used in the analysis to normalize the population of slip rates are designated by **N** in brackets and are generally the same as in Wong *et al.* (2004), except as noted in footnotes. **WM** is the weighted mean value of the distribution. See Table 5-4 for recurrence models and weights for fault sources.

[9] Preferred slip rate for the Cañoncs fault is the same as used in Wong *et al.* (1995) as no new data are available for this category C fault (see footnote 80 in their Table 7-1).

[10] N revised to 0.01 mm/yr for the Lobato Mesa fault based on 20 m of offset on the Puye Formation (Kempter *et al.*, 2005).

[11] Revised from Wong *et al.* (2004) as per Plate 1 and USGS database (Version 1.0 at http://qfaults.cr.usgs.gov).

[12] Geometry and nomenclature of the Embudo fault system (EFS) revised from Machette *et al.* (1998) based on recent mapping studies (Koning *et al.*, 2004a; Kelson *et al.*, 2004a). Note that the southwestern section was modeled with a curvilinear geometry.

[13] Revised based on 1.5 m-high scarp on latest Pleistocene to Holocene fan along Reach C (Kelson *et al.*, 1997; 2004a).

[14] N revised to 0.1 mm/yr based on 307 m of net slip on the 3-Ma Servilleta Basalt, yielding a long-term slip rate of 0.1 mm/yr (Bauer and Kelson, 2004a). Note that net Quaternary slip rates can also be estimated for the Northeastern section of the EFS from vertical offsets and horizontal to vertical slip ratios measured by Kelson *et al.* (2004a). For example, 10 m of vertical slip since 1.27 Ma, with a 1.8:1.0 slip ratio yields a net slip rate of 0.016 mm/yr, and 2 m of late Pleistocene (assumed 130 ka) vertical slip with the same slip ratio yields a net rate of 0.03 mm/yr. However, all of these Quaternary estimates are for single scarps and not the entire fault, which consists of multiple strands forming a broad zone (Kelson *et al.*, 2004a; Bauer and Kelson, 2004a, 2004b). Therefore, we considered these estimates as minimum for the entire zone and use the long-term rate as our preferred value for the Northeastern section of the EFS. We also assume this rate for the unsegmented model of the entire (unsegmented) EFS.

[15] Downweighted by the effective weight of 0.01 given to RS-e, where rupture of the Pajarito fault system extends onto the Southwestern section of the Embudo fault system.

[16] N revised to 0.04 mm/yr based on 10 to 13 m of vertical offset across Qtcgl strath terraces that are estimated to be about 620 ka (Koning, 2005), and assuming lateral to vertical slip ratios of 1.7:1, similar to the southernmost portion of the northeastern section of the EFS (Kelson *et al.*, 2004a). This rate is comparable to Pliocene vertical rates of 0.035 to 0.048 mm/yr (Koning *et al.*, 2004a).

[17] Depiction and extent of northern traces revised as per Koning *et al.* (2004) and ongoing mapping of the Chili 7.5' Quadrangle (D. Koning, NMBMG, personal communication, May 2005). As a result, maximum rupture length decreases from 19 (in Machette *et al.*, 1998) to 16 km.

[18] Although a recent paleoseismic trench exposed evidence for two late Pleistocene surface-faulting events on the Cañon section (Kelson *et al.*, 2004b), ages were poorly constrained so that slip rats or recurrence intervals could not be estimated. Therefore, we retain the slip rates and recurrence intervals originally used by Wong *et al.* (1995) for this category A fault. See footnotes 106 and 107 in Table 7-1 of Wong *et al.* (1995) for the bases for these distributions.

[19] Slip rates based on data in Machette *et al.* (1998) of: 50 to 150 m of displacement on early Pleistocene rocks (Machette and Personius, 1984), and 50 to 150 m of offset on 4.4 to 26.8 Ma basalts (Lipman, 1975).

[20] Slip rates based on 5 to 20 m of offset on the 2.3 to 4.8-Ma Servilleta Basalt. Maximum assumes all slip is post-750-Ma (Machette *et al.*, 1998).

[21] Slip rates remain unchanged from Wong *et al.* (1995) for this category A fault (see footnote 109 in their Table 1-1 for discussion).

[22] Revised length and geometry based on mapping from Lewis *et al.* (2005; see Plate 2). Modeled with a curvilinear geometry. Note that the Sawyer Canyon fault is likely part of the Pajarito fault system but is considered as an independent source for simplicity and because it lies north of and dips away from LANL.

[23] In light of new data for the San Francisco fault, N was revised to 0.15 mm/yr based on 200 m of vertical offset of the 1.6-Ma Otowi member of the Bandelier Tuff (Smith and Kuhle, 1998).

[24] The northern La Bajada fault offsets the 1.14-Ma basaltic andesite of Cochiti Cone and may offset the 55-ka El Cajete pumice (Minor *et al.*, in press).

[25] Minor *et al.* (in press) observed dominantly normal slip on 50° to 60° west-dipping faults along the La Bajada fault. N was revised to 0.2 mm/yr for the La Bajada fault based on long-term rates of 0.08 to 0.24 mm/yr from: 90 m vertical offsets on the 1.16-Ma basaltic andesite of Tank 19; 250 m vertical offset on the 2.4-Ma Cerros del Rio basalt (S.F. Personius, unpublished data, 1996, cited in Machette *et al.*, 1998); and 375 m to 600 m offset on the Cerros del Rio basalt further south (Smith and Kuhle, 1998; Minor *et al.*, in press).

[26] McCalpin and Harrison (2000) found evidence for four surface-faulting events on the western strand of the Calabacillas fault; the youngest event was estimated to have occurred about 14 ka.

[27] Recurrence interval distribution based on evidence of 4 events between 14 and 151 ka, an average recurrence interval of ~46 ky and estimates of individual intervals of 18 ky, 45 ky, and 74 ky (McCalpin and Harrison, 2000). Late Quaternary slip rates by McCalpin and Harrison (2000) were not used because they are only for one fault strand and likely are minimums for the entire fault.

[28] Recurrence intervals based on evidence for 3 late Quaternary events occurring on the County Dump fault around 30 ka, 35 to 40 ka, and 75 to 95 ka (McCalpin *et al.*, in press).

[29] N for the County Dump fault revised to 0.02 mm/yr based on long-term vertical slip rates of 0.016 to 0.03 mm/yr for 800 ka to 1.5 Ma, and late Quaternary rates of 0.008 to > 0.07 mm/yr (McCalpin *et al.*, in press).

[30] Preferred maximum magnitude for the East Paradise fault based on an average estimate using: surface rupture length of 13 km; and average displacement per event of 0.5 to 1.25 m (Personius and Mahan, 2000). Slip rates for the East Paradise fault based on: 2.75 ± 0.1 m of vertical offset since 286 ± 26 ka, and vertical slip rates for the past two complete seismic cycles of 0.004 to 0.019 mm/yr (Personius and Mahan, 2000).

[31] Preferred maximum magnitude for the Zia fault based on average of length-based and displacement-based expected values assuming an average displacement per event of 1.3 m (McCalpin and Harrison, 2001).

[32] Slip rates for the Zia fault based on: 6.5 m of throw since >63 to 119 ka (McCalpin and Harrison, 2001), and 60 m of offset on Santa Fe Group sediments (Kelley, 1977) assumed to be 1.6 Ma (Machette *et al.*, 1998).

[33] Although paleoseismic data indicates that these faults are likely segmented (Machette *et al.*, 1998), we assumed a single independent fault model for simplicity and because the faults are far away from the map area boundary.

TABLE 5-1. SEISMIC SOURCE PARAMETERS FOR REGIONAL FAULTS INCLUDED IN THE LANL ANALYSIS[1]

[34] Slip rate distribution for the Socorro Canyon fault is modified from the N = 0.04 mm/yr distribution based on late Pleistocene slip rates of 0.02 to 0.03 mm/yr for the past two complete seismic cycles (Phillips *et al.*, 2003), and early to mid Pleistocene rates based on scarp morphology data of 0.02 to 0.06 mm/yr (Machette *et al.*, 1982).

[35] Includes western and central splays of Personius *et al.* (2001), Personius and Mahan (2003, and Olig *et al.* (2004; in review).

[36] Preferred maximum magnitude based on an average estimated using: surface rupture length of 43 km; maximum displacement of 4.7 m, and average displacement of 1.7 m (Olig *et al.*, 2004; in review).

[37] Preferred slip rate is a cumulative (for western and central splays) average vertical rate for the past 4 complete seismic cycles, based on 10.5 m of slip occurring between 70 and 12 ka (Olig *et al.*, 2004; in review). Minimum and maximum values based on minimum and maximum rates calculated for individual seismic cycles.

[38] Distributions based on the combined paleoseismic record for the western splay (Personius *et al.*, 2001; Personius and Mahan, 2003) and central splay (Olig *et al.*, 2004; in review) that indicates evidence for at least 4, probably 5 late Quaternary surface-faulting events, resulting in an average recurrence interval of 19 (+5, -4) ky, with individual intervals of 17, 27, and 19 ky for coseismic rupture events, but recurrence interval estimates are as short as 12 ky if independent rupture events of the central splay are also included (Olig *et al.*, 2004; in review).

[39] Slip rates based on scarp morphology data (Machette and McGimsey, 1983) suggesting 3 m of offset on possible late Pleistocene deposits (assumed to be 10 to 130 ka) and 8 m of offset on middle Pleistocene deposits (assumed to be 130 to 750 ka).

[40] As slip rate data is lacking, N for the Coyote fault was assumed to be between rates of the Sandia fault to the north (N = 0.05 mm/yr) and the Manzano fault to the south (N = 0.02 mm/yr).

[41] From Koning *et al.* (2004a).

[42] Due to lack of slip rate data for these newly recognized late Quaternary faults, we assumed a long term slip rate of N = 0.05 mm/yr, between the nearby Lobato Mesa (#2004) and La Cañada del Amagre (#2005) fault zones.

[43] This newly recognized fault (Maldonado *et al.*, 1999) was not included in Machette et al. (1998), but was included in Wong *et al.* (2004). It is not shown separately on Plate 1, but it includes the westernmost traces of the McCormick Ranch faults as shown by Machette et al. (1998), and so our modeling of the zone for the McCormick Ranch faults (#2135) excluded these traces. We have also extended the maximum length of the Palace-Pipeline fault (from 27 to 48 km) to include fault scarps as far south as Abo Arroyo. This is based on our ongoing mapping of Quaternary fault scarps on the southern Llano de Manzano under USGS NEHRP Award No. HQGR0079. As is the case with our modeling of many poorly understood intrabasin faults in the rift, we conservatively assumed these faults behave independently of each other for simplicity, but the Palace-Pipeline fault may very well coseismically rupture with the McCormick Ranch faults and/or the Hubbell Spring fault. Steeper dips were assumed for this relatively large intrabasin fault based on the cross section of Maldonado *et al.* (1999). N based on scarps as high as 15m on the Sunport and Llano de Manzano surfaces that are estimated to be between 0.5 and 1.5 Ma (Maldonado *et al.*, 1999).

Table 5-2
Updated Slip Rate Analysis for Faults in the Rio Grande Rift[1]

Fault Name	Site	Data Source	Time Period (ka) min[2]	Time Period (ka) max[3]	Time Interval[4] (ky)	Displace-ment[5] (m)	Short- term Slip Rate (mm/yr)	Long-term Slip Rate (mm/yr)	Normal-ization Factor[6] (with N=0.1)	Normal-ized Slip Rate[7] (mm/yr)
County Dump	**County Dump**	**McCalpin *et al.* 2006**	**30**	**40**	**10**	**0.4**	**0.04**	**0.023**	**4.35**	**0.1739**
			40	**85**	**45**	**0.35**	**0.0078**	**0.023**	**4.35**	**0.0339**
Southern Sangre de Cristo		Menges 1990	0	140	140		0.045	0.17	0.59	0.0265
			0	4000	4000		0.175	0.17	0.59	0.1029
Northern Sangre de Crusto	Major Creek	McCalpin 1982	8	13	5		0.48	0.06	1.67	0.8000
			13	25	12		0.43	0.06	1.67	0.7167
			25	140	115		0.05	0.06	1.67	0.0833
			140	400	260		0.035	0.06	1.67	0.0583
	San Isabel Creek		8	13	22		0.24	0.1	1.00	0.2400
			13	25	30		0.09	0.1	1.00	0.0900
			25	140	80		0.1	0.1	1.00	0.1000
			140	400	260		0.09	0.1	1.00	0.0900
	Willow Creek		8	25	17		0.09	0.04	2.50	0.2250
			25	35	10		0.38	0.04	2.50	0.9500
			35	400	365		0.02	0.04	2.50	0.0500
	Uracca Creek		8	25	17		0.18	0.08	1.25	0.2250
			25	35	10		0.04	0.08	1.25	0.0500
			35	400	365		0.09	0.08	1.25	0.1125
	Blanca Creek		15	60	45		0.08	0.05	2.00	0.1600
			60	140	80		0.01	0.05	2.00	0.0200
			140	400	260		0.05	0.05	2.00	0.1000
Caballo	Ash Springs	Machette 1987a	10	125	115		0.029	0.035	2.86	0.0829
			125	250	125		0.044	0.035	2.86	0.1257
			250	750	500		0.0285	0.035	2.86	0.0814
San Andres	Central Section	Machette 1987b	10	125	115		0.0525	0.105	0.95	0.0500
			125	250	125		0.14	0.105	0.95	0.1333
Organ Mountains	Cox Ranch	Machette 1987b	3	5	2		1.65	0.1	1.00	1.6500
			5	15	10		0.43	0.1	1.00	0.4300
			25	125	100		0.054	0.1	1.00	0.0540
			125	250	125		0.085	0.1	1.00	0.0850

Table 5-2
Updated Slip Rate Analysis for Faults in the Rio Grande Rift[1]

Fault Name	Site	Data Source	Time Period (ka) min[2]	Time Period (ka) max[3]	Time Interval[4] (ky)	Displacement[5] (m)	Short- term Slip Rate (mm/yr)	Long-term Slip Rate (mm/yr)	Normalization Factor[6] (with N=0.1)	Normalized Slip Rate[7] (mm/yr)
East Franklin	Ft. Bliss	Machette 1987b	15	125	110		0.003	0.08	1.25	0.0038
			125	250	125		0.064	0.08	1.25	0.0800
			250	400	150		0.137	0.08	1.25	0.1713
			400	750	350		0.078	0.08	1.25	0.0975
Hubbell Spring	**Cumulative (Carrizo Spring site-Central splay, Hubbell Spring site-Western splay)**	**Olig *et al.* 2004, 2005; Olig *et al.*, in review; Personius *et al.*, 2001; Personius & Mahan 2003**	**12**	**20**	**8**	**3.7**	**0.46**	**0.18**	**0.56**	**0.2556**
			20	**29**	**9**	**0.4**	**0.044**	**0.18**	**0.56**	**0.0244**
			29	**56**	**27**	**1.7**	**0.063**	**0.18**	**0.56**	**0.0350**
			56	**70**	**14**	**4.7**	**0.34**	**0.18**	**0.56**	**0.1889**
Socorro Canyon	**Socorro Canyon**	**Phillips *et al.*, 2003; Machette, 1982**	**1.5**	**28**	**26.5**	**0.5**	**0.0188**	**0.04**	**2.50**	**0.0470**
			28	**92**	**64**	**1.8**	**0.028**	**0.04**	**2.50**	**0.0700**
Calabacillas	**Southern (near CASA Facility)**	**McCalpin *et al.*, in prep.; McCalpin & Harrison, 2000**	**14**	**32**	**18**	**0.1**	**0.0056**	**0.041**	**2.44**	**0.0137**
			32	**77**	**45**	**0.3**	**0.0067**	**0.041**	**2.44**	**0.0163**
			77	**151**	**74**	**0.55**	**0.0074**	**0.041**	**2.44**	**0.0180**
East Paradise	**Arroyo de las Calabacillas**	**Personius & Mahan 2000**	**10**	**75**	**65**	**1.25**	**0.019**	**0.01**	**10.00**	**0.1900**
			75	**208**	**133**	**0.5**	**0.0038**	**0.01**	**10.00**	**0.0380**
Guaje Mountain	**Cabra and Chupaderos Canyons**	**Gardner *et al.*, 2003; Lewis *et al.*, 2005**	**5.35**	**39.6**	**34.25**	**1.5**	**0.044**	**0.013**	**7.69**	**0.3385**
Central Sangre de Cristo	**Rito Seco Creek**	**Crone and Machette, 2005; R. Kirkham, written comm. 7-05**	**9**	**23.4**	**14.4**	**2.3**	**0.16**	**0.21**	**0.48**	**0.076**
			23.4	**30**	**6.6**	**1.45**	**0.22**	**0.21**	**0.48**	**0.1048**
			30	**45**	**15**	**2.0**	**0.13**	**0.21**	**0.48**	**0.0619**

[1] Analysis updated from McCalpin (1995) to incorporate new paleoseismic data (shown in **bold**). Only slip rate data for complete seismic cycles (i.e., the slip per faulting event/recurrence interval preceding that event) were added to the updated analysis, even though these data criteria were not used in the original analysis.

[2] This column heading is shown the same as in McCalpin (1995), but for the new data in bold this column can be better described as the time of the younger surface-faulting event.

[3] This column heading is shown the same as in McCalpin (1995), but for the new data in bold this column can be better described as the time of the older surface-faulting event.

Table 5-2
Updated Slip Rate Analysis for Faults in the Rio Grande Rift[1]

[4] The interval between the ages specified in the two preceding columns. For the data pertaining to complete seismic cycles that were added in this study, this is the recurrence interval between events. Note that this heading was shown in McCalpin (1995) as "Elapsed Time", but we don't repeat that term here as "elapsed time" is more typically used to refer to the time since the most recent faulting event.

[5] This column was not included in McCalpin (1995), but is shown here for the new data added for this study. For complete seismic cycles, this is the displacement that occurred in the younger event.

[6] This example is normalized to 0.1 mm/yr so the normalization factor for each fault or fault segment is derived by dividing the long-term average slip rate for each fault into 0.1 mm/yr.

[7] Normalized slip rate is the short-term rate for the given interval multiplied times the normalization factor for that fault. The number of normalized slip rate observations for the complete updated dataset is 49.

Table 5-3
Comparison of Slip Rate Distributions (mm/yr) for N = 0.07 mm/yr
Using Different Rio Grande Rift Fault Slip Rate Datasets

Percentile (and weight) [1]	1995 Analysis (for n = 34)[2]	2005 Update – All Data (for n = 49)[4]	2005 Update – Subset (for n = 17)[5]
3.5 (0.1)	0.015	0.011	0.011
21 (0.24)	0.038	0.033	0.020
50 (0.32)	0.069	0.063	0.043
79 (0.24)	0.16	0.13	0.13
96.5 (0.1)	0.65	0.59	0.20
	WM: 0.14[3]	**WM: 0.12**	**WM: 0.071**

[1] This is the 5-point distribution of Miller and Rice (1983). See Figure 5-8 for a plot comparing complete distributions.

[2] See Table 7-3 in Wong *et al.* (1995) for data.

[3] **WM** is the weighted mean for the 5-point distribution. For comparison, the 3-point distribution used in Wong *et al.* (1995) of the 5th, 50th, and 95th percentiles, which were respectively weighted 0.2, 0.6, and 0.2, results in an even more skewed weighted mean of 0.16 mm/yr.

[4] All the data shown in Table 5-8 of this study.

[5] Only the data for complete seismic cycles added for this study (shown in bold in Table 5-8).

Table 5-4
Weights on Recurrence Models for Fault Sources

Recurrence Model	Assigned Weight		
	Segmented Faults	Unsegmented Faults	Zones of Faults
Characteristic	0.8	0.7*	0.5
Maximum Magnitude	0.1	0.1	0
Truncated Exponential	0.1	0.2	0.5

*Using a slightly wider range for the characteristic event as discussed in Section 2.2.5.

Table 5-5
Paleoseismic Data Summary for Pajarito Fault System[1]

Event	Fault and Trench Site[2]																						
	PAF																			GM			RC
	97-3[3]	97-3[4,5]	97-4[3]	97-4[4,6]	97-5[4]	97-6[4]	97-7[3]	97-7[4]	97-7a[3]	97-7a[4]	EOC-2[3,11]	WETF-2c[3,20]	98-4[3]	98-4[4]	98-5[3]	98-6[3]	98-6[22]	Pajarito Canyon[7,8]	Water Tanks[7,8]	Cabra Cyn[3,15]	Sportsmen's Club[7,8,21]	Chupaderos Cyn[3,15]	Guaje Pines[7,9,10]
P1		1.3 2.2		<2.3 (<4.5)			1.4 2.2	1.4 4	1.2[12] 2.2	~1.4		*1.3* *7.3*											
P2	2.2 20		2.1 19								*5.5* *8.6*				*3* *12*	2.4 7.0	2.4 16			4.2 6.5	age?	3.4 10	
P3								>2.2			8.6 10.5	9 10.9	*10* *21*	*10* *18*	*11* *44*	*2.7* *24*							>8.6
P4	20 45	~20	age?	age?	3 or 4 events since 177 to 184 *(Possibly 7 events since 492)*	At least 2 events since 25 to 132 *(Possibly 8 events between 4 and 445)*						>14.1	<31[17]	*14* *60*			41 58				*age?*	38.8 40.4	*age?*
P5	36 97	≤ 81	age?	age?				45 63[15]			At least 5 events >43					At least 1 event between 58 and 1,220		age?	50[18] *61*				60 75
P6 (?)								2 events between 61 and 1,220										*age?*	50[18] *63*				
P7		*81* *106*		age?													*78* **<1,220**		*Possibly 5 events between 57 and 1,220*				age?
P8		**~100[19]**																					
P9		**~110[19]** (97-117)																					
P10		**age?**																*>137*			**>144[16]** 300		*>140* *<1,220*
P11		*1,100* *1,220*																**age?**					
P12																		*Possibly 3 events between 137 and 1,220*					
P13																							
P14																							

[1] Minimum and maximum ages constraining the timing of surface faulting events in thousands of years. *Italics* /non-bold indicates event may be non-tectonic or evidence is ambiguous. Shading indicates evidence exists to preclude occurrence of event at that site. Hatchures indicate correlative section was not exposed. Note that most trenches show evidence for an incomplete stratigraphic record due to significant unconformities associated with hiatuses in deposition and/or erosion. An incomplete stratigraphic record inherently results in an incomplete paleoseismic record. The record is judged to be most complete for the past ~40 ka (P1 through P4), but is still not necessarily complete. Ages in blue constrained by radiocarbon dates (calendar calibrated unless noted otherwise). Ages in green constrained by luminescence analyses. Ages in dark orange constrained by PDI or other soil-based estimates. Note that McDonald (1999) reported soil profile development index (PDI) ages as ranges (typically with ~20% uncertainties if no stripping occurred). We have considered 20% uncertainties or larger in using PDI ages throughout this analysis. Ages in purple constrained by Ar-Ar anlyses or stratigraphic correlations to units dated by Ar-Ar. Ages in black are from other techniques as noted.

[2] PAF: Pajarito fault; GM: Guaje Mountain fault; RC: Rendija Canyon fault. Some trench sites are shown with multiple columns to compare different interpretations of the data. Note that trenches 97-7 and 97-7a were on the same fault trace. Similarly, trenches 97-3 and 97-4 were on the same fault trace. Plate 2 shows locations.

[3] Source: Gardner *et al.* (in prep.). Note that their re-evaluation focused on the latest Quaternary record (P1 through P4) because it is the most complete and best understood. The lack of older events shown for Trenches 97-3 and 97-4 (older than P5), and Trench 97-7 (older than P1) does not indicate disagreement with the identification of these events by McCalpin (1998; 2005).

[4] Sources: McCalpin (2005; excluding Figure 18), McCalpin (1998) and McCalpin (1999).

[5] Preferred age by McCalpin (1998, 2005) for the youngest event in Trench 97-3 is ~1.5 ka based on radiocarbon age, PDI age estimate, and stratigraphic relations. Evidence for Event P7(?) (Event W of McCalpin) is herein considered somewhat ambiguous in Trench 97-3

Table 5-5

Paleoseismic Data Summary for Pajarito Fault System[1]

because it had no apparent offset and there is limited evidence for this event as the associated crack fill (Unit 10) may have been deposited with Unit 8 during Event P8.

[6] According to McCalpin (1998, 2005), the youngest event occurred after 2.1 - 4.5 ka, and most likely after 2.3 ka. Ages for other events poorly constrained but the four events assumed to likely correlate to four youngest events in Trench 97-3.

[7] Source: Wong *et al.* (1995)

[8] Source: Olig *et al.* (1996)

[9] Source: Kelson *et al.* (1996)

[10] Luminescence ages for MRE are 19 to 27 ka (Kelson *et al.*, 1996) and may be anomalously old due to only partial solar resetting and so radiocarbon age of >8.2 ka (Kelson *et al.*, 1996) is preferentially reported here.

[11] Source: Reneau *et al.* (2002)

[12] For the youngest event in Trench 97-7a, an age of 1.4 ± 0.2 ka is preferred for the preferred interpretation of 3 possible scenarios whose ages range from 1.4 to 2.2 ka (Gardner *et al.*, in review).

[13] Event not included in McCalpin (2005), but from McCalpin (1998).

[14] Age from McCalpin (1998)

[15] Source: Gardner *et al.* (2003). Age for the penultimate event constrained by both radiocarbon (uncalibrated as ages are older than calibration curves) and optically stimulated luminescence ages. Note that Gardner *et al.* (2003) discussed speculative evidence for occurrence of a possible additional event at ~40 ka, but we judged the evidence to be too ambiguous to include the event here.

[16] Minimum cosmogenic age from Phillips *et al.* (1998)

[17] Too old to calendar calibrate

[18] Older than El Cajete pumice, which is estimated to be 50 to 60 ka based on radiocarbon and luminescence analyses, Reneau *et al.* (1996)

[19] Preferred ages based on luminescence ages for younger deposits, stratigraphic, and pedologic relations. McDonald's age estimate of the base of buried soil Bt2b3 ranges from 68 to 118 ka, and provides a minimum-limiting age for Event P9 in Trench 97-3, whereas the base of buried soil Bt2b4 is estimated to be 98 to 150 ka and provides a maximum limiting age for this event. Overlying luminescence sample ages of 94 ± 8 and 106 ± 9 ka are somewhat consistent with the soil ages, even though the luminescence ages themselves are stratigraphically reversed. They also support McCalpin's preferred age estimate of 110 ka for Event P9, even though actual soil age constraints have a broader range than reported in McCalpin (2005) or Gardner et al. (in review).

[20] Paleoseismic evidence is not from trenches but from stratigraphic and structural evidence in boreholes.

[21] Paleoseismic evidence is not from trenches but from differential offsets of fluvial terraces that suggest at least two possibly three events occurred on the GM within the past 150 to 300 ka (Wong *et al.*, 1995, Olig *et al.*, 1996). Two youngest events assumed to correlate to events at Chupaderos Canyon trench site.

[22] Source: McCalpin (1999). Not included in McCalpin (2005). Note that McCalpin (1999) quoted a minimum age of 2.7 ka (based on a PDI age estimate) for the youngest event in the Executive Summary, but discussion in the text (McCalpin, 1999, p. 80) cites a radiocarbon age of 2.4 ka for a minimum, which is used here because the PDI age estimate of this horizon within Unit 3a does not provide a minimum age for faulting of Units 2c and 3a. Note also that McCalpin (2000) revised his interpreation and age for the youngest event to be between 7 and 9.2 ka based on two IRSL ages bracketing the top of Unit 2b, but these ages are stratigraphically reversed, probably not completely reset (McCalpin, 2000, p. 17-18), and do not agree with the radiocarbon age of 2.4 ka. Additionally, McCalpin (1999) clearly states that Unit 2b is unfaulted, and thus the base of Unit 2b, not the top, would be the event horizon. We have considered all of these uncertainties in our analysis here by bracketing the age to be between 2.4 ka and 16 ka for the youngest event as originally cited in McCalpin (1999). Additionally, although (McCalpin 1999, 2000) estimates an age of 41 to 58 ka for the penultimate event based on PDI estimates of the base of Units 4 and 5, this event post-dates Unit 5 and pre-dates Unit 4 (see p. 80 and 81, McCalpin, 1999), and thus an age of ~30 to 50 ka is actually used in our analysis here for the 6-event scenario (Table 6), based on PDI age estimates of 32 to 51 ka (Table 2 in McCalpin, 1999) for the base of Unit 4b, which is McCalpin's interpretted event horizon. Similarly, we assumed an age estimate of 60 to 100 ka in our analysis for the third event back in Trench 98-6, based on PDI age estimates of 62 to 99 ka (Table 2 in McCalpin, 1999) for the base of Unit 6a in Trench 98-6.

Table 5-6
Scenario for Nine Late Quaternary Events (with three Holocene) on the PAF[1]

Paleoearthquake	Rupture Source or Participating Segments (Trench Sites[2])	Estimated Time (ka)
P1	**PAF** (97-3, 97-4, 97-7, 97-7a, *WETF-2c*)	1.4 ± 0.2
P2	**PAF** (*EOC-2*, *98-5*, 98-6) **GM** (Cabra Cyn., *Sportsmen's Club*, Chupaderos Cyn.)	4.2 to 6.5
P3	**PAF** (97-7, EOC-2, WETF-2c, *98-4*) **RC** (Guaje Pines)	9 to 10.5
P4	**PAF** (97-3, 97-4, WETF-2c, *98-4*, *98-5*, 98-6) **RC** (*Guaje Pines*) **GM** (Chupaderos Cyn., *Sportsmen's Club*)	39.6 ± 0.8
P5	**PAF** (97-3, 97-4, 97-7, Pajarito Cyn., *Water Tanks*)	45 to 63
P6(?)	**PAF** (*Pajarito Cyn.*, *Water Tanks*) **RC** (Guaje Pines)	60 to 75
P7	**PAF** (*97-3*, 97-4) **RC** (Guaje Pines)	80 to 106
P8	**PAF** (97-3)	100 ± 20
P9	**PAF** (97-3)	~110 (100 – 150)

[1] Scenario was developed from data summarized in Table 5-5.

[2] *Italics* indicates evidence for surface-faulting event is ambiguous. Underline indicates time is poorly constrained and so correlation is ambiguous.

Table 5-7
Scenario for Six Late Quaternary Events (with two Holocene) on the PAF[1]

Paleoearthquake	Rupture Source or Participating Segments (Trench Sites[2])	Estimated Time(ka)
P1	**PAF** (97-7, 97-7a *WETF-2c*)	1.4 ± 0.2
P2	**GM** (Sportsmen's Club, Cabra Cyn., Chupaderos Cyn.)[3]	4.2 to 6.5
P3	**PAF** (97-3, 97-4, 97-7, EOC-2, WETF-2c, 98-6[4]) **RC** (Guaje Pines)	9 to 10.5
P4	**PAF** (97-3, 97-4, *WETF-2c*, 98-6) **GM** (Sportsmen's Club, Chupaderos Cyn.)	39.6 ± 0.8
P5	**PAF** (97-3, 97-4, 97-7, Pajarito Cyn.)[5] **RC** (Guaje Pines)	60 to 75
P8	**PAF** (97-3, 97-4) **RC** (Guaje Pines)	100 ± 20
P9	**PAF** (97-3)	~110 (100 – 150)

[1] Scenario was developed from data summarized in Table 5-5.

[2] *Italics* indicates evidence for surface-faulting event is ambiguous. Underline indicates time is poorly constrained and so correlation is ambiguous.

[3] In this scenario, Event P2 only ruptures the GM, which triggers a rockfall to create the 5.5 to 8.6 ka stone line at Trench EOC-2, and slope movement at Trench 98-5.

[4] In this scenario, we assume time estimates of 2.4 to 20 ka, 30 to 50 ka, and 60 to 100 ka for the three youngest events in Trench 98-6 as discussed in Footnote 22 of Table 5-5.

[5] In this scenario, we consider the possibility that the soil-based age estimates for the third event back at Trench 97-7 has uncertainties > 20% and PDI age estimates shown in Table 5-5 may be minimums.

Table 5-8
Footnotes to the Logic Tree for the Pajarito Fault System
(See Figure 5-8)

[1] **The Pajarito Fault System** – The Pajarito fault system (PFS) as defined here includes the following fault segments: Pajarito (PAF), Rendija Canyon (RC), Guaje Mountain (GM), and Santa Clara Canyon (SCC) faults (Figure 5-4). Although the Sawyer Canyon (SC) fault is close to the PFS and likely is part of this fault system, it was modeled as a separate source for simplicity and because it dips to the east, away from the rest of the PFS and LANL.

[2] **Rupture Models** – Based on the structural relations between fault segments of the PFS, the available paleoseismic data and displacement patterns discussed in the text, we originally developed three rupture models for the PFS: two segmented models (Models A and B), and an unsegmented model (Model C). However, during the moment balancing we found that Rupture Model A required unreasonably large displacements on the SCC (> 4 m and 50% larger than those on the PAF for the same scenario) and so we eliminated Rupture Model A. We strongly favored the unsegmented model (Model C) because we believe this best fits our structural model and the complex rupture patterns indicated by the paleoseismic data as discussed in the text.

[3] **Rupture Scenarios** – Rupture sources for the various rupture scenarios of the PFS and their lengths are shown on Figures 5-9a through 5-9d. All scenarios are modeled with curvilinear planes. Scenarios, rupture sources, and weights are shown in Table 5-9 and were based on data discussed in the text. Surface rupture lengths were measured along a straight line, end to end for each principal plane, in ARC-GIS.

[4] **Dip RC and GM** – This distribution remains unchanged from Wong *et al.* (1995). Fault plane measurements made during detailed bedrock mapping along the RC and GM show dips ranging from 60° W to 90° and averaging about 75° to 79° W (K.E. Carter, LANL, personal communication, 1993). Weights were based on these data and an overall linear surface trace, which suggests a steep dip.

[5] **Dip PAF and SCC** – This distribution is slightly revised from Wong *et al.* (1995) to better reflect uncertainties. Deep subsurface data on the PAF and SCC are lacking, but interpretation of seismic reflection data across the Albuquerque Basin indicates that, to the south, many rift-related normal faults flatten with depth (Russell and Snelson, 1990). Some of these listric faults shallow at 10 km depth, with upper portions dipping 60° and deeper portions dipping as low as 20°. In contrast, based on seismic, gravity, and geologic data, Baldridge *et al.* (1994) found that rift-bounding structures near the Abiquiu embayment in the northern rift were high-angle planar normal faults. In addition, observations of historical earthquakes in the western U.S. (including the RGR) show no evidence for earthquakes rupturing low-angle (<35°) or listric fault planes (Doser and Smith, 1989). Therefore, we assumed faults are planar in this analysis and used dips that we judged represent averages throughout the seismogenic crust in the rift. Based on existing data, the likely average dip is about 60°. A value of 45° is included to allow for lower average dips or a possible listric geometry. A value of 75° is also included to account for cases in which faults flatten deeper than 10 to 15 km and/or have a possible larger component of lateral slip. Weights are assumed based on a symmetric distribution about 60°.

[6] **Depth** – Depths and weights are the same as in Wong *et al.* (1995) and are based on observations of historical seismicity in both the Basin and Range province (typically about 15 km) and RGR (typically about 12 km) (*see* Section 5 of Wong *et al.*, 1995), and to reflect uncertainty and variability in observations (i.e., the possibility of ruptures as deep as 17 km for large magnitude events which tend to nucleate at or slightly below the base of the seismogenic crust). Note that shallower depths were given a slightly higher weight for the PFS weighted-mean depth was 14.2 km) than for regional faults (weighted-mean depth was 15 km) because of the proximity to the Valles caldera (Plate 1).

Table 5-8
Footnotes to the Logic Tree for the Pajarito Fault System
(See Figure 5-8)

[7] **Type of Multisegment Rupture** – Several critical LANL facilities are located between segments of the PFS and so we considered two types of multisegment rupture: simultaneous and synchronous. Simultaneous ruptures are treated as rupture of multiple segments in one large event (e.g., the 1992 **M** 7.2 Landers earthquake, [Wald and Heaton, 1994]), which is traditionally how multisegment ruptures are modeled in probabilistic seismic hazard analyses. Synchronous ruptures treat multisegment ruptures as multiple (in this case two) smaller subevents and the ground motions are summed at the site for each subevent using a sum of the squares formulation within the hazard code (see Section 2.3.2). The 1959 **M** 7.3 Hebgen Lake earthquake is a good example of synchronous rupture of multiple fault segments (Doser, 1985). We slightly favored the simultaneous rupture because the large displacements per event observed on the RC and GM are more consistent with this model.

[8] **Empirical Relation** – Maximum magnitudes for fault sources can be estimated using empirical relations (e.g., Wells and Coppersmith, 1994; Mason, 1996; Anderson *et al.*, 1996; Stirling *et al.*, 2002; Hanks and Bakun, 2002) for surface rupture lengths, surface rupture areas, slip rates, displacements, or a combination of these parameters (see de Polo and Slemmons [1990] for more discussion on estimating maximum magnitudes). We used the empirical relations from Wells and Coppersmith (1994) for all fault types because they found no statistically significant difference between relations for faults with different types of slip. The Wells and Coppersmith's relations were selected because they compiled the most comprehensive database on historical surface ruptures, verifying observations from original reports and maps. However, we recognize that data from large historical normal-faulting earthquakes are still few, particularly from continental rift environments similar to the RGR. Rupture length and appropriate displacement relations were used when displacement data were available. Relations are as follows:

$M_w = 5.08+1.16 \log L$, $s = 0.28$;

$M_w = 6.69+0.74 \log MD$, $s = 0.40$; and

$M_w = 6.93+0.82 \log AD$, $s = 0.39$

(where L is surface rupture length measured end to end in a straight line in kilometers, s is the standard deviation, MD is maximum displacement in meters, and AD is average displacement in meters). Empirical relations based on rupture area were not used because area-based magnitude estimates appear to systematically underestimate magnitudes compared to those based on length and displacement for the PFS, perhaps because of large uncertainties in estimating areas for complex, multiple-plane, interconnecting fault systems such as the PFS.

[9] **Maximum Magnitude** – Maximum magnitudes and their associated weights were calculated for each fault geometry and displacement branch, depending on the type of multisegment rupture. Weighted-mean maximum magnitudes were then calculated from the distribution for each rupture scenario of the PFS (see Table 5-10 for simultaneous ruptures and Table 5-11 for synchronous ruptures). We used this weighted-mean, weighted at 0.6, as our best estimate, and then included values at ± 0.3 of a magnitude unit around this best estimate, weighted at 0.2, to adequately account for uncertainty as discussed in the text.

[10] **Recurrence Model** – These were the same as for regional faults. See Table 5-4 and discussion in Sections 2 and 5.1.

[11] **Slip Rate/Recurrence** – See discussion in PFS Rates of Activity under Section 5.1.

Table 5-8
Footnotes to the Logic Tree for the Pajarito Fault System
(See Figure 5-8)

[12] **Displacement RS-h** – The PAF is characterized by a wide distributed deformation zone that includes multiple, discontinuous and anastomozing fault traces, warping, tilting, and monoclinal folding (Plate 2; see McCalpin, 1997 for further discussion). Due to this complexity, measured displacements per event across the entire PAF have large uncertainties owing to questions of whether all the deformation is included. Additionally, displacement data on the SCC are lacking. Therefore, we used data on displacement per event for the RC and GM (see footnotes 8 and 9 on Table 5-10) as minima for the maximum displacement per event on the entire fault system. This is based on the assumption that if rupture occurred on the PAF and one or both of the other faults, displacement likely would be greater on the PAF as the master fault. Therefore, a minimum value of 1.0 m for maximum displacement per event is likely (see footnotes 8 and 9). To estimate the range in maximum displacement per event, we followed the approach of Wong *et al.* (1995, see Footnote 33 in Table 7-1). They used maximum displacement data from earthquakes on normal faults throughout the world that produced more than 10 km of surface rupture (Wells and Coppersmith, 1994). The Wells and Coppersmith database shows 19 historical normal-fault earthquakes having a range in maximum displacement from 0.2 to 6.6 m (*Table 7-7 in Wong et al., 1995*). They assumed that this population was applicable to the Pajarito fault system, with the exception of the displacements that are less than 1 m, which was below the minimum value cited above. They plotted the cumulative frequency distribution of the 14 measurements satisfying these criteria. To estimate displacement values for the logic tree, they chose to use the 10th, 50th, and 90th percentiles of the cumulative frequency plot weighted at 0.3, 0.4, 0.3, respectively, because this three-point approximation is best when the tails of a distribution are not well-defined (Keefer and Bodily, 1983). These percentiles correspond to displacement values of 1.1, 2.5, and 5.8 m, respectively. For simplicity, they assigned values of 1.5, 2.5, and 5.5 m to the three branches, which yields a weighted mean of 3.1 m.

[13] **Recurrence Method RS-h** – Both slip rate and recurrence interval methods are used for RS-h, with the floating earthquake rupture source. However, we favored the recurrence method (weighted 0.7) over the slip rate method (weighted 0.3) for several reasons, including (1) recurrence intervals better characterize the most recent behavior on the PFS, and more directly incorporate fault specific uncertainties than the long term Quaternary slip rates; (2) recurrence intervals are more directly used in PSHA calculations whereas the use of slip rates is indirectly dependent on fault geometry and the type of recurrence models used (Wong and Olig, 1998); and (3) the lateral component of slip is not well-constrained for the PFS (although this is likely small compared to other uncertainties). However, we did not discount slip rate data altogether because: (1) despite the considerable gains in knowledge since 1995 of the late Quaternary paleoseismic record for the PFS, the record still remains incomplete particularly for the PAF; and (2) the 1.2-Ma Tshirigee member of the Bandelier tuff provides an excellent marker to measure Quaternary throw along nearly the entire PFS and, as such, this datum provides a measure of rate of activity that is not dependent on how events correlate between trenches, which is fraught with uncertainties.

[14] **Slip Rate RS-h** – To determine a slip rate distribution for RS-h we assumed long-term slip rates similar to the PAF. Slip rate values for the PAF are based on throw measured on the Tshirigee member of the 1.2-Ma Bandelier Tuff (RS-a on Figure 5-6), and on comparison with published slip rates within the RGR as previously discussed (Table 5-2, Section 5.1, *Probabilities and Rates of Activity*). The average throw on the Unit 3t/Unit 4 contact in the Tshiregee Member of the Bandelier Tuff along the PAF is estimated to be 115 m (Lewis *et al.*, 2005; Figure 5-6), which yields an average long-term vertical slip rate of 0.1 mm/yr (Figure 5-6). Applying our slip rate analysis (to account for temporal variations in slip rate and other uncertainties – see Section 5.1) and multiplying vertical rates by 123% to convert vertical rates to net rates (assuming a 60° dip and a 70° rake), yields net slip rates of: 0.02, 0.06, 0.11, 0.23, and 1.0 mm/yr, for the 3.5th, 21st, 50th, 79th, and 96.5 percentiles, respectively. These slip rates were then weighted 0.1,

Table 5-8
Footnotes to the Logic Tree for the Pajarito Fault System
(See Figure 5-8)

0.24, 0.32, 0.24, and 0.1, respectively. This distribution yields a weighted mean slip rate of 0.21 mm/yr.

[15] **Clustered Versus Random Behavior for RS-h** – A comprehensive evaluation of the paleoseismic data from numerous studies (cited in footnotes of Table 5-5) along the PFS indicates that at least two, probably three, events have occurred on the PFS since 10.9 ka (Events P3, P2, and P1 on Table 2). This is in contrast to evidence for at least 5, probably 6 or more, and possibly 9 events occurring on the PFS during the late Quaternary (Tables 5-5, 5-6 and 5-7). This suggests that large earthquakes on the PAF may be temporally clustered and that the fault is presently within a cluster. Therefore, we explicitly considered and favored this possibility in developing recurrence interval distributions for the RS-h. Furthermore, the data also suggest that an earlier cluster of two or three events may have occurred around 80 to 110 ka (Table 5-5). However, ages for events, particularly older events are large and correlating events between trenches is problematic and fraught with uncertainties. Therefore, we also consider the possibility that ruptures are occurring randomly with large variations in rates resulting in the observed patterns of occurrence merely by chance. This branch for random behavior also accounts for the possibility that the PFS is actually coming out of a temporal cluster, with events occurring occasionally between clusters, but less frequently and more randomly (Events P6(?), P5, and P4 in Table 5-5 are possible examples of such behavior).

[16] **PAF Clustered Behavior Recurrence Intervals** – See text for a general discussion of the paleoseismic record for the PFS. Our preferred recurrence interval for clustered behavior on the PAF is 4,000 years and is based on the occurrence of 3 events on the PAF between about 1.4 and 9 to 10 ka (Events P1, P2, and P3 on Table 5-5). Our maximum for this distribution of 9,000 yrs assumes only 2 events occurred and is based on the maximum estimate for the interval between these events (10.9 – 1.4 ky). Note that although the cumulative evidence strongly favors the occurrence of three separate Holocene events (P1, P2, and P3), evidence for all three as separate events is dependent on ages and correlating events between sites as evidence for all three events has not been identified at any one site. Given the uncertainties both in various event interpretations and ages (Table 5-5), it is possible that Event P2 is not a distinctly separate tectonic event (i.e., Event P2 in trenches 97-3 and 97-4 actually correlates to Event P1 in trenches 97-7, 97-7a and WETF-2c; and Event P2 in trench 98-6 actually correlates to Event P3 at trench EOC-2 and WETF-2c). Finally, our minimum recurrence interval for this clustered behavior branch is based on the minimum estimate between Events P1 and P2 (2.4 – 1.4 ka).

[17] **PAF Random Behavior Recurrence Intervals** – Regardless of the uncertainties and differences of interpretations, the paleoseismic data provide evidence for the occurrence of at least 5, probably 6 or more, possibly 9, late Quaternary surface-faulting events on the PAF (Events P9 through P1 on Table 5-

Table 5-8
Footnotes to the Logic Tree for the Pajarito Fault System
(See Figure 5-8)

5). At least two, probably three of these events occurred in the between 1.3 and 10.9 ka. Considering all the data in Table 5-5 and all of the uncertainties discussed in the text, we determined the following distribution and bases:

4,000 yrs (0.15):	Assumes three events (P3, P2, and P1) occurred between 1.4 and 9 to 10 ka, our preferred age for P3.
12,000 yrs (0.4):	Assumes nine events occurred since 110 ka (see Tables 5-6 and 5-12)
18,000 yrs (0.3):	Assumes 6 events occurred between since 110 ka (see Table 5-7 and 5-12)
45,000 yrs (0.2):	Maximum interval between events P4 and P5 (63 – 20 ka).

This results in a weighted-mean recurrence interval for the random behavior branch of 17,600 years.

Table 5-9
Rupture Scenarios and Weights for Rupture Model B of the Pajarito Fault System[1]

Rupture Scenario	Rupture Source	Initial Weights[2]	Revised Weights After Moment Balancing[3]		
			Minimum Recurrence Branch	Preferred Recurrence Branch	Maximum Recurrence Branch
RS-a	PAF	0.55	0.523	0.4440	0.470
RS-e	PAF + RC + GM + SCC + EFS/SW	0.10	0.091	0.0804	0.085
RS-f	PAF + RC + SCC	0.20	0.174	0.2679	0.325
RS-g	PAF + GM + SCC	0.15	0.212	0.2077	0.120

[1] Rupture scenarios are shown in Figures 5-9a through 5-9d. Note that scenarios which were originally only considered as part of Rupture Model A (RS-b, RS-c, and RS-d on Figures 5-9a and 5-9b) were discounted after moment balancing calculations showed that Model A resulted in unreasonably large displacements per event on the SCC segment (exceeding 4 m and 50% greater than on the PAF).

[2] Originally proportioned based on total Quaternary throw for participating segments of the rupture source.

[3] These weights, combined with the calculated segment slip rates and geometries in Table 5-14 yield the target recurrence intervals shown in Table 5-13.

Table 5-10
Weighted-Mean Maximum Magnitudes for Simultaneous Rupture Scenarios of the Pajarito Fault System

Rupture Scenario[1]	Displacement[2] (m)	Assigned Weight	Displacement-Based Magnitude[3]	Cumulative Rupture Length[4] (km)	Length-Based Magnitude	Weighted Mean Maximum Moment Magnitude[5]
RS-a[6] (PAF)	***1.5***	***0.30***	7.01	36.1	6.89	**6.94**
	2.5	***0.40***				
	5.5	***0.30***				
RS-e[7] (PAF + RC + GM + SCC +EFS/SW)	1.5	0.20	7.26	77.8	7.27	**7.27**
	2.6	0.60				
	3.7	0.20				
RS-f[8] (PAF + RC + SCC)	1.5	0.20	7.22	59.0	7.13	**7.17**
	2.3	0.60				
	3.1	0.20				
RS-g[9] (PAF + GM + SCC)	1.0	0.10	7.17	58.4	7.13	**7.15**
	1.5	0.20				
	2.0	0.40				
	3.0	0.30				
RS-h[10] (PAF + RC + GM + SCC: Partial Floating Rupture)	***1.5***	0.30	7.01	36	6.89	**6.94**
	2.5	0.40				
	5.5	0.30				

[1] PAF = Pajarito fault; RC = Rendija Canyon fault; GM = Guaje Mountain fault; SCC = Santa Clara Canyon fault; EFS/SW = southwestern section of the Embudo fault system. Geometries are shown on Figures 5-9a through 5-9d.

[2] ***Bold italics*** indicate maximum values, all others are average displacements.

[3] Weighted-mean moment magnitude calculated using empirical relations of Wells and Coppersmith (1994) as discussed in footnote 8 of Table 5-8.

[4] Cumulative rupture length is straight-line distance summed for each fault segment. For example, for RS-f (PAF + RC + SCC), the length of the PAF (36.1 km) added to the length of the RC and SCC (22.9 km) yields a cumulative length of 59.0 km (cf., the straight-line, end-to-end distance of 49.8 km for this scenario; see Figures 5-9a through 5-9d).

Table 5-10
Weighted-Mean Maximum Magnitudes for Simultaneous Rupture Scenarios of the Pajarito Fault System

[5] Weighted-mean calculated using 0.6 weight for length-based and 0.4 weight for displacement-based magnitudes. This is the preferred (weighted 0.6) maximum or characteristic magnitude assigned for the corresponding rupture scenario.

[6] We assumed displacements for RS-a similar to those used for RS-h (see Footnote 12 in Table 5-8).

[7] As data are lacking on the EFS/SW, SSC and PAF, displacements for RS-e are based on displacement data are from the Guaje Pines Cemetery site along the RC (see footnote 8) and sites along the GM (see footnote 9). In this case, all values were considered averages and weights were determined by averaging the RC and GM displacement probabilities.

[8] Displacement per event data for the RC were considered most appropriate for RS-f because of the lack of displacement data for individual events on the SCC and PAF. Displacements per event for the RC are estimated from observations at the Guaje Pines Cemetery site (Wong *et al.*, 1995). Values of 2 and 2.5 m are determined from trench logs and models of scarp degradation. A value of 1.5 m is included because eolian or overbank deposits may have thickened colluvial wedges, resulting in overestimation of displacement, which were based on colluvial wedge thickness. A maximum value of 3.1 m was considered because ruptures include not just the RC but also the PAF and SCC. We used the average displacement empirical relation in this case because the Guaje Pines site is not at the location of peak displacement for the PAF, SCC, and RC (Figure 5-6), and these estimates would likely be closer to averages than maxima.

[9] For RS-g we used displacement data for the GM due to the lack of displacement data on the PAF and SCC. Data from trenches at Chupaderos and Cabra Canyons suggest vertical displacements of 1.5 to >2 m respectively, for the youngest event on the GM (Gardner *et al.*, 2003). The penultimate event at Chupaderos Canyon resulted in about 0.5 m of vertical offset, but it appeared to be dominated by strike-slip and net slip estimates could not be constrained (Gardner *et al.*, 2003). Displacement data from terrace profiles in Rendija Canyon are permissive of 1.0 to 2.5 m of displacement per event on the GM (Wong *et al.*, 1995). Weights were based on overlap of data sets. Empirical relations for average displacement were used because Cabra, Chupaderos, and Rendija Canyons are located where post-1.2 Ma displacement for the PAF, GM, and SCC is more similar to the average than maximum displacement along all these faults (Figure 5-6).

[10] See Footnote 12 in Table 5-8 for discussion of displacements for RS-h.

Table 5-11
Weighted-Mean Maximum Magnitudes for Synchronous Rupture Scenarios of the Pajarito Fault System

Rupture Scenario (Rupture Source[1])	Displacement[2] (m)	Assigned Weight	Displacement-Based Magnitude[3]	Segment(s) of 1st Subevent	1st Subevent Cumulative Rupture Length[4] (km)	1st Subevent Length-Based Magnitude	1st Subevent Weighted Mean Maximum Magnitude[5]	Segment(s) of 2nd Subevent	2nd Subevent Cumulative Rupture Length[4] (km)	2nd Subevent Length-Based Magnitude	2nd Subevent Weighted Mean Maximum Magnitude[5]
RS-e (PAF + RC + GM + SCC +EFS/SW)	1.5	0.20	7.26	PAF	36.1	6.89	**7.03**	RC+GM+SCC+ EFS/SW	41.7	6.96	**7.08**
	2.6	0.60									
	3.7	0.20									
RS-f (PAF + RC + SCC)	1.5	0.20	7.22	PAF	36.1	6.89	**7.02**	RC+SCC	22.9	6.66	**6.88**
	2.3	0.60									
	3.1	0.20									
RS-g (PAF + GM + SCC)	1.0	0.10	7.17	PAF	36.1	6.89	**7.00**	GM+SCC	15.7	6.47	**6.75**
	1.5	0.20									
	2.0	0.40									
	3.0	0.30									
RS-h (PAF + RC + GM + SCC: Partial Floating Rupture)	***1.5***	0.30	7.01	Northern PFS[6]	26.8[7]	6.74	**6.85**	RC	9.2[7]	6.20	**6.52**
	2.5	0.40									
	5.5	0.30									

1 PAF = Pajarito fault; RC = Rendija Canyon fault; GM = Guaje Mountain fault; SCC = Santa Clara Canyon fault; EFS/SW = southwestern section of the Embudo fault system. Geometries are shown on Figures 5-9c through 5-9d.

2 Values in ***Bold italics*** indicate maximum displacements, all others are average displacements.

3 Weighted-mean moment magnitude calculated using empirical relations of Wells and Coppersmith (1994) as discussed in footnote 10 of Table 5-4.

4 Cumulative rupture length is straight-line distance summed for each fault segment, irregardless of gaps or overlaps.

5 Weighted-mean calculated using 0.6 weight for length-based and 0.4 weight for displacement-based magnitudes. Weighted mean values (in **bold**) are preferred (weighted 0.6) with ± 0.3 values weighted 0.2.

6 Synchronous rupture for this floating scenario only occurs at northern end of PFS, from the intersection of fault traces E and F on Figure 5-3 to the northern end of the SCC.

7 Length for 1st subevent determined by subtracting length of 2nd subevent (assumed to be same as RC length, 9.2 km) from total length of 36 km assumed for RS-h simultaneous type of rupture.

Table 5-12
Recurrence Intervals Based on Poisson Earthquake Recurrence Rates (λ) Using a Normalized Maximum-Likelihood Approach[1]

Case	n (number of events observed)	t (time in thousands of years)	Recurrence Interval $^1/\lambda$ (in thousands of years)		
			5th Percentile	50th Percentile	95th Percentile
1	6	110	9	18	34
2	9	110	7	12	20
3	3	10	1.3	3.3	7.4
4	2	10	1.6	5.0	12.3
5	3	110	14	37	81
6	4	110	12	28	56
7	3	300	39	100	220
8	2	60	10	30	74
9	1	110	23	110	311
10	2	300	48	150	368

[1] λ is the Poisson rate (events/year) determined from the observation of n events in t years; the percentiles for each case are from a normalized maximum-likelihood function of λ.

Table 5-13
Target Recurrence Intervals for Rupture Scenarios Used in Rupture Model B of the Pajarito Fault System

Rupture Scenario	Rupture Source	Target Recurrence Interval (years)	Assigned Weight	Weighted-Mean Recurrence (years)
RS-a [1]	PAF	4,000 (min) 20,000 (pref) 56,000 (max)	0.2 0.6 0.2	24,000
RS-e [2]	PAF + RC + GM + SCC + EFS/SW	23,000 (min) 110,000 (pref) 311,000 (max)	0.2 0.6 0.2	133,000
RS-f [3]	PAF + RC + SCC	12,000 (min) 33,000 (pref) 81,000 (max)	0.2 0.6 0.2	38,400
RS-g [4]	PAF + GM + SCC	10,000 (min) 42,000 (pref) 220,000 (max)	0.2 0.6 0.2	71,200

[1] Target recurrence intervals for RS-a are based on paleoseismic data compiled in Table 5-5 and appropriate rate estimates in Table 5-12. The paleoseismic data suggest that at least two (Table 5-7), probably four (Table 5-5), or more events occurred on the PAF independently since 110 ka. Indeed, if all events on the RC and GM occurred separately from events on the PAF, perhaps as triggered slip from events on the PAF, as many as 9 events may have occurred on the PAF independently since 110 ka (case 2 in Table 5-12). We considered these possibilities, as well as 2 or 3 independent PAF ruptures in the Holocene (cases 3 and 4 in Table 5-12), in developing our distribution for RS-a. Thus, our preferred target recurrence interval of 20,000 years is based on an average of 50th percentile values for cases 2 and 6 (Table 5-12). Our minimum value of 4,000 years is based on an average of 50th percentile values for cases 3 and 4 (Table 5-12). Our maximum values of 56,000 years is based on the 95th percentile for case 6 (Table 5-12), which is also generally consistent with only 2 events in 110 years.

[2] Although definitive evidence for late Quaternary rupture of the EFS/SW with the PFS is lacking, this scenario (RS-e) cannot be precluded given the evidence for 10 to 13 m of vertical offset since 760 ka on the EFS/SW (Koning, 2005), which is along strike and nearly continuous with the northeastern end of the PFS. The timing of events on the SCC and EFS/SW are unknown, but based on the available paleoseismic data (Table 5-5), there are two events that could have ruptured the entire PFS, events P4 and P10. Therefore, our recurrence interval distribution for scenario RS-e is based on assuming 1 or 2 events occurred since 110 or 300 ka, respectively (cases 9 and 10 in Table 5-12), and favoring the former (1 event since 110 ka).

[3] As data on the timing of events on the SCC are lacking, we assumed recurrence intervals applicable to rupture of the PAF and RC for this scenario (RS-f). These recurrence intervals are based on data compiled in Table 5-5 and estimates of Poisson rate parameter for cases 5 and 6 in Table 5-12. Our preferred value of 33,000 years is based on 3 or 4 events occurring since 110 ka, and averaging 50th percentiles for cases 5 and 6 (Table 5-12). Our minimum for RS-f of 12,000 years is based on the 5th percentile of case 6, whereas our maximum is based on the 95th percentile for case 5.

[4] As data on the timing of events on the SCC are lacking, we assumed recurrence intervals applicable to rupture of the PAF and GM for this scenario (RS-g). These recurrence intervals are based on data compiled in Table 5-5 and estimates of Poisson rate parameter for cases 7 through 9 in Table 5-12, favoring the occurrence of 2 events since 60 ka. Thus, our preferred interval of 42,000 years is based on a weighted average of 50th percentiles for case 8 (weighted 0.85) and case 9 (weighted 0.15). The minimum of 10,000 years for RS-g is based on the 5th percentile for case 8 in Table 5-12, whereas the maximum of 220,000 years is based on the 95th percentile for case 7.

Table 5-14
PFS Parameters Used in Moment Balancing of Rupture Model B and Resulting Balanced Slip Rates[1]

Segment	Segment Length (km)	Downdip Width[2] (km)	Long-term (since 1.22 Ma) Segment Slip Rate (mm/yr)[3]	Calculated Segment Slip Rates (mm/yr) Needed to Yield Target Recurrence Intervals[4]		
				Minimum Recurrence Branch[5]	Preferred Recurrence Branch[6]	Maximum Recurrence Branch[7]
PAF	36.1	17.3	0.12	1.014	0.2532	0.0840
RC	9.2	15.2	0.023	0.1944	0.04853	0.0161
GM	8.6	15.2	0.013	0.1099	0.02743	0.0091
SCC	12.3	17.3	0.040	0.3380	0.0844	0.0280
EFS/SW	13.7	17.3	0.00041[8]	0.00346	0.000865	0.000287

[1] The fault segment parameters shown here, combined with the revised rupture scenario weights in Table 5-9, and the maximum magnitudes in Table 5-10, yield the target recurrence intervals in Table 5-13 (within 2%).

[2] Assuming a dip of 60° for PAF, SCC, and EFS/SW; and a dip of 80° for RC and GM.

[3] Based on the throw measured on the top of the Tshirege member of the Bandelier Tuff as shown in Figure 5-6.

[4] Target recurrence intervals for rupture scenarios used in Rupture Model B are shown in Table 5-13.

[5] Long-term segment rates were scaled by a factor of x 8.45 to yield minimum target recurrence intervals.

[6] Long-term segment rates were scaled by a factor of x 2.11 to yield preferred target recurrence intervals.

[7] Long-term segment rates were scaled by a factor of x 0.70 to yield maximum target recurrence intervals.

[8] As the EFS/SW is expected to rupture separately and independently from the PFS most of the time (99%), the rate used here is only 1% of the total rate of 0.041 mm/yr (see footnote 14 in Table 5-1 for basis of EFS slip rate).

Table 5-15
Maximum Magnitudes of Background Seismicity and Seismogenic Crustal Thicknesses

Seismotectonic Province	Maximum Magnitude (M)	Seismogenic Crustal Thickness (km)
RGR	6½ ± ¼	12 to 18
Colorado Plateau	6½ ± ¼	12 to 18
Southern Great Plains	6½ ± ¼	12 to 18
SSA	6½ ± ¼	12 to 18

In this section, we describe the ground motion attenuation relationships used in the PSHA, including selected empirical relationships and site-specific stochastic relationships developed as part of this study. The evaluation of kappa and topographic effects are also described.

6.1 SELECTION OF EMPIRICAL ATTENUATION RELATIONSHIPS

A combination of both empirical and site-specific attenuation relationships were used in the PSHA as was done in the 1995 study. At the time the PSHA calculations were initiated in this study, only two empirical relationships were available and appropriate for extensional tectonic regimes, e.g., the RGR and Basin and Range Province, and deep soil site conditions (see following discussion): Spudich *et al.* (1999) and Abrahamson and Silva (1997) modified for normal faulting by Norm Abrahamson as part of the Yucca Mountain Project (N. Abrahamson, written communication, 1998). In the planning of this project, the intention was to use the NGA relationships being developed in a project supported by the PEER Center. However, these models had not been officially released at the time of our PSHA calculations. Hence we were constrained to using available published relationships. The bases for selecting these relationships is described in Table 6-1. In addition to the two relationships appropriate for extensional regimes, three other western U.S. (WUS) relationships appropriate for tectonically active regions but not necessarily extensional regimes were used to include a measure of epistemic variability. These were the state-of-the-practice relationships of Boore *et al.* (1997), Sadigh *et al.* (1997), and Campbell and Bozorgnia (2003). Agreed-upon weights were assigned to the five relationships by Norm Abrahamson, Walter Silva, and Ivan Wong. The weights and their basis are described in Table 6-1. The attenuation relationships for peak horizontal ground acceleration (PGA unless specified otherwise as in vertical PGA) and 1.0 sec horizontal spectral acceleration (SA) are shown in Figures 6-1 and 6-2 for **M** 7.0, approximately the controlling earthquake at all structural frequencies and exceedance levels (Section 7.1.2).

A deep firm soil was assumed for the empirical attenuation relationships because this site condition was adopted for LANL in the 1995 study based on comparisons of the site-specific V_S profiles and generic WUS deep firm soil profiles (Wong *et al.*, 1995). However, unlike the 1995 study, the hazard results using the generic WUS soil site condition were adjusted for LANL site-specific conditions using Approach 3 (Section 8). Note that the extensional attenuation relationship of Pankow and Pechmann (2004) was not considered in this current study because it was only for a rock site condition. A value of 280 m/sec appropriate for deep firm WUS soil was used for V_S30 (average shear-wave velocity in the top 30 m) in applying the relationships of Boore *et al.* (1997).

In applying the attenuation relationships of Sadigh *et al.* (1997), the faulting type was assumed to be strike-slip; their relationships have no specific coefficients for normal faulting. Similarly, Campbell and Bozorgnia (2003) suggest that the coefficients in their ground-motion relations for strike-slip faulting also be used for cases of normal faulting. A value of 2 km was used in their relationships for the depth to basement based on an estimate of this parameter in the LANL region.

Because it was judged by Walter Silva, Norm Abrahamson, and Ivan Wong that there was insufficient epistemic variability provided by the five sets of empirical attenuation relationships, it was decided to scale all the relationships to obtain a total sigma (ln) of 0.4 for the empirical

models. Low epistemic uncertainty in current empirical attenuation relationships has been recognized by others, e.g., Ken Campbell (ABS Consulting, personal communication, 2006). For each empirical relationship we used (1) the median relationship, (2) the median multiplied by a scaling factor, and (3) the median divided by a scaling factor, resulting in a total of 15 relationships (3 x 5). A sigma (ln) of 0.4 was based on the Yucca Mountain ground motion experts' judgment of the epistemic variability within a distance of 10 km (Figure 6-3; CRWMS M&O, 1998). Although the uncertainty from the Yucca Mountain experts is distance-dependent, an average sigma (ln) value of 0.4 appears appropriate at distances less than 5 to 10 km where the hazard at LANL is being controlled by the Pajarito fault (Section 7.1; Figure 6-3).

To compute the scaling factors, PGAs, 0.2 sec, and 1.0 sec SAs were calculated using the empirical attenuation relationships for a **M** 6.6 normal-faulting earthquake at a rupture distance of 7.6 km and a soil V_S30 of 280 m/sec. The models were weighted as shown in Table 6-1. The unscaled median values were weighted 0.6, and the two corresponding scaled values were weighted 0.2 each. The sigma (ln) of the 15 values was then calculated. Figure 6-4 shows the results of varying scale factors and the resulting sigma. The scale factor of 1.88 for a sigma (ln) of 0.4 was then selected. Thus, the PSHA calculations used the median attenuation relationships, weighted 0.6, the models scaled up by 1.88, weighted 0.2, and the models divided by 1.88, scaled 0.2. The scaled relationships are also shown on Figures 6-1 and 6-2.

6.2 SELECTION OF KAPPA

The subsurface geology beneath a site influences ground motions in two competing ways. A positive velocity gradient (velocity increasing with depth) amplifies motions, whereas material damping reduces motions. In the stochastic ground motion model, the near-surface (top 1 to 2 km) damping is parameterized by κ (Anderson and Hough, 1984) and the amplification is modeled by propagation through a site-specific velocity profile. Because κ is such a critical factor affecting high frequency ($\geq$ 5 Hz) ground motions, it was evaluated in 1995 by analyzing several earthquakes recorded at LANL (Wong *et al.*, 1995).

In the 1995 study, seven small earthquakes (including two possible explosions) were well enough recorded at three 3-component stations of the LANL Seismographic Network to be analyzed (see Appendix D). Magnitudes (M_D coda duration) ranged from about 0.0 to 1.5, and epicentral distances from about 2 to 81 km. Two of the events, on 26 October and 27 October 1989, may have been local explosions but were included because of the small amount of useable data. Seismographic stations ATE, PLS, and PFM (Figure 6-5) were selected on the basis of similarity of subsurface site conditions to those at LANL, i.e., located on Bandelier tuff. The stations were equipped with Mark Products L4-C and L4-3D seismometers with 1-Hz nominal frequency, low-pass filtered at 30 Hz. In this study, an attempt was made to evaluate any recorded earthquakes since the completion of the 1995 study. However, only two additional events were recorded at any of the three stations: an earthquake of M_D 2.5 on 19 March 1998 and one of M_D 2.0 on 31 August 2000. For all the seismic events (Table 6-2), the velocity recordings were corrected for gain and instrument response and differentiated to produce acceleration time histories.

Because any one seismic event was recorded at only a few sites (generally two, Table 6-2) and there was considerable uncertainty in the computed distances and depths as well as in the

measured amplitudes (because of uncertainty in the reliability of instrumental calibrations), full inversions (Silva *et al.*, 1996) to estimate kappa and stress drop were not successful.

Kappa estimates were based on comparison of Fourier amplitude spectra between the point-source model predictions for **M** 1.0 and 2.0 at a range of distances with a stress parameter of 60 bars (Figures D-1 to D-4) and recorded motions (Figure D-5 to D-22). For these kappa estimates, the general slopes are compared, particularly the overall slopes between about 5-10 Hz and 25 Hz. Based on these visual comparisons, the most consistent kappa value is quite high, near 0.08 sec.

However, because these events are so small, their source corner frequencies are very high ($\geq$ 20 to 30 Hz), resulting in an ambiguity in kappa estimates. If the Fourier amplitude spectra at high frequency ($\approx$ 5 to 20 Hz) are not corrected for the source corner-frequency being beyond the bandwidth over which the spectral slope (kappa) is estimated, the resulting kappa values have an average of about 0.035 sec (corrected for path Q) (Wong *et al.*, 1995), close to the WUS average of 0.04 sec (Silva and Darragh, 1995). This approach is equivalent to assuming an anomalously low stress drop (< 1 bar). Assuming a stress drop of 60 bars and correcting the Fourier amplitude spectra results in a significantly larger kappa estimate of about 0.08 sec (Appendix D). Ideally, the resulting ambiguity in kappa, 0.035 sec versus 0.08 sec, should be treated as epistemic variability, with hazard computed for both kappa values, weights applied, and then the weighted hazard computed. As a practical matter, doubling all analyses was not considered a viable option and the conservative value of 0.035 sec was adopted after consultation with the Steering Committee. This value was used to constrain the total low-strain kappa at each site. The total kappa value of 0.035 sec is set by summing the low-strain damping for each base case profile (converted to kappa) and then adding the remainder to the control motion source spectra. In other words, the total kappa value for each site was set at 0.035 sec, which included the low-strain damping from the assigned damping curves (Section 4.5).

6.3 SITE-SPECIFIC STOCHASTIC ATTENUATION RELATIONSHIPS

To compensate for the lack of region-specific attenuation relationships, the well-known stochastic ground motion modeling approach (Silva *et al.*, 1996; Atkinson and Boore, 1995; Frankel *et al.*, 1996) was used, as it was in 1995 (Wong *et al.*, 1995), to develop such relationships for LANL. The point-source version of the stochastic methodology (Silva *et al.*, 1996) was used to model earthquakes of **M** 4.5, 5.5, 6.5, 7.5, and 8.5 in the distance range of 1 to 400 km (Table 6-3). Relationships were developed for CMRR, TA-3, TA-16, and TA-55 (SHB-1 borehole). A rock relationship for dacite beneath LANL was also developed.

To accommodate finite-source effects at large magnitude, model simulations included an empirical magnitude-dependent short-period saturation as well as a magnitude-dependent, far-field fall-off (Silva *et al.*, 1996). These effects are accommodated by adding a magnitude-dependent term to the source depth as well as a magnitude-dependent geometrical attenuation. Coefficients for the two models are based on the Abrahamson and Silva (1997) empirical attenuation relationship for WUS (Silva *et al.*, 1996). Both the magnitude saturation and magnitude-dependent far-field fall-off are similar to the empirical trends exhibited in the Abrahamson and Silva (1997) attenuation relationship.

Aleatory variabilities in stress drop, magnitude-dependent point-source depths, the crustal attenuation parameters Q_o and η, and kappa were included in the computations of the attenuation relationships through parametric variations (Table 6-3). Site-specific profiles (velocities and depths to dacite; Section 4.3) as well as modulus reduction and hysteretic damping curves (Section 4.5) were also randomly varied (Table 6-4). Velocity variation used a generic soil correlation model appropriate for spatial variations over hundreds of feet (Silva *et al.*, 1996). Depth to dacite was site-specific and varied uniformly ± 150 ft about mean depths. Modulus reduction and damping curves were varied assuming lognormal distributions with a $\sigma_{ln} = 0.15$ and 0.30 at cyclic shear-strains of about 3 x 10^{-2}% for G/Gmax and hysteretic damping, respectively. Magnitude-dependent point-source depths were adopted from Wong *et al.* (2004) (Table 6-3). A median kappa of 0.035 sec as previously described was assumed.

A review of crustal attenuation (Q(f)) studies in the intermountain U.S. was performed (Table 6-5) and revealed no new information was available for northern New Mexico. Thus the Q_o of 370 and η of 0.35 used in 1995 were assumed to be still valid (Table 6-3). Ranges of magnitude-dependent stress drops appropriate for extensional regimes were used (Table 6-3). These ranges have been estimated from the studies of Silva *et al.* (1996) and subsequent studies carried out as part of the Yucca Mountain Project (Becker and Abrahamson, 1997). An S-wave crustal velocity model used by LANL in locating earthquakes in northern New Mexico was used in the calculations (Table 6-3). The site-specific profiles (Section 4.3) were placed on top of the regional crustal models (e.g., Figure 6-6).

Variability (aleatory) in the regression of the simulated data is added to the modeling variability (Silva *et al.*, 1996) to produce 16th, 50th (median), and 84th percentile attenuation relationships. A total of 30 simulations was made for each magnitude and distance (total of 4050 analyses), and the results fitted with a functional form that accommodates magnitude-dependent saturation as well as far-field fall-off. The functional form is:

$$\text{Ln } Y = C_1 + C_2 \bullet \mathbf{M} + (C_6 + C_7 \bullet \mathbf{M}) \bullet \text{Ln}[R + \exp(C_4)] + C_{10} (\mathbf{M}\text{-}6)^2,$$

where Y is the median (average horizontal component) ground motion parameters, R is rupture distance, and C_1 through C_{10} are coefficients fit to the data. The total aleatory variability (vector sum of the parametric and modeling variability) is also listed in Table 6-3.

The stochastic relationships for PGA and 1.0 sec SA and **M** 7.0 at CMRR, TA-3, TA-16, TA-55, and dacite are shown in Figures 6-7 to 6-16. The site epistemic variability for CMRR was treated as follows (Table 6-4):

M1P1 = Profile A, unadjusted dynamic curves

M1P2 = Profile B, unadjusted dynamic curves

M2P1 = Profile A, adjusted dynamic curves

M2P2 = Profile, B, adjusted dynamic curves

Thus for three values of stress drops, there are a total of 12 attenuation relations for CMRR.

The range in median stress drops (low, preferred, high) with a factor of two about the median (Table 6-3) combined with the recommended weights results in a σ_{ln} of 0.49 for stress drop epistemic variability. Combined with stress drop aleatory variability (sigma [ln] = 0.5) results in a total variability of sigma (ln) of 0.7. This is the generally accepted value for the central and eastern U.S. (CEUS), a region of sparse data. The WUS total variability is about sigma (ln) = 0.5 combining shallow and deep ruptures, or about sigma (ln) of 0.4 for each if shallow and deep ruptures are separated. Because the database for normal faulting mechanisms is quite sparse, especially in the WUS, the CEUS total variability was considered appropriate. This additional epistemic variability for WUS was also accommodated in the empirical relations.

Figure 6-17 shows the PGA stochastic attenuation relationships for CMRR and M1P1 site epistemic as a function of magnitude. Figure 6-18 shows the effect of stress drop for **M** 6.5 at CMRR and M1P1. As expected, the effect is significant with a factor of two in stress drop resulting in a 50% difference in PGA. Similarly, Figure 6-19 shows the effect on PGA at CMRR from the four combinations of velocity profiles and dynamic material curves (Table 6-4). As can be seen, the differences are small.

Acceleration response spectra for **M** 4.5 to 8.5 at CMRR at an epicentral distance of 3 km derived from the stochastic relationships are shown in Figure 6-20 for M1P1. The spectra reflect a range in magnitude at close distance and display fundamental and higher mode column resonances. The fundamental mode shifts to lower frequency as loading level increases. Higher modes (e.g., near 10 Hz) become suppressed at very high strains (0.5 g) due to the softening primarily of the Qbt3L low velocity zone (Figure 6-20).

Figure 6-21 shows the parametric, modeling, and total sigmas for the CMRR stochastic attenuation relationships for M1P1. Modeling sigma is based on the modeling misfit at over 500 sites for about 19 earthquakes recorded in tectonically active areas (Silva *et al.*, 1996). Parametric sigma includes site dynamic material properties (shear-wave velocity, layer thickness, depth to basement material, modulus reduction and hysteretic damping curves) as well as source and path properties listed in Table 6-3.

For TA-3, TA-16, and TA-55 there were nine attenuation relationships derived from three stress drops, one velocity profile (P1), and three sets of dynamic material properties (M1 to M3) (Table 6-4). The third set of dynamic curves (M3) are the LANL curves used in the 1995 study (Section 4.5). There are six attenuation relationships for dacite derived from one profile, two sets of dynamic curves, and three stress drops (Table 6-4). The coefficients for all the site-specific attenuation relationships are listed in Appendix E.

6.4 EVALUATION OF TOPOGRAPHIC EFFECTS

In the 1995 study, attention was focused on potential topographic effects on ground motions due to the location of LANL facilities at the top of mesas (Wong *et al.*, 1995). In general, the results of the 2D topographic modeling performed in the 1995 study suggest that stable features of topographic amplification (5%-damped horizontal response spectra) are likely to occur at LANL. For mesa-top sites, amplifications of 10 to 20% over the frequency range studied (1 to 5 Hz) were suggested. At canyon sites, the amplifications in Fourier amplitude spectra were found to depend on distance from the base of the mesa, being either minimal amplification or

deamplification at large distances from the base (≥ one base width) and adjacent sites and 5 to 10% for sites in between. These results were generated for a material damping of 1.25%. At high levels of motion, the damping will increase significantly, which should result in a reduction of amplification.

In the 1995 study, the average slope angle across the sites was estimated at 35° (Wong *et al.*, 1995). This estimate, based on recent more detailed review of topographic maps, is too large by nearly a factor of two. Slope angles across the three mesa (TA-3, TA-16, and TA-55) sites average about 17° (Table 6-6) with shape ratios near about 0.3. As a result, because topographic effects increase with slope angle and are minor for ridges with slope angles less than about 20° (Bouchon, 1973), the 1995 SH wave analyses likely showed too large of an effect on ground motions.

To better quantify these topographic effects, it was recommended that further analytical as well as empirical studies be performed (Wong *et al.*, 1995). Analyses should consider ranges in mesa structure, velocities, damping values, and additional wave types (P-SV).

In a study performed for CMRR by Silva (2005), the results of the SH-wave 2D topographic modeling suggest that, in general, large and stable features of topographic amplification are not likely to occur at the proposed location of the CMRR facility (average slope angle = 17°, Table 6-6). For mesa-top sites, maximum amplification of about 10% over the frequency range studied (0.9 to 15.0 Hz) is suggested by the SH-wave analyses (Silva, 2005). Including incident inclined SV-waves, other studies have suggested 15 to 20% increase in amplification over SH-waves (Paolucci, 2002) resulting in an expected average amplification of about 10 to 20%. At canyon sites, the maximum amplification is even less. These results are for a material damping of about 1.2%.

These modeling studies are consistent with both observations and other simulations that show an increase in topographic amplification as slope angle increases (Ashford and Sitar, 1997; Pedersen *et al.*, 1994; Geli *et al.*, 1988; Bouchon, 1973) and relatively small horizontal amplification for gentle slopes (slope angle less than about 25°).

For vertical motions, a site-specific 2D SASSI study for a CMRR layered profile performed by Costantino and Houston (2005) as well as other 2D modeling results (Ashford and Sitar, 1997) for incident inclined SV-waves suggest potentially significant topographic scattering with ratios of vertical ridge motions to horizontal free-field motions of about 0.5 over the frequency range of 5-10 Hz, even for gentle slopes. While these analyses and the previous SH-wave analyses (Silva, 2005; Wong *et al.*, 1995) have not benefited from actual validations with recorded motions to assess potential model bias and were limited by a small number of deterministic analyses (e.g., constant two-dimensional mesa structures), the results as well as observations (Paolucci, 2002; Geli *et al.*, 1988) suggest consideration of modest amplifications for horizontal components with increased amplification for vertical components. Based on (1) the LANL modeling results, (2) other modeling results and observations in the literature, and (3) Eurocode 8 (EC8, 2000) recommendations, a suite of topographic amplification factors was developed for LANL. Following EC8 as well as the French Seismic Code (AFPS, 1995), the factors are based on slope angles (Table 6-6). To accommodate a fully probabilistic hazard analysis, both median estimates and standard deviations were developed, based on ranges of factors in modeling results and

observations. This variability is likely epistemic, but is herein treated as aleatory variability using the analytical (approximate) hazard analysis approach of Bazzuro and Cornell (2004). For deterministic analyses, the mean topographic amplification factors are recommended. The mean horizontal factors are similar to those in EC8[1] with the vertical factors exceeding the horizontal by about 20%. To illustrate the effect of variability: for a slope angle of 17°, the horizontal median factor is 1; if one then considers a (log, log) slope in the hazard curve of 3 (reasonable average value), the effect of variability (σ_{ln} = 0.3) is to increase the horizontal factor to about 1.15 with a corresponding vertical factor of about 1.25.

Table 6-1
Attenuation Relationships

Wt.	Source and Description of Relationship
0.45	Abrahamson and Silva (1997) Possibly the most widely used relationship in practice. Modified for normal faulting as part of the ground motion expert elicitation process for the Yucca Mountain Project (N. Abrahamson, written communication, 1998). The only relationship that explicitly accommodates both hanging wall effects and nonlinear soil response. Unmodified version was used in 2002 USGS National Hazard Maps.
0.35	Spudich *et al.* (1999) Next highest weight for the only relationship previously developed for extensional faulting albeit the strong motion dataset is limited. Drawbacks are the same magnitude-scaling at all source distances as well as linear soil response. Relationship also used in 2002 USGS National Hazard Maps. (No 20 Hz value.)
0.10	Campbell and Bozorgnia (2003) Three California-based relations are included to incorporate a degree of epistemic variability into the hazard analysis. Although a "limited update" of Campbell (1997), the relationship is preferred over the next two relationships because the issue of normal versus strike-slip faulting was analyzed. Relationship also used in 2002 USGS National Hazard Maps.
0.05 each	Sadigh *et al.* (1997) and Boore *et al.* (1997) Two of the most widely-used and accepted pre-NGA attenuation relationships. Boore *et al.* (1997) did not consider normal faulting and use the same magnitude scaling at all source distances as well as linear soil response. (No 20 Hz value in Boore *et al.*, 1997.) Sadigh *et al.* (1997) combined the small amount of normal-faulting strong motion data with strike-slip data. Strike-slip strong motion data from both compressional and extensional regimes are used in both relations. Both relationships were used in 2002 USGS National Hazard Maps.

[1] Note: Both the Eurocode and French Seismic Codes treat only horizontal components explicitly.

Table 6-2
Seismic Recordings Used for Kappa Estimates

Event Date	Moment Magnitude (M)	Focal Depth (km)	Station	Epicentral Distance (km)
26 October 1989	0.0	0.0	PFM	3.6
			PLS	6.5
27 October 1989	0.5	0.0	PFM	2.1
			PSL	5.3
27 April 1990	0.9	10.0	ATE	78.4
			PFM	80.7
24 May 1990	1.2	10.0	ATE	8.0
			PFM	8.7
5 July 1990	1.5	14.9	ATE	11.4
			PFM	16.2
3 September 1990	1.0	13.7	ATE	12.3
			PFM	14.1
			PLS	13.8
13 September 1990	1.4	10.0	ATE	44.5
			PFM	48.4
19 March 1998	2.5	10.0	PFM	60.1
			PLS	62.6
31 August 2000	2.0	9.8	PFM	74.8
			PLS	71.6

Table 6-3
Source and Path Input Parameters and Standard Errors Used in the Development of Stochastic Attenuation Relationships

Parameter	Values			Standard Errors σ_{ln}
Magnitude (**M**)	4.5, 5.5, 6.5, 7.5, 8.5			
Distance (km)	1, 5, 10, 20, 50, 75, 100, 200, 400			—
Magnitude-Dependent Point-Source Depth (km)[1]				
M 4.5	7.5 (4, 12)[2]			
M 5.5	7.5 (4, 12)[2]			0.6
M 6.5	7.5 (5, 10)[2]			
M 7.5	7.5 (5, 10)[2]			
M 8.5	7.5 (5, 10)[2]			
Magnitude-Dependent Stress Drop (bars)[1]	Low	Preferred	High	
M 4.5	30	60[4]	120	
M 5.5	30	60	120	0.5
M 6.5	22	45	90	
M 7.5	18	36	72	
M 8.5	14	27	54	
Crustal Attenuation[1]				
Q_0	370			0.4
η	0.35			—
Kappa (sec)[1]	0.035			0.3
Crustal Model (shallow)	Site-Specific			—
Crustal Model[3] (deep)	1.615 km/sec (1-2 km thick) 3.46 km/sec (17 km thick)			—

[1] Parameters randomly varied where σ_{ln} is based on observations
[2] Upper- and lower-bound values
[3] From LANL seismic network
[4] Median preferred stress drop (**M** 5.5 to **M** 7.5) is 46 bars. Stress drops were weighted 0.2, 0.6, and 0.2, respectively.

Table 6-4
Site-Specific Profiles and Dynamic Material Properties

CMRR	Weight
Profile A, Unadjusted Curves	0.25
Profile B, Unadjusted Curves	0.25
Profile A, Adjusted Curves	0.25
Profile B, Adjusted Curves	0.25
TA-03, TA-16, TA-55 (SHB-1)	
Profile, Unadjusted Curves	0.33
Profile, Adjusted Curves	0.34
Profile, Stokoe 94 Curves	0.33
Dacite	
Profile, Unadjusted Curves	0.5
Profile, Adjusted Curves	0.5

Table 6-5
Summary of Q(f) in the Rio Grande Rift and Basin and Range

Q_0	η	Source	Region
370	0.35	Singh and Herrmann (1983)	RGR, New Mexico; measured at Albuquerque station
400	0.20	Singh and Herrmann (1983)	Salt Lake City, Utah
235 ± 11	0.56 ± 0.04	Benz *et al.* (1997)	Basin and Range Province (Nevada and western Utah)
200	0.68	Erickson *et al.* (2004)	Basin and Range Province (Nevada and western Utah)
160	0.75	Jeon and Herrmann (2004)	Utah
354	0.51	McNamara *et al.* (2004)	Colorado Plateau (eastern Utah, western Colorado), and western Wyoming

Table 6-6
Topographic Factors for 5% Damped Response Spectra

Slope Angle	Horizontal			Vertical		
	Mean	Median	σ_{ln}	Mean	Median	σ_{ln}
i > 30°	1.4	1.2	0.5	1.8	1.4	0.5
25° < i < 30°	1.2	1.1	0.4	1.4	1.2	0.4
15° < i < 25°	1.1	1.0	0.3	1.2	1.1	0.3
i < 15° (h < 30 m)°	1.0	1.0	0.0	1.0	1.0	0.0

	Slope Angle (deg)	Shape Ratio
CMRR/TA-55	17	0.3
TA-03	17	0.3

Probabilistic seismic hazard was calculated for CMRR, TA-3, TA-16, and TA-55. The hazard was also calculated at CMRR for a reference rock datum (dacite). Site-specific stochastic and empirical western U.S. soil attenuation relationships were used (Sections 6.1 and 6.3) and the hazard was calculated separately for each type of relationship. The sets of adjusted empirical (Section 8.2) and site-specific stochastic attenuation relationships were then weighted equally in the PSHA to arrive at the final mean hazard (Section 8.4). Hence in this section, it should be noted that the discussion of the deaggregated hazard and sensitivities is not for the final hazard. Differences in the hazard composition, however, are unlikely between the hazard using the unadjusted empirical and stochastic attenuation relationships and the final combined and weighted hazard (Section 8.4).

The equal weights between the adjusted empirical and stochastic attenuation relationships were agreed upon by Walt Silva, Norm Abrahamson, and Ivan Wong. In the 1995 study, the stochastic relationships were weighted 0.60 and the empirical models 0.40 (Wong *et al.*, 1995). The slightly higher weight was assigned to the stochastic models because they were site- and region-specific to LANL. In the 1995 study, the empirical deep soil attenuation relationships were used without adjustment. In this analysis, the empirical relationships were adjusted for site-specific conditions using amplification factors (Section 8.2.2) and so it was judged by Silva, Abrahamson, and Wong that they should receive equal weight to the site-specific stochastic relationships.

The results of the PSHA are presented in terms of ground motion as a function of APE. The average return period of a specific level of ground motion is the reciprocal of its APE. The hazard is calculated at TA-3 and TA-16 at the locations of the boreholes SHB-2 and SHB-3, respectively. We calculate the hazard at TA-55 at the same location as CMRR but use an additional site-specific attenuation relationship derived from the SHB-1 velocity profile (Section 4.2).

The uncertainty in ground motion attenuation was included in the PSHA by using the log-normal distribution about the median values as defined by the standard deviation associated with each attenuation relationship. Three standard deviations about the median value were included in the analysis.

7.1 INITIAL HAZARD RESULTS

Figures 7-1 to 7-7 show the mean, median (50th percentile), 5th, 15th, 85th, and 95th percentile hazard curves for PGA. Similar curves for the 1.0 sec horizontal SA hazard are shown on Figures 7-8 to 7-14. For each site, separate plots show the hazard using the empirical and stochastic attenuation relationships, respectively; for TA-55 the empirical hazard results are the same as for CMRR, so plots are shown only for the stochastic results. PGA values for the return periods of 500, 1,000, 2,500, and 10,000-year return periods are listed in Table 7-1 Note that the PGAs computed from the empirical soil and site-specific stochastic attenuation relationships are generally similar (Section 7.2.3).

The fractiles in the hazard plots indicate the range of epistemic uncertainty about the mean hazard. For example, in Figure 7-1, at a return period of 10,000 years, there is a very large factor of 6 difference between the 5th and 95th percentile values at CMRR using the empirical

attenuation relationships. A factor of 4.5 difference is present in the hazard for CMRR using the stochastic attenuation relationships at 10,000 years (Figure 7-2). At 1.0 sec SA, the spread between the fractiles is even larger (e.g., Figure 7-8) due mostly to the uncertainties in the attenuation relationships at this spectral period.

At return periods longer than 100,000 years (annual exceedance probabilities smaller than 10^{-5}), the ground motions become large (Figures 7-1 to 7-14). At some level, they become physically unrealizable. This issue has been raised in the Yucca Mountain Project and the "bounding" of ground motions is being addressed by several different groups including DOE and the U.S. Nuclear Regulatory Commission. Addressing unrealistic ground motions is outside the scope of work in this study but the reader should be aware of the issue if very low annual exceedance probabilities are desired in future risk analyses.

7.1.1 Seismic Source Contributions

The contributions of the various seismic sources to the mean PGA hazard are shown on Figures 7-15 to 7-21. The PGA hazard at all sites is controlled almost totally by the PFS at all return periods. The PFS similarly controls the hazard at LANL for longer-period ground motions, e.g., 1.0 sec SA (Figures 7-22 to 7-28). Background seismicity in the RGR, which contributed to the hazard at LANL in the 1995 study (Wong *et al.*, 1995), is not a significant contributor in this analysis (Figures 7-15 to 7-28). This is probably due to the increased activity rate of the PFS. In addition, although the calculated rate of background seismicity decreased in this study compared to the 1995 study, accounting for some of the decrease, Gaussian smoothing was also used in the PSHA, whereas it was not in 1995. This may have also account for a small decrease in the hazard contribution from the RGR.

It is interesting to note that the background seismicity appears to be contributing slightly more and the PFS slightly less to the hazard when comparing the results from the stochastic versus empirical attenuation relationships (e.g., Figures 7-19 and 7-20). This may be due to the greater nonlinearity in the stochastic attenuation relationships resulting in proportionately more contribution from smaller events compared to larger events.

7.1.2 Magnitude and Distance Contributions

By deaggregating the hazard for PGA, 0.2 sec, and 1.0 sec horizontal SA from the empirical and stochastic attenuation relationships into magnitude (M) and distance (D) bins, Figures 7-29 to 7-46 illustrate the contributions at CMRR. The M and D results are nearly the same at the other sites. At a 1,000-year return period, the PGA hazard predominantly comes from earthquakes of **M** 5 to 7 at distances less than 20 km, with the greatest contribution at **M** 6.6 to 7.2 (Figures 7-29 and 7-32). As the return period increases, there is less contribution from other sources such as the La Bajada and Sawyer Canyon faults (Figures 7-15 and 7-16) and the PFS becomes more dominant (e.g., Figures 7-30 and 7-33). At 1.0 sec SA and for a 1,000-year return period, the PFS contributes the most to the hazard, but other distant faults also contribute (Figures 7-41 and 7-44). As the return period increases, the PFS becomes more dominant (e.g., Figures 7-42 and 7-45).

Table 7-2 lists the modal magnitude (M^{mode}), distance (D^{mode}), and epsilon (ε) for all the sites for PGA and 1.0 sec SA. Epsilon is the difference between the logarithm of the ground motion amplitude and the mean logarithm of ground motion (for that M and D) measured in units of the standard deviation (σ) of the logarithm of the ground motion. As expected, the controlling earthquake is generally a **M** 6.8 from the PFS at distances less than 5 km (Table 7-2).

7.2 SENSITIVITY OF THE INITIAL HAZARD RESULTS

We have evaluated the sensitivity of the probabilistic hazard at LANL to the ground motion attenuation models and to the characterization of the controlling seismic source, the PFS.

7.2.1 Sensitivity to Attenuation Relationships

Figures 7-47 to 7-50 illustrate the sensitivity of the hazard at CMRR to the choice of attenuation relationships, both empirical and stochastic; sensitivity results are shown separately for mean PGA and mean 1.0 sec horizontal SA. Each hazard curve in the plots is labeled with one of the attenuation relationships that was solely used to calculated that curve. Recall there are 15 empirical attenuation curves as a result of scaling to increase the total uncertainty (Section 6.1) and 6 to 12 stochastic attenuation curves (Section 6.3). For PGA hazard based on the unscaled empirical relationships, Figure 7-47 shows that the two extensional attenuation relationships, that is, those of Abrahamson and Silva (1997, modified, see Section 6.1) and Spudich *et al.* (1999), give the lowest hazard as expected (Figure 7-47), whereas the relationship of Boore *et al.* (1997) gives the highest hazard. For PGA based on the stochastic relationships (Figure 7-48), the single-corner, variable-low-stress-drop model gives the lowest hazard within the low-stress-drop grouping, regardless of dynamic curves or velocity profiles. The hazard increases going from the unadjusted (M1) to adjusted dynamic curves (M2) and from basecase profile A (P5) to profile B (P6) (Figure 7-48). At 1.0 sec SA (Figure 7-49), the relationship of Spudich *et al.* (1999) gives the lowest hazard, followed by those of Sadigh *et al.* (1997), Campbell and Bozorgnia (2003), Abrahamson and Silva (1997, modified), and Boore *et al.* (1997). For the stochastic relationships, the pattern for 1.0 sec SA is similar to that observed for the PGA results (Figures 7-48 and 7-50).

7.2.2 Sensitivity to PFS Characterization

The hazard at LANL is dominated by the PFS. To evaluate the sensitivity of the hazard to the selection of various source-characterization parameters, calculations were performed giving full weight to specific branches on the PFS logic tree. For a representative analysis, hazard was calculated at CMRR using the empirical attenuation relationships.

Figure 7-51 shows the impact of rupture model B or C on the hazard curve for PGA. Rupture model C gives significantly higher hazard because it allows for temporal clustering in which significant weight was assigned to shorter recurrence intervals ("in a cluster," Figure 5-8). Thus, higher hazard results from being in a cluster (shorter recurrence intervals) versus being out of a cluster (Figure 7-52). The hazard from synchronous versus simultaneous rupture (Section 5.1.1) is shown on Figure 7-53. The hazard is higher for synchronous rupture because the ground motions will be larger from seismic slip involving two subevents versus more uniform slip in a

single albeit larger simultaneous event. Interestingly, the hazard from synchronous rupture approaches that for simultaneous rupture at return periods longer than 100,000 years.

The effect of the choice of recurrence model for the PFS is illustrated on Figure 7-54. The truncated exponential model gives the highest hazard because it predicts the highest rate of moderate magnitude earthquakes (**M** 5 to 6). For a similar reason, the characteristic model, which partly includes exponential recurrence, results in the next highest hazard. The maximum magnitude model results in the lowest hazard. The hazard curves for all three recurrence models converge at very long return periods due to characteristic events dominating over moderate-sized earthquakes when the recurrence intervals of the latter are short relative to the return period, e.g., 1 million years. Finally, the effect of rupture-scenario rates of the PFS is shown on Figure 7-55 for rupture model B. Recurrence intervals and weights for branches corresponding to the minimum, preferred, and maximum rates are shown on Tables 5-13 and 5-14. As expected, the higher the rate, the greater the hazard.

7.2.3 Sensitivity to Site Location and Profile

Figures 7-56 and 7-57 compare the hazard at CMRR (and TA-55), TA-3, and TA-16, based on empirical attenuation relationships, for mean PGA and mean 1.0 sec SA. The PGA hazard is not very sensitive to site location at return periods of interest, e.g., 10,000 years (Figure 7-56). At the same return periods, the corresponding hazard curves for 1.0 sec SA (Figure 7-57), show a slight site-to-site variability. The trend from lower to slightly higher hazard going from TA-16, to CMRR/TA-55, to TA-3 is due to a decrease in average distances to rupture elements of the PFS (Figure 5-4). TA-3 has a relatively higher hazard because of its location between the PAF and RC, where ground motions from either synchronous or simultaneous rupture are predicted to be higher than at the other sites. Figures 7-58 and 7-59 compare the hazard at CMRR, TA-55, TA-3, and TA-16, based on site-specific attenuation relationships. Here the differences principally reflect the impact of the site-specific velocity profiles. The less the damping in the site profiles, the higher the hazard (Figures 7-58 and 7-59).

In Figures 7-60 to 7-65, the empirical and stochastic hazard results are compared at each site, first for mean PGA and then for mean 1.0 sec horizontal SA. In general, the PGA hazard is similar for return periods up to about 10,000 years (Figures 7-60 to 7-62). At longer return periods, the larger sigma for the stochastic attenuation relationships increases the hazard relative to the empirical relationships. At 1.0 sec SA, the larger stochastic sigma results in higher hazard than for the empirical relationships at almost all return periods (Figures 7-63 to 7-65).

7.3 ROCK HAZARD

The probabilistic hazard at CMRR was calculated for dacite. The hazard from empirical attenuation relationships was not calculated for rock but the empirical soil relationships were adjusted for dacite using transfer functions (Section 8.2.2). This approach was taken because there were no WUS empirical attenuation relationships available at the time appropriate for firm to hard rock with $V_S \sim 5300$ ft/sec. The hazard using the site-specific stochastic attenuation relationships for dacite is shown on Figure 7-66 and 7-67 for PGA and 1.0 sec SA, respectively. Figures 7-68 and 7-69 compare the hazard from the CMRR-specific dacite and tuff stochastic attenuation relationships for PGA and 1.0 sec SA, respectively. The hazard on tuff is

significantly higher than the dacite as would be expected reflecting the amplification occurring in the overlying Bandelier tuff. At a return period of 10,000 years, the PGA hazard is a factor of two higher than the dacite (Figure 7-68). The amplification at 1.0 sec horizontal SA from the tuff is even greater resulting in higher surface motions (Figure 7-69).

Table 7-1
Probabilistic Ground Motions

PGA	CMRR		TA-55		TA-3		TA-16	
RP (yrs)	Empirical	Stochastic	Empirical	Stochastic	Empirical	Stochastic	Empirical	Stochastic
500	0.16	0.14	0.16	0.14	0.16	0.15	0.16	0.15
1,000	0.28	0.27	0.28	0.23	0.29	0.25	0.28	0.25
2,500	0.52	0.52	0.52	0.41	0.54	0.45	0.51	0.45
10,000	0.94	1.00	0.94	0.81	0.98	0.93	0.92	0.91

0.2 Sec SA	CMRR		TA-55		TA-3		TA-16	
RP (yrs)	Empirical	Stochastic	Empirical	Stochastic	Empirical	Stochastic	Empirical	Stochastic
500	0.37	0.24	0.37	0.25	0.39	0.25	0.39	0.36
1,000	0.65	0.43	0.65	0.42	0.68	0.43	0.66	0.59
2,500	1.20	0.81	1.20	0.75	1.25	0.77	1.18	1.04
10,000	2.21	1.58	2.21	1.46	2.31	1.56	2.16	2.07

1.0 Sec SA	CMRR		TA-55		TA-3		TA-16	
RP (yrs)	Empirical	Stochastic	Empirical	Stochastic	Empirical	Stochastic	Empirical	Stochastic
500	0.16	0.24	0.16	0.22	0.17	0.23	0.17	0.13
1,000	0.33	0.46	0.33	0.38	0.35	0.41	0.33	0.23
2,500	0.72	0.96	0.72	0.72	0.78	0.80	0.70	0.45
10,000	1.57	2.06	1.57	1.57	1.70	1.85	1.48	1.06

RP = Return Period

Table 7-2
Controlling Earthquakes

	TA-03					
	PGA (g)			1.0 Sec SA (g)		
	1,000 yr	2,500 yr	10,000 yr	1,000 yr	2,500 yr	10,000 yr
Mmode	6.8	6.8	6.8	6.8	6.8	6.9
Dmode (km)	6.5	2.5	2.3	6.5	2.5	2.5
Epsmode	0.16	0.64	1.28	0.16	0.36	1.35

	TA-16					
	PGA (g)			1.0 Sec SA (g)		
	1,000 yr	2,500 yr	10,000 yr	1,000 yr	2,500 yr	10,000 yr
Mmode	6.8	6.7	6.8	6.8	6.8	6.9
Dmode (km)	5.5	2.5	2.5	6.0	2.5	2.5
Epsmode	0.17	0.60	1.44	0.13	0.36	1.27

	CMRR					
	PGA (g)			1.0 Sec SA (g)		
	1,000 yr	2,500 yr	10,000 yr	1,000 yr	2,500 yr	10,000 yr
Mmode	6.7	6.8	6.8	6.8	6.8	7.0
Dmode (km)	4.4	2.5	2.5	6.5	2.7	2.5
Epsmode	0.04	0.68	1.58	0.16	0.44	1.27

In calculating the probabilistic ground motions at LANL, the surface motions must be hazard consistent (i.e., the annual exceedance probability of the soil UHS should be the same as the rock UHS). In NUREG/CR-6728 (McGuire *et al.* 2001), several site response approaches are recommended to produce soil motions consistent with the rock outcrop hazard. These approaches also incorporate site-specific aleatory variabilities of soil properties into the soil motions. McGuire *et al.* (2001) identified four basic approaches for determining the UHS at a soil site. The approaches range from a PSHA using ground motion attenuation relations for the specific site (or location) of interest (Approach 4) to scaling the rock UHS on the basis of a site response analysis using a broadband input motion (Approach 1). Conceptually, Approach 4 is the ideal approach and other approaches are approximations to it. (Approaches 1 to 4 are described more fully for the reader in Section 8.1.) To compute the site-specific ground-shaking hazard at LANL, we used two different approaches, using (1) empirical attenuation relationships for WUS generic deep firm soil adjusted for site-specific conditions, and (2) site-specific attenuation relationships (Section 7). In the case of the latter, the site response is contained in the stochastic attenuation relationships, which is called Approach 4 (see below). For the empirical attenuation relationships, the computed generic soil hazard curves from the PSHA need to be adjusted for the site-specific site conditions at each of the LANL sites and the more accurate Approach 3, over the simpler Approach 2(A or B), was used.

Typically rock outcrop hazard is specified for a particular site condition, e.g., hard or soft rock, through a standard PSHA. In the WUS, where empirical attenuation relations are available, the preferred reference condition for sites founded on deep soil ($\geq$ 200 ft) is deep firm soil. WUS empirical relations are better constrained for this condition since deep soil sites reflect the majority ($\approx$ 2/3) of recordings. Converting from empirical deep soil or rock to site-specific hazard then entails the same process of transfer functions (amplification factors), but computed either for WUS generic rock or deep firm soil relative to site-specific velocity profiles. Thus in a departure from Approach 3 as described in NUREG/CR-6728 (McGuire *et al.*, 2001), the hazard in this study was computed from empirical attenuation models appropriate for deep soil, not rock, and then adjusted using amplification factors to arrive at the hazard at the top of each site-specific geologic profile. Although the initial site condition, soil rather than rock, is different, the process is the same.

8.1 APPROACHES TO DEVELOP SITE-SPECIFIC MOTIONS/HAZARD

The following is discussed to provide a framework for the rationale for our approach. In general there are four fairly distinct approaches to develop site-specific design motions or hazard.

These four approaches to this conversion process are characterized by increasing accuracy defined as preserving the desired probability in the site-specific hazard or motions (hazard-consistent) as well as accommodating site-specific aleatory and epistemic variabilities.

Approach 1: This approach is fundamentally deterministic and involves using the outcrop UHS to drive the overlying site-specific soil column(s). By definition it assumes a rock outcrop hazard (UHS) but has no mechanism to conserve the outcrop APE. For cases where the hazard is dominated by earthquakes with significantly different **M** at low and high (or intermediate) structural frequencies, the outcrop UHS may be quite broad, unlike any single earthquake, resulting in unconservative high-frequency motions (too nonlinear in site response). Even if only

a single earthquake is the major contributor at all structural frequencies, variabilities incorporated in the hazard analysis may result in a broad spectrum, again unlike any single earthquake. For these reasons, this approach is discouraged (McGuire *et al.*, 2001) and Approach 2, an alternative semi-deterministic method, may be used.

Approach 2: This approach is intended to avoid the broad-band control motion of Approach 1 and uses low-and high-frequency (and intermediate if necessary) deterministic spectra computed from the weighted attenuation relations used in the PSHA, scaled to the UHS at the appropriate frequencies (e.g., NRC Regulatory Guide 1.165). These scaled motions, computed for the modal deaggregation **M** and *D* are then used as control motions to develop multiple (typically 2 to 3) mean transfer functions based on randomized soil columns. The mean transfer functions are then enveloped with the resulting transfer function applied to the outcrop (rock or soil) UHS. This method was termed Approach 2A in NUREG/CR-6728 (McGuire *et al.*, 2001). The use of mean (rather than median) transfer functions followed by enveloping is an empirical procedure to conservatively maintain the outcrop exceedance probability (NUREG/CR-6728 and CR-6769; McGuire *et al.*, 2001; 2002). Hazard consistency is typically maintained to a mean APE of about 10^{-4} and may be slightly unconservative at high frequency and for a mean APE of 10^{-5} and below (NUREG/CR-6769; McGuire *et al.*, 2001), particularly for highly nonlinear sites.

For cases where there may be a wide magnitude range contributing to the hazard at low or high frequency and (or) the site has highly nonlinear dynamic material properties, low, medium, and high **M**, control-motion spectra may be developed at each frequency of interest. A weighted mean transfer function (e.g., with weights of 0.2, 0.6, 0.2 reflecting 5%, mean, and 95% **M** contributions, respectively) is then developed at each structural frequency of interest. Following Approach 2A, the weighted-mean transfer functions for each frequency of interest are then enveloped with the resultant applied to the outcrop UHS. This more detailed analysis procedure was termed Approach 2B. In the 1995 LANL PSHA, site-specific attenuation relationships (Approach 4) were used together with unadjusted (for LANL site conditions) empirical relationships. Comparisons detailed in McGuire *et al.* (2001) indicate that Approach 2B is adequately conservative at APEs down to 10^{-4} with respect to Approach 4.

Approach 3: This approach is a fully probabilistic analysis procedure which moves the site response, in an approximate way, into the hazard integral. The approach is described by Bazzurro and Cornell (2004) and NUREG/CR-6769 (McGuire *et al.* 2002). In this approach, the hazard at the soil surface is computed by integrating the site-specific hazard curve at the bedrock level with the probability distribution of the amplification factors (Lee *et al.*, 1998; 1999). In this study, the hazard is desired at the top of Bandelier tuff (unit Qbt) and the bedrock-level hazard is replaced with that for generic WUS deep firm soil. The soil site-specific amplification, relative to WUS deep firm soil, is characterized by a suite of frequency-dependent amplification factors that can account for nonlinearity in soil response. Approach 3 involves approximations to the hazard integration using suites of transfer functions, which result in complete hazard curves at the ground surface for specific ground motion parameters (e.g., spectral accelerations) and a range of frequencies.

The basis for Approach 3 is a modification of the standard PSHA integration:

$$P[A_S>z] = \iiint P\left[AF > \frac{z}{a} | m,r,a \right] f_{M,R|A}\ (m,r;a) f_A(a) dm dr da \qquad (8\text{-}1)$$

where A_S is the random ground-motion amplitude on soil at a certain natural frequency; z is a specific level of A_S; m is earthquake magnitude; r is distance; a is an amplitude level of the random rock ground motion, A, at the same frequency as A_S; $f_A(a)$ is derived from the rock hazard curve for this same frequency (namely it is the absolute value of its derivative) ; and $f_{M,R|A}$ is the deaggregated hazard (i.e., the joint distribution of M and R, given that the rock amplitude is level a). AF is an amplification factor defined as:

$$AF = A_S/a \qquad (8\text{-}2)$$

where AF is a random variable with a distribution that can be a function of m, r, and a. To accommodate epistemic uncertainties in site dynamic material properties, multiple suites of AF may be used and the resulting hazard curves combined with weights to properly reflect mean hazard and fractiles.

Soil response is controlled primarily by the level of rock motion and m, so Equation 8-1 can be approximated by:

$$P[A_S>z] = \iint P[AF > \frac{z}{a}(m,a) f_{M|A}(m;a) f_A(a) dm da \qquad (8\text{-}3)$$

where r is dropped because it has an insignificant effect in most applications (McGuire *et al.*, 2001). To implement Equation 8-3, only the conditional magnitude distribution for relevant amplitudes of a is needed. $f_{M|A}(m;a)$ can be represented (with successively less accuracy) by a continuous function, with three discrete values or with a single point, (e.g., $m^1(a)$, the mean magnitude given a). With the latter, Equation 8-3 can be simplified to:

$$P[A>z] = \iint P[AF > \frac{z}{a} | a, m^1(a)] f_A(a) da \qquad (8\text{-}4)$$

where, $f_{M|A}(m;a)$ has been replaced with m^1 derived from deaggregation. With this equation, one can integrate over the rock acceleration, a, to calculate $P[A_S>z]$ for a range of soil amplitudes, z.

It is important to note there are two ways to implement Approach 3. The first is the full integration method whereas the second is to simply modify the attenuation relation ground motion value during the hazard analysis with a suite of transfer functions (Cramer, 2003). Both approaches will tend to double-count site aleatory variability: once in the suite of transfer-function realizations and again in the aleatory variability about each median attenuation relation. The full integration method tends to lessen any potential impacts of the large total site aleatory variability (Bazzuro and Cornell, 2004). Approximate corrections for the large site component of aleatory variability may be made by implementing the approximate technique (below) with C = 0, AF =1, and a negative exponential, where a_{rp} = the soil amplitude and σ is the component of variability that is removed. For the typical aleatory variability of the transfer functions ($\sigma_{ln} \approx$

0.2-0.3) and the typical hazard curve slopes at LANL, the reduction in motion is about 10%. Based on a recommendation of the Steering Committee, this correction was not applied.

Approach 4: Approach 4 entails the use of site-specific attenuation relationships, which incorporate the site-response characteristics of the site. The PSHA is performed using these site-specific relationships for the specified APE. This approach is considered the most accurate as it is intended to accommodate the appropriate amounts of aleatory variability into site- and region-specific attenuation relations. Epistemic variability is appropriately captured through the use of multiple attenuation relations. Approach 3 is considered to be a fully probabilistic approximation to Approach 4.

8.1.1 Approach 3 – Full Integration Method

The soil hazard curve can be calculated using the discretized form of Equation 3 from Bazzurro and Cornell (2004):

$$G_Z(z) = \sum_{all\ x_j} P\left[Y \geq \frac{z}{x} \middle| x_j\right] p_X(x_j) = \sum_{all\ x_j} G_{Y|X}\left(\frac{z}{x} \middle| x_j\right) p_X(x_j) \tag{8-5}$$

where $G_Z(z)$ is the hazard curve for $S^s_a(f)$, that is, the annual probability of exceeding level z. On the right-hand side,

$$G_{Y|X}\left(\frac{z}{x} \middle| x\right) = \hat{\Phi}\left(\frac{ln\left[\frac{z}{x}\right] - ln\left[\hat{m}_{Y|X}(x)\right]}{\sigma_{\ln Y|X}}\right) \tag{8-6}$$

where $G_{Y|X}$ is the complementary cumulative distribution function of Y = AF(f), conditional on a rock amplitude x;

$\hat{\Phi} = 1 - \Phi$ is the widely tabulated complementary standard Gaussian cumulative distribution function;

$\hat{m}_{Y|X}$ is the conditional median of Y;

$\sigma_{\ln Y|X}$ is the conditional standard deviation of the natural logarithm of Y; and

$p_X(x_j)$ is the probability that the rock input level is equal to (in the neighborhood of) x_j.

This approach is implemented in the computer program SOILUHSI (Figure 8-1).

8.1.2 Approach 3 – Approximate Method

An alternative solution to Equation 8-4 can also be calculated using Equation (8-7) from Bazzuro and Cornell (2004). This is a closed form approximation of the integration of the amplification factor over a range of rock amplitudes.

$$z_{rp} = a_{rp}\ \overline{AF_{rp}}\ \exp(\tfrac{1}{2}\, k\, \sigma_\delta^2 / (1\text{-}C)) \qquad (8\text{-}7)$$

where z_{rp} is soil amplitude z associated with return period r_p; a_{rp} is the rock acceleration a associated with return period r_p; $\overline{AF_{rp}}$ is the geometric mean (mean log) amplification factor for the rock motions with return period r_p; k is the log-log slope of the rock hazard curve that is calculated at each point from the input rock hazard curve points; C is the log-log slope of input amplification factor that is calculated at each point from the input amplification factors, AF; and σ_δ is the log standard deviation of the AF, which is read from the input file. This approach is implemented in the computer program SOILUHS (Figure 8-1).

8.2 IMPLEMENTATION OF APPROACH 3

In Approach 3, the following steps are taken for each site:

- Randomization of base case site-dynamic material properties to produce a suite of velocity profiles as well as G/Gmax and hysteretic damping curves that incorporate site randomness.
- Computation of transfer functions (hereafter termed amplification factors) as characterized by a mean and distribution for each set of base case site properties using the RVT-based equivalent-linear site response model.
- Full integration of the generic WUS deep firm soil fractile and mean hazard curves and amplification factors to arrive at a distribution of site-specific hazard curves.
- Computation of site-specific UHS.

Specifically, the suites of WUS soil hazard curves are first combined into a single suite and site-specific amplification factors applied using Approach 3. Combining the empirical hazard curves, rather than applying Approach 3 to each suite independently, results in the same mean hazard—the desired product—but does not properly preserve the full epistemic variability in the fractile estimates. As a result, the range in probability reflected in the resulting fractiles is likely somewhat underestimated. Although the fractiles are likely not significantly in error since the differences in hazard fractiles between the empirical relations are not large, the site-specific hazard fractiles should not be used for hazard or risk assessment.

Approach 3 is implemented through a number of computer programs, which are described below (Figure 8-1). The computation of the amplification factors is the first phase of the calculations and is similar to what is done in other site-response approaches.

8.2.1 RVT-Based Equivalent-Linear Site Response Approach

To compute the ground motions at the ground surface, the results of the PSHA are modified using a site-response model. The conventional approach to estimating the effects of local shallow rock and soil on strong ground motions involves development of a set (1-, 2-, or 3-component) of time histories compatible with the specified outcrop response spectra to serve as control (or input) motions. The control motions are then used to drive a nonlinear computational formulation to transmit the motions through the site profile. Simplified analyses generally assume vertically-propagating S-waves for horizontal components and vertically-propagating P-waves for vertical motions.

The computational formulation that has been most widely employed to evaluate 1D site response assumes vertically-propagating plane S-waves. Departures of soil response from a linear constitutive relation are treated in an approximate manner through the use of the equivalent-linear formulation. The equivalent-linear formulation, in its present form, was introduced by Idriss and Seed (1968). A stepwise analysis approach was formalized into a 1D, vertically propagating S-wave code called SHAKE (Schnabel *et al.*, 1972). Subsequently, this code has become the most widely used and validated analysis package for 1D site response calculations.

Validation exercises between equivalent-linear and fully nonlinear formulations using recorded motions (peak horizontal acceleration) from 0.05 to 0.5 g showed little difference in results. Both formulations compared favorably to recorded motions, suggesting both the adequacies of the vertically-propagating S-wave model and the approximate equivalent-linear formulation. While the assumptions of vertically propagating S-waves and equivalent-linear soil response represent approximations to actual conditions, their combination has achieved demonstrated success in modeling observations of site effects and represent a stable, mature, and reliable means of estimating the effects of site conditions on strong ground motions (Schnabel *et al.*, 1972; Schneider *et al.*, 1993; Silva *et al.*, 1996).

The RASCALS code, which was used in this study for horizontal motions (Figure 8-1), and the SHAKE code represent an implementation of the equivalent-linear formulation of Seed and Idriss (1969) applied to 1D site response analyses. RASCALS is an random vibration theory (RVT)-based equivalent-linear approach, which propagates an outcrop (control motion) power spectral density through a 1D soil column. RVT is used to predict peak time domain values of shear strain based upon the shear-strain power spectrum. In this approach, the control-motion power spectrum is propagated through the 1D rock/soil profile using the plane-wave propagators of Silva (1976). Both P-SV (vertically polarized S-wave, RASCALP) and SH (horizontally polarized S-wave, RASCALS) waves are included in the analysis and have specified angles of incidence.

Inputs to RASCALS and RASCALP are as follows:

- Location of input and output motions within the site profile.
- Input (control) motions characterized by earthquake power spectra.
- Incidence angles of input motion.

- A representation of the rock and soil at the site, consisting of homogeneous layers with specified thickness, seismic velocity, and density.

- A representation of the dynamic material properties of the rock and soil at the site, consisting of strain-dependent shear modulus and damping curves for each layer.

Control motions (power spectral density) must be calculated for input into the site response analysis that are representative of the earthquake magnitude and distance dominating the hazard at the desired rate of exceedance. The basis for the control motions are the magnitude and distances specified by the hazard deaggregation. Control motions may be specified by a response spectrum, which is then followed by an RVT spectral match to generate a power spectral density. This is then input to the site column as an outcrop motion at the control point. The appropriate control response spectrum should be based on the rock attenuation relations used in developing the rock outcrop UHRS (e.g., NRC Regulatory Guide 1.165). Alternatively, as in the case of LANL where the hazard based on empirical relations was computed for deep firm WUS soil, the stochastic point-source was used to generate the control-point power spectrum. Evaluation of site-response using the equivalent-linear site response model is based on convolution of appropriate control motions through randomized velocity profiles combined with randomized G/Gmax and hysteretic damping curves. Based on modeling recorded motions for WUS sites at intermediate-to-high loading levels, nonlinearity is assumed to occur only over the top 500 ft both at LANL and for the WUS deep soil (Silva *et al.*, 1996). The randomized profiles and curves are generated from base case velocity and nonlinear dynamic properties. The convolutions yield transfer functions for 5%-damped response spectra and peak particle velocity.

For the computation of spectra for a site with uncertain properties and exhibiting a degree of lateral variability, a best-estimate (mean) base case velocity profile (or profiles) is developed and used to simulate a number of V_S profiles using the computer program RANPAR (Figure 8-1). Additionally, strain-dependent shear modulus and hysteretic damping are also randomized about best-estimate base cases. A large number of simulations can be required to achieve stable statistics on the response. The simulations attempt to capture the variability in the soil or rock parameters and layer thickness. To achieve statistical stability, 30 randomizations were produced using RANPAR (Figure 8-1) and the velocity correlation models for each base case velocity profile and each base case nonlinear dynamic property curve. The correlation model used was for WUS soil (Silva *et al.*, 1996).

Input control motions at each location are computed using RASCALS or RASCALP for each set of 30 velocity profiles and dynamic property curves (Figure 8-1). RASCALS is used for horizontal spectra using normally-incident and inclined SH-waves. For each control motion, LOGNORM is used to compute the mean and standard deviation of the 30 response spectra (from 30 randomized profiles). Thirty realizations result in stable estimates. Comparison of mean and sigma estimates with 60 realizations showed little difference with corresponding statistics computed from 30 realizations; as a result 30 realizations were adopted for all analyses. The mean response spectrum from the 30 convolutions is divided by the mean (log) spectrum for WUS soil spectrum using SMRATIO (Figure 8-1) to produce the amplification factors. The amplification factors include the effects of the inherent aleatory variability (randomness) of the site properties about each base case and any possible effects of magnitude of the control motions.

Epistemic variability (uncertainty) is captured in consideration of alternate base case (mean) profiles and properties.

The WUS deep firm soil ($\overline{V_S}$ [30m] = 270 m/sec, Silva *et al.*, 1998) has a mean depth of about 500 ft, randomized assuming a uniform distribution from 30 to 1,000 ft (Silva *et al.*, 1998). The California Peninsular Range curves were used to approximate nonlinear response over the top 500 ft, with linear response below (Silva *et al.*, 1996). The generic WUS profile has a generic California crustal model below (Silva *et al.*, 1998) with a point-source stress drop of 60 bars, $Q(f) = 275\ f^{0.6}$, and total kappa value of 0.04 sec. These crustal parameters are for the Los Angeles area whose strong motion recordings dominate the 1997 empirical attenuation relationships. The stress drop reflects an average value over a range in **M**. The LANL site-specific profiles, including crustal model and total kappa value, are then substituted for the WUS profile and kappa value, and ground motions are simulated. Ratios of 5%-damped median response spectra (site/WUS) then appropriately reflect only site differences, retaining the WUS empirical wave propagation, source mechanism, and site-location effects in the hazard. Since the distances are constrained by a desired suite of expected WUS median peak acceleration values, the resulting amplification factors are not highly sensitive to stress drop or Q(f) model.

8.2.2 Amplification Factors

RASCALS was used to generate a control motion, an acceleration power response spectrum for a **M** 7.0, which is approximately the controlling earthquake at LANL (Table 7-2). The **M** 7.0 event was placed at a suite of distances to produce expected median WUS deep soil peak accelerations of 0.05, 0.10, 0.20, 0.40, 0.50, 0.75, 1.00, 1.25, 1.50, 2.00, and 3.00 g. The amplification factors (the ratios of the response spectra at the top of the site profiles to the WUS soil) are a function of the reference (WUS deep firm soil) peak acceleration (or SA), spectral frequency, and nonlinear soil response (Appendix F). Figure 8-2 compares the WUS firm deep soil V_S profile with CMRR base case profile B. Interpolation was used to obtain amplification factors at other reference datum peak motions (SA). Amplification factors were computed for CMRR (4 sets), TA-3 (3 sets), TA-16 (3 sets), and TA-55 (3 sets), based on the velocity profiles and properties listed in Table 6-4. Only one set was computed for the dacite using the unadjusted Stokoe dynamic properties.

Figure 8-3 displays the strain- (peak acceleration) dependent amplification factors for 0.01 to 3.0 g for one combination of base case velocity profiles and dynamic properties. The variation in amplification and deamplification as a function of frequency and input motion are shown on these plots. At increasing ground motion, the nonlinearity in the tuff increases resulting in increasing deamplification. Appendix F are the peak- acceleration-dependent amplification factors for 0.01 to 3.0 g for all the sites.

Figure 8-4 illustrates the discrete horizontal amplification factors relative to WUS deep firm soil for CMRR using base case profile A and the unadjusted dynamic material properties. The amplification factors are for the range of frequencies of 0.1 to 100 Hz (0.01 to 10 sec). There are three other sets of amplification factors for CMRR: (1) base case A and adjusted curves; (2) base case B, unadjusted curves; and (3) base case B, adjusted curves. These are shown in Appendix F. One set of amplification factors for the dacite is shown on Figure 8-5.

8.3 DEVELOPMENT OF V/H RATIOS

As in the 1995 study, the point-source stochastic model as employed in the computer code RASCALP was used to compute site-specific V/H ratios (Appendix G). To model vertical motions, incident inclined P-SV waves are modeled from the source to the site using the plane-wave propagators of Silva (1976) assuming a shear-wave point-source spectrum (Silva, 1997). The angle of incidence at the top of the layer containing the source is computed by two-point ray tracing through the crust and site-specific profile. To model site response, the near-surface V_P and V_S profiles described in Section 4.2 are placed on top of the crustal structure (Section 6.3), the incident P-SV wavefield is propagated to the surface, and the vertical (or radial) motions are computed.

For typical crustal structures without strong near-surface V_P gradients and at close distances, the predominant motion on the vertical component is principally due to the SV wavefield. In a soil column (particularly deep profiles), however, because there is usually a large V_P gradient (larger for P-waves than for S-waves as Poisson's ratio generally decreases with depth), the vertical component is usually controlled by the compressional wavefield at short period. The separation of rock and soil sites in terms of predominant wavefields in the vertical component depends on specific velocity profiles (site-specific as well as the underlying rock and crustal profile), source depth and mechanism through their effect on incidence angles, as well as the depth of the water table.

In the current implementation of the equivalent-linear approach to estimate V/H response spectral ratios, the horizontal component analyses are performed for vertically-propagating shear waves using the RVT methodology (RASCALS). To compute the vertical motions, a linear analysis is performed for incident inclined P-SV waves using low-strain, V_P and V_S derived from the profiles (Section 4.2) using RASCALP. The P-wave damping is assumed to be equal to the low strain S-wave damping (Johnson and Silva, 1981). The horizontal component and vertical component analyses are assumed to be independent.

The approximations of linear analysis for the vertical component and uncoupled vertical and horizontal components have been validated by Silva *et al.* (1996) in the following ways. First, results of fully nonlinear analyses at two reference sites (Gilroy 2 and Treasure Island) were compared to recorded vertical and horizontal motions from the 1989 Loma Prieta earthquake (EPRI, 1993). Second, similar validation comparisons were made for both horizontal and vertical-component motions at more than 50 sites that recorded the 1989 **M** 6.9 Loma Prieta and 1992 **M** 6.7 Northridge earthquakes.

To model the site-specific V/H ratios using RASCALS (equivalent-linear) for the horizontals and RASCALP for the verticals, the same **M**, stress drops, and, suite of distances are used as in developing the site-to-WUS soil transfer functions. For the vertical analyses, a total kappa value of 0.017 sec, half that of the horizontal was used. This factor of 50% is based on observations of kappa at strong motion sites (Anderson and Hough, 1984), validation exercises (Silva *et al.*, 1996), as well as the observation that the peak in the vertical spectral acceleration (5% damped) is generally near 10 to 12 Hz compared to the horizontal peak at about 5 Hz, conditional on **M** 6.5 at a distance of about 10 to 30 km. In this analysis, both the numerator and denominator reflect site-specific profiles (Section 4.2) as well as nonlinear dynamic material properties. Site-specific epistemic variability is accommodated with alternate mean (best estimate) shear-

modulus reduction and hysteretic damping curves (Section 4) and, for CMRR, alternate best-estimate profiles.

To accommodate model epistemic variability following the approach used for the horizontal hazard analyses, empirical deep firm soil V/H ratios were incorporated with equal weights between the stochastic and empirical models. The empirical relations that specified both horizontal and vertical components included those of Abrahamson and Silva (1997) and Campbell and Bozorgnia (2003). Because the Abrahamson and Silva (1997) relations included hanging-wall site location, it was given a higher weight of 0.6 with a remaining weight of 0.4 for the Campbell and Bozorgnia (2003) relation.

The site-specific V/H ratios computed for the CMRR site for base-case profiles A and B as well as unadjusted and adjusted curves are shown in Figures 8-6 to 8-9. The empirical WUS soil V/H ratios are shown in Figures 8-10 and 8-11. The V/H ratios for all the sites are shown in Appendix G. Conditional on **M**, the V/H ratios are strongly dependent on distance or, equivalently, expected PGA (Silva, 1997). Similarity in shape and trends is seen between the site-specific and empirical WUS deep firm soil for equivalent or similar PGA values. The maximum empirical peak acceleration at the minimum rupture distance (Joyner-Boore distance for the point-source) of 1 km is about 0.5 g. For the stochastic point-source model, larger values (up to 3.0 g) are accommodated by reducing the mean point-source depth of 8 km. The resulting V/H ratios for expected median PGA values exceeding about 0.5 g are considered very conservative due to the linear analyses for the vertical and are not used in the hazard analysis. Both the empirical and site-specific V/H ratios share a common saturation for **M** 7.0 at a rupture distance of 1 km and are applied as functions of expected PGA up to 0.5 g. The 0.5 g, or 1 km V/H ratios are applied for PGAs exceeding 0.5 g.

8.4 SITE-SPECIFIC HORIZONTAL AND VERTICAL HAZARD

The hazard curves derived using the empirical attenuation relationships (Section 7.1) and the amplification factors derived for each site relative to WUS deep firm soil were used in SOILUHSI to calculate site-specific tuff-amplified hazard curves (Appendix H). Figure 8-12 shows the CMRR horizontal PGA hazard curves for each set of amplification factors and the mean curve. The differences in hazard curves are very small. Figure 8-13 shows the combined CMRR mean PGA hazard from the site-specific stochastic and the adjusted empirical attenuation relationships.

The hazard curves from SOILUHSI and the hazard curves using the site-specific stochastic attenuation relationships were then input into SOILUHS where the topographic amplification factors and V/H ratios were applied. Figure 8-14 shows the CMRR PGA mean hazard curves and the effect of applying the topographic factors (Table 6-6). In applying the V/H ratios, the aleatory variability, σ_{ln}, was set to 0.2 to accommodate the slightly larger variability in the vertical components compared to the average horizontal component (Abrahamson and Silva, 1997). This process properly incorporates the variabilities (epistemic and aleatory) in the V/H ratios as well as topographic factors and results in horizontal and vertical hazard as well as UHRS and DRS with the desired probabilities across structural frequency for both horizontal and vertical components. Figure 8-15 shows the mean peak vertical acceleration hazard curves for CMRR adjusted with the V/H ratios from the numerical modeling and those from empirical

ratios weighted equally. Figure 8-16 shows the mean vertical hazard at CMRR adjusted for topographic effects.

The uncertainty or epistemic variability in seismic hazard is typically represented by a set of weighted hazard curves. Using these sets of curves as discrete probability distributions, they can be sorted by the frequency of exceedance at each ground-motion level and summed into a cumulative probability mass function. When the cumulative probability mass function for a particular exceedance frequency equals or exceeds fractile y, then the exceedance frequency represents the y^{th} fractile. The weighted-mean hazard curve is the weighted average of the exceedance frequency values. This approach is a standard practice in PSHA. These procedures are contained in the computer program FRACTILE, which was used to produce the final site-specific hazard curves.

HAZUHS was used to calculate the UHS for each selected return period based on the suite of hazard curves from FRACTILE. Finally, HCSCP interpolates the strain-compatible properties for a given hazard curve or ground motion value. The interpolation is done in log-log space based on the given probability level (i.e., ground motion value) as defined by the input hazard curve. The program can operate on the individual hazard curves from SOILUHS or the fractiles hazard curves from FRACTILE. The input ground motion values should be at the same site conditions as the input hazard curve used for the interpolation.

The combined site-specific CMRR hazard curves for horizontal and vertical motions for the range of periods from 0.01 sec (peak acceleration; 100 Hz) to 2.0 sec (0.5 Hz) are shown on Figures 8-17 to 8-38. Hazard curves for TA-3, TA-16, TA-55, and the rock-outcrop dacite are shown on Figures 8-39 to 8-50 for horizontal PGA (100 Hz), 0.2 sec (5.0 Hz), and 1.0 sec (1.0 Hz) SA. The remaining hazard curves are shown in Appendix H.

The mean and median hazard curves indicate the central tendency of the calculated exceedance probabilities. The separation between the 15th and 85th percentile curves conveys the effect of epistemic uncertainty on the calculated exceedance probabilities. As shown on Figure 8-17 for CMRR, the mean hazard at APE smaller than 10^{-3} is biased to the 85th percentile hazard. This indicates that the mean hazard is being controlled by a branch on the logic tree that has been assigned a low weight but predicts much higher hazard than the rest of the logic tree. At an APE of 10^{-4} (10,000-year return period), the PGA is about 1 g (Figure 8-17). At lower APEs, the PGAs may reach levels where they become physically unrealizable. Seismic risk analyses are anticipated for some of the facilities at LANL such as CMRR and thus truncation of epsilon in the PSHA (Section 8.4) seems appropriate.

In this section, UHRS and DRS are described for site-specific cases (CMRR, TA-3, TA-16, and TA-55), for dacite, and for the site-wide case. Strain-compatible properties for the site-specific and site-wide cases are also presented. Site-specific, dacite, and site-wide time histories have also been developed and are presented.

When using the dacite UHRS in seismic analysis, the ground motions should be applied at the top of dacite as an outcrop motion. Also for sites not underlain by dacite or the Cerros del Rio basalt as an alternative, e.g., TA-16, the dacite UHRS should be input at a depth where the V_S is close to 5300 ft/sec. The dacite motions have been corrected for topographic effects (Section 8.5). Sites located on mesas where the slope angle is less than 15° do not require corrections for topographic effects. Dacite UHRS and DRS without the topographic effects are presented in a supplementary report that will be incorporated into the LANL Engineering Standards Manual.

9.1 UHRS AND DRS

Based on the site-specific hazard curves presented in Section 8.5, mean horizontal UHRS are computed for CMRR, TA-3, TA-16, and TA-55 (Figures 9-1 to 9-4). The UHRS are computed at the periods of 0.01 to 2.0 sec as specified in Section 8.5. The TA-55 UHRS is an envelope of the hazard curves of CMRR and the hazard curve developed from incorporating the SHB-1 borehole velocity profile into the base case site profiles (Section 7).

Figures 9-5 and 9-6 show the dacite and site-wide mean horizontal UHRS. Similar to TA-55, the site-wide UHRS is an envelope of the hazard curves of CMRR, TA-3, TA-16, and TA-55. Figures 9-7 to 9-11 show the site-wide mean horizontal UHRS for the return periods of 1000 to 100,000 years as well as the individual site UHRS. The mean vertical UHRS computed from the vertical hazard curves (Section 8.5) are shown in Figures 9-12 to 9-17. Table 9-1 lists the horizontal and vertical PGA values for the UHRS.

DRS were computed based on ASCE/SEI 43-05 (also in NUREG/CR-6728 [McGuire *et al.*, 2001]). In ASCE/SEI 43-05, the DRS is given by

$$DRS = DF \times UHRS \tag{9-1}$$

where DF is the Design Factor, defined below, at each spectral frequency.

For each spectral frequency at which the UHRS is defined, a slope factor, A_R shall be determined from

$$A_R = \frac{SA_{0.1H_D}}{SA_{H_D}} \tag{9-2}$$

where SA_{H_D} is the SA at the mean exceedance probability, H_D, and $SA_{0.1H_D}$ is the SA at $0.1H_D$. Then the DF, at this spectral frequency is given by

$$DF = \text{Maximum } (DF_1, DF_2) \tag{9-3}$$

$$DF_2 = 0.6(A_R)^{\alpha} \quad (9\text{-}4)$$

where DF_1 and α are defined in Table 9-2.

The horizontal DRS for CMRR, TA-3, TA-16, TA-55, dacite, and site-wide for SDC-3 (2,500 years), -4 (2,500 years), and -5 (10,000 years) are shown on Figures 9-18 to 9-23. The DRS spectral values are listed in Appendix I. DRS for dacite were computed in the case where facilities may be built on rock whose V_S is close to 5300 ft/sec. Figures 9-24 to 9-26 show the site-wide horizontal DRS for SDC-3, -4, and -5 as well as the individual site DRS that they envelop. Table 9-3 lists the horizontal and vertical PGA values for the DRS. Figures 9-27 to 9-32 show the vertical DRS for the various cases. On Figures 9-33 to 9-50 corresponding horizontal and vertical DRS are shown for direct comparison. They illustrate the exceedance of the vertical DRS over the horizontal DRS at moderate to high frequencies reflecting the V/H ratios (Section 8.4).

The vertical DRS contained in this report need to be modified for incorporation into the LANL Engineering Standards Manual and so these preliminary versions should not be used.

9.2 STRAIN-COMPATIBLE PROPERTIES

In the current approach to develop site-specific design motions (UHRS, DRS), a fully probabilistic method was used which correctly preserves the annual exceedence probabilities of the generic site probabilistic hazard analysis (Section 8), while properly incorporating variabilities (aleatory and epistemic) in site-specific dynamic material properties. For structural analyses, strain-compatible material properties are desired which are consistent with the probabilistically-based design motions. To achieve hazard consistency in the strain compatible properties, they must reflect both the hazard level (ground motion and exceedence probability) as well as the aleatory and epistemic components in site-specific dynamic material properties incorporated in developing the design motions.

Simply using control motions based on a generic rock site hazard to drive the site-specific soil column (NUREG/CR-6728, McGuire *et al.*, 2001; RG 1.165, NRC, 1997) will, in general, not result in strain-compatible properties consistent with the site-specific soil hazard developed using a fully probabilistic approach (e.g., Approaches 3 or 4). Additionally, this approach is not viable when the generic hazard is developed for soil or soft rock conditions as control motions, appropriate for the base of the soil conditions, are not generally available.

To achieve both the desired exceedence probability as well as consistency with the level of motion would require an approach analogous to an Approach 3 for properties. That is, during the integration of the generic site hazard curves with the suites of amplification factors (comprising aleatory and epistemic variability), corresponding strain-compatible properties and weights would need to be accumulated for each layer in the profiles. The strain compatible properties would then be sorted to produce 15th, 50th, and 85th percentile estimates, reflecting a range in properties that is consistent with the hazard used for design analyses. While this would be the most accurate approach and is conceptually straightforward, implementation reflects some practical as well as theoretical issues.

Developing or modifying an Approach 3 code to import, catalogue, and then properly weight and sort the extremely large number of strain-compatible properties is a manageable challenge. However, because the hazard integration used in developing hazard-consistent site-specific design motions is performed at each period separately, in principal there are corresponding strain-compatible properties at each structural period, possibly as a result of the change in magnitude contribution and corresponding amplification factors with the change in structural period. The optimum approach in combining these sets of period-dependent properties, should they differ significantly, is an unresolved issue. Additionally, horizontal motions are developed separately from vertical motions with the latter employing suites of V/H ratios applied probabilistically to the horizontal site specific hazard curves to achieve fully hazard-consistent vertical motions. As with the multiple periods, a probabilistically rigorous approach to combining the horizontal and vertical properties is not unambiguous.

As a result, because the range in strain-compatible material properties used in structural analyses is not rigorously defined in terms of hazard consistency and fractiles (ASCE/SEI 43-05), an approximate approach has been developed. The approach assumes strain-compatible properties are approximately lognormally-distributed, consistent with observed strong ground motion parameters (Abrahamson and Shedlock, 1997), and makes use of the distributions of strain-compatible properties catalogued during development of the suites of amplification factors. Specifically, the approximate approach examines the site-specific horizontal or vertical hazard curves at the APE of interest, determines the ground motion (interpolating logarithmically as necessary), and locates the corresponding amplification factors and associated strain-compatible properties at the ground motion levels determined from the hazard curve. For each case of epistemic variability, median and sigma estimates (over aleatory variability) are interpolated (logarithmically) to the appropriate ground motion as specified by the site-specific hazard curve at the desired annual exceedence probability. To accommodate epistemic variability in site-specific properties, the same weights used in developing the site-specific hazard curves are applied to the corresponding strain compatible properties. The weighted median (mean log) set of strain compatible properties (for each layer) is given by Equation 9-5 while the associated variance includes both the aleatory component for each epistemic case as well as the variability of mean properties for each base-case (Equation 9-6).

The approach approximately accommodates both the median estimates as well as aleatory and epistemic variabilities in strain-compatible properties that are consistent with the site-specific horizontal and vertical hazard used for design. To examine consistency in strain-compatible properties across structural frequencies, the entire process is performed at PGA (typically 100 Hz), and again at low frequency, typically 1 Hz. Since amplification factors are typically developed for a range in magnitude reflecting contributions at low ($\leq$ 2 Hz) and high ($\geq$ 2 Hz) frequencies, the consistency check at PGA and 1 Hz covers the typical range in control motions. If the differences in properties at high- and low- frequency is less than 10%, the high-frequency properties are used since this frequency range typically has the greatest impact on soil nonlinearity. If the difference exceeds 10%, two sets of properties are developed with the recommendation that separate structural analyses be performed. For all of the LANL technical areas, the 100 Hz and 1 Hz sets of strain-compatible properties were within 10%.

In summary, the properties are interpolated to the desired peak acceleration (mean hazard) and a consistency check is performed at 1.0 sec. The properties are calculated for each case of

epistemic uncertainty. Each case has median (μ_i) and $\pm \sigma_i$ properties. Each case of epistemic is then combined by the weighted median properties

$$\overline{\mu_{ln}} = \Sigma W_i \mu_{ln_i} \tag{9-5}$$

The weighted variances include site epistemic (different medians) in combined properties through

$$\text{Var}(ln) = \Sigma\left[W_i \sigma_{ln_i}^2 + W_i \left(\mu_{ln_i} - \overline{\mu}\right)^2\right] \tag{9-6}$$

Strain-compatible properties including V_S, V_S sigma, S-wave damping, S-wave damping sigma, V_P, V_P sigma, P-wave damping, and strains as a function of depth are shown on Figures 9-51 to 9-130 for return periods of 2,500 and 10,000 years.

9.3 TIME HISTORIES

Time histories were developed in a manner consistent with the approach used in the 1995 study (Wong *et al.*, 1995). Time histories were spectrally matched following the recommended guidelines contained in NUREG/CR-6728 (McGuire *et al.*, 2001; Section 5.3). These guidelines are summarized below in paraphrased form:

- The artificial accelerogram should achieve approximately a mean-based fit to the target spectrum. The average ratio of the SA calculated from the accelerogram to the target, calculated frequency by frequency, is only slightly greater than 1 to insure there are no significant gaps and the result is not biased high with respect to the target.

- Records should have a sufficiently small frequency increment and sufficiently high maximum frequency (or alternatively time increment and maximum duration). The total duration of the record can be increased by zero packing to satisfy these frequency requirements. It is recommended that records have a maximum frequency increment of 0.05 Hz with a Nyquist frequency of at least 50 Hz or a time increment of at most 0.01 sec for a total duration of 20 sec.

- SAs at 5% damping should be computed at a minimum of 100 points per frequency decade, uniformly spaced over the log frequency scale from 0.1 Hz to 50 Hz or the Nyquist frequency. The computed 5%-damped response spectrum of the accelerogram (if one artificial motion is used for analysis) or the average of all accelerograms (if a suite of motions is used for analysis) should not fall more than 10% below the target spectrum at any one frequency point. No more than 9 adjacent spectral points may be allowed to fall below the target spectrum at any frequency. This corresponds to a moving frequency window of $\pm$ 10% centered on the frequency.

- The computed 5%-damped response spectrum of the artificial ground motion (if one motion is used for analysis) or the average of the 5%-damped response spectra (if a suite of motions is used for analysis) should not exceed the target spectrum at any frequency by more than 30% and the average ratio should exceed 1 in the frequency range between 0.2 Hz and 25 Hz.

- Artificial motions should have durations, and ratios PGV/PGA and PGA*PGD/PGV^2 that are generally consistent with appropriate WUS or CEUS magnitude and distance bin median values. PGV and PGD are peak ground velocity and peak ground displacement, respectively.

- The upper limit for the zero-lag cross-correlation coefficient between any two design ground motions (acceleration time histories) is recommended to be 0.3.

These criteria ensure that no gaps in the power spectral density or Fourier amplitude spectrum will occur over a significant frequency range.

Time histories were developed by combining a Fourier amplitude spectrum (which is generated by matching target DRS) with a phase spectrum from an observed strong ground motion recording using the technique described by Silva and Lee (1987). To improve the fit to the target spectrum, additional spectral matching is performed using the response spectrum computed from the synthetic time history. Additionally, a baseline correction is included by high-pass filtering the record at 10 sec. The result is a synthetic time history, which closely matches the target spectrum and which possesses realistic integrations to velocity as well as displacement.

The two most important criteria in selecting the phase from a recorded earthquake for the hypothetical event are that the **M** and the source-to-site distance should be comparable. These criteria produce synthetic records with appropriate durations and timing of the major phase arrivals so that the distribution of energy with time in the synthetic record appears reasonable. The time histories are intended to approximate expected duration, and as such, they are appropriate for nonlinear analyses of structures, embankments, and soil profiles. DRS time histories for acceleration, velocity, and displacement were generated by spectrally matching the target DRS.

The phase spectra were taken from the 23 November 1980 (1934 GMT) **M** 6.9 Irpinia, Italy, earthquake recordings at the Sturno strong motion site (Figure 131). The earthquake was the result of normal faulting and the rupture distance was 11 km. This earthquake is similar to the LANL modal earthquake although its source-to-site distance is somewhat longer (Table 7-2). The Sturno site is a firm soil site. The 1980 earthquake was the result of complex normal faulting, which involved three main episodes of rupture and several fault segments (Bernard and Zollo, 1989). Because this event consisted of subevents, the appropriateness of its time histories for use as a seed has been questioned. Subevents in normal faulting earthquakes are not unusual (e.g., 1959 **M** 7.3 Hebgen Lake) and a large event on the PFS could very well be the result of rupture of several faults (Section 5.1.1). Also we understand that "design follows linear methods of analysis and the closeness of the fit to the target is the primary concern, not the details of the time history (Arias energy growth with time, for example) especially for the types of structures being built at LANL" (C. Costantino, written communication, 2007). Thus we deem the use of the time histories of the 1980 earthquake to be appropriate.

The horizontal and vertical target spectra, spectral matches, spectral ratios between the match and the target spectrum, and the resulting horizontal and vertical time histories for all the sites, dacite, and site-wide are shown on Figures 9-132 to 9-311 for SDC-3, -4, and -5. The criteria stated earlier were adhered to in developing the time histories.

9.4 DRS AT OTHER DAMPINGS

DRS at other dampings of 0.5%, 1%, 2%, 3%, 7%, and 10% were computed from the 5%-damped DRS using the damping ratios of Abrahamson and Silva as described in Appendix A of Silva *et al.* (1996). The damping ratios do not have a significant dependence on site condition or distance. The coefficients for both horizontal and vertical components are listed in Appendix A of Silva *et al.* (1996). The damped horizontal and vertical spectra are shown in Figures 9-312 to 9-347 for each site, dacite, and site-wide for each SDC. The DRS spectral values at other dampings are listed in Appendix I.

9.5 COMPARISON WITH 1995 HAZARD RESULTS AND NATIONAL HAZARD MAPS

In Table 9-4, we compare the PGAs from this study with the values from the 1995 study (Wong *et al.*, 1995) for the return periods of 1000, 2500, and 10,000 years. As shown in the table, the estimated probabilistic hazard has increased significantly (including other spectral values). The percentage increase gets larger with return period due to differences in slope of the hazard curves (Figure 9-348). For example, at a 1,000-year return period, the increase from the 1995 PGA values to the current study is about 29%. At 10,000 years, the increase is 84% (Table 9-4). This increase may be due to a number of factors including the increase in the activity rate of the PFS.

In Figure 9-348, the 1995 PGA hazard curves for TA-55 and the contribution from the PFS are shown together with the hazard curves using the stochastic attenuation relationships from this study. The latter contains the site response and so this provides the best comparison with the 1995 hazard curves. The difference in hazard from the two studies is significant. The difference in the slopes of the hazard curves is partially, if not largely, due to the amount of epistemic uncertainty in both the empirical and stochastic attenuation relationships (Section 7.2.3). This is illustrated in Figure 9-349, which shows the hazard at CMRR using the empirical attenuation relationships with and without the increased epistemic uncertainty (Section 6.1). Note at a return period of 2,500 years, the hazard shows little impact by the increased epistemic uncertainty. The increased epistemic uncertainty from the more complex characterization of the PFS in this study (e.g., synchronous versus simultaneous rupture) may also be contributing to the difference in slopes.

In this regard, it is difficult to assess specific impacts of the seismic source characterization of the PFS on the current hazard estimates relative to the 1995 results because of the complex characterization of the PFS and because rupture models fundamentally changed (Figure 5-8 this study and Figure 7-1a through 7-1g in Wong *et al.*, 1995). We do know that the recurrence rates have increased significantly on the PFS because of the new paleoseismic trenching data and evidence for temporal clustering of two or three surface-faulting events since 11 ka (Section 5.1.2.2.1). In the 1995 study, recurrence intervals were not used for most of the 26 rupture scenarios due to the lack of recurrence interval data. The weighted-mean recurrence interval was 32,000 years when they were used and the weighted-mean slip rate for most of the rupture scenarios was 0.182 mm/yr. In comparison, the weighted-mean recurrence for Rupture Model C, the strongly favored (weighted 0.85) model in this study is 8,400 years and the weighted-men slip rate is 0.211 mm/yr (Figure 5-8). Sensitivity studies show that these higher rates have a significant impact on the hazard (Section 7.2.2) and so we know that increased rates on the PFS

likely contributed measurably to the increase in hazard for this study, but we cannot specify exactly how much.

A comparison between the empirical soil attenuation relationships for a **M** 7.0 at TA-55 used in 1995 and the current relationships (Sadigh *et al.*, written communication, 1987 is not shown) shows little difference in the means of the relationships. A comparison of the stochastic relationships, however, shows the 1995 relationship for the mesa top that was used site-wide is significantly lower than the average of the various 2007 stochastic relationships. The difference at 1 km is about 50% for a **M** 7.0 at TA-55. Thus the updated site response at least at TA-55 appears to be a significant factor in the increased ground motions.

The 2002 USGS National Hazard Maps (Frankel *et al.*, 2002) indicate a 2,500-year return period peak horizontal acceleration of 0.20 g for a firm rock site condition (NEHRP site class B/C). The low hazard shown on their maps for the LANL area is due to a number of factors including their assigned low slip rate of 0.09 mm/yr for the PFS, the use of a single value of Mmax of **M** 7.3, which gives lower hazard when slip rates are used, and the lack of incorporating epistemic uncertainty in their fault parameters. A prime example of the latter is the USGS did not fully model the rupture behavior of the PFS, e.g., no segmentation.

Table 9-1
LANL Mean PGA Values (g) From the UHRS

Return Period (years)	CMRR		TA-3		TA-16		TA-55		Site-Wide		Dacite	
	Horizontal	Vertical	Horizontal	Vertical	Horizontal	Vertical	Horizontal	Vertical	Horizontal	Vertical	Horizontal	Vertical
1,000	0.27	0.32	0.27	0.32	0.25	0.31	0.27	0.32	0.27	0.32	0.13	0.12
2,500	0.52	0.60	0.52	0.59	0.47	0.57	0.52	0.60	0.52	0.60	0.27	0.27
10,000	1.03	1.21	1.03	1.10	0.93	1.05	1.03	1.21	1.03	1.21	0.65	0.65
25,000	1.47	1.79	1.45	1.57	1.33	1.50	1.47	1.79	1.47	1.79	1.01	0.97
100,000	2.30	3.01	2.29	2.79	2.11	2.57	2.30	3.01	2.30	3.01	1.69	1.65

Table 9-2
Design Response Spectrum Parameters

SDC	H_D	P_F	R_P	DF_1	α
3	$4x10^{-4}$	$\sim 1x10^{-4}$	4	0.8	0.40
4	$4x10^{-4}$	$\sim 4x10^{-5}$	10	1.0	0.80
5	$1x10^{-4}$	$\sim 1x10^{-5}$	10	1.0	0.80

$$R_P = \frac{H_D}{P_F}$$

Table 9-3
LANL PGA Values (g) From the DRS

SDC	CMRR		TA-3		TA-16		TA-55		Dacite		Site-Wide	
	Horizontal	Vertical	Horizontal	Vertical	Horizontal	Vertical	Horizontal	Vertical	Horizontal	Vertical	Horizontal	Vertical
3	0.47	0.56	0.47	0.53	0.43	0.50	0.47	0.60	0.28	0.27	0.47	0.56
4	0.72	0.87	0.71	0.78	0.65	0.74	0.72	0.86	0.47	0.45	0.72	0.86
5	1.17	1.50	1.17	1.39	1.07	1.29	1.17	1.50	0.84	0.82	1.17	1.50

Table 9-4
Comparison of Probabilistic Peak Horizontal Accelerations in g's
From 1995 and Current Studies

Return Period	1,000 Years		2500 Years		10,000 Years	
Source	**1995**	**This Study**	**1995**	**This Study**	**1995**	**This Study**
CMRR	—	0.27	—	0.52	—	1.03
TA-03	0.21	0.27	0.33	0.52	0.56	1.03
TA-16	0.21	0.25	0.32	0.47	0.53	0.93
TA-55	0.22	0.27	0.33	0.52	0.56	1.03

Based on the studies completed to date, the following are recommendations for future investigations. The results of such studies will aid in refining specific seismic source and site parameters, which have been incorporated into the PSHA, and reduce their associated uncertainties.

- Recalculate the hazard using the NGA ground motion attenuation relationships. Four relationships are now available for use and they display significant differences with the earlier generation of relationships, i.e., the ones used in the current study (Section 6.1). It would be prudent to evaluate the impact of these new relationships on the LANL hazard after they have had time to be fully vetted.

- Conduct additional detailed/high-precision mapping and displacement measurements along the SCC segment of the PFS, similar to what has been done on the PAF segment of the PFS. The purpose of this would be threefold: (1) better define fault trace geometry for the SCC and verify the gap between the PAF and SCC; (2) better define long-term displacements and slip rates for the SCC; and (3) identify potential paleoseismic trenching sites.

- Conduct paleoseismic trenching studies of the SCC to determine the timing and size of prehistoric surface-faulting earthquakes. This will help better define rupture models and scenarios for the PFS. It may also help better determine maximum magnitudes and recurrence intervals for rupture scenarios.

- Reevaluate the entire dataset for the RGR fault slip rate analysis using only data for complete seismic cycles and more complete documentation of long-term data (both displacements and applicable time periods). This more robust analysis will likely reduce slip rate uncertainties and result in a more symmetric RGR slip rate distribution.

- Conduct additional studies to better constrain kappa. Kappa is a key parameter in assessing the hazard at LANL (Section 6.2). Focused efforts should be made to evaluate kappa using data from the LANL seismographic network. Improvements in the network may be necessary to improve data quality.

- Conduct V_S measurements of dacite. There is no reliable V_S data for the dacite (Section 4.2.3) and thus velocity data would confirm the value used in this study. Measuring the velocity of the dacite beneath the laboratory requires deep boreholes and so although not ideal, shallow velocity surveys where the rock outcrops is probably the only economical alternative.

Abrahamson, N.A. and Bommer, J., 2006, Program on technology innovation: Truncation of the lognormal distribution and value of the standard deviation for ground motion models in the central and eastern United States: EPRI Technical Report 1014381.

Abrahamson, N. and Shedlock, K., 1997, Some comparison between recent ground-motion relations: Seismological Research Letters, v. 68, p. 9-23

Abrahamson, N.A. and Silva, W.J., 1997, Empirical response spectral attenuation relations for shallow crustal earthquakes: Seismological Research Letters, v. 68, p. 94-127.

Acocella, V., Morvillo, P., and Funiciello, R., 2005, What controls relay ramps and transfer faults within rift zones? Insights from analogue models: Journal of Structural Geology, v. 27, p. 397-408.

AFPS, The 1995 French Seismic Code, 1995, Guidelines for seismic microzonation studies.

Aki, K., 1983, Seismological evidence in support of the existence of "Characteristic Earthquakes:" Earthquake Notes, v. 54, p. 60-61.

Aldrich, M.J., Jr., 1986, Tectonics of the Jemez Lineament in the Jemez Mountains and Rio Grande rift: Journal of Geophysical Research, v. 91, p. 1753-1762.

Anderson, J.G. and Hough, S.E., 1984, A model for the shape of the Fourier amplitude spectrum of acceleration at high frequencies: Bulletin of the Seismological Society of America, v. 74, p. 1969-1993.

Anderson, J.G., Wesnousky, S.G., and Stirling, M.W., 1996, Earthquake size as a function of fault slip rate: Bulletin of the Seismological Society of America, v. 86, p. 683-690.

Arabasz, W.J. and Robinson, R., 1976, Microseismicity and geologic structure in the northern South Island, New Zealand: New Zealand Journal of Geology and Geophysics, v. 19, p. 561-601.

American Society of Civil Engineers, 2005, Seismic design criteria for structures, systems, and components in nuclear facilities: ASCE/SEI 43-05, 96 p.

Ashford, S.A. and Sitar, N., 1997, Analysis of topographic amplification of inclined shear waves in a steep coastal bluff: Bulletin of the Seismological Society of America, v. 87, p. 692-700.

Atkinson, G.M. and Boore, D.M., 1995, Ground motion relations for eastern North America: Bulletin of the Seismological Society of America, v. 85, p. 17-30.

Baldridge, W.S., Ferguson, J.F., Braile, L.W., Wang, B., Eckhardt, K., Evans, D., Schultz, C., Gilpin, B., Jiracek, G.R., and Biehler, S., 1994, The western margin of the Rio Grande Rift in northern New Mexico: An aborted boundary?: Geological Society of America Bulletin, v. 89, p. 1073-1090.

Baltz, E.H., 1976, Seismotectonic analysis of the central Rio Grande rift, New Mexico, A progress report on geological investigations: New Mexico Bureau of Mines and Mineral Resources Preliminary Report, 93 p.

Baltz, E.H., 1978, Resume of Rio Grande depression in north-central New Mexico: New Mexico Bureau of Mines and Mineral Resources Circular 163, p. 210-228.

Bauer, P.W., Kelson, K.I., Lyman, J., Heynekamp, M.R., and McCraw, D.J., 1999, Geology of the Ranchos de Taos 7.5 minute quadrangle, Taos County, New Mexico: New Mexico Bureau of Mines and Mineral Resources Open-File Geologic Map OFGM 33, scale 1:24,000.

Bauer, P.W. and Kelson, K.I., 2004a, Cenozoic structural development of the Taos area, New Mexico: New Mexico Geological Society Guidebook, 55th Field Conference, Geology of the Taos Region, p. 129-146.

Bauer, P.W. and Kelson, K.I., 2004b, Rift extension and fault slip rates in the southern San Luis basin, New Mexico: New Mexico Geological Society Guidebook, 55th Field Conference, Geology of the Taos Region, p. 172-180.

Bazzurro, P. and Cornell, C.A., 2004, Nonlinear soil-site effects in probabilistic seismic-hazard analysis: Bulletin of the Seismological Society of America, v. 94, p. 2110-2123.

Bechtel SAIC Company, 2004, Development of earthquake ground motion input for preclosure seismic design and postclosure performance assessment of a geologic repository at Yucca Mountain, NV, MDL-MGR-GS-000003 REV 01: prepared for the U.S. Department of Energy, Office of Civilian Radioactive Waste Management.

Becker, A.M. and Abrahamson, N.A., 1997, Stress drops in normal faulting earthquakes (abs.): Seismological Research Letters, v. 68, p. 322.

Benz, H.M., Frankel, A., and Boore, D.M., 1997, Regional Lg attenuation for the continental United States: Bulletin of the Seismological Society of America, v. 87, p. 606-619.

Bernard, P. and Zollo, A., 1989, The Irpinia (Italy) 1980 earthquake: Detailed analysis of a complex normal faulting: Journal of Geophysical Research, v. 94, p. 1631-1647.

Brister, B.S. and Gries, R.R., 1994, Tertiary stratigraphy and tectonic development of the Alamosa Basin (northern San Luis Valley), Rio Grande rift, south-central Colorado, *in* Keller, G.R. and Cather, S.M. (eds.), Basins of the Rio Grande Rift; Structure, Stratigraphy, and Tectonic Setting: Geological Society of America Special Paper 291, p. 39-58.

Boore, D.M., Joyner, W.B., and Fumal, T.E., 1997, Equations for estimating horizontal response spectra and peak acceleration from western North American earthquakes: A summary of recent work: Seismological Research Letters, v. 68, p. 128-153.

Bosworth, W., 1985, Geometry of propagating continental rifts: Nature, v. 316, p. 625-627.

Bouchon, M., 1973, Effect of topography on surface motion: Bulletin of the Seismological Society of America, v. 63, p. 615-632.

Broxton, D.E. and Vaniman, D.T., 2005, Geologic framework of a groundwater system on the margin of a rift basin, Pajarito Plateau, north-central New Mexico: Vadose Zone Journal, v. 4, p. 522-550.

Bull, W.B. and Pearthree, P.A., 1988, Frequency and size of Quaternary surface ruptures of the Pitaycachi fault, northeastern Sonora, Mexico: Bulletin of the Seismological Society of America, v. 78, p. 956-978.

Campbell, K.W. and Bozorgnia, Y., 2003, Updated near-source ground motion (attenuation) relations for the horizontal and vertical components of peak ground acceleration and acceleration response spectra: Bulletin of Seismological Society of America, v. 93, p. 314-331.

Cather, S.M., 1992, Suggested revisions to the Tertiary tectonic history of north-central New Mexico, New Mexico Geological Society, 43rd Field Conference Guidebook, p. 109-122.

Chapin, C.E., 1971, The Rio Grande Rift, Part 1: Modifications and additions: New Mexico Geological Society, 22nd Field Conference Guidebook, p. 191-202.

Chapin, C.E. and Cather, S.M., 1994, Tectonic setting of the axial basins of the northern and central Rio Grande rift, *in* G.R. Keller and S.M. Cather (eds.), Basins of the Rio Grande Rift: Structure, Stratigraphy, and Tectonic Setting: Geological Society of America Special Paper 291, p. 5-25.

Connell, S.D., Love, D.W., Sorrell, J.D., and Harrison, J.B.J, 2001, Plio-Pleistocene stratigraphy and geomorphology of the central part of the Albuquerque basin; 45th Field Conference of the Rock Mountain Cell of the Friends of the Pleistocene: New Mexico Bureau of Geology and Mineral Resources Open-File Report 454C and D, variously paginated.

Cornell, C. A., 1968, Engineering seismic risk analysis: Bulletin of the Seismological Society of America, v. 58, p. 1583-1606.

Cornell, C.A. and Van Marke, E.H., 1969, The major influences on seismic risk: Proceedings of the Third World Conference on Earthquake Engineering, v. A-1, p. 69-93.

Costantino, C.J. and Houston, T.W., 2005, Sensitivity studies to estimate potential 2-dimensional effects at the CMRR site on design ground motions: unpublished technical report, 27 p.

Cramer, C.H., 2003, Site-specific seismic hazard analysis that is completely probabilistic: Bulletin of the Seismological Society of America, v. 93, p. 1841-1846.

Crone, A.J. and Machette, M.N., 2005, Paleoseismic activity on the Sangre de Cristo fault near San Luis, Colorado: Geological Society of America Abstracts with Programs, v. 37, p. 558.

CRWMS M&O (Civilian Radioactive Waste Management System Management and Operating Contractor), 1998, Probabilistic seismic hazard analyses for fault displacement and vibratory fround motion at Yucca Mountain, Nevada: Milestone SP32IM3, September 23, 1998, three volumes.

Davis, P.M., 1991, Continental rift structures and dynamics with reference to teleseismic studies of the Rio Grande and East African rifts, *in* A.F. Gangi (ed.), World Rift Systems, Tectonophysics, v. 197, p. 309-325.

dePolo, C.M., 1994, The maximum background earthquake for the Basin and Range Province, western North America: Bulletin of the Seismological Society of America, v. 84, p. 466-472.

dePolo, C.M. and Slemmons, D.B., 1990, Estimation of earthquake size for seismic hazards: Geological Society of America Reviews in Engineering Geology, v. VII, p. 1-27.

Doser, D.I., 1985, Source parameters and faulting processes of the 1959 Hebgen Lake, Montana, earthquake sequence: Journal of Geophysical Research, v. 90, p. 4537-4555.

Doser, D.I. and Smith, R.B., 1989, An assessment of source parameters of earthquakes in the Cordillera of the western United States: Bulletin of the Seismological Society of America, v. 79, p. 1383-1409.

Doser, D.I. and Yarwood, D.R., 1991, Strike-slip faulting in continental rifts: Examples from Sabukia, East Africa (1928), and other regions, *in* A.F. Gangi (ed.), World Rift Systems, Tectonophysics, v. 197, p. 213-224.

DuBois, S.M., Smith, A.W., Nye, N.K., and Norwak, T.A., 1982, Arizona earthquakes, 1776-1980: Arizona Bureau of Geology and Mineral Technology Bulletin 193, 456 p.

Electric Power Research Institute (EPRI), 1993, Guidelines for determining design basis ground motions: EPRI TR-102293, v.1.

Erickson, D., McNamara, D.E., and Benz, H.M., 2004, Frequency-dependent L*g* Q within the continental United States: Bulletin of the Seismological Society of America, v. 94, p. 1630-1643.

European Committee for Standardization, 2000, (EC8) Design provisions for earthquake resistance of structures, Part 1-1: General Rules-Seismic Actions and General Requirements for Structures, prEN. 1998-5, Brussels.

Frankel, A., 1995, Mapping seismic hazard in the central and eastern United States: Seismological Research Letters, v. 66, p. 8-21.

Frankel, A., Mueller, C., Barnard, T., Perkins, D., Leyendecker, E.V., Dickman, N., Hanson, S., and Hopper, M., 1996, National seismic-hazard maps; documentation June 1996: U.S. Geological Survey Open-File Report 96-532, 110 p.

Frankel, A., Peterson, M., Mueller, C., Haller, K., Wheeler, R., Leyendecker, E., Wesson, R., Harmsen, S., Cramer, C., Perkins, D., and Rukstales, K., 2002, Documentation for the 2002 update of the National Seismic Hazard Maps: U.S. Geological Survey Open-File Report 02-420, 33 p.

Galusha, T. and Blick, J.C., 1971, Stratigraphy of the Santa Fe Group, New Mexico: American Museum of Natural History Bulletin, v. 144, art. 1.

Gardner, J.K. and Knopoff, L., 1974, Is the sequence of earthquakes in Southern California, with aftershocks removed Poissonian?: Bulletin of the Seismological Society of America, v. 65, p. 1363-1367.

Gardner, J.N., 1985, Tectonic and petrologic evolution of the Keres group: Implications for the development of the Jemez volcanic field, New Mexico, PhD Thesis, University of California, Davis, 293 p.

Gardner, J.N., Goen, L.K., House, L.S., Keller, M.D., Volkman, D.E., 1994, Los Alamos National Laboratory draft seismic program plan, prepared for the U.S. Department of Energy, 100 p. plus appendices.

Gardner, J.N. and Goff, F., 1984, Potassium-argon dates from the Jemez volcanic field: implications for tectonic activity in the north-central Rio Grande rift: New Mexico Geological Society Guidebook 35, p. 75-81.

Gardner, J.N., Goff, F., Garcia, S., and Hagan, R.C., 1986, Stratigraphic relations and lithologic variations in the Jemez Volcanic field, New Mexico: Journal of Geophysical Research, v. 91, p. 1763-1778.

Gardner, J.N. and House, L., 1987, Seismic hazards investigations at Los Alamos National Laboratory, 1984-1985: Los Alamos National Laboratory Report LA-11072-MS, 76 p. +maps.

Gardner, J.N., Lavine, A., Lewis, C.J., and Reneau, S.L., 2004, Review and re-evaluation of paleoseismic event chronology from the Pajarito fault system: Los Alamos National Laboratory, New Mexico, 35 p. with figures and tables, 12-06-04 Draft manuscript (in review).

Gardner, J.N., Lavine, A., WoldeGabriel, G., Krier, D., Vaniman, D., Caporuscio, F., Lewis, C., Reneau, P., Kluck, E., and Snow, J.J., 1999, Structural geology of the northwestern portion of Los Alamos National Laboratory, Rio Grande rift, New Mexico: Implications for seismic surface rupture potential from TA-3 to TA-55: Los Alamos National Laboratory Report LA-13589-MS, 112 p.

Gardner, J.N., Lavine, A., WoldeGabriel, G., and Vaniman, D., 1998, High-precision geologic mapping to evaluate the potential for seismic surface rupture at TA-55, Los Alamos National Laboratory: Los Alamos National Laboratory Report LA-13456-MS, 13 p.

Gardner, J.N., Reneau, S.L., Krier, D., Lavine, A., Lewis C.R., WoldeGabriel, G., and Guthrie, G., 2001, Geology of the Pajarito fault zone in the vicinity of S-Site (TA-16), Rio Grande rift, New Mexico: Los Alamos National Laboratory Report LA-13831-MS, 86 p. with 1:6,000 scale geologic map.

Gardner, J.N., Reneau, S.L., Lavine, A., Lewis, C.J., Katzman, D., McDonald, E.V., Lepper, K., Kelson, K.I., and Wilson, C., 2003, Paleoseismic trenching in the Guaje Mountain fault zone, Pajarito fault system, Rio Grande rift, New Mexico: Los Alamos National Laboratory Report LA-14087-MS, 68 p. with 5 plates.

Geli, L., Bard, P.Y., and Jullien, B., 1988, The effect of topography on earthquake ground motion: a review and new results: Bulletin of the Seismological Society of America, v. 78, p. 42-63.

Geovision, 2005, CMRR site, Los Alamos National Laboratory, New Mexico, boreholes SSC-1, SSC-2A, SSC-3, SSC-4, DSC-1B, and DSC-2A suspension P and S velocities: Report 5273-01 Volume 1 of 2, 114 p.

Goff, F., Gardner, J.N., Baldridge, W.S., Hulen, J.B., Nielson, D.L., Vaniman, D., Heiken, G., Dungan, M.A., and Broxton, D., 1989, Excursion 17B: Volcanic and hydrothermal evolution of Valles caldera and Jemez volcanic field: New Mexico Bureau of Mines & Mineral Resources Memoir 46, p. 381-433.

Griggs, R.L., 1964, Geology and groundwater resources of the Los Alamos area, New Mexico: U.S. Geological Survey Water Supply Paper 1753.

Hanks, T.C. and Bakun, W.H., 2002, A bilinear source-scaling model for M-log A observations of continental earthquakes: Bulletin of the Seismological Society of America. v. 92, p. 1841-1846.

Hanks, T.C. and Kanamori, H. 1979, A moment magnitude scale: Journal of Geophysical Research, v. 84, p. 2348-2350.

Hauksson, E., Jones, L.M., Hutton, D., and Eberhart-Phillips, D., 1993, The 1992 Landers earthquake sequence: Seismological observations: Journal of Geophysical research, v. 98, p. 19,835-19,858.

Hawley, J.W., 1986, Physiographic provinces (and) landforms of New Mexico *in* Williams, J.L. (ed.), New Mexico in Maps: Albuquerque, The University of New Mexico Press, p. 28-31.

Hawley, J.W., Haase, C.S., and Lozinsky, R.P., 1995, An underground view of the Albuquerque basin; *in* Ortega-Klett, C.T. (ed.), The water future of Albuquerque and the middle Rio Grande basin: New Mexico Water Resources Research Institute, p. 27-55.

Hawley, J.W., Kottlowski, F.E., Seager, W.R., King, W.E., Strain, W.S., and LeMone, D.V., 1969, The Santa Fe Group in the south-central New Mexico border region: New Mexico Bureau of Mines and Mineral Resources, Circular 104, p. 235-274.

Heiken, G.F., Goff, J., Stix, S., Tamanyu, S., Shafiqullah, M., Garcia, S., and Hagan, R.C., 1986, Intracladera volcanic activity, Toledo caldera and embayment, Jemez Mountains, New Mexico: Journal of Geophysical Research, v. 91, p. 1799-1815.

Idriss, I.M. and Seed, H.B., 1968, Seismic response of horizontal soil layers: Journal of the Soil Mechanics and Foundations Division, v. 94, p. 1003-1031.

Jeon, Y-S. and Herrmann, R.B., 2004, High-frequency earthquake ground-motion scaling in Utah and Yellowstone: Bulletin of the Seismological Society of America, v. 94, p. 1644-1657.

Johnson, L.R. and Silva, W.J., 1981, The effects of unconsolidated sediments upon the ground motion during local earthquakes: Bulletin of the Seismological Society of America, v. 71, p. 127-142.

Kanamori, H., Thio, H.K., Dreger, D., Hauksson, E., and Heaton, T., 1992, Initial investigation of the Landers, California, earthquake of 28 June 1992 using TERRAscope: Geophysical Research Letters, v. 19, p. 2267-2270.

Keefer, D.I. and Bodily, S.E., 1983, Three-point approximations for continuous random variables: Management Science, v. 26, p. 595-609.

Keller, G.R. and Cather, S.M., 1994, Introduction, *in* G.R. Keller and S.M. Cather (eds.), Basins of the Rio Grande Rift: Structure, Stratigraphy, and Tectonic Setting: Geological Society of America Special Paper 291, p. 1-3.

Keller, G.R., Cordell, L., Davis, G.H., Peeples, W.J., and White, G., 1984, A geophysical study of the San Luis Basin: New Mexico Geological Society Guidebook, 35th Field Conference, p. 51-57.

Keller, G.R., Khan, M.A., Morgan, P., Wendlandt, R.F., Baldridge, W.S., Olsen, K.H., Prodehl, C., and Braile, L.W., 1991, A comparative study of the Rio Grande and Kenya rifts, *in* A.F. Gangi (ed.): World Rift Systems, Tectonophysics, v. 197, p. 355-371.

Kelley, S.A., 1995, Evidence for post-Laramide displacement on the Picuris-Pecos Fault: New Mexico Geological Society Guidebook 46, 32-33.

Kelley, V.C., 1977, Geology of the Albuquerque Basin, New Mexico: New Mexico Bureau of Mines and Mineral Resources Memoir 33, 60 p.

Kelley, V.C., 1978, Geology of the Española Basin, New Mexico, New Mexico Bureau of Mines and Mineral Resources Geologic Map 48.

Kelson, K.I., Bauer, P.W., Connell, S.D., Love, D.W., Rawling, G.C., and Mansell, M., 2004b, Initial paleoseismic and hydrogeologic assessment of the southern Sangre de Cristo fault at the Taos Pueblo site, Taos County, New Mexico: New Mexico Geological Society Guidebook, 55th Field Conference, Geology of the Taos Region, p. 289-299.

Kelson, K.I., Bauer, P.W., Unruh, J.R., and Bott, J.D.J., 2004, Late Quaternary characteristics of the northern Embudo fault, Taos County, New Mexico: New Mexico Geological Society Guidebook, 55th Field Conference, Geology of the Taos Region, p. 147-157.

Kelson, K.I., Hemphill-Haley, M.A., Olig, S.S., Simpson, G.D., Gardner, J.N., Reneau, S.L., Kolbe, T.R., Forman, S.L., and Wong, I.G., 1996, Late Pleistocene and possible Holocene displacement along the Rendija Canyon fault, Los Alamos, County, New Mexico: New Mexico Geological Society Guidebook 47, p. 153-160.

Kelson, K.I., Unruh, J.R., and Bott, J.D.J., 1997, Field characterization, kinematic analysis, and initial paleoseismologic assessment of the Embudo fault, northern New Mexico: Geological Society of America Abstracts with Programs, p. A-72.

Kempter, K., Kelley, S., Koning, D., Ferguson, C., Osburn, B., and Fluk, L., 2005, Preliminary geologic map of the Vallecitos 7.5-minute quadrangle, northern Jemez Mountains, New Mexico: New Mexico Bureau of Geology and Mineral Resources Open-File Geologic Map OF-GM108, scale 1:24,000.

Kleinfelder, Inc., 2006, Baseline dynamic properties, Chemistry and Metallurgical Research Replacement (CMRR), Los Alamos National Laboratory, Los Alamos, New Mexico, 91 p.

Kluth, C.F. and Schaftenaar, C.H., 1994, Depth and geometry of the northern Rio Grande rift in the San Luis Basin, south-central Colorado, *in* G.R. Keller and S.M. Cather (eds.), Basins of the Rio Grande Rift: Structure, Stratigraphy, and Tectonic Setting: Geological Society of America Special Paper 291, p. 27-37.

Koning, D.J., 2005, Quaternary terrace deposits along the lower Rio Chama and the Rio Chama-Rio Grande confluence: stratigraphic relations and possible displacement by the Santa Clara fault [minipaper on First-Day Road Log]: New Mexico Geological Society, 56th Field Conference Guidebook Geology of the Chama Basin, p. 6-7.

Koning, D.J., Ferguson, J.F., Jackson Paul, P., and Baldridge, W.S., 2004a, Geologic structure of the Velarde graben and the southern Embudo fault system, north-central New Mexico: New Mexico Geological Society Guidebook, 55th Field Conference, Geology of the Taos Region, p. 158-171.

Kulkarni, R.B., Sadigh, K., and Idriss, I.M., 1979, Probabilistic evaluation of seismic exposure: Proceedings, Second U.S. National Conference on Earthquake Engineering, p. 90-99.

Larsen, S., Reilinger, R., and Brown, L., 1986, Evidence of ongoing crustal deformation related to magmatic activity near Socorro, New Mexico: Journal of Geophysical Research, v. 91, p. 6283-6293.

Lavine, A., Gardner, J.N., and Reneau, S.L., 2003a, Total station geologic mapping: an innovative approach to analyzing surface-faulting hazards: Engineering Geology, v. 70, p. 71-93.

Lavine, A., Lewis, C.J., Katcher, D.K., Gardner, J.N., and Wilson, J., 2003b, Geology of the north-central to northeastern portion of Los Alamos National Laboratory, New Mexico: Los Alamos National Laboratory Report LA-14043-MS, 44 p. with 1:4,000 scale geologic map.

Lee, R., 2005, Review of Geovision (2005) and Redpath (2005), measurement of P- and S-wave velocities collected in boreholes SSC-1, SSC-2A, SSC-3, SSC-4, DSC-1B, and DSC-2A for the CMRR project, unpublished memorandum, 35 p.

Lee, R., 2006a, Review of preliminary interpretation of University of Texa crosshole measurements of P- and S-wave velocities collected between boreholes CHS-4 and SSC-4, CHS-2 and CHS-2A and SSC-2A, CHS-1 and DSC-1A, and CHS-1 and DSC-1B for the CMRR project, unpublished memorandum, 5 p.

Lee, R., 2006b, Draft interpretation of Geophex P-wave velocites, unpublished memorandum.

Lee, R., Maryak, M.E., and Kimball, J., 1999, A methodology to estimate site-specific seismic hazard for critical facilities on soil or soft-rock sites: Seismological Research Letters, v. 70, p. 230.

Lee, R., Silva, W.J., and Cornell, C.A., 1998, Alternatives in evaluating soil- and rock-site seismic hazard: Seismological Research Letters, v. 69, p. 81.

Lewis, C.J., Gardner, J.N., Olig, S., Reneau, S.L., Lavine, A., and Schultz, E.S., 2005, Dilational normal faulting on the Pajarito Plateau, Rio Grande rift, New Mexico: Geological Society of America Abstracts with Programs, v. 37, p. 496.

Lewis, C.J., Gardner, J.N., Schultz, E., Lavine, A., Olig, S., and Reneau, S.L., 2007, Lateral displacement variation and fault interaction, in the Pajarito fault system, Rio Grande rift, New Mexico: Geosphere (in review).

Lewis, C.J., Lavine, A., Reneau, S.L., Gardner, J.N., Channell, R., and Criswell, C.W., 2002, Geology of the western part of Los Alamos National Laboratory (TA-3 to TA-16), Rio Grande rift, New Mexico: Los Alamos National Laboratory Report LA-13960-MS, 98 p. with 1:6,000 scale geologic map.

Lipman, P.W. 1975, Evolution of the Platoro caldero complex and related volcanic rocks, southeastern San Juan Mountains, Colorado: U.S. Geological Survey Professional Paper 852, 128 p.

Lozinsky, R.P., 1994, Cenozoic stratigraphy, sandstone petrology, and depositional history of the Albuquerque Basin, central New Mexico, *in* G.R. Keller and S.M. Cather (eds.), Basins of the Rio Grande Rift: Structure, Stratigraphy, and Tectonic Setting: Geological Society of America Special Paper 291, p. 73-81.

Machette, M.N., 1978a, Dating Quaternary faults in the southwestern United States by using buried calcic paleosols: U.S. Geological Survey Journal of Research, v. 6, p. 369-382.

Machette, M.N., 1978b, Late Cenozoic geology of the San Acecia-Bernardo area: New Mexico Bureau of Mines and Mineral Resources Circular 163, p. 135-137.

Machette, M.N., 1982, Quaternary and Pliocene faults in the La Jencia and southern part of the Albuquerque-Belen basins, New Mexico: Evidence of fault history from fault-scarp morphology and Quaternary geology: New Mexico Geological Society Guidebook, 33rd Field Conference, p. 161-169.

Machette, M.N., 1985, Calcic soils of the southwestern United States, in D.L. Weide (ed.), Soils and Quaternary Geology of the Southwestern United States: U.S. Geological Survey Special Paper 203, p. 1-22.

Machette, M.N., 1998, Contrasts between short- and long-term records of seismicity in the Rio Grande rift – Important implications for seismic hazard assessments in areas of slow extension, *in* W.R. Lund (ed.), Western States Seismic Policy Council Proceedings Volume, Basin and Range Province Seismic Hazards Summit, Utah Geological Survey Miscellaneous Publication 98-2, p. 84-95.

Machette, M.N. and McGimsey, R.G., 1983, Map of Quaternary and Pliocene faults in the Socorro and western part of the Fort Sumner 1° x 2° quadrangles, central New Mexico: U.S. Geological Survey Miscellaneous Field Studies, Map MF-1465-A, scale 1:250,000.

Machette, M.N. and Personius, S.F., 1984, Quaternary and Pliocene faults in the eastern part of the Aztec quadrangle and the western part of the Raton quadrangle, northern New Mexico: U.S. Geological Survey Map MF-1465-B, Scale 1:250,000.

Machette, M.N., Personius, S.F., Kelson, K.I., Haller, K.M., and Dart, R.L., 1998, Map and data for Quaternary faults and folds in New Mexico: U.S. Geological Survey Open-File Report 98-521, 443 p., 1 plate, scale 1:750,000.

Maldonado, F., Connell, S.D., Love, D.W., Grouch, V.J.S., Slate, J.L., McIntosh, W.C., Jackson, P.B., and Byers, F.M., Jr., 1999, Neogene geology of the Isleta Reservation and vicinity, Albuquerque basin, New Mexico, *in* Pazzaglia, F.J. and Lucas, S.G. (eds.), Albuquerque geology: New Mexico Geological Society Guidebook, v. 50, p. 175-188.

Manley, K., 1979a, Stratigraphy and structure of the Española Basin, *in* R.E. Riecker (ed.), Rio Grande Rift: Tectonics and Magmatism: American Geophysical Union, p. 71-86.

Mason, D.B., 1996, Earthquake magnitude potential of the Intermountain Seismic Belt, USA, from surface-parameter scaling of Late Quaternary faults: Bulletin of the Seismological Society of America, v. 86, p. 1487-1506.

McCalpin, J., 1982, Quaternary geology and neotectonics of the west flank of the Northern Sangre de Cristo Mountains, south-central Colorado: Colorado School of Mines Quarterly, v. 77, 89 p.

McCalpin, J.P., 1995, Frequency distribution of geologically determined slip rates for normal faults in the western U.S.: Bulletin of the Seismological Society of America, v. 85, p. 1867-1872.

McCalpin, J.P., 1997, Geomorphology and structure of the Pajarito fault zone west of Los Alamos National Laboratory, New Mexico: unpublished report prepared for Los Alamos National Laboratory by GEO-HAZ Consulting, Inc., Estes Park, Colorado, 56 p.

McCalpin, J.P., 1998, Late Quaternary faulting on the Pajarito fault, west of Los Alamos National Laboratory, north-central New Mexico: Results from seven trenches excavated in summer of 1997: unpublished report prepared for Los Alamos National Laboratory by GEO-HAZ Consulting Inc., Estes Park, Colorado, 112 p., and appendices.

McCalpin, J.P., 1999, Late Quaternary faulting on the Pajarito fault, west of Los Alamos National Laboratory, north-central New Mexico: Results from seven trenches excavated in summer of 1998: unpublished report prepared for Los Alamos National Laboratory by GEO-HAZ Consulting Inc., Estes Park, Colorado, 104 p.

McCalpin, J.P., 2000, Late Quaternary faulting on the Pajarito fault, west of Los Alamos National Laboratory, north-central New Mexico: Summary chronology of Quaternary faulting events: unpublished report prepared for Los Alamos National Laboratory by GEO-HAZ Consulting Inc., Estes Park, Colorado, 104 p.

McCalpin, J.P., 2005, Late Quaternary activity of the Pajarito fault, Rio Grande rift of northern New Mexico, USA: Tectonophysics, v. 408, p. 213-236.

McCalpin, J.P. and Harrison, J.B.J., 2000, Paleoseismicity of Quaternary faults near Albuquerque, New Mexico: unpublished semi-final Technical Report submitted to U.S. Geological Survey by GEO-HAZ Consulting, Inc., 46 p.

McCalpin, J.P. and Harrison, J.B.J., 2001, Paleoseismicity of Quaternary faults near Albuquerque, New Mexico: unpublished Final Technical Report submitted to U.S. Geological Survey by GEO-HAZ Consulting, Inc., 58 p.

McCalpin, J.P., Harrison, J.B.J., and Berger, G.W., Tobin, H.C., 2000, Paleoseismicity of a low-slip normal fault in the Rio Grande rift, U.S.A.: The Calabacillas fault, Albuquerque, New Mexico: Draft manuscript in preparation.

McCalpin, J.P., Olig, S.S., Harrison, J.B.J., and Berger, G.W., 2006, Quaternary faulting and soil formation on the County Dump fault, Albuquerque, New Mexico: New Mexico Bureau of Mines and Geology, Circular 212, 36 p.

McGuire, R.K., Silva, W.J., and Costantino, C.J., 2001, Technical basis for revision of regulatory guidance on design ground motions: Hazard- and risk-consistent ground motion spectra guidelines: U.S. Nuclear Regulatory Commission NUREG/CR-6728.

McGuire, R.K., Silva, W.J., and Costantino, C.J., 2002, Technical basis for revision of regulatory guidance on design ground motions, report prepared for U.S. Nuclear Regulatory Commission NUREG/CR-6769.

McNamara, D.E., Frankel, A.D., Wesson, R.L., and Benz, H.M., 2004, Lg Q in the North American mid-continent: Bulletin of the Seismological Society of America, v. 94, p. 1630-1643.

Mendoza, C. and Hartzell, S.H., 1988, Inversion for slip distribution using teleseismic P waveforms: North Palm Springs, Borah Peak and Michoacan Earthquakes: Bulletin of the Seismological Society of America, v. 78, p. 1092-1111.

Menges, C.M, 1988, The tectonic geomorphology of mountain front landforms in the northern Rio Grande rift, New Mexico, Albuquerque, Ph.D. Thesis, University of New Mexico, 140 p.

Menges, C.M., 1990a, Late Cenozoic rift tectonics and mountain-front landforms of the Sangre de Cristo Mountains near Taos, Northern New Mexico, New Mexico Geological Society Guidebook, 41st Field Conference, New Mexico, p. 113-122.

Menges, C.M., 1990b, Late Quaternary fault scarps, mountain-front landforms, and Pliocene-Quaternary segmentation on the range-bounding fault zone, Sangre de Cristo Mountains, New Mexico, *in* E.L. Krinitzsky and D.B. Slemmons (eds.), Neotectonics in Earthquake Evaluation: Geological Society of America Reviews in Engineering Geology, v. 8, p. 131-156.

Miller, A.C. and Rice, T.R., 1983, Discrete approximations of probability distributions: Management Science, v. 29, p. 352-362.

Minor, S.A., Hudson, M.R., Grauch, V.J.S., and Sawyer, D.A., 2005, Structure of the Santo Domingo basin and La Bajada constriction (Chapter E), *in* Scott A. Minor (ed.), The Cerrillos Uplift, La Bajada Constriction, and Hydrogeologic Framework of the Santo Domingo Basin, Rio Grande Rift, New Mexico: U.S. Geological Survey Professional Paper 16XX (in press).

Morley, C.K., Nelson, R.A., Patton, T.L., and Munn, S.G., 1990, Transfer zones in the East African rift system and their relevance to hydrocarbon exploration in rifts: American Association of Petroleum Geologists Bulletin, v. 74, p 1234-1253.

Muehlberger, W.R., 1979, The Embudo fault between Pilar and Arroyo Hondo, New Mexico: An active intracontinental transform fault: New Mexico Geological Society Guidebook, 30th Field Conference, p. 77-82.

Olig, S.S., Eppes, M.C., Forman, S.L., Love, D.W., and Allen, B.D., 2004, Paleoseismic investigation of the central Hubbell Spring fault, central New Mexico: URS Corporation unpublished final technical report to the U.S. Geological Survey, NEHRP Award No. 99HQGR0089, variously paginated.

Olig, S.S., Eppes, M.C., Forman, S.L., Love, D.W., and Allen, B.D., 2005, Prehistoric earthquakes on the Hubbell Spring fault: Evidence for coseismic noncharacteristic rupture of intrabasin faults in the Rio Grande rift, *in* Proceedings Volume of the Basin and Range Province Seismic Hazards Summit II, Lund, W.R., (ed.), Utah Geological Survey Miscellaneous Publication 05-2, p. 114-117.

Olig, S.S., Kelson, K.I., Gardner, J.N., Reneau, S.L., and Hemphill-Haley, M., 1996, The earthquake potential of the Pajarito fault system, New Mexico: New Mexico Geological Society Guidebook 47, p.143-151.

Olig, S.S., Youngs, R., and Wong, I.G., 1998, Probabilistic seismic hazard analysis for surface fault displacement at TA-3, Los Alamos National Laboratory: unpublished report prepared for Los Alamos National Laboratory by Woodward-Clyde Federal Services.

Olig, S.S., Youngs, R., and Wong, I.G., 2001, Probabilistic seismic hazard analysis for surface fault displacement at TA-16, Los Alamos National Laboratory: unpublished report prepared for Los Alamos National Laboratory by URS Corporation.

Olig, S., Zachariasen, J., Wong, I., and Dober, M., 2007, Paleoseismic evidence for longer and more complex rupture patterns on the Hubbell Spring fault system, Rio Grande rift, New Mexico: implications for recurrence models and their use in hazard analysis (abs.): Seismological Research Letters, v. 78, p. 315.

Olsen, K.H., 1979, The seismicity of north-central New Mexico with particular reference to the Cerrillos earthquake of May 28, 1918: New Mexico Geology Society Guidebook v. 30, p. 65-75.

Pankow, K.L. and Pechmann, J.C., 2004, The SEA99 ground motion predictive relations for extensional tectonic regimes: Revisions and a new peak ground velocity relation: Bulletin of the Seismological Society of America, v. 94, p. 341-348.

Paolucci, R., 2002, Amplification of earthquake ground motion by steep topographic irregularities: Earthquake Engineering Structural Dynamics, v. 31, p. 1831-1853.

Pedersen, H., Le Brun, B., Hatzfeld, D., Campillo, M., and Bard, P.–Y., 1994, Ground-motion amplitude across ridges: Bulletin of the Seismological Society of America, v. 84, p. 1786-1800.

Personius, S.F., Eppes, M.C., Mahan, S.A., Love, D.W., Mitchell, D.K., and Murphy, A., 2001, Log and data from a trench across the Hubbell Spring fault zone, Bernalillo County, New Mexico: U.S. Geological Survey Miscellaneous Field Studies Map MF-2348, v. 1.1.

Personius, S.F. and Mahan, S.A., 2000, Paleoearthquake recurrence on the East Paradise fault zone, metropolitan Albuquerque, New Mexico: Bulletin of the Seismological Society of America, v. 90, p. 357-369.

Personius, S.F. and Mahan, S.A., 2003, Paleoearthquakes and eolian-dominated fault sedimentation along the Hubbell Spring fault zone near Albuquerque, New Mexico: Bulletin of the Seismological Society of America, v. 93, p. 1,355-1,369.

Phillips, F.M., Ayarbe, J.P., Harrison, B.J., and Elmore, D., 2003, Dating rupture events on alluvial fault scarps using cosmogenic nuclides and scarp morphology: Earthquake and Planetary Science Letters, v. 215, p. 203-218.

Phillips, W.M., McDonald, E.V., Reneau, S.L., and Poths, J., 1998, Dating soil sand alluvium with cosmogenic ^{21}Ne depth profiles: Case studies from the Pajarito Plateau, New Mexico: Earth and Planetary Science Letters, v. 160, p. 209-223.

Redpath Geophysics, 2005, Downhole velocity surveys for the Los Alamos CMRR project: unpublished report prepared for Kleinfelder, Inc.

Reid, H.F., 1911, Remarkable earthquakes in central New Mexico in 1906 and 1907: Bulletin of the Seismological Society of America, v.1, p.10-16.

Reiter, M., Clarkson G., and Shearer, C., 1979, Geothermal characteristics of the Rio Grande rift within the southern Rocky Mountain complex, *in* R.E. Riecker (ed.), Rio Grande Rift-Tectonics and Magmatism, American Geophysical Union, p. 253-267.

Reneau, S.L., Gardner, J.N., and Forman, S.L., 1996, New evidence for the age of the youngest eruptions in the Valles caldera, New Mexico: Geology, v. 24, p. 7-10.

Reneau, S.L., Gardner, J.N., Lavine, A., McDonald, E.V., Lewis, C., Katzman, D., WoldeGabriel, G., Krier, D., Bergfeld, D., and Heikoop, J., 2002, Paleoseismic investigation of trench EOC-2, Pajarito fault zone, Los Alamos National Laboratory, New Mexico: Los Alamos National Laboratory Report LA-13939-MS, 65 p. with four plates.

Rosendahl, B.R., 1987, Architecture of continental rifts with special reference to East Africa: Annual Review of Earth and Planetary Sciences, v. 15, p. 445-503.

Russell, L.R. and Snelson, S., 1990, Structural style and tectonic evolution of the Albuquerque basin segment of the Rio Grande rift, *in* B. Pinet and C. Bois (eds.), The Potential of Deep Seismic Profiling for Hydrocarbon Exploration, p. 175-207.

Russell, L.R. and Snelson, S. 1994. Structure and tectonics of the Albuquerque Basin segment of the Rio Grande rift: Insights from reflection seismic data, *in* G.R. Keller and S.M. Cather (eds.), Basins of the Rio Grande Rift: Structure, Stratigraphy, and Tectonic Setting, Geological Society of America Special Paper 291, p. 83-112.

Sadigh, K., Chang, C.-Y., Egan, J.A., Makdisi, F., and Youngs, R.R., 1997, Attenuation relationships for shallow crustal earthquakes based on California strong motion data: Seismological Research Letters, v. 68, p. 180-189.

Sanford, A.R., Jaksha, L.H., and Cash, D.J., 1991, Seismicity of the Rio Grande rift in New Mexico, *in* D.B. Slemmons, E.R. Engdahl, M.D. Zoback, and D.D. Blackwell (eds.), Neotectonics of North America, Geological Society of America Decade Map, v. 1, p. 229-244.

Sanford, A.R., Lin, K.W., Tsai, I.C., and Jaksha, L.H., 2002, Earthquake catalogs for New Mexico and bordering areas: 1869-1998: New Mexico Bureau of Mines and Mineral Resources Circular 210, 101 p.

Sanford, A.R., Olsen, K.H., and Jaksha, L.H., 1979, Seismicity of the Rio Grande rift, *in* R.E. Riecker (ed.), Rio Grande Rift: Tectonics and Magmatism: American Geophysical Union, p. 145-168.

Sanford, A.R., Olsen, K.H., and Jaksha, L.H., 1981, Earthquakes in New Mexico, 1849-1977: New Mexico Bureau of Mines and Mineral Resources Circular 171, 20 p.

Schnabel, P.B., Lysmer, J. and Seed, H.B., 1972, SHAKE - A computer program for earthquake analysis of horizontally layered sites: Earthquake Engineering Research Center, University of California, Berkeley, Report No. EERC 72-12.

Schneider, J.F., Silva, W.J., and Stark, C.L., 1993, Ground motion model for the 1989 M 6.9 Loma Prieta earthquake including effects of source, path and site: Earthquake Spectra, v. 9, p. 251-287.

Schultz, E.S., Lewis, C.J., Lavine, A., Gardner, J.N., and Reneau, S.L., 2003, Along-strike variation in a faulted monocline, Pajarito fault, Los Alamo, New Mexico: Geological Society of America Abstracts with Programs, v. 34, p. 581-582.

Schwartz, D.P. and Coppersmith, K.J., 1984, Fault behavior and characteristic earthquakes--examples from the Wasatch and San Andreas fault zones: Journal of Geophysical Research, v. 89, p. 5681-5698.

Schwartz, D.P., Coppersmith, K.J., and Swan III, F.H., 1984, Methods for estimating maximum earthquake magnitudes: Proceedings of the Eighth World Conference on Earthquake Engineering (Prentice-Hall), p. 279-285.

Seed, H.B. and Idriss, I.M., 1969, The influence of soil conditions on ground motions during earthquakes: Journal of the Soil Mechanics Foundation Engineering Division, v. 95, p. 99-137.

Self, S., Kircher, D.E., and Wolff, J.A., 1988, The El Cajete Series, Valles caldera, New Mexico: Journal of Geophysical Research, v. 93, p. 6113-6127.

Senior Seismic Hazard Analysis Committee (SSHAC), 1997, Recommendations for probabilistic seismic hazard analysis-guidance on uncertainty and use of experts: U.S. Nuclear Regulatory Commission NUREG/CR-6327, variously paginated.

Sieh, K., Jones, L., Hauksson, E., Hudnut, K., Eberhart-Phillips, D., Heaton, T., Hough, S., Hutton, K., Kanamori, H., Lilje, A., Lindval, S., McGill, S.F., Mori, J., Rubin, C., Spotila, J.A., Stock, J., Thio, H., Treiman, J., Wernicke, B., and Zachariasen, J., 1993, Near-field investigation of the Landers earthquake sequence, April to July, 1992: Science, v. 260, p. 171-176.

Silva, W.J., 1976, Body waves in a layered anelastic solid: Bulletin of the Seismological Society of America, v. 66, p. 1539-1554.

Silva, W.J., 1997, Characteristics of vertical strong ground motions for applications to engineering design, *in* I.M. Friedland, M.S Power, and R. L. Mayes (eds.), Proceedings, FHWA/NCEER Workshop on the National Representation of Seismic Ground Motion for New and Existing Highway Facilities, Technical Report NCEER-97-0010.

Silva, W.J., 2005, Evaluation of the potential for topographic effects at the proposed location of the CMRR facility (TA-55), unpublished report, 15 p.

Silva, W.J., Abrahamson, N., Toro, G., and Costantino, C, 1996, Description and Validation of the Stochastic Ground Motion Model: unpublished report prepared for Brookhaven National Laboratory by Pacific Engineering and Analysis.

Silva, W.J., Costantino, C., and Li, S., 1998, Quantification of nonlinear soil response for the Loma Prieta, Northridge, and Imperial Valley California earthquakes, *in* Irikura, Kudo, Okada & Sasatani (eds.), Proceedings, The Second International Symposium on the Effects of Surface Geology on Seismic Motion Seismic Motion, p. 1137—1143.

Silva, W.J. and Darragh, R., 1995, Engineering characterization of earthquake strong ground motion recorded at rock sites: Electric Power Research Institute, Final Report RP 2556-48.

Silva, W.J. and Lee, K., 1987, WES RASCAL code for synthesizing earthquake ground motions: State-of-the-art for Assessing Earthquake Hazards in the United States, Report 24: U.S. Army Engineer Waterways Experiment Station Miscellaneous Paper S-73-1, 120 p.

Singh, S. and Herrmann, R.B., 1983, Regionalization of crustal coda Q in the continental United States: Journal of Geophysical Research, v. 88, p. 527-538.

Smith, R.L. and Bailey, R.A., 1968, Resurgent cauldrons: Geological Society of America Memoir 116, p. 613-662.

Smith, R.L., Bailey, R.A., and Ross, C.S., 1970, Geologic map of the Jemez Mountains, New Mexico: U.S. Geological Survey Miscellaneous Investigation Map I-571.

Smith, G.A. and Kuhle, A.J., 1998, Geologic map of the Santo Domingo Pueblo quadrangle, Sandoval County, New Mexico: New Mexico Bureau of Mines and Mineral Resources Open-File Digital Map OF-DM 15, 1 sheet, scale 1:24,000.

Spudich, P., Joyner, W.B., Lindh, A.G., Boore, D.M., Margaris, B.M., and Fletcher, J.B., 1999, SEA99 - A revised ground motion prediction relation for use in extensional tectonic regimes: Bulletin of the Seismological Society of America, v. 89, p. 1156-1170.

Stearns, C.E., 1953, Tertiary geology of the Galisteo-Tonque area, New Mexico: Geological Society of America Bulletin, v. 64, p. 459-508.

Steven, T.A., 1975, Middle Tertiary volcanic field in the southern Rocky Mountains, in Cenozoic history of the southern Rocky Mountains: Geological Society of America Memoir 144, p. 75-94.

Stirling, M., Rhoades, D., and Berryman, K., 2002, Comparison of earthquake scaling relations derived from data of the instrumental and preinstrumental era: Bulletin of the Seismological Society of America, v. 92, p. 812-830.

Stokoe, K.H., Hwang, S.K., and Laird, J.P., 1993, Dynamic properties of undisturbed soil samples from Los Alamos, New Mexico, unpublished report prepared for Woodward-Clyde Federal Services.

Suter, M. and Contreras, J., 2002, Active tectonics of northeastern Sonora, Mexico (southern Basin and Range Province) and the 3 May 1887 M_W 7.4 earthquake: Bulletin of the Seismological Society of America, v. 92, p. 581-589.

Uhrhammer, R.A., 1986, Characteristics of northern and central California seismicity (abs.): Earthquake Notes, v. 57, p. 21.

University of Texas at Austin (UTA), Geotechnical Research Center, 2006a, Seismic crosshole testing at Los Alamos National Laboratory, CMRR site, unpublished report.

University of Texas at Austin (UTA), Geotechnical Research Center, 2006b, Laboratory data report, intact dacite, tuff, and soil specimens, Chemistry and Metallurgical Research Replacement (CMRR) project, Los Alamos National Laboratory, Report No. GR06-01, Volume I of IV.

U.S. Nuclear Regulatory Commission (NRC), 1997, Identification and characterization of seismic sources and determination of safe shutdown ground motion: Regulatory Guide 1.165.

Vernon, J.H. and Riecker, R.E., 1989, Significant Cenozoic faulting, east margin of the Española Basin, Rio Grande rift, New Mexico: Geology, v. 17 p. 230-233.

Wald, D.J. and Heaton, T.H., 1994, Spatial and temporal distribution of slip for the 1992 Landers, California, earthquake: Bulletin of the Seismological Society of America, v. 84, p. 668-691.

Weichert, D.H., 1980, Estimation of the earthquake recurrence parameters for unequal observation periods for different magnitudes: Bulletin of the Seismological Society of America, v. 70, p. 1337-1346.

Wells, D. L. and Coppersmith, K. J., 1994, Analysis of empirical relationships among magnitude, rupture length, rupture area, and surface displacement: Bulletin of the Seismological Society of America, v. 84, p. 974-1002.

Wesnousky, S.G., 1986, Earthquakes, Quaternary faults, and seismic hazard in California: Journal Geophysical Research, v. 91, p. 12,587-12,631.

Wong, I.G., Cash, D., and Jaksha, L., 1984, The Crownpoint, New Mexico earthquakes of 1976 and 1977: Bulletin of the Seismological Society of America, v. 74, p. 2435-2449.

Wong, I.G. and Chapman, D.S., 1990, Deep intraplate earthquakes in the western U.S. and their relationship to lithospheric temperatures: Bulletin of the Seismological Society of America, v. 80, p. 589-599.

Wong, I.G. and Humphrey, J.R., 1989, Contemporary seismicity, faulting, and the state of stress in the Colorado Plateau: Geological Society of America Bulletin, v. 101, p. 1127-1146.

Wong, I., Kelson, K., Olig, S., Bott, J., Green, R., Kolbe, T., Hemphill-Haley, M., Gardner, J., Reneau, S., and Silva, W., 1996, Earthquake potential and ground shaking hazard at the Los Alamos National Laboratory, New Mexico: New Mexico Geological Society Guidebook 47, p.135-142.

Wong, I., Kelson, K., Olig, S., Kolbe, T., Hemphill-Haley, M., Bott, J., Green, R., Kanakari, H., Sawyer, J., Silva, W., Stark, C., Haraden, C., Fenton, C., Unruh, J., Gardner, J., Reneau, S., and House, L., 1995, Seismic hazard evaluation of the Los Alamos National Laboratory: unpublished final report prepared for the Los Alamos National Laboratory and the U.S. Department of Energy, 3 volumes.

Wong, I.G. and Olig, S.S., 1998, Seismic hazards in the Basin and Range Province: Perspectives from probabilistic analyses, *in* Western States Seismic Policy Council, Proceedings Volume, Basin and Range Province Seismic-Hazards Summit, W.R. Lund (ed.), Utah Geological Survey Miscellaneous Publication 98-2, p. 110-127.

Wong, I., Olig, S., Dober, M., Silva, W., Wright, D., Thomas, P., Gregor, N., Sanford, A., Lin, K., and Love, D., 2004, Earthquake scenario and probabilistic ground-shaking hazard maps for the Albuquerque-Belen-Santa Fe, New Mexico corridor: New Mexico Geology, v. 26, p. 3-33.

Woodward, L.A., 1977, Rate of crustal extension across the Rio Grande Rift near Albuquerque, New Mexico: Geology, v. 5, p. 269–272.

Woodward-Clyde Federal Services (WCFS), 1995, Seismic hazards evaluation of the Los Alamos National Laboratory: unpublished report prepared for the Los Alamos National Laboratory, 3 volumes.

Working Group for California Earthquake Probabilities (WGCEP), 2003, Earthquake probabilities in the San Francisco Bay area: 2002-2031: U.S. Geological Survey Open-File Report 03-214.

Youngs, R.R. and Coppersmith, K.J., 1985, Implications of fault slip rates and earthquake recurrence models to probabilistic seismic hazard estimates: Bulletin of the Seismological Society of America, v. 75, p. 939-965.

Youngs, R.R., Arabasz, W.J., Anderson, R.E., Ramelli, A.R., Ake, J.P., Slemmons, D.B., McCalpin, J.P., Doser, D.I., Fridrich, C.J., Swan III, F.H., Rogers, A.M., Yount, J.C., Anderson, L.W., Smith, K.D., Bruhn, R.L., Knuepfer, P.L.K., Smith, R.B., dePolo, C.M., O'Leary, D.W., Coppersmith, K.J., Pezzopane, S.K., Schwartz, D.P., Whitney, J.W., Olig, S.S., and Toro, G.R., 2003, A methodology for probabilistic fault displacement hazard analysis (PFDHA): Earthquake Spectra, v. 19, p. 191-219.

Youngs, R.R., Swan, F.H., Power, M.S., Schwartz, D.P., and Green, R.K., 2000, Probabilistic analysis of earthquake ground shaking hazard along the Wasatch Front, Utah, *in* P.L. Gori and W.W. Hays (eds.), Assessment of Regional Earthquake Hazards and Risk Along the Wasatch Front, Utah: U.S. Geological Survey Professional Paper 1500-K-R, p. M1-M74.

Zoback, M.D. and Zoback, M.L., 1991, Tectonic stress field of North America and relative plate motions, *in* Slemmons, D.B., Engdahl, E.R., Zoback, M.D., and Blackwell, D. (eds.), Neotectonics of North America: Geological Society of America, Decade Map Volume I, p. 339-366.